VOLUME 18 NUMBER 11 NOVEMBER 2012
www.nature.com/naturemedicine

nature medicine

Oxidative regulation of leukemia stem cells
Targeted therapies for spinal muscular atrophy
Chromothripsis in cancer

BENTHAM SCIENCE

www.benthamscience.com

ESSENTIAL JOURNALS IN MOLECULAR MEDICINE

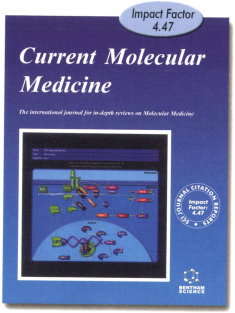
Impact Factor 4.47
Current Molecular Medicine
The international journal for in-depth reviews on Molecular Medicine
BENTHAM SCIENCE

www.benthamscience.com/cmm

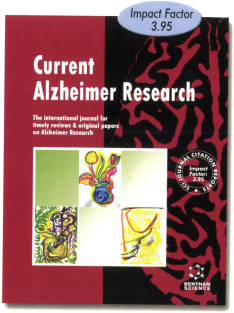
Impact Factor 3.95
Current Alzheimer Research
The international journal for timely reviews & original papers on Alzheimer Research
BENTHAM SCIENCE

www.benthamscience.com/car

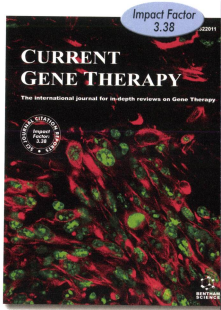
Impact Factor 3.38
CURRENT GENE THERAPY
The international journal for in-depth reviews on Gene Therapy
BENTHAM SCIENCE

www.benthamscience.com/cgt

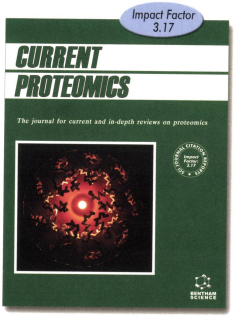

www.benthamscience.com/cp

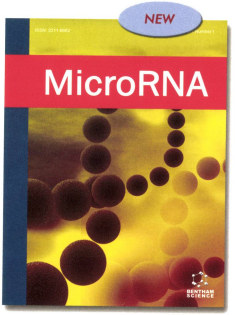

www.benthamscience.com/mirna

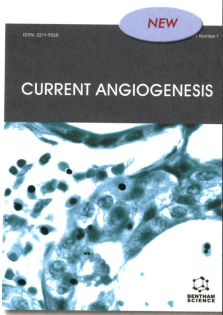

www.benthamscience.com/cag

Publishers of Quality Research

For Subscriptions
Contact: subscriptions@benthamscience.org

For Advertising & Free Online Trials
Contact: marketing@benthamscience.org

VOLUME 18 NUMBER 11 NOVEMBER 2012

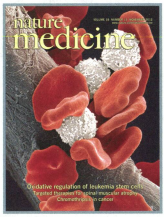
nature medicine
Oxidative regulation of leukemia stem cells
Targeted Disease Pathway Inhibitor and Cocaine Addiction

In this issue, Andrew Weng and his colleagues uncover a new mechanism by which oncogenes regulate leukemia stem cells. Notch-driven inactivation of PKCδ attenuates the accumulation of reactive oxygen species to lower oxidative stress in the stem cell population of T cell acute lymphoblastic leukemia (ALL), contributing to tumorigenesis. The image shows an electron micrograph of erythrocytes and lymphocytes from a patient with ALL. Photo by Steve Gschmeissner/Science Photo Library.

Prisons fail to deliver full access to new Hep C drugs (p 1594)

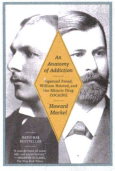

Cocaine, sex and physicians (p 1608)

nature medicine

EDITORIAL

1593 Toward clinical transparency

NEWS

1594 Prisoners, hard hit by hepatitis C, decry lack of access to drugs
1595 Group purchasing plan launched to save on research supplies
1596 Europe plays catch-up on neonatal screening as US skips ahead
1597 Targeted vaccines against feline dander could be the cat's meow
1598 New NIH effort seeks to find ways to make trials run smoother
1598 Spain sees worrying dip in research spending by drug companies
1599 Q&A: David Baker
1600 NEWS IN BRIEF
1602 NEWS FEATURE: Call in the backup
1607 OPINION: Clinical trials must cope better with multiplicity

BOOK REVIEW

1608 An Anatomy of Addiction: Sigmund Freud, William Halsted, and the Miracle Drug Cocaine
Howard Markel
Reviewed by John Mendelson

NEWS AND VIEWS

1609 Not just a rush of blood to the head
Andrew J Brumm & S Thomas Carmichael ▸*see also p 1658*

1611 SAMHD1 does it again, now in resting T cells
Nan Yan & Judy Lieberman ▸*see also p 1682*

1613 Waking up HSCs: a new role for E-selectin
Malcolm A S Moore ▸*see also p 1651*

1614 Protective immunity from a germinal center sanctuary
Harriet L Robinson & Rama Rao Amara ▸*see also p 1673*

1616 A sweet surprise for HIV broadly neutralizing antibodies
Johannes P M Langedijk & Hanneke Schuitemaker ▸*see also p 1688*

1617 A sirtuin link between metabolism and heart disease
Keith A Webster ▸*see also p 1643*

1619 Small airways, big challenge: measuring the unseen?
Salman Siddiqui & Omar S Usmani ▸*see also p 1711*

Nature Medicine (ISSN 1078-8956) is published monthly by Nature Publishing Group, a trading name of Nature America Inc. located at 75 Varick Street, Fl 9, New York, NY 10013-1917. Periodicals postage paid at New York, NY and additional mailing post offices. **Editorial Office:** 75 Varick Street, Fl 9, New York, NY 10013-1917. Tel: (212) 726 9325, Fax: (212) 683 5751. **Annual subscription rates:** USA/Canada: US$225 (personal), US$4,677 (institution). Canada add 7% GST #140911595rt001; Euro-zone: €287 (personal), €3,713 (institution); Rest of world (excluding China, Japan, Korea): £185 (personal), £2,400 (institution); Japan: Contact NPG Nature Asia-Pacific, Chiyoda Building, 2-37 Ichigayatamachi, Shinjuku-ku, Tokyo 162-0843. Tel: 81 (03) 3267 8751, Fax: 81 (03) 3267 8746. **POSTMASTER:** Send address changes to *Nature Medicine*, Subscriptions Department, 75 Varick Street, 9th Floor, New York, NY 10013-1917. **Authorization to photocopy** material for internal or personal use, or internal or personal use of specific clients, is granted by Nature Publishing Group to libraries and others registered with the Copyright Clearance Center (CCC) Transactional Reporting Service, provided the relevant copyright fee is paid direct to CCC, 222 Rosewood Drive, Danvers, MA 01923, USA. Identification code for *Nature Medicine*: 1078-8956/04. **Back issues:** US$45, Canada add 7% for GST. CPC PUB AGREEMENT #40032744. Printed on acid-free paper by The Sheridan Press, Hanover, PA, USA. Copyright © 2012 Nature Publishing Group. Printed in USA.

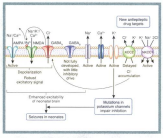

Understanding the roots of epilepsy (p 1624)

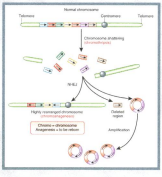

Chromosome shattering mechanisms (p 1630)

Unraveling doxorubicin toxicity (p 1639)

1622 **COMMUNITY CORNER:** Defeating dengue: a challenge for a vaccine

BETWEEN BEDSIDE AND BENCH

BEFORE EPILEPSY UNFOLDS

1624 **Opening up the potassium door in neonatal seizures**
Rod C Scott & Gregory L Holmes

1626 **Finding the epileptogenesis switch**
Annamaria Vezzani

1628 **RESEARCH HIGHLIGHTS**

PERSPECTIVE

1630 **Chromoanagenesis and cancer: mechanisms and consequences of localized, complex chromosomal rearrangements**
A J Holland & D W Cleveland

BRIEF COMMUNICATION

1639 **Identification of the molecular basis of doxorubicin-induced cardiotoxicity**
S Zhang, X Liu, T Bawa-Khalfe, L-S Lu, Y L Lyu, L F Liu & E T H Yeh

ARTICLES

1643 **The sirtuin SIRT6 blocks IGF-Akt signaling and development of cardiac hypertrophy by targeting c-Jun**
N R Sundaresan, P Vasudevan, L Zhong, G Kim, S Samant, V Parekh, V B Pillai, P V Ravindra, M Gupta, V Jeevanandam, J M Cunningham, C-X Deng, D B Lombard, R Mostoslavsky & M P Gupta ▸*see also p 1617*

1651 **Vascular niche E-selectin regulates hematopoietic stem cell dormancy, self renewal and chemoresistance**
I G Winkler, V Barbier, B Nowlan, R N Jacobsen, C E Forristal, J T Patton, J L Magnani & J-P Lévesque ▸*see also p 1613*

1658 **Angiogenesis induced by CNS inflammation promotes neuronal remodeling through vessel-derived prostacyclin**
R Muramatsu, C Takahashi, S Miyake, H Fujimura, H Mochizuki & T Yamashita ▸*see also p 1609*

1665 **Immunomodulatory glycan LNFPIII alleviates hepatosteatosis and insulin resistance through direct and indirect control of metabolic pathways**
P Bhargava, C Li, K J Stanya, D Jacobi, L Dai, S Liu, M R Gangl, D A Harn & C-H Lee

1673 **Lymph node T cell responses predict the efficacy of live attenuated SIV vaccines**
Y Fukazawa, H Park, M J Cameron, F Lefebvre, R Lum, N Coombes, E Mahyari, S I Hagen, J Y Bae, M D Reyes III, T Swanson, A W Legasse, A Sylwester, S G Hansen, A T Smith, P Stafova, R Shoemaker, Y Li, K Oswald, M K Axthelm, A McDermott, G Ferrari, D C Montefiori, P T Edlefsen, M Piatak Jr, J D Lifson, R P Sékaly & L J Picker ▸*see also p 1614*

Sirtuins protect the heart
(pp 1617 and 1643)

New therapeutic targets for lymphoma
(p 1699)

Tracking COPD progression by CT
(pp 1619 and 1711)

LETTERS

1682 SAMHD1 restricts HIV-1 infection in resting CD4⁺ T cells
H-M Baldauf, X Pan, E Erikson, S Schmidt, W Daddacha, M Burggraf, K Schenkova, I Ambiel, G Wabnitz, T Gramberg, S Panitz, E Flory, N R Landau, S Sertel, F Rutsch, F Lasitschka, B Kim, R König, O T Fackler & O T Keppler ▸*see also p 1611*

1688 Evolution of an HIV glycan–dependent broadly neutralizing antibody epitope through immune escape
P L Moore, E S Gray, C K Wibmer, J N Bhiman, M Nonyane, D J Sheward, T Hermanus, S Bajimaya, N L Tumba, M-R Abrahams, B E Lambson, N Ranchobe, L Ping, N Ngandu, Q A Karim, S S A Karim, R I Swanstrom, M S Seaman, C Williamson & L Morris ▸*see also p 1616*

1693 NOTCH1 promotes T cell leukemia-initiating activity by RUNX-mediated regulation of PKC-θ and reactive oxygen species
V Giambra, C R Jenkins, H Wang, S H Lam, O O Shevchuk, O Nemirovsky, C Wai, S Gusscott, M Y Chiang, J C Aster, R K Humphries, C Eaves & A P Weng

1699 PDGFR blockade is a rational and effective therapy for NPM-ALK–driven lymphomas
D Laimer, H Dolznig, K Kollmann, P W Vesely, M Schlederer, O Merkel, A-I Schiefer, M R Hassler, S Heider, L Amenitsch, C Thallinger, P B Staber, I Simonitsch-Klupp, M Artaker, S Lagger, S D Turner, S Pileri, P P Piccaluga, P Valent, K Messana, I Landra, T Weichhart, S Knapp, M Shehata, M Todaro, V Sexl, G Höfler, R Piva, E Medico, B A Ruggeri, M Cheng, R Eferl, G Egger, J M Penninger, U Jaeger, R Moriggl, G Inghirami & L Kenner

1705 The Toll-like receptor 5 ligand flagellin promotes asthma by priming allergic responses to indoor allergens
R H Wilson, S Maruoka, G S Whitehead, J F Foley, G P Flake, M L Sever, D C Zeldin, M Kraft, S Garantziotis, H Nakano & D N Cook

TECHNICAL REPORT

1711 Computed tomography–based biomarker provides unique signature for diagnosis of COPD phenotypes and disease progression
C J Galbán, M K Han, J L Boes, K A Chughtai, C R Meyer, T D Johnson, S Galbán, A Rehemtulla, E A Kazerooni, F J Martinez & B D Ross ▸*see also p 1619*

NATURE MEDICINE CLASSIFIED

See back pages.

RNAscope®

in situ hybridization
easy. powerful.

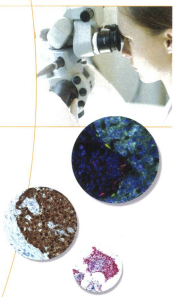

VISUALIZE
single-copy RNA expression
for virtually ANY gene

Biomarker Analysis
Target ID & Validation
Molecular Pathology
Companion Dx
Validate IHC Results
Non-coding RNA
Stem Cell Research
Tumor Heterogeneity
Rare-cell Analysis

1-877-576-3636 | www.acdbio.com

ACD
Building the shortest path to personalized medicine
ADVANCED CELL DIAGNOSTICS, INC

nature medicine

www.nature.com/naturemedicine

EDITORIAL OFFICE medicine@us.nature.com
75 Varick Street, Fl 9, New York, NY 10013-1917
Tel: (212) 726 9325, Fax: (212) 683 5751
Chief Editor: Juan Carlos Lopez
Senior News Editor: Roxanne Khamsi
News Editor: Elie Dolgin
Editorial Interns, News: Susan Matthews, Kathleen Raven
Associate Editors, Reviews and News and Views: Carolina Pola, Meera Swami
Senior Editors, Research Manuscripts: Michael Basson, Eva Chmielnicki, Alison Farrell, Randy Levinson
Associate Editors, Research Manuscripts: Victoria Aranda, Kevin Da Silva
Editor, Technical Reports: Diane Gershon
Copy Editors: Katherine Goen, Heidi Reinholdt
Senior Production Editor: Matt Hansen
Production Editor: Jamel Wooten
Senior Illustrator/Cover Design: Katie Vicari
Illustrator: Marina Corral
Editorial Assistant: Somaliyah Al-Mahdi

MANAGEMENT OFFICES
NPG New York
75 Varick Street, Fl 9, New York, NY 10013-1917
Tel: (212) 726 9200, Fax: (212) 696 9006
Publisher: Melanie Brazil
Executive Editor: Veronique Kiermer
Chief Technology Officer: Howard Ratner
Commercial Director/EVP of Sales: Dean Sanderson
Head of Nature Research & Reviews Marketing: Sara Girard
Marketing Manager: Samantha Savalio
Production Coordinator: Diane Rios
Head of Web Services: Anthony Barrera
Web Production Editor: Eddie Jones

NPG London
The Macmillan Building, 4 Crinan Street, London N1 9XW
Tel: 44 207 833 4000, Fax: 44 207 843 4996
Managing Director: Steven Inchcoombe
Publishing Director: Alison Mitchell
Editor-in-Chief, Nature Publications: Philip Campbell
Director of Web Publishing: Dan Pollock

NPG Nature Asia-Pacific
Chiyoda Building, 2-37 Ichigayatamachi, Shinjuku-ku, Tokyo 162-0843
Tel: 81 3 3267 8751, Fax: 81 3 3267 8754
Regional Managing Director — Asia-Pacific: David Swinbanks
Director — Asia-Pacific: Antoine E. Bocquet
Operations Director: Hiroshi Minemura
Senior Marketing Manager: Sachiyo Ikeda
Asia-Pacific Sales Director: Kate Yoneyama
Asia-Pacific Sales Manager: Ken Mikami

DISPLAY ADVERTISING display@us.nature.com (US/Canada)
display@nature.com (Europe)
nature@natureasia.com (Asia)
Global Head of Advertising and Sponsorship: Andrew Douglas, Tel: 44 207 843 4975, Fax: 44 207 843 4996
Global Head of Display Advertising and Sponsorship: Gerard Preston, Tel: 44 207 843 4965, Fax: 44 207 843 4749
Asia-Pacific Sales Director: Kate Yoneyama, Tel: 81 3 3267 8765, Fax: 81 3 3267 8752
Display Account Managers:
New England: Sheila Reardon, Tel: (617) 399 4098, Fax: (617) 426 3717
New York/Mid-Atlantic/Southeast: Jim Breault, Tel: (212) 726 9334, Fax: (212) 696 9481
Midwest: Mike Rossi, Tel: (212) 726 9255, Fax: (212) 696 9481
West Coast: George Lui, Tel: (415) 781 3804, Fax: (415) 781 3805
Germany/Switzerland/Austria: Sabine Hugi-First, Tel: 41 52761 3386, Fax: 41 52761 3419
UK/Ireland/Scandinavia/Spain/Portugal: Evelina Rubio-Hakansson, Tel: 44 207 843 4079, Fax: 44 207 843 4749
France/Belgium/The Netherlands/Luxembourg/Italy/Israel/Other Europe: Nicola Wright, Tel: 44 207 843 4959, Fax: 44 207 843 4749
Asia-Pacific Sales Manager: Ken Mikami, Tel: 81 3 3267 8765, Fax: 81 3 3267 8752
Greater China/Singapore: Gloria To, Tel: 852 2811 7191, Fax: 852 2811 0743

SPONSORSHIP g.preston@nature.com
Global Head of Sponsorship: Gerard Preston, Tel: 44 207 843 4965, Fax: 44 207 843 4749
Business Development Executive: David Bagshaw, Tel: (212) 726 9215, Fax: (212) 696 9591
Business Development Executive: Patrick Murphy, Tel: (617) 475 9216, Fax: (617) 494 4960
Business Development Executive: Reya Silao, Tel: 44 207 843 4977, Fax: 44 207 843 4996
Business Development Manager: Will Piper, Tel: 44 207 014 4181

NATUREJOBS naturejobs@us.nature.com (US/Canada)
naturejobs@nature.com (Europe)
nature@natureasia.com (Asia)
US Sales Manager: Ken Finnegan, Tel: (212) 726 9248, Fax: (212) 696 9482
European Sales Manager: Dan Churchward, Tel: 44 207 843 4966, Fax: 44 207 843 4596
Asia-Pacific Sales & Business Development Manager: Yuki Fujiwara, Tel: 81 3 3267 8765, Fax: 81 3 3267 8752

SITE LICENSE BUSINESS UNIT
Americas: Tel: (888) 331 6288 institutions@us.nature.com
Asia/Pacific: Tel: 81 3 3267 8769 institutions@natureasia.com
Australia/New Zealand: Tel: 61 3 9825 1160 nature@macmillan.com.au
India: Tel: 91 124 2881054/55 npgindia@nature.com
ROW: Tel: 44 207 843 4759 institutions@nature.com

CUSTOMER SERVICE www.nature.com/help
Senior Global Customer Service Manager: Gerald Coppin
For all print and online assistance, please visit **www.nature.com/help**
Purchase subscriptions:
Americas: *Nature Medicine*, Subscription Dept., 75 Varick Street, Fl 9, New York, NY 10013-1917, USA. Tel: (866) 363 7860, Fax: (212) 334 0879
Europe/ROW: *Nature Medicine*, Subscription Dept., Macmillan Magazines Ltd., Brunel Road, Houndmills, Basingstoke RG21 6XS, United Kingdom. Tel: 44 1256 329 242, Fax: 44 1256 812 358
Asia-Pacific: *Nature Medicine*, NPG Nature Asia-Pacific, Chiyoda Building, 2-37 Ichigayatamachi, Shinjuku-ku, Tokyo 162-0843. Tel: 81 3 3267 8751, Fax: 81 3 3267 8752
India: *Nature Medicine*, NPG India, 3A, 4th Floor, DLF Corporate Park, Gurgaon 122002, India. Tel: 91 124 2881054/55, Fax: 91 124 2881052

REPRINTS reprints@us.nature.com
Nature Medicine, Reprint Department, Nature Publishing Group, 75 Varick Street, Fl 9, New York, NY 10013-1917, USA.
For commercial reprint orders of 600 or more, please contact:
UK Reprints: Tel: 44 1256 302 923, Fax: 44 1256 321 531
US Reprints: Tel: (617) 494 4900, Fax: (617) 494 4960

EDITORIAL

nature medicine

Toward clinical transparency

Big pharma has historically made some substantial missteps regarding the full reporting of clinical trial results, but a new initiative by GlaxoSmithKline is a move in the right direction.

On 11 October, GlaxoSmithKline (GSK) announced that it will make detailed anonymized patient-level data from their clinical trials available to qualified researchers (http://www.gsk.com/media/press-releases/2012/GSK-announces-further-initiatives-to-tackle-global-health-challenges.html). According to the GSK press release announcing the initiative, the move will help further the aim of GSK to increase the transparency of its studies, and it may allow researchers "to examine the data more closely or to combine data from different studies in order to conduct further research, to learn more about how medicines work in different patient populations and to help optimise the use of medicines with the aim of improving patient care."

This announcement follows on the heels of GSK's development of a public website in 2004 that lists summary results and protocols of its trials. In view of the pharmaceutical industry's checkered history in reporting clinical trial data, GSK's further commitment to increasing openness and transparency is a welcome development. Last year, GSK was itself the subject of a US government lawsuit accusing the company of promoting Paxil and Wellbutrin for unapproved uses in children and adolescents, in spite of GSK trials—in the case of Paxil—that did not show effectiveness and raised safety concerns. In the same lawsuit, GSK was accused of promoting Advair as a superior medication for asthma, basing its assertion on a study whose claims the US Food and Drug Administration had evaluated and rejected. As a result of this lawsuit, the company agreed to pay a $3 billion fine, although GSK told *Nature Medicine* that the plans for the new transparency initiative have been in the works for the past 18 months and were not related to the lawsuit.

To implement the new program, GSK will create a secure website containing detailed patient data and the full protocols of clinical trials GSK has conducted for approved and discontinued drugs. GSK plans to make the data accessible after regulatory approval and publication of the trial results in the scientific literature. For data that are associated with trials that did not lead to drug approval or that are not published, the plan is to offer access within a reasonable timeframe. The new policy will apply to global clinical trials from 2007 and to all clinical trials starting in 2013.

External access to the detailed data should provide unprecedented insight into GSK's clinical trial results, particularly for failed trials, which might otherwise not see the light of day. But access will not be open to all. According to James Shannon, the company's chief medical officer, to ensure "this information is not misused, which could be detrimental to medical science and patient care, research requests will need to be submitted with proposals, which will be reviewed for scientific merit by an independent panel of experts." But it's unknown who will decide the makeup of the panel and what criteria will determine the "scientific merit" of the proposals. Would researchers from competing companies working on similar drugs be allowed access to the detailed patient data? Moreover, a lot of money could be at stake, so the mechanisms that will be used to protect against conflicts of interest (for both the review board members and those applying to access the data) must be made transparent, and the reviews should be done in a timely manner.

With regard to the firewall, the company has expressed concern about patient privacy and that the data might be misinterpreted by nonexperts. Accordingly, the company will place certain conditions on researchers who are granted access. Namely, they must use the data only as outlined in their proposal, keep it confidential, not attempt to identify patients in the study, and inform regulatory authorities and GSK of any safety concerns they might uncover. It remains unclear how GSK would react if important safety concerns were identified and the economic interests of the company put at risk.

We applaud GSK for taking this step and hope the rest of the industry follows suit. Databases of this sort are bound to improve trial data analysis, as highly qualified outside experts will have a chance to offer their own independent assessments. They may also enable repurposing of drugs that were safe but failed to show efficacy for a particular indication, and perhaps improve future trial designs. And their utility will increase as pharmacogenomic data become more readily available. The ability of outside researchers to analyze clinical trial data should ultimately help companies learn how to better target their drugs to the patients that can benefit from them the most.

Baby steps:
Europe looks to harmonize newborn-screening programs

Dander gander:
Next-generation cat allergy vaccines near market approval

SMA smackdown:
Targeted therapies advance against deadly pediatric disease

Prisoners, hard hit by hepatitis C, decry lack of access to drugs

David Proulx was diagnosed with hepatitis C in 2003, but he suspects he contracted the virus decades earlier. He injected drugs in the 1970s and picked up several tattoos when he was first incarcerated in the early 1980s. Over the years, the infection wreaked havoc on his liver. Within a year of diagnosis, he received antiviral drugs to treat the disease, but the medicine failed to eliminate the virus. Proulx had run out of options. In 2011, however, the US Food and Drug Administration approved two new medications to treat hepatitis C. Clinical trials indicated that these drugs could help individuals like Proulx who had previously failed other therapies. But Proulx can't access them. He's incarcerated at the Massachusetts Treatment Center within the correctional complex in Bridgewater, and the state has not yet begun administering the new medications to inmates, according to Joel Thompson, a lawyer and prisoner advocate based in Boston.

The hepatitis C virus is the leading cause of liver cancer and the most common chronic blood-borne infection in the US, affecting approximately 3.2 million people. Among prisoners, the infection is rampant. Between 12% and 31% of the roughly 1.6 million people living in state or federal prisons in the US are infected with the virus, as a result of exposures such as injection drug use and unsafe tattooing.

Fortunately, the infection can be cured. Antivirals can eliminate the infection in about half of all cases. Adding to the case to treat incarcerated individuals, a paper published last month by researchers from Wisconsin concluded that inmates receiving traditional hepatitis C therapy fare just as well as individuals being treated in the community (*Hepatology* **56**, 1252–1260, 2012). However, the newest, most effective medicines cost tens of thousands of dollars. Today, prison officials are facing tough choices about which inmates to treat and which medicines to administer.

"Prisoners are guaranteed access to community-standard health care," says Josiah Rich, an infectious disease expert at Brown University's Alpert Medical School in Providence, Rhode Island, and director of the university's Center for Prisoner Health and Human Rights. But "this community-standard treatment is now, all of a sudden, god-awful expensive."

Budget buster

The American Association for the Study of Liver Diseases, a Virginia-based professional society for hepatologists, now recommends that people infected with the most common strain of hepatitis C receive the traditional combination of two antiviral medications, pegylated interferon and ribavirin, as well as one of two new protease inhibitors approved in 2011, Victrelis (boceprevir) from New Jersey's Merck or Incivek (telaprevir) from Massachusetts-based Vertex Pharmaceuticals. The traditional combination therapy already costs between $15,000 and $30,000 per patient, depending on the length of treatment. The new protease inhibitors will add at least $26,000 and as much as $50,000 to the cost. "It could potentially be a budget buster," says Robert Trestman, executive director of Correctional Managed Health Care at the University of Connecticut Health Center in Farmington, which cares for inmates in the state's penitentiaries.

> "There is an enormous incentive to make this move as slowly as possible."

Patient selection and drug adherence present additional challenges. Not every individual who is infected with hepatitis C is eligible for treatment. "They need to meet certain criteria," says Trestman. For example, because the medications have serious side effects, individuals must have signs of liver damage to receive them. That may happen years after the initial infection.

Prison officials also want to be sure that inmates can complete their treatment, which typically lasts a year, before they're released. That's because inmates often have trouble accessing the drugs and sticking with the complicated dosing regimen once they're back in the community, and missing just two or three doses of the new protease inhibitors can "eliminate the significant portion of the benefits," according to Owen Murray, vice president of offender health services at the University of Texas Medical Branch (UTMB) in Galveston, which provides care for most of the state's inmates.

Rules about treatment eligibility were at the heart of a lawsuit filed in 2005 in which four current and former inmates of the Logan Correctional Center in Lincoln, Illinois sued the medical director and top administrators of the state's Department of Corrections after they were denied treatment. Some were turned down because of insufficient evidence of liver damage, others had sentences that were deemed too short to complete the therapy while incarcerated.

In 2008, the jury ruled in favor of the plaintiffs, awarding damages in excess of $8 million. A year later, however, a district court overruled the judgment for three of the four inmates. Only in the case of Edward Roe did the court find that the medical director showed deliberate indifference to the inmate's medical condition by failing to biopsy Roe's liver and to consider him as a candidate for treatment. Roe died in 2007 from cirrhosis. A federal appeals court upheld the district court's decision.

State of affairs

Earlier this year, the Federal Bureau of Prisons released new guidelines for hepatitis C treatment that recommend the use of the new protease inhibitors, which its representatives say it has implemented. Treatment policies in state prisons, however, vary widely. In Connecticut, for example, 17 of the state's approximately 17,500 inmates are currently receiving the new protease inhibitors. Yet, in neighboring Massachusetts, the state's Department of Correction has not even developed a protocol for the use of the new medications.

Thompson, a staff attorney at Prisoners' Legal Services in Boston, has fielded calls from at least 25 inmates—most of whom are still infected with hepatitis C despite previous treatment with interferon and ribavirin—wanting to know how they can receive the newer drugs. That's a question state officials have yet to answer.

"We've been very vocal with the department and with its medical contractor about the need to get a protocol in place and to bring these new medications online," Thompson told *Nature Medicine*.

In a July 2012 letter, Lawrence Weiner, assistant deputy commissioner for the Massachusetts Department of Correction's Clinical Services Division, wrote that the state was considering adopting practices that match the federal guidelines and noted that the University of Massachusetts Medical School in Worcester, which oversees inmate health care, had committed to completing the new protocol by the end of that month. At press time, however, the revision had not yet been completed, according to Diane Wiffin, a Department of Correction spokesperson. Because of the high cost of the newer agents, "there is an enormous incentive to make this move as slowly as possible," Thompson says.

A 2011 report on inmate healthcare costs commissioned by the Massachusetts Department of Correction suggested that one way to cut medication costs would be to offer inmates who require hepatitis C treatment the older medications initially and save the new drugs for inmates who don't respond within the first 12 weeks.

Treatment options going south

Texas, the state with the largest prison population in the US, hasn't yet made the drugs available to its inmates, either. "We're working on our guidelines right now for these newer therapies," says UTMB's Murray. The protease inhibitors must be administered every eight hours with a snack. Given those requirements, Murray says it may make sense to create special hepatitis C treatment facilities. The committee charged with developing the new guidelines, which includes representatives from UTMB as well as the Texas Department of Criminal Justice, is considering all these possibilities. In the meantime, Murray says, UTMB physicians have restricted the number of new inmates starting the older two-drug therapy. The need for treatment is rarely urgent, he says. "There is no reason to put patients on suboptimal therapy."

Inmates in Georgia are in a similar situation, according to Anne Spaulding, an infectious disease physician at Emory University's Rollins School of Public Health in Atlanta who was hired in 2003 by the Georgia Department of Corrections to care for inmates with hepatitis C. "I was told I could use the new antivirals when they came out," she says. But even after the new drugs were approved, Spaulding couldn't access them. "I kept on being strung along," she says.

Spaulding says she developed a protocol for the use of the medications, but it was never implemented. It's not clear whether any inmates in Georgia are taking the protease inhibitors today. Spaulding was let go earlier this year due to budget cuts. At that time, the medications were not available, she says. Dabney Weems, a spokesperson for the Georgia Department of Corrections, declined to say whether the new drugs are being used. She wrote in an email that all inmates "receive individualized care based on their patient factors."

For inmates such as Proulx, who couldn't be cured by the old regimen, these new drugs may mean the difference between life and death. "I worry if I do not get treatment in the near future, my condition will worsen," he wrote last year in a letter to the Massachusetts Department of Public Health. "I should not be denied medical treatment when the drugs to treat [my] condition are available, based on my status as a prisoner."

Thompson agrees. He and his colleagues have already talked about filing a lawsuit if they don't see progress. "There is no shortage of clients willing to participate if that's what it takes to get triple therapy implemented," he says.

Cassandra Willyard

Group purchasing plan launched to save on research supplies

For most shoppers, buying in bulk means stocking up at big-box retailers such as Costco and Walmart to save on groceries and other household goods. But the discounts found in bulk shopping go well beyond the home. For more than 30 years, hospitals have banded together to purchase expensive drugs at discounted rates. Now, a new effort has brought together academic research centers for a similar savings.

Companies such as Texas-based Novation have long provided what's known as group purchasing options (GPOs) for hospitals. But the supplies needed by basic biomedical research teams at academic medical institutions differ from those used by clinicians. To fill the gap, a group representing academic hospitals, the Academy for Medical Development and Collaboration (AMDeC), has created a GPO to enable its members to combine their purchasing power to yield savings on essential lab supplies.

According to Maria Mitchell, who has served as president and chief executive of AMDeC since its inception in 1997, the organization is uniquely qualified to head the new GPO operation, which was approved by its board late last year and in August closed its first purchasing deal with GenScript, a supplier in Piscataway, New Jersey, that produces reagents and other key lab necessities. It's a first for GenScript as well: although the company has worked with some large companies in the past on big orders, "this is the first time" that the company has made a purchasing agreement with a GPO, says Frank Zhang, its chief executive.

A penny-wise proposition

Unlike hospital GPOs, which focus on frequently used drugs and hospital equipment, AMDeC's GPO will focus more on "reagents, primers [and other] things that are used in laboratories day in and day out," Mitchell says. The labs of AMDeC members typically spend a total of $400 million on these products annually, but if they take full advantage of the GPO, they stand to save around 10% of these costs, says Mitchell.

AMDeC is primarily made up of New York–based institutions such as New York University's Langone Medical Center and the Memorial Sloan-Kettering Cancer Center, but it has expanded to include medical labs affiliated with Rutgers, the State University of New Jersey, and it hopes to become nationwide, according to Mitchell. All institutions already a part of AMDeC are invited to participate in the GPO, and Mitchell estimates that 90–95% of them will do so.

The move is particularly important given that funding for research, whether through hospital budgets, philanthropic organizations or government grants, has decreased because of the poor economy, says Mitchell. Research-focused hospitals must "spend their dollars where they need them and not invest in the profit margins of companies" by overpaying for supplies.

GPOs have come under government scrutiny before because they can become large enough that they are able to dictate the market, edging toward a monopoly, says Einer Elhauge, a professor at Harvard Law School in Cambridge, Massachusetts. But Elhauge says that there is no reason not to launch one for basic biomedical labs looking for savings: "GPOs can be efficient and procompetitive when they do not command such a big share of the market as to have [illegal] market power."

Susan Matthews

Europe plays catch-up on neonatal screening as US skips ahead

It's a case of transatlantic drift. In September, when the American College of Medical Genetics and Genomics (ACMG) announced the launch of a new centralized virtual repository of newborn dried blood spots, an envious EU looked on, its national constituents unable to agree even on which conditions newborns should be screened for. But things are beginning to change. There are now concerted efforts underway by European health professionals to redress this lack of harmony, and, in mid-November, specialists on newborn screening from across the continent will meet in Brussels, the home of the European Parliament, to discuss the first concrete steps needed to bring into line member states' policies on such tests.

The US has led the world in newborn screening ever since the 1960s, when microbiologist Robert Guthrie, then based at the Buffalo Children's Hospital in New York, first devised an ingeniously simple test for the metabolic disorder phenylketonuria. Guthrie's sampling method—a small prick to a baby's heel to collect drops of blood onto filter paper—is still used worldwide today (although back then phenylketonuria was still screened for using a culture-based bacterial assay).

Today, the introduction of tandem mass spectrometry to look for telltale enzymes and other molecules in the blood has expanded the number of genetic diseases screened for in the US to include a core of 29 conditions, tested on a mandatory basis in every newborn across the country as part of state-based public health programs. The picture in Europe, by contrast, couldn't be more different.

Even within a small country such as Belgium there are notable discrepancies in screening practices between regions, says KU Leuven's Pascal Borry, a bioethicist who, together with VU University Medical Center's Martina Cornel, will convene the meeting on 19 November in Brussels. In the French-speaking south of the country, the regular newborn-screening panel consists of seven conditions, compared with 11 in the Flemish north, Borry explains. Variation among EU countries is even starker: Austria screens for a total of 29 conditions, whereas Finland screens for just one, congenital hypothyroidism.

The differences run much deeper than the individual countries' screening panels. In the first ever comparative study of newborn-screening practices in Europe, released by the EU late last year, Cornel and other scientists found that even the thresholds of metabolites used for screening the same disorder are different not only across countries but also between screening laboratories within the same country.

© Scott Kaufman/Associated Press

On the spot: Europe's newborn screening.

Screen test

In the US, national newborn-screening standards were established in 2010, just four years after the publication of pivotal recommendations from the Bethesda, Maryland-based ACMG (*Genet. Med.* **8**, 1S–252S, 2006). But cultural hurdles and the vagaries of European politics mean that harmonization of newborn testing, if it can ever be achieved in Europe, presents a tougher challenge. Adding further complications, procedures related to obtaining informed consent, storing samples and using them in research vary from country to country across the EU. As such, forging a consensus on newborn screening is going to take considerable patience, says Gerard Loeber, past president of the International Society for Neonatal Screening (ISNS) in Amsterdam.

"Ideally, policy makers on the level of the EU would sit together and come to consensus," says Loeber, who still serves on the ISNS's governing council. However, he continues, "as long as member states refuse to transfer some power to Brussels, policy makers on the EU level cannot proceed".

Cornel contends that the goal should not be a single EU-wide decree on newborn screening. Instead she argues that efforts should be focused on developing best-practice guidelines that member states can adapt to fit their own health systems and, in some cases, legal systems. Rules governing informed consent, for example, are deeply embedded in national laws and are unlikely to be amenable to change in the short or even medium term, she explains. But there are aspects of newborn screening, such as the assessment of new screening techniques, education, counseling, follow-up and oversight, that might lend themselves to high-level, EU-wide organization.

Even in the US, the establishment of minimum national newborn-screening standards two years ago has not led to a complete standardization of screening practices. In addition to the core 29 conditions there is a 'secondary panel' of 25 further conditions, from which states can pick and choose what to screen for. In some cases, states have started to screen for conditions not included in either of the recommended primary or secondary panels. For example, Illinois has begun screening for Pompe disease, contrary to advice from the Advisory Committee on Heritable Disorders in Newborns and Children within the US Department of Health and Human Services. And Utah is gearing up to start testing for spinal muscular atrophy, despite the lack of proven therapies (see page 1602).

Cornel says that the EU should seek a model with this type of flexibility. "Europe can take note that harmonized, top-down recommendations might work towards promoting a high-quality, basic package, rather than towards dictating totally uniform practices," she says.

Meanwhile, the US continues to forge ahead with fresh innovations in newborn screening. In August, the US National Institutes of Health announced that it was canvassing for research on how best to integrate genomic sequencing into the country's harmonized newborn-screening program. And last month a team largely based out of the Children's Mercy Hospital in Kansas City, Missouri, reported that they had developed a rapid, 50-hour test for genetic disorders using whole-genome sequencing, intended to be used in neonatal intensive care units (*Sci. Transl. Med.* **4**, 154ra135, 2012). What form Guthrie's legacy takes in the decades to come will depend on how society, and the regulators it appoints, answers the many questions posed by these new and constantly evolving screening technologies.

David Holmes

Targeted vaccines against feline dander could be the cat's meow

A man and a woman walk into a doctor's office. She has a cat allergy; he has a cat. "They say, 'You've got to do something or we can't get married,'" says Michael Blaiss. It sounds like the beginning of a bad joke, but it's actually a typical day at Blaiss's private allergy practice in Memphis, Tennessee. People often face tough decisions when a loved one cannot cohabit with feline companions.

Cat dander—microscopic pieces of dry cat skin coated with Fel d 1, a protein responsible for most cat allergies that is secreted by cat glands onto the skin and transferred to fur from cat saliva through grooming—elicits a reaction in an estimated 17% of individuals in the US. Antihistamines and steroids can dull the symptoms, but the only disease-modifying therapy currently available is a series of injections made of cat dander extract, a soup of proteins literally washed from cat fur and bottled. Whole allergen treatment is time consuming, involving some 30–80 shots over three to five years, and risky, with the chance of rare life-threatening anaphylactic reactions to the injections.

An Oxford, UK–based company, Circassia, hopes to change all that with its new ToleroMune cat allergy vaccine, a molecular approach to the problem. The vaccine is made of seven synthetic peptides, each only 15–20 amino acids long and derived from Fel d 1. The carefully selected peptides quiet the immune system's aberrant T cell response but avoid activating mast cells, which cause allergic reactions and anaphylaxis.

"We know exactly what is in every vial," says Steve Harris, Circassia's chief executive.

In a recently published phase 2 study, 21 people received four injections of the therapeutic vaccine over a three-month period in which they were exposed to cat dander. A year after starting the treatment, these individuals showed a significantly greater reduction in nose- and eye-related symptoms than 29 participants who received a placebo and the same allergen hazard (*J. Allergy Clin. Immunol.* doi:10.1016/j.jaci.2012.07.028, 2012).

In early October, Circassia announced the launch of a phase 3 study of the vaccine in approximately 110 centers across the US, Canada and Europe. The company expects to complete the trial by mid-2014.

"This is what people have been trying to do for the last 25 years in immunotherapy—increase immunogenicity and decrease the likelihood of the vaccine triggering an allergic reaction," says Blaiss, who also teaches at the University of Tennessee Health Sciences Center in Memphis and was not affiliated with the Circassia trial. "This is the most impressive peptide study that I've seen."

istockphoto

Felling Fel d 1: New vaccines target the protein responsible for most cat allergies.

The cat's out of the bag

Circassia's vaccine may be one of the furthest along of its kind, but is it not the only allergy vaccine based on a molecular approach. Tunitas Therapeutics, a San Francisco–based biotechnology company, has genetically engineered a cat allergy vaccine by fusing a Fel d 1 peptide to a portion of a human immunoglobulin G protein that inhibits mast cell activation. "We block the allergy component by using this brake, but the [Fel d 1] protein is still available to drive tolerance," says Nolan Sigal, president and chief executive of Tunitas. The company initiated a phase 1 trial of their cat allergy vaccine in 2011 but halted the trial when the vaccine did not block local reactions to cat dander as expected. "We learned a lot, but it was not good enough to move forward into full-scale clinical development," he adds. The company is now making a second attempt at a cat allergy vaccine based on the same principle but testing different molecules to act as the brake.

Vienna-based Biomay has taken a similar tack, fusing parts of Fel d 1 to a noninfectious hepatitis B virus protein. The allergen peptides cause immunization without activating mast cells, whereas the hepatitis peptides subdue inflammatory T cells, which can cause late-stage side effects. "We wanted to add another layer of security," says Rudolf Valenta at the Medical University of Vienna, inventor of the vaccine technology and a consultant for Biomay. Biomay's cat allergy vaccine is only in preclinical development, but the company has a grass pollen allergy vaccine based on the same concept that requires just three doses over two months and is in phase 2 trials.

Meanwhile, Thomas Kündig at the University of Zurich Hospital recently designed and tested a cat allergy vaccine that fuses Fel d 1 sequences to two additional peptides: an HIV-derived peptide that whisks the protein quickly into immune cells and a human peptide that targets the construct straight to the endoplasmic reticulum so that it is not degraded in the lysosome. In a clinical trial reported earlier this year, three injections of the vaccine into the lymph node over two months led to an increase in tolerance to cat dander in 12 allergy sufferers versus 8 who took placebo (*J. Allergy Clin. Immunol.* **129**, 1290–1206, 2012). Unfortunately, the project is currently stalled, says Kündig, as he has been unable to find a partner or additional funding to pursue the vaccine.

All in all, "if these things work, it would be game changing," says Robert Wood, director of the allergy and immunology division at the Johns Hopkins Children's Center in Baltimore. Cat lovers may rejoice, but Fido aficionados with allergies will have to wait a bit longer. Cat allergies are far more common than dog allergies and often lead to asthma attacks, which dog allergies rarely do. "Dog is on the list," says Circassia's Harris, "but it's some way down."

Megan Scudellari

New NIH effort seeks to find ways to make trials run smoother

With multiple sites and complicated protocols, clinical trials do not always run as smoothly as desired. So the US National Institutes of Health (NIH) has created a new initiative to determine how researchers can maximize the use of electronic medical records and engage patients over the internet to improve these trials, all of which is designed to help bring down the spiraling costs of running a clinical trial.

The NIH launched the Health Care Systems (HCS) Research Collaboratory on 25 September, awarding seven researchers a total of $11.3 million in grants to consider everything from the most efficient means of recruiting participants for trials to best ways of designing an experiment and handling large amounts of data. "Although the clinical projects deal with distinct diseases, the overall goal is to develop the research methods and best practices that can be readily used," says Catherine Meyers, director of the Office of Clinical and Regulatory Affairs within the NIH's National Center for Complementary and Alternative Medicine, in Bethesda, Maryland.

For example, one of the grants went to internist Gary Rosenthal of the University of Iowa Carver College of Medicine in Iowa City. Rosenthal is investigating whether switching people from daytime to nighttime doses of antihypertensive drugs lowers the risk of heart attack—but the exact subject of the study isn't relevant to the HCS Research Collaboratory. The new grant is designed to help Rosenthal assess how best to identify prospective participants through electronic health records and obtain consent online. The award should also allow Rosenthal's team to design the experiment so that participants can report when they take the drugs and how they're feeling through a website. Researchers conducting clinical trials have made use of the Web for years, Rosenthal notes, but it has been a bit haphazard, lacking the unified protocol explaining best practices that this project hopes to establish.

The initiative also considers how pragmatic trials, which use information already collected in healthcare systems and run during the course of routine medical practice, can yield results comparable to those found under idealized trial conditions. That's the goal of Gloria Coronado, a grant recipient from the Kaiser Foundation Hospitals in Portland, Oregon. She's designing pragmatic studies to pinpoint who needs colorectal cancer screening and to analyze which methods of encouraging people to get tested work best. Pragmatic trials are "cost-saving and more akin to what happens in the real world, outside of clinical trial settings," she says.

Susan Matthews

Spain sees worrying dip in research spending by drug companies

BARCELONA — Spanish pharmaceutical companies last year cut their investment in research and development for the first time in a decade, from €1.03 billion ($1.35 billion) in 2010 to €974 million in 2011, according to a survey of 49 companies published on 24 September by Farmaindustria.

"R&D has been cut because of the recession," says Javier Urzay, vice president of Farmaindustria, the trade organization representing the country's pharmaceutical industry, based in Madrid. "And the slashing of public pharmaceutical spending has reduced incomes."

The sector has been hit hard by the global financial crisis in the form of federal legislation to reduce the country's annual drug expenditures from €12.7 billion (the record reached in May 2010) to an expected €8 billion by the end of 2013. To make matters worse, these declines in spending come at a time when Spain's overall pharmaceutical market is contracting: it shrank by 6% last year—the worst performance among the five largest markets in Europe, according to the 2011 World Pharmaceutical Market Summary published this year by the New Jersey–based consulting company IMS Health.

The new Farmaindustria survey "may be a message to the government," says José Luis García López, a biotechnology expert at the Center for Biological Research in Madrid and a former advisor to the country's Ministry of Science and Innovation. He says that if the rewards for developing good drugs decline, companies will invest even less in research.

Guzmán Lozano

Falling capital: Madrid's cash flow problem.

Joan Guinovart, director of the Institute for Research in Biomedicine (IRB) in Barcelona, has not seen many research contracts cancelled. But public funding for biomedical research has suffered its part of the 34% cut applied to the government's research and development budget from 2010 to 2012. Experts note that the Consortium for the Support of Networked Biomedical Research (CAIBER), created by the government to carry on noncommercial clinical trials, has seen its annual budget shrink from €10 million in 2008 to €3 million in each of the last two years.

As an upshot, the cuts are pushing private companies and public research centers to work closer together than ever before. In June, for example, the Spanish National Cancer Research Centre in Madrid signed an agreement with the Swiss drugmaker Roche to develop early-stage ideas for anticancer medicines. And in September, Esteve, a leading Spanish pharmaceutical company, announced that it would move all its discovery and preclinical development laboratories to the Barcelona Science Park, home to the IRB and the National Centre for Genomic Analysis.

Michele Catanzaro

Correction

In the September 2012 issue, the article entitled "Controversial egg-producing stem cells promise better IVF" (*Nat. Med.* **18**, 1311, 2012) incorrectly stated the age range for OvaScience's first clinical trial as 35 to 42 and the anticipated time frame for commercial product launch as late 2013. The correct age range is 38 to 42, and the commercial product launch will be in 2014. The errors have been corrected in the HTML and PDF versions of the article.

David Baker

Straight talk with… David Baker

Thirty years ago, technology companies began nestling their facilities close to academia, and the idea of the university research park was born. Soon after, the concept took off in the field of medicine, and today it's not hard to find such innovation hubs that house biomedical startups drawing on the brainpower of professors and students alike.

In late September, the Tucson, Arizona–based Association of University Research Parks—which includes about 170 research parks—announced that David Baker would serve as president of the organization's board of directors for the next year and help guide its strategic goals for the next five years. Baker, who is also the executive director of the University Technology Park at the Illinois Institute of Technology in Chicago, spoke with **Roxanne Khamsi** about how the organization hopes to branch out and transform these workplaces.

First off, what exactly is a university research park?

A university research park is a real estate entity that is attached to, run by and owned by a university—or directly adjacent to a university—and has been created for the purpose of undertaking both active university research and in promoting the growth of companies using the intellectual property generated by those research centers, medical schools, teaching hospitals, et cetera. A research park, while it may have university labs located in the park, is mainly focused on the promotion of for-profit companies.

How have these parks changed in recent years?

In the 1970s, '80s and '90s, research parks were mainly places for the co-location of corporate entities that wanted to be near universities. Now the emphasis is on a combination of having companies locate their facilities in these parks but also on the incubation of new companies with intellectual property that has been generated either by the university or by people near the university. There's the development of more multi-tenant buildings as compared to more stand-alone individual tenant buildings. I've seen it just by visiting parks across the country.

What do you think is driving that?

I think it's the pressure for more economic development in urban spaces. [Governments and universities] have started to look at the big urban campuses of the major research centers for the location of these parks. Most recently you see it in Baltimore, for instance, with the research park at Johns Hopkins University.

Why do companies join research parks these days?

The biggest challenge for a little company is to gain access to high-quality research equipment, people, students and consultants at a very low price. So when you're in the space of developing a product through biomedicine, you're particularly challenged, particularly at the early stage because you need the most sophisticated equipment available to high-end university research labs, but you can't buy that equipment yourself. The role of the parks is to act as a broker with the university to establish access to these facilities [with this equipment]. You wouldn't even imagine these companies growing up without this kind of accommodation. And usually there's a faculty member whose research is being developed into a company. They obviously want to have the startup company nearby them so that they can be involved in it and provide the scientific guidance.

What types of policy does your organization advocate?

We have been quite involved in policy the last several years. We were able to help establish a provision in the America Competes Act that authorizes loan guarantees for university research parks that are building major facilities. The program is in place—it passed—but the appropriation has to be reauthorized in 2013.

Financial times are tough, though. Do you see the US government scaling back its financial support for research parks?

Inevitably. I think there's going to be less capital funding available with the federal government trying to deal with the deficit. Europe is a little different. The have all the same challenges, but they seem bent on continuing to provide subsidies for the emergence of science parks, particularly in the new EU countries. I certainly saw that in Poland and the Czech Republic when I visited there recently. [The EU] is talking about a new round of funding in 2014.

You're putting together a five-year plan. What are you hoping to achieve?

Many of our science parks [in the US] depend on private-sector investments, for the companies at least. We have a variety of funding strategies for our buildings, including boosting private-sector input with various types of tax incentives, as opposed to direct subsidies here in the US. So I see that as a major area of focus. Another area that I think we're going to be working on is the evolution of our research parks as live, workplace environments—bringing in restaurants, condos, schools, that kind of thing—particularly for the bigger parks.

Why so?

People want to live near work. The first test of this, like that seen [at the University Park at MIT] in Cambridge, Massachusetts, has been very successful. So this is another strategic area for investigation that we may be looking at in terms of programming. Because what this does is change the character of the money needed [to build the park] and the kind of developer you're going to use. It requires the more sophisticated partnerships where you're looking residential real estate developers being involved with you rather than just commercial real estate developers or laboratory developers. This is a kind of mix that many of us have not been involved with before.

Biomedical briefing

POLICY

Patient push

Patient advocacy groups' lobbying for research funding seems to be paying off. According to a study published in the October issue of *American Sociological Review* (77, 780–803, 2012), the more a disease nonprofit spends to pressure the US government on focused science spending, the more that federal funding agencies allocate to the specific disease that the organization concentrates on. "This is an area where advocacy can be incredibly successful," says study author Rachel Kahn Best, a public health fellow at the University of Michigan–Ann Arbor. Best looked at lobbying activities and budget allocations for 53 diseases over a span of 19 years. She found that for every $1,000 a group spent on lobbying, the US National Institutes of Health or the Department of Defense dished out an additional $25,000 on average in funding for that disease the following year.

Compound interest

The outbreak of fungal meningitis in the US last month, which was traced to tainted steroid shots, has renewed calls for heightened oversight of pharmacies that repackage or recombine drugs, often for off-label use. Such 'compounding' pharmacies mostly tailor drug dosages and formulations for individual patients, which puts them under the scrutiny of state regulators. But with drug-dispensing centers increasingly compounding large lots of medicines for nationwide use—as the New England Compounding Center in Framingham, Massachusetts, was doing with the contaminated back pain medication at the heart of the October meningitis outbreak—critics say it's time for the US Food and Drug Administration (FDA) to exert greater authority. "If they're acting like a manufacturer, the FDA should be able to step in," says Allen Vaida, executive vice president of the Institute for Safe Medication Practices, a Pennsylvania-based advocacy organization.

Research revamp

In the face of budget constraints, South Africa's Medical Research Council (MRC) has announced plans to streamline its programs, cutting the agency's intramural research units from the current 23 to 12, and overhaul its external peer-review system, among other measures. The restructuring, according to MRC president Salim Abdool Karim, who also directs the Centre for the AIDS Programme of Research in South Africa (known as CAPRISA) in Durban, will result in a "coherent intramural research program based on the highest priorities as defined by the local burden of disease, specifically the top ten causes of death in South Africa."

SCIENCE

Peptide painkillers found in black mamba snake venom

The lethal bite of a black mamba snake packs quite a punch. A single squirt from the African serpent's fangs contains enough neurotoxin to kill more than a dozen adult humans. Yet the venomous cocktail of compounds also includes two proteins that, at least in mice, can ease pain as effectively as the most potent analgesics with fewer complications. Eric Lingueglia and his colleagues at the Institute of Molecular and Cellular Pharmacology in Valbonne, France, discovered the proteins, dubbed mambalgins. Reporting last month in *Nature* (doi:10.1038/nature11494, 2012), Lingueglia's team injected the mambalgins, which inhibit acid-sensing ion channels, into mice and showed that their pain-relieving properties were as strong as morphine's but with no respiratory side effects and a weaker propensity for causing drug tolerance. "In pain, it's important to find new molecules working through different pathways than the ones we already know," Lingueglia says.

PEOPLE

Nobel nods

Health-related discoveries dominated this year's Nobel-lauded accomplishments. On 8 October, the Nobel Committee announced that Shinya Yamanaka of the University of Kyoto, Japan, and John Gurdon of the University of Cambridge, UK, had won the 2012 physiology or medicine prize for their discoveries that adult cells can be reprogrammed to an immature state. The chemistry prize, unveiled two days later, went to two biochemists—Robert Lefkowitz of

Duke University Medical Center in Durham, North Carolina, and Brian Kobilka of Stanford University School of Medicine in California—for their work on G protein–coupled receptors, the target of approximately one-third of all marketed pharmaceuticals. Meanwhile, the University of California–Los Angeles's Lloyd Shapley and Stanford's Alvin Roth took home the economics award for developing the 'matching' theories that, most notably, have helped facilitate kidney donor exchanges and medical residency placements.

BUSINESS

Pharma, transcended

Ten of the world's largest pharmaceutical companies joined forces in September in an effort to cut the cost of running clinical trials. Through a new nonprofit, called TransCelerate BioPharma, the industry hopes to standardize how physician-scientists are trained and the ways that clinical studies are recorded. The project will also work on a common internet portal for doctors running trials and devise a way for companies to obtain already marketed medicines from other firms for use in comparative drug studies. The companies involved are Abbott, AstraZeneca, Boehringer-Ingelheim, Bristol-Myers Squibb, Eli Lilly, GlaxoSmithKline, Johnson & Johnson, Pfizer, Roche's Genentech division and Sanofi.

Merck on the march

In its latest effort to lower operating expenses, the New Jersey–based drugmaker Merck announced plans on 9 October to shutter its global headquarters in Whitehouse Station and move its key offices about 25 miles east to Summit, where the company inherited facilities after acquiring Schering-Plough in 2009. "The relocation of our headquarters will help us achieve our future vision, reduce the size of our operating footprint and increase agility," said Kenneth Frazier, chairman and chief executive of Merck, in a press release. No new job losses are expected as a direct result of the relocation, although Merck announced plans last year to shed as many as 13,000 positions by the end of 2015.

RESEARCH

Eggs from stem cells

Stem cells from mice can be coaxed to form viable eggs capable of giving rise to healthy offspring (pictured), according to a Japanese study published on 4 October in *Science* (doi:10.1126/science.1226889, 2012). Last year, the same team from Kyoto University successfully used both embryonic and reprogrammed mouse stem cells to make functional sperm (*Cell* **146**, 519–532, 2011). But, relatively speaking, "sperm is easy," says Jonathan Tilly, a reproductive biologist at the Massachusetts General Hospital in Boston. The new work "accomplishes something very important for the female side of the story." If the approach can be translated to humans,

Katsuhiko Hayashi

it could provide an unlimited source of eggs for research. See go.nature.com/oe4znR for more.

Strike a chordoma

Historically, many so-called single nucleotide polymorphisms (SNPs) associated with cancer are linked to only a modest increase in disease risk. But individuals carrying SNPs within the brachyury gene are a whopping five times more likely to develop a rare bone cancer known as chordoma, according to a study published in October (*Nat. Genet.* doi:10.1038/ng.2419, 2012). "The SNP loads the gun," says study author Adrienne Flanagan, of University College London. "It predisposes people to developing [chordoma]." In September, the same team also reported that blocking the brachyury gene, which encodes a transcription factor involved in normal development, stopped cancer growth in human cell culture, further flagging this gene as a potential target for therapy (*J. Pathol.* **228**, 274–285, 2012).

Brain puzzle

Healthy carriers of a known indicator of Alzheimer's disease actually have lower levels of amyloid-beta, the protein fragments that accumulate in the brains of people with the neurodegenerative disease. The surprising finding, reported last month in *Biological Psychiatry* (10.1016/j.biopsych.2012.08.015, 2012), suggests that the high-risk variant of the complement receptor 1 gene may not have a direct cause on driving Alzheimer's progression, as researchers had previously thought. Now, further work is needed to "understand how genes interact to understand how they influence beta amyloid," says Madhev Thambisetty, a neurologist at the US National Institute on Aging in Bethesda, Maryland, who led the study.

Speedier drug reviews linked to safety problems

Priority reviews are often used by drug regulators to help patients gain quicker access to lifesaving medicines. That haste, however, comes with a cost. According to a study published last month by Joel Lexchin, a health policy researcher at York University in Toronto, drugs approved by Health Canada between 1995 and 2010 following an expedited review were almost twice as likely to be slapped with a black-box safety warning or get withdrawn from the market compared to drugs approved via the standard review process (*Arch. Intern. Med.* doi:10.1001/archinternmed.2012.4444, 2012). Lexchin controlled for both the types of drugs given priority review and the severity of the disease treated. As such, "it is the length of time that is taken to review the drugs that accounts for the difference between standard and priority review drugs," he told *Nature Medicine*.

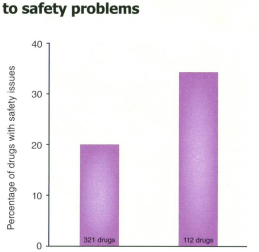

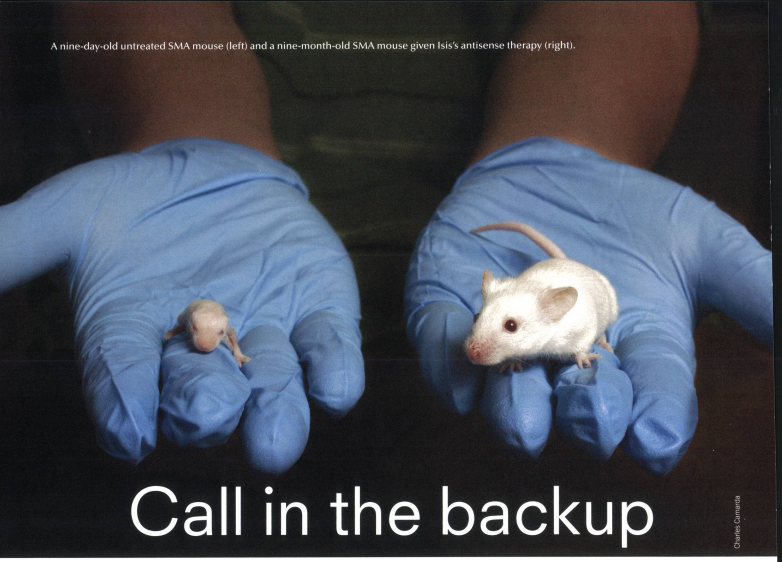

A nine-day-old untreated SMA mouse (left) and a nine-month-old SMA mouse given Isis's antisense therapy (right).

Charles Camarda

Call in the backup

The most common genetic killer of infants, a disease known as spinal muscular atrophy, is caused by mutations in a single gene. The human genome contains its own backup system—near-identical copies of the defective gene—yet these secondary sequences rarely get used correctly. As **Elie Dolgin** finds out, drug companies hope to change that, with the first wave of targeted therapies that reboot the body's backup system now entering clinical trials.

Vivienne is stacking toy blocks on the coffee table in her family's living room in Millville, Massachusetts. She adds a sixth block to the growing column and carefully nudges the cube into place. "It's Rapunzel's tower," she exclaims.

For a three-year-old with a hereditary neuromuscular disease, the fine motor skills in Vivienne's fingers are surprisingly refined. And as she talks to her parents, switching effortlessly between English, Polish and German, it's clear that she's exceptionally bright. But Vivienne's condition betrays itself as she attempts to pile the blocks higher. Her shoulders bunch up. Her arms strain under their own weight.

Vivienne has spinal muscular atrophy (SMA), a condition caused by mutations in the gene *SMN1*. Under normal conditions, this gene produces the 'survival of motor neuron' (SMN) protein, which, among its many functions, has a crucial role in maintaining the specialized nerve cells that control muscle movement. In individuals with SMA, however, working versions of SMN are in short supply, causing crucial motor neurons to progressively die off. This leaves people with poor muscle tone as well as difficulties with eating, moving and breathing. The resulting whole-body paralysis typically leads to early death.

Even though SMA affects around 1 in 10,000 babies born worldwide, there are currently no drug treatments that influence the course of the disease. Unless one is developed soon, Vivienne will probably die before she reaches her 30s. Many others won't make it past infancy.

Vivienne's parents Helena and Helge (who asked that *Nature Medicine* withhold their family's last name) are both carriers for mutations in *SMN1*. They learned of their genetic status—and Vivienne's diagnosis—in March 2011, when Helena was eight months pregnant with their second daughter Lara. Fortunately, Lara inherited only one faulty copy of the *SMN1* gene, and she is now a healthy and active toddler. "We call her 'hurricane category 5'," says Helena, as she chases Lara around the living room picking up tossed-aside stuffed animals on a Saturday morning in mid-July. In contrast, Vivienne—her legs bowed, her knee joints extended—can barely take measured steps and, even then, only with the help of someone holding her hands or with something solid to lean on.

She feels confident enough to try to walk again, though, which wasn't always the case. Thanks to an experimental drug from Isis Pharmaceuticals that Vivienne received six weeks earlier as part of a phase 1 clinical trial, her parents now say she has more strength, more poise and more self-assurance. She sits more upright on the horse at the equine therapy clinic she attends each Monday. She can now wade through the water on

her own during her weekly aquatic therapy sessions. "She shows significant signs of improvement—improvement that shouldn't be there in her type of disease and improvement that I believe can only be explained by the trial," says her father Helge.

Isis's drug, called SMNRx, works to boost levels of SMN protein. In most animals, mutations in the *SMN1* gene cause embryos to die during development. But because of a duplication on chromosome 5 of the human genome, most people (and all those with SMA) have varying copy numbers of a nearly identical backup gene, dubbed *SMN2*, that can partially rescue SMN protein production.

"We have a drug that will have a big impact on the disease."
– Frank Bennett

SMN2 differs from the normal, functioning version of *SMN1* by just a single nucleotide change: in *SMN2*, the sixth letter of the gene's seventh coding region, known as exon 7, is a T rather than a C. That small difference has big consequences, though. The altered DNA letter usually causes the RNA processing machinery to splice out exon 7, leading to the creation of a shortened, less stable version of the SMN protein that rapidly degrades. Only around 5–10% of the time does the exon get left in place to yield a full-length, functional protein.

The more copies of *SMN2* people with SMA carry, the more full-length protein they produce and the less severe their disease. One or two copies usually results in type 1 SMA, the most common and deadly form of the disease. Around 60% of all children with SMA are in this category. They never develop the ability to sit, stand or walk, and most will die under the age of 2. People with type 2 or type 3 SMA typically have at least three copies of *SMN2*, and, despite physical and respiratory disabilities, these individuals can live into early adulthood and beyond. Then there are rare individuals who harbor four or more copies of *SMN2*. Despite lacking a functional version of *SMN1*, these people have much milder forms of the disease and, in some cases, show practically no symptoms at all.

The dream for scientists, physicians and pharmaceutical companies alike is to bring more people with SMA effectively into this last category by helping affected children make the most of the *SMN2* genes they already have. A number of different strategies are being pursued, including small-molecule drugs and antisense therapies, all with the same goal in mind: to therapeutically boost the levels of full-length SMN protein. "Nature gave us this second copy [of *SMN*] that can make a little bit of full-length protein," says Basil Darras, director of clinical neurology at Boston Children's Hospital and a site coordinator in the Isis trial. "And now everybody is trying to develop drugs that will induce more full-length SMN protein production from the *SMN2* gene."

With multiple therapeutic approaches now either in early clinical trials or nearing human testing, optimism is starting to mount that one of these approaches will ultimately prove a success. "There's an excitement in the field," says Karen Chen, chief scientific officer of the SMA Foundation, a New York–based research organization. "There's now more hope for a treatment for SMA in the near future—more than at any other time."

Keep the motor neuron running

SMNRx is the first therapy that specifically targets the underlying splicing defect behind SMA to be tested in children with the disease. In Isis's first phase 1 trial, which launched in December 2011, doctors administered a single injection of SMNRx directly into the fluid-filled space at the base of the spinal cord in 28 children with type 2 or type 3 SMA. Vivienne, a type 2 with three copies of *SMN2*, received a six-milligram injection at Boston Children's Hospital in May of this year.

The therapy is an 18-letter string of DNA that corrects aberrant splicing by binding a unique sequence on *SMN2*'s messenger RNA located just downstream of the crucial seventh exon, thereby obstructing components of the RNA splicing machinery (see 'Bring to one's antisenses'). "We displace some negative regulatory proteins, which allows proper splicing to occur," explains Frank Bennett, head of research at Isis, which is headquartered in Carlsbad, California. In mouse models in which the endogenous *Smn1* gene has been knocked out and human versions of *SMN2* have been swapped in, the Isis therapy—a so-called 'antisense oligonucleotide'—delivered to the mouse central nervous system (CNS) increased the expression of full-length SMN protein in motor neurons, improved muscle strength

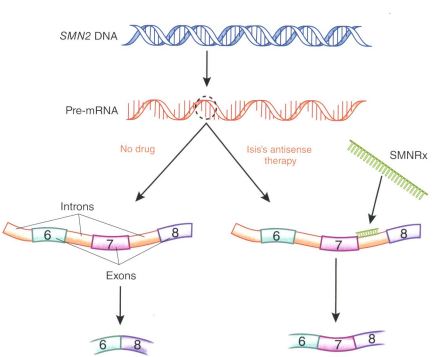

Bring to one's antisenses: Isis's antisense therapy, SMNRx, promotes the inclusion of exon 7.

Lining up against a genetic killer: The SMA drug pipeline.

Mechanism	Developer	Drug type (name)	Phase
SMN splicing	Isis Pharmaceuticals & Biogen Idec	Antisense oligonucleotide (ISIS-SMNRx)	1
	Roche & PTC Therapeutics	Small molecule	Preclinical
	Novartis	Small molecule	Preclinical
	Paratek Pharmaceuticals	Small molecule	Preclinical
SMN translation	Repligen	Small molecule (RG3039)	1
SMN stabilization	NINDS	Small molecule (ALB-111)	Preclinical
	Nationwide Children's Hospital	Viral vector	Preclinical
SMN1 gene therapy	Genzyme	Viral vector	Preclinical
	Généthon & INSERM	Viral vector	Preclinical
Neuroprotection[a]	Trophos	Small molecule (olesoxime)	2

INSERM, Institut National de la Santé et de la Recherche Médicale; NINDS, National Institute of Neurological Disorders and Stroke.
[a]Olesoxime, a mitochondrial pore modulator, is designed to protect neurons but does not affect SMN levels.

in behavioral tests and extended the rodents' median lifespan from 16 days to 26 days[3]. "We think we have a drug that will have a big impact on the disease," Bennett says.

Isis, which is co-developing its drug together with Biogen Idec of Weston, Massachusetts, is hardly alone in its endeavor to correct *SMN2* splicing—but it is the only one currently using an oligonucleotide approach. Other companies, including the Swiss drug giants Novartis and Roche, along with Boston's Paratek Pharmaceuticals, are developing ingestible small-molecule drugs designed to increase the inclusion of *SMN2*'s exon 7. Of note, splice-modulation therapy is also being pursued for other rare neuromuscular disorders. For example, the exon-skipping drug drisapersen, from the UK's GlaxoSmithKline, is currently being tested worldwide in a 180-person, phase 3 study for the treatment of Duchenne muscular dystrophy, an X-linked disease that affects approximately 1 in every 3,500 boys.

Before adopting this splicing-correction strategy for SMA, many researchers tried increasing the amount of SMN protein in a nontargeted fashion. For example, by using histone deacetylase (HDAC) inhibitors, which, by remodeling chromatin structure, are thought to promote gene expression broadly, including for *SMN2*, numerous groups showed that they could increase SMN protein levels—both truncated and full-length—in mouse models of SMA as well as in patient-derived cell lines. And because several HDAC-blocking drugs are commonly used in other fields of medicine, including neurology, it proved relatively straightforward for physicians to take some of these drugs into clinical trials in patients with SMA. However, even though there are case reports of some children showing dramatic improvements on the drugs, no study has yet demonstrated a statistically significant overall benefit.

Kathryn Swoboda has repeatedly seen HDAC inhibitors disappoint. As director of the pediatric motor disorders research program at the University of Utah School of Medicine in Salt Lake City, she led the Project Cure SMA Investigators Network, a trial consortium that recently published the results of two placebo-controlled trials of the HDAC-blocking agent valproic acid, neither of which demonstrated much clinical advantage from the drug[1,2]. Looking ahead, Swoboda, now one of the four site directors for Isis's phase 1 trial, expects more from the experimental splicing-directed therapy. "I'm more excited about this approach than anything I've been excited about in a very, very long time," she says.

"I'm more excited about this approach than anything I've been excited about in a very, very long time."
– Kathryn Swoboda

Fellow trial site director and pediatric neurologist Claudia Chiriboga, of the Columbia University Medical Center in New York, agrees. "I'm very optimistic that once we find the optimal timing and the optimal dosing we're going to see results that are life altering," she says. Isis's drug, Chiriboga adds, "could change the face of SMA as we know it."

Still, many investigators—and their big pharma backers—see potential in boosting SMN levels through mechanisms other than splicing modulation. These alternate strategies include using small-molecule drugs that affect RNA metabolism or protein stability, as well as administering modified viruses for therapeutic gene delivery (see 'Getting a fix on SMA').

"It's one thing to only try to correct splicing events, but there are a lot more opportunities in terms of drug targets," says Gideon Dreyfuss, a biochemist at the University of Pennsylvania Perelman School of Medicine in Philadelphia who is working with the New Jersey–based pharmaceutical firm Merck to discover new compounds. "Nothing's a winner yet," adds Elliot Androphy, a molecular biologist and dermatologist at the Indiana University School of Medicine in Indianapolis who has conducted many of his own chemical screening experiments. "The world is open to people getting more compounds and several companies have expressed interest in this space."

One need not look further than the drug in late-stage preclinical development at the US National Institute of Neurological Disorders and Stroke (NINDS) in Bethesda, Maryland. Through its SMA Project, a $32 million contract therapeutics development program that ran from 2003 until earlier this year, the agency identified a lead compound, dubbed ALB-111, that induces the read-through of stop codons during protein production. This creates extended SMN proteins that, even though they still lack the seventh exon, may have some functionality or may help stabilize the small amounts of full-length protein. "We are discussing the merits of this compound, the [SMA] Project and its assets with a whole panel of external interested parties—foundations as well as companies—to see if we can establish a licensing agreement where this could be developed further," says Rajan Ranganathan, head of the NINDS's Office of Translational Research.

Capping it off

A separate $13 million nonprofit drug discovery program, this time funded by Families of SMA, an Illinois-based research and advocacy organization, yielded the compound being advanced by Repligen, a small biotech located in Waltham, Massachusetts. The licensed drug, now called RG3039, blocks an enzyme called DcpS that normally takes a protective cap structure off of

Getting a fix on SMA

The predominant therapeutic strategy for treating SMA has focused on using what's already there in the genome. Take the *SMN2* gene and make it work better, the reasoning goes. But another tactic involves putting back what's missing. The *SMN2* gene doesn't work all that well anyway. Why not re-introduce fully functioning copies of *SMN1* instead?

That's the approach being pursued by Brian Kaspar and his colleagues at the Nationwide Children's Hospital in Columbus, Ohio. "We're putting back exactly the target that one needs," Kaspar says. Using an adeno-associated virus as a vector, Kaspar's group has successfully introduced extra copies of the sequence for the human SMN protein into mouse models of SMA. Not only did this extend the animals' lifespans from a matter of weeks to months and sometimes years, but it also restored motor function to near-normal levels (*Nat. Biotechnol.* **28**, 271–274, 2010).

"Gene delivery studies have demonstrated some of the most remarkable survival spans," Kaspar says. Similar preclinical results with comparable gene therapy products have also been reported by scientists at Genzyme, a Massachusetts-based subsidiary of the French drug giant Sanofi, and at Généthon, a nonprofit organization funded by the French Muscular Dystrophy Association (*J. Clin. Invest.* **120**, 1253–1264, 2010; *Hum. Mol. Genet.* **20**, 681–693, 2011).

With an eye to the clinic, Kaspar and his colleagues have also administered their viral construct to newborns from two larger animal species: pigs and cynomulgus macaque monkeys. The researchers showed that both blood- and brain-targeted injections led to successful viral uptake, with the introduced gene being expressed throughout the central nervous systems of these young animals with few adverse effects (*Mol. Ther.* **19**, 1971–1980, 2011).

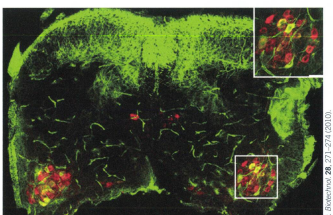

Nat. Biotechnol. **28**, 271–274 (2010).

Deliver the goods: Injection of the Ohio group's gene therapy construct results in gene expression (green) within dorsal root ganglia and motor neurons (red) in the spinal cords of SMA mice.

Now the Ohio team is working on generating the toxicology and pharmacokinetic data necessary for a full regulatory application. Led by Jerry Mendell, director of the Center for Gene Therapy at Nationwide Children's Hospital, the researchers intend to start clinical trials involving infants with type I SMA within the next year. "We think we have a very convincing argument," says Mendell, "and we'll have good safety data that we'll be able to move into a clinical trial in the zero- to six-month-old children." —*ED*

messenger RNA transcripts and primes them for destruction. By inhibiting that process, researchers have shown that they can increase the levels of SMN transcripts—both truncated and full length—resulting in elevated overall protein production and improvements in behavior and survival among mouse models of the disease[4]. "We're changing the steady-state metabolism of RNA," says James Rusche, head of research at Repligen.

In mouse studies, RG3039 increased the expression of SMN in central nervous system tissue by only about 50%—a "pretty modest" amount, admits Rusche. But that may be enough to generate real therapeutic benefits. "The production of SMN protein doesn't need to increase by much to go from almost no survival to almost no disease," Rusche says. "That appears to be true in the natural history of patients, and it appears to be true in the animal models as well."

"Maybe we'll be able to achieve cure if we intervene early."
– Basil Darras

Although Isis's drug was the first SMN-targeting agent tested in children, RG3039 was actually the first SMN-directed drug discovery program to enter human trials, albeit in a healthy adult population. Repligen launched a single-dose, phase 1 trial involving 32 adult volunteers in May 2011. A year later, at the 2012 Annual Meeting of the American Academy of Neurology in New Orleans, the company announced that its oral liquid formulation of RG3039 proved safe, with molecular signs that the compound inhibited DcpS in peripheral blood cells. A multidose safety study among a second 32-person adult cohort kicked off in September of this year.

The drug's effect in peripheral blood cells is not inconsequential. Studies are beginning to show that SMA might not simply be a disease of the motor neurons, but one borne out in the peripheral muscles and other tissues, too. If validated, these emerging—and, it should be said, somewhat controversial—findings could mean that SMN-targeted drugs will need to work throughout the body, not just in the CNS, to have maximal therapeutic effect.

By default, that's already the case for small-molecule drugs such as the ones under development at Repligen and Roche. "If it gets in the brain, it gets in every cell in the body," notes Luca Santarelli, head of neuroscience at Roche, which is co-developing its splicing-targeted drug with PTC Therapeutics of Piscataway, New Jersey. It's trickier for oligonucleotide approaches, such as Isis's antisense therapy, which, in its first phase 1 study, was administered only into the CNS.

Although researchers found that delivering the Isis drug directly into the brain nearly doubled survival time in a mouse model of SMA[3], systemic administration in the rodents—which usually die within two weeks—has been shown to extend median survival by up to eight months. "The results unequivocally say that you need high levels of SMN somewhere in peripheral tissues to have a healthy mouse," says study author Adrian Krainer, a molecular biologist at the Cold

A pillar of strength: Vivienne (right), shown here in August 2012 with her sister Lara (left), feels stronger and more confident after the Isis therapy.

Spring Harbor Laboratory in Long Island, New York, who has been working with Isis since 2004.

Beyond location, there is also the question of timing. A recent preclinical study that involved an experimental oligonucleotide drug similar to SMNRx found that waiting to administer the therapy drastically reduced its effectiveness. Mice treated four days after birth had a median survival of 41 days; by comparison, most mice treated immediately after birth lived for 100 days or longer[6], a finding that mirrors earlier gene therapy studies[7]. "The later you go, the worse the impact gets," says study author Arthur Burghes, a molecular geneticist at Ohio State University in Columbus. "Where are those time points in a human individual with SMA? We don't absolutely know."

Getting there early

In its first safety tests, Isis's drug is being tested only in children who are over the age of 2. (A second, phase 1 study involving multiple doses of SMNRx and a similar demographic of patients is scheduled to begin recruitment before the end of the year.) But as the company gears up to test for signs of efficacy, Basil Darras, Vivienne's doctor at Boston Children's Hospital, expects to see the most pronounced effects in the youngest cohorts. "Maybe we'll be able to achieve cure if we intervene early—shortly after birth or before you develop symptoms," he says. This consideration has led to increased interest in SMA screening for all newborns. For example, Kathryn Swoboda plans to launch a state-wide pilot screening program in Utah sometime early next year.

Cure is the ultimate goal, especially for the thousands of children born each year with type 1 SMA. But for people with type 2 or type 3 SMA, "the reality is that any sort of treatment would be a blessing," says Jill Jarecki, research director of Families of SMA who, in a previous job, led the small-molecule screening effort that yielded RG3039, the Repligen compound. "Typically what the patients say is, 'Of course we want a cure. Of course we want the slam dunk. But just give us something that will stop progression.'"

That's all that Vivienne's parents were realistically expecting at the onset of the trial. Yet, Vivienne's renewed abilities have continued to defy expectations. In September, she went from lying down to a sitting position all on her own. She also took a single, unaided walking step. She hadn't managed to perform either of those actions for well over a year.

"If that's already the effect of one injection of just six milligrams," says her father Helge, "the question that arises of course is, 'What would more of the drug do?'" Vivienne and her family may soon know the answer to that question. As part of a planned follow-up study, Vivienne is scheduled to receive another dose of the drug sometime next year.

Elie Dolgin is a news editor with* Nature Medicine *in Cambridge, Massachusetts.

1. Swoboda, K.J. *et al. PLoS One* **5**, e12140 (2010).
2. Kissel, J.T. *et al. PLoS One* **6**, e21296 (2011).
3. Passini, M.A. *et al. Sci. Transl. Med.* **3**, 72ra18 (2011).
4. Butchbach, M.E. *et al. Hum. Mol. Genet.* **19**, 454–467 (2010).
5. Hua, Y. *et al. Nature* **478**, 123–126 (2011).
6. Porensky, P.N. *et al. Hum. Mol. Genet.* **21**, 1625–1638 (2012).
7. Foust, K.D. *et al. Nat. Biotechnol.* **28**, 271–274 (2010).

Clinical trials must cope better with multiplicity

Janet Wittes

Janet Wittes

Clinical trials typically address more than one question. But in attempting to protect against misleading results that are due to chance when multiple interrelated tests are run simultaneously, researchers sometimes apply overly strict statistical devices that mask true effects. They should give more consideration to choosing the type of statistical analysis that fits best.

After pouring millions of dollars into developing a drug, researchers want to learn not only whether a drug works but what the magnitude of its effect is, what clinical outcomes it affects and who should receive it. Thus they ask many questions of data collected in clinical studies. However, these interwoven questions can present a challenge when it is time for the statistical analysis of the trial's results. With the increasing complexities of clinical trials, scientists need to be more thoughtful when it comes to choosing how they crunch the numbers. Biomedical researchers do not always choose the statistical constructs that suit their studies best, and as a result the studies they publish might miss real effects from the interventions under investigation.

In designing a trial under a classical statistical framework, researchers typically preselect a type I error rate, an effect size, and statistical power. Conventionally set at 0.05 in medical statistics, the type I error rate is the probability of declaring two therapies different if they are exactly the same. When a study ends, scientists calculate the probability that two identical medical treatments would have yielded a difference at least as large as the one observed and hope this P value comes out to less than 0.05, indicating that the results are statistically significant.

Physicians, regulators and patients should worry about both type I errors—finding a benefit when there is none—and type II errors, where calculations fail to show a statistically significant benefit of an effective product. There's good reason for these concerns. Some scientists declare any comparison with a P value of less than 0.05 statistically significant. Those who object to *post hoc* data dredging might prespecify many hypotheses but still declare success for any of those hypotheses whose P value is less than 0.05. But the more shots at a target, the higher the chance of hitting it (or, in the context of experimentation, the more a researcher looks at the data, the more apparently statistically significant results he or she will find even if the experimental therapy yields results no different from the control). The difficulty of making reliable inferences in the face of many hypotheses is the problem of multiplicity.

To deal with multiplicity, statisticians have developed methods to limit the probability of making a type I error; these methods lower probability of finding benefit of a product that in reality acts no better than the control therapy. To use the commonly applied Bonferroni's correction, investigators who ask a number of prespecified questions declare any comparison significant if its P value is less than 0.05 divided by the number of questions. This strict method does indeed limit type I errors, but sometimes Bonferroni's corrections mask true effects because, as is common in medical trials, not all comparisons are independent of each other, not all have equal statistical power and not all are equally credible.

Yet Bonferroni's test treats all comparisons equally. For example, Rios *et al.*, in a meta-analysis of omega-3 fatty acids, examined eight outcomes: all-cause mortality, cardiac death, sudden death and myocardial infarction, each tested once to compare relative risk and once to compare absolute risk (*JAMA* **308**, 1024–1033, 2012). The paper has engendered considerable interest in the popular press. But, simultaneously, the findings have come under scrutiny stemming from the study's approach to multiplicity (M. Beck, *Wall Street Journal* D1, 2 October 2012). The authors declared comparisons statistically significant only for P values less than 0.05 / 8, or 0.0063. None of the eight comparisons passed that hurdle. The relative risk for cardiac death, however, was 0.91 with a P value of 0.01. Had the authors looked only at cardiac death, or had they tested only the relative risks, they would have found statistically significant evidence of benefit on cardiac death.

How should scientists deal with interwoven hypotheses within a clinical trial? For better or worse, a multiplicity of approaches to multiplicity is available. On one extreme are those who urge reporting observed uncorrected P values, thus raising the specter of finding many results that will later be shown to be incorrect. Bonferroni-ites sit on the other extreme; ignoring the structure of the hypotheses, they simply divide by the number of questions they ask. This method is subject to abuse too: to show a product does not work, list a host of hypotheses to make the criterion for benefit so stringent that the chance of finding anything statistically significant will be very low.

Indeed, sometimes Bonferroni's corrections are not applied when they should be. Consider, for example, a 12 October briefing document from the US Food and Drug Administration's Gastrointestinal Drugs Advisory Committee that detailed a three-arm trial comparing 0.10 milligrams per kilogram body weight per day and 0.05 milligrams per kilogram body weight per day of the peptide drug teduglutide (Gattex, made by New Jersey's NPS Pharmaceuticals) to placebo in adults with short bowel syndrome. The analysis specified comparing the low dose to placebo only if the P value comparing high dose to placebo was less than 0.05. The P value for the high dose was 0.17, allowing no further formal statistical testing. The observed P value for the low dose was 0.007. Under Bonferroni's correction, the low dose would be called statistically superior to placebo. Why decide to preclude testing of a low dose if a high dose is not statistically significant.

Saying that something doesn't work when it actually does is bad for both drug development and public health. The methods must account for biological relationships among outcomes (for example, cardiac death is a subset of death) and the relative importance of the questions asked. Biomedical researchers and doctors dealing with statisticians who propose a Draconian-seeming method for avoiding type I errors should not hesitate to push for a technique that better reflects their understanding of the underlying biology. And, statisticians should work together with clinicians and bench scientists to develop an approach to multiplicity that comports with important questions being asked.

Janet Wittes is president and founder of Statistics Collaborative, in Washington, DC, and a fellow of the American Statistical Association.

Cocaine, Sex and Physicians

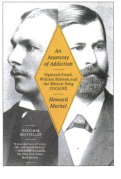

An Anatomy of Addiction: Sigmund Freud, William Halsted, and the Miracle Drug Cocaine

Howard Markel

Pantheon, 2011
352 pp., hardcover, $28.95
ISBN: 0375423303

Reviewed by John Mendelson

Howard Markel's wonderful book *An Anatomy of Addiction: Sigmund Freud, William Halsted, and the Miracle Drug Cocaine* is a rare treat that excels on several planes. Markel, a physician and professor of history at the University of Michigan, has crafted a book that is both a learned history and a salacious read. He tells the story of two of the most important physicians of the last 200 years: Sigmund Freud and William Stewart Halsted. And the story he tells is one of brilliance, invention and ambition intertwined with drugs, sex and near catastrophe. Markel chronicles the nineteenth century discovery by Europeans of cocaine and describes the purification and commercialization of the drug by European and American chemists. He then uses Freud's and Halsted's stories to delve into the complexities of drug abuse and the development of addiction and to illuminate the origins of our systems for understanding and treating surgical and psychiatric diseases.

Freud is a household name—who hasn't heard of the unconscious or psychoanalysis? Halsted, in contrast, although perhaps less well known than Freud to the layperson, laid the foundations for modern surgical technique and practice. He invented many basic suturing techniques and operations (such as the radical mastectomy) that are still in use and was the first to insist on sterile operating fields and clean clothing—if you have ever worn a surgical scrub, you can thank Halsted. Along with William Osler, William Welch and Howard Kelly, he was one of the four founding physicians of the Johns Hopkins Hospital. What is less well known is that both Freud and Halsted were cocaine addicts.

We meet Freud and Halsted as young, ambitious and personable physician-scientists and follow their separate stories as cocaine initially helps, but then nearly destroys, their careers and lives. Each started using cocaine as a therapeutic drug—Freud for its mood-altering properties and Halsted as a local anesthetic—and, through self-experimentation, both became addicted. Freud conducted and published human studies, often as both the subject and investigator, where he came to believe that cocaine was a wonder drug that could cure most anything. Along with Wilhelm Fliees, an early pioneer in otolaryngology, he promoted a bizarre theory that the nose is the most important organ in the body, directly regulating health and human sexuality. Together, they treated scores of patients with intranasal cocaine, nearly killing some and addicting many.

Although Freud did not appear to suffer long-term complications of his addiction, Halsted paid a huge personal price for his experimentation with cocaine. He ended up as the first patient admitted to an insane asylum for cocaine addiction and suffered a complete change in personality due to regular use of cocaine. Interestingly, Freud promoted and tested the use of cocaine to treat opiate addiction, but for Halsted opiates became the substitute for cocaine that allowed him to function in society; he injected ~200 mg of morphine every day for most if not all of his time as the Chief of Surgery at Hopkins. Thus, Halsted also has the unique distinction of being the first person to demonstrate the efficacy of opiate substitution therapy.

What would a tell-all story be without sex? It turns out that Freud and Halsted had complex sex lives: Freud was bisexual and Halsted was almost certainly gay. It seems Freud was at his most libidinous while using cocaine; only after quitting was he able to maintain the stable family life that allowed him to produce his best work. Halsted, following the death of his presumed lover, descended into a deeper dependence on cocaine. Consistent with what we know today about the consequences of addiction on relationships, Halsted seems to have been unable to form any lasting intimate relationships for the remainder of his life, an observation supported by a late-in-life marriage of convenience that seemed designed to provide more supervision than love.

It is hard to envision either of these incredible intellects and innovators surviving in the modern medical community. Imagine today's Halsted having to explain a two-year hiatus from his practice for psychiatric treatment or being allowed to self-treat cocaine addiction with morphine injections and continue to perform major surgery. Or imagine Freud rising in academia and achieving public acceptance after nearly killing several patients with cocaine overdoses, exhibiting cocaine-induced paranoia and engaging in poorly veiled infidelities. Markel lets us see that, despite the emotional and physical damage wrought by repeated cycles of intoxication, withdrawal, craving and relapse, both of these giants were able to maintain a place in the scientific and medical communities and make a mark on history.

Importantly, *An Anatomy of Addiction* offers more than just juicy reading. Markel also weaves into his narrative lucid and clear explanations of the psychology and pharmacology of addiction; he provides a clear and well-crafted distillation of a huge volume of science. But what makes this book a must-read are the stories of our intellectual fathers, their journeys into darkness and their stunning achievements despite their struggles with the very real demons of addiction. I recommend this wonderful book for all physicians and scientists.

COMPETING FINANCIAL INTERESTS
The author declares no competing financial interests.

John Mendelson is at the Addiction and Pharmacology Research Laboratory, California Pacific Medical Center Research Institute, San Francisco, California, USA.
e-mail: john.mendelson@cpmcri.org

Not just a rush of blood to the head

Andrew J Brumm & S Thomas Carmichael

Angiogenesis is a key feature of central nervous system injury. A neovessel-derived signal mediated by prostacyclin triggers axonal sprouting and functional recovery in a mouse model of inflammatory spinal cord injury (pages 1658–1664). Are such angiocrine signals relevant to neurovascular remodeling and recovery in other neurological contexts?

Acute central nervous system (CNS) injury induces damage but also a process of delayed tissue repair. Neural repair involves remodeling the boundaries of the lesion, forming new blood vessels, elaborating new neuronal connections and generating new populations of neurons and glia. The formation of new blood vessels through sprouting from preexisting vessels[1], a phenomenon called angiogenesis, occurs in stroke, traumatic brain and spinal cord injury, and multiple sclerosis during the repair phase of the disease process[2,3]. Angiogenesis has been correlated with improved functional outcome in both animal models and human stroke[2]; however, causative roles for angiogenesis in neural repair and recovery after CNS injury remain poorly defined.

Neovessels are formed in perilesional tissue in both inflammatory and traumatic spinal cord injury[3,4]. In this issue of *Nature Medicine*, Muramatsu *et al.*[5] use a highly targeted inflammatory injury to the thoracic spinal cord that damages descending corticospinal tract (CST) projections from the brain to model some aspects of human multiple sclerosis. The neovessels formed around the injured tissue secrete a factor called prostacyclin that binds damaged CST neurons, enhancing axonal growth and motor recovery in mice with spinal cord injury. The findings unveil a link between angiogenesis and axonal sprouting and identify a potential pathway to target in CNS disease.

A previous study using a similar model of spinal cord injury has shown that these CST axons sprout in response to injury to form new connections with propriospinal or intersegmental circuits, the local projections within the spinal cord that can bypass the lesion[6]. Although the formation of these new CST connections mediated elements of functional recovery[6,7], what initiated their formation and how they are developed in topographic relationship to the injury and to the cell bodies of the intersegmental neurons are still unclear.

The link between angiogenesis and axonal growth has been well documented in the peripheral nervous system (PNS)—common signaling systems mediate molecular interactions between the developing vasculature and the PNS[1]. In ischemic stroke or in brain or spinal cord trauma, angiogenesis occurs too late to facilitate recovery through an effect on blood flow. During tissue remodeling after stroke, however, neuronal dendrites reshape along vascular profiles[8], and in the case of spinal cord injury, axonal sprouting occurs in close association to blood vessels[4,9,10]. Certain drugs and cell-based therapies such as statins, a modified form of activated protein C and progenitor cell transplants stimulate both angiogenesis and axonal sprouting[11,12]. These data have established the physical proximity of neuronal processes and axonal sprouting with blood vessels in the regenerating CNS but have not revealed the vessel-derived molecular signals that mediate their interaction.

Muramatsu *et al.*[5] showed that new blood vessels form in the spinal cord proximal to the injury site and the descending projections from the motor cortex sprout collaterals in this same region in injured mice. In the circuitry of the injured spinal cord, amounts of PGI_2 (prostaglandin I_2 or prostacyclin) synthase (PGIS), the final enzyme in prostacyclin production, and of the prostacyclin metabolite 6-keto-PGF1α are elevated during the peak of post-injury angiogenesis. The prostacyclin receptor, IP receptor, which was expressed in motor cortical neurons, was involved in functional recovery, as siRNA knockdown of this receptor well away from the site of injury blocked axonal sprouting and delayed motor recovery[5]. Selective knockdown of PGIS in the blood vessels of the injured spinal cord also had the same blocking effect. Direct delivery of IP receptor agonists such as iloprost promoted axonal sprouting, enhanced axonal signaling through the lesion site and improved functional recovery, whereas delivery of antagonists such as PGIS or siRNA-mediated knockdown of IP receptor blocked these processes. Interestingly, deletion of PGIS in blood vessels near the injury site did not block angiogenesis, suggesting that angiogenesis and neovessel formation *per se* are not responsible for axonal sprouting and recovery; instead, the eicosanoid signaling pathway through prostacyclin from these vessels to nearby axons is the key element.

The evidence begins to describe the molecular links between angiogenesis, axonal sprouting and CNS recovery from injury; however, there are also important limitations. In development and in preclinical studies of disease models of axonal sprouting, axons and blood vessels are physically associated. Yet no such physical link was demonstrated by Muramatsu *et al.*[5]. Is this vessel-derived prostacyclin signal trophic or tropic? Prostacyclin activation of its IP receptor on neurons elevates intracellular cyclic AMP levels, which in most axonal outgrowth systems promotes axonal sprouting as well as directional growth cone movement toward the source of the molecule that promotes elevated cyclic AMP[12]. It is surprising that vessel-derived prostacyclin, as a local signal for cyclic AMP induction in a growing axon, does not localize this axon to the source (along or in close proximity to the neovessels). The targeted inflammatory injury model used by Muramatsu *et al.*[5] has the advantage of providing for focal delivery of

Andrew J. Brumm and S. Thomas Carmichael are in the Department of Neurology, Geffen School of Medicine at the University of California–Los Angeles, Los Angeles, California, USA.
e-mail: scarmichael@mednet.ucla.edu

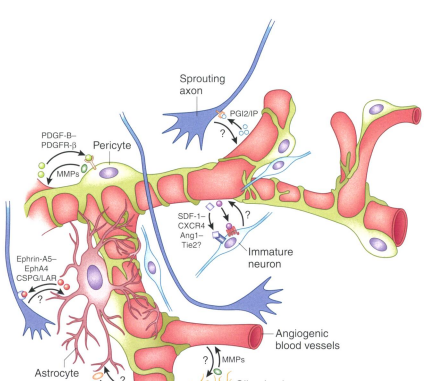

Figure 1 The regenerative neurovascular niche. Acute CNS injury induces new blood vessels (angiogenesis), new neurons (neurogenesis) and new connections (axonal sprouting). These regenerative processes occur in tissue adjacent to the primary injury site in perilesional tissue. The cellular elements of this regenerative environment are the angiogenic blood vessels, pericytes, astrocytes, immature neurons and sprouting axons. Muramatsu *et al.*[5] show in a mouse spinal cord injury model that prostacyclin is secreted by angiogenic blood vessel endothelial cells and signals through its IP receptor on corticospinal tract neurons to induce axonal sprouting into perilesional tissue. Other studies have identified molecular signals that communicate among the other cellular elements of the regenerative neurovascular niche. Angiocrine factors, such as stromal-derived factor 1 (SDF-1) and angiopoietin 1 (Ang1) from angiogenic blood vessels attract migrating immature neurons that express cognate receptors, such as CXCR4 and Tie2, respectively; the localization of these into injured tissue is associated with recovery[13]. Platelet-derived growth factor B (PDGF-B) secreted by endothelial cells is trophic for pericytes that express its cognate receptor, platelet-derived growth factor receptor β (PDGFR-β). PDGFR-β that is expressed by neurons and astrocytes within this niche mediates neuroprotection and glial scar formation after injury. Astrocyte-derived ephrin-A5 (a vascular signaling molecule) binds EphA4 receptor and blocks growth of sprouting axons. Reactive astrocytes alter endothelial cell production of tissue plasminogen factor via transforming growth factor β (TGF-β). Reactive astrocytes produce large amounts of chondroitin sulfate proteoglycans (CSPGs), which form a strong barrier for regenerating axons that express CSPG receptors, such as the leukocyte common antigen-related phosphatase receptor (LAR). Both pericytes and oligodendrocyte precursor cells are a source of matrix metalloproteinases (MMPs), which regulate blood vessel remodeling.

experimental manipulations. However, it is further afield from the human multiple sclerosis condition and involves a complicated delivery of three inflammatory stimuli (systemic myelin basic protein in Freund's adjuvant, focal tumor necrosis factor-α and γ-interferon, and systemic delivery of pertussis toxin). For clinical relevance, it will be important to confirm that this prostacyclin signaling system is active in other multiple sclerosis models, such as the traditional experimental autoimmune encephalitis models. If the finding that neovessel-derived prostacyclin induces local axonal sprouting and functional recovery in other CNS injury and regeneration models, then this might be clinically targeted with focal delivery of prostacyclin agonists into recovering tissue.

Tissue repair after acute CNS injury occurs in a unique cellular environment adjacent to the injury site that involves cellular events not normally active in most brain areas—angiogenesis is linked to neurogenesis in an area of active axonal sprouting and tissue remodeling. The new study from Muramatsu *et al.*[5] adds to a body of evidence demonstrating a unique regenerative neurovascular niche in perilesional tissue that mediates many processes in recovery of function (**Fig. 1**). For example, angiogenic blood vessels signal to newly born neurons after stroke to localize to peri-infarct tissue[13]. In this neurovascular niche after stroke, neurogenesis is causally regulated by angiogenesis and dependent on angiogenic vessel–derived, or angiocrine, factors[13]. As with the relationship of axons and blood vessels in the developing PNS, common molecular factors—ephrins, vascular endothelial growth factor, semaphorins and others—participate in axon and vascular signaling in the regenerative neurovascular niche[14]. Common cellular signaling events, or molecular control points, crucial for the regenerative neurovascular niche may therefore be identified that can serve as targets to promote tissue repair at multiple levels after acute CNS injury.

Well outside of their traditional conception as passive blood flow conduits, angiogenic blood vessels are a rich tissue source for secreted and membrane-bound signaling molecules that have been shown to form instructive vascular niches in cancer and peripheral injury environments. The paracrine signaling role described by Muramatsu *et al.*[5] for spinal cord endothelial cells may be part of an emerging wavefront in the study of angiogenesis and neural repair in acute CNS injury.

COMPETING FINANCIAL INTERESTS
The authors declare no competing financial interests.

1. Quaegebeur, A., Lange, C. & Carmeliet, P. *Neuron* **71**, 406–424 (2011).
2. Ergul, A., Alhusban, A. & Fagan, S.C. *Stroke* **43**, 2270–2274 (2012).
3. Oudega, M. *Cell Tissue Res.* **349**, 269–288 (2012).
4. Loy, D.N. *et al. J. Comp. Neurol.* **445**, 308–324 (2002).
5. Muramatsu, R. *et al. Nat. Med.* **18**, 1658–1664 (2012).
6. Kerschensteiner, M. *et al. J. Exp. Med.* **200**, 1027–1038 (2004).
7. Bareyre, F.M. *et al. Nat. Neurosci.* **7**, 269–277 (2004).
8. Brown, C.E., Li, P., Boyd, J.D., Delaney, K.R. & Murphy, T.H. *J. Neurosci.* **27**, 4101–4109 (2007).
9. Dray, C., Rougon, G. & Debarbieux, F. *Proc. Natl. Acad. Sci. USA* **106**, 9459–9464 (2009).
10. Chen, J. *et al. Ann. Neurol.* **53**, 743–751 (2003).
11. Thiyagarajan, M., Fernández, J.A., Lane, S.M., Griffin, J.H. & Zlokovic, B.V. *J. Neurosci.* **28**, 12788–12797 (2008).
12. Zheng, J.Q. & Poo, M.M. *Annu. Rev. Cell Dev. Biol.* **23**, 375–404 (2007).
13. Ohab, J.J., Fleming, S., Blesch, A. & Carmichael, S.T. *J. Neurosci.* **26**, 13007–13016 (2006).
14. Overman, J.J. *et al. Proc. Natl. Acad. Sci. USA* **109**, E2230–E2239 (2012).

SAMHD1 does it again, now in resting T cells

Nan Yan & Judy Lieberman

A long-standing question in the HIV field is why HIV-1 fails to replicate in resting CD4$^+$ T cells. A new study shows that host deoxynucleoside triphosphate triphosphohydrolase (dNTPase) sterile α motif and histidine/aspartic domain–containing protein 1 (SAMHD1), previously shown to block HIV infection in myeloid cells, also restricts HIV replication in resting CD4$^+$ T cells by hydrolyzing dNTPs, which are needed for reverse transcription of the virus (pages 1682–1687).

One of the puzzles of HIV-1 biology is why the virus barely replicates in resting CD4$^+$ T lymphocytes, whereas activated CD4$^+$ T lymphocytes support robust HIV-1 replication. In HIV-infected people, very few T lymphocytes in the peripheral blood or lymph node are actively infected (even in the absence of antiviral treatment), and viral replication is mostly restricted to activated CD4$^+$ T cells. In resting CD4$^+$ T cells, reverse transcription, which copies the viral genomic RNA to cDNA soon after viral entry before nuclear import and chromosomal integration, is very inefficient, and other barriers to viral production appear at later steps in the viral life cycle[1,2].

The study by Baldauf *et al.*[3] in this issue *of Nature Medicine* provides a simple and elegant explanation for HIV-1 restriction in resting T cells (**Fig. 1**). The authors identify SAMHD1, a dNTPase that removes the triphosphate from dNTPs, as a host restriction factor for HIV-1 in resting CD4$^+$ T cells.

Mutations in *SAMHD1* are associated with Aicardi-Goutières syndrome (AGS), an autoinflammatory genetic brain disorder of newborns that mimics congenital infection and is characterized by elevated amounts of type I interferons[4]. SAMHD1 was identified in 2011 as the long-sought restriction factor for productive infection by HIV of myeloid dendritic cells, monocytes and macrophages[5,6]. SAMHD1 limits HIV-1 replication in these cells by depleting intracellular dNTPs, thus blocking HIV DNA synthesis by reverse transcription[7]. High dNTP concentrations are not needed in nondividing cells and are kept low; myeloid cells have about 1% of the concentration of dNTPs in activated T cells. Although HIV-1 reverse transcriptase very efficiently uses dNTPs, the dNTP concentration in myeloid cells is rate limiting. The small lentiviral accessory protein Vpx (from SIV or HIV-2, which is missing in HIV-1) targets SAMHD1 for ubiquitination and degradation. Supplying Vpx or knocking down SAMHD1 at the time of HIV-1 infection enhances dNTP concentrations within hours, promotes reverse transcription and drastically improves HIV-1 replication in myeloid cells[5,6].

The original papers describing SAMHD1 (refs. 5,6) assumed that this factor was not operating in T cells because the authors did not detect SAMHD1 expression in T cell lines. However, Baldauf *et al.*[3] found that supplying Vpx before or at the time of HIV-1 challenge greatly enhanced reverse transcription and HIV gene expression in resting T cells, as it had in myeloid cells. Consistent with these results, they showed that SAMHD1 is as highly expressed in resting primary human CD4$^+$ T cells as in the THP-1 monocyte cell line, but is not expressed in Jurkat T cells (as previously reported). Vpx does not alter the quiescent state of resting T cells but elevates cellular dNTP concentrations to facilitate HIV reverse transcription by activating proteasomal degradation of SAMHD1. To confirm that SAMHD1 is the restriction factor overcome by Vpx, the authors knocked down SAMHD1 in resting CD4$^+$ T cells and observed increased HIV replication[3]. Incubation of resting CD4$^+$ T cells with dNTPs also enhanced their infection with HIV-1. The authors also found that resting CD4$^+$ T cells from a patient with AGS with a nonsense mutation in *SAMHD1* are permissive for HIV-1. This result is consistent with a previous study that found that *SAMHD1* deficiency significantly enhanced HIV-1 replication in peripheral blood mononuclear cells (PBMCs) compared with normal controls, but only when the PBMCs were not activated[8].

Baldauf *et al.*[3] also made several unexpected observations about SAMHD1 expression. First, SAMHD1 expression was similar in resting and activated CD4$^+$ T cells. As T cell activation is linked to cell proliferation and dividing cells need dNTPs for DNA replication, one would expect reduced SAMHD1 expression following T cell activation. This is not the case[3], suggesting that dNTP concentrations are maintained in activated T cells by other enzymes, that SAMHD1 activity is regulated post-translationally or requires interaction with other host factors, or that its expression is tightly controlled during the cell cycle and is only degraded transiently around the time of DNA synthesis when elevated dNTP concentrations are needed (only a fraction of activated T cells are in S phase at any time). Consistent with this last idea, the authors found that a proliferation marker (Ki67) and SAMHD1 were never concurrently expressed in immune cells in human tonsil sections[3]. However, a more careful analysis of SAMHD1 expression and dNTP concentrations (and HIV-1 susceptibility) in activated T cells at different phases of the cell cycle is also warranted.

Another unexpected finding by Baldauf *et al.*[3] was that SAMHD1 localizes to both the nucleus and cytoplasm in T cells and monocyte-derived macrophages, as previous studies suggested that SAMHD1 is mostly located in the nucleus[4,8–10]. Vpx arrives in the cytoplasm with the incoming virion, but it is actively transported to the nucleus. Where in the cell Vpx and SAMHD1 interact needs to be clarified, especially given that there are conflicting reports about whether leptomycin B, which inhibits nuclear export of proteins, interferes with Vpx-mediated SAMHD1 degradation[9,10].

But how much does SAMHD1 contribute to the overall restriction of HIV-1 replication in resting CD4$^+$ T cells? Most of the experiments in this study[3] and in the previous myeloid cell papers[5–7,9–12] compared the effects of supplying Vpx or exogenous dNTPs or knocking down SAMHD1 on early steps in the viral life cycle by measuring the amounts of early reverse transcripts or HIV-1 long terminal repeat (LTR)-driven transcription from a single round of replication of an integrated reporter virus. Baldauf *et al.*[3] found that HIV-1 transcription from Vpx-treated resting CD4$^+$

Nan Yan is in the Department of Internal Medicine and Department of Microbiology, University of Texas Southwestern Medical Center, Dallas, Texas, USA. Judy Lieberman is in the Program in Cellular and Molecular Medicine, Boston Children's Hospital, and Department of Pediatrics, Harvard Medical School, Boston, Massachusetts, USA.
e-mail: nan.yan@utsouthwestern.edu or lieberman@idi.harvard.edu

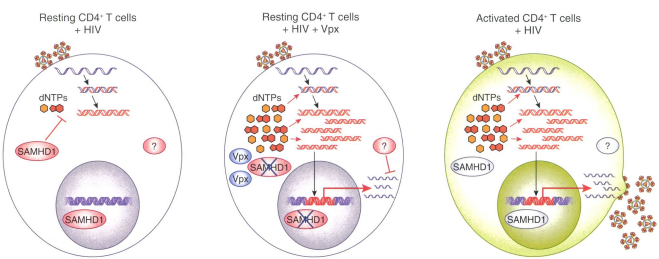

Figure 1 SAMHD1 restricts HIV-1 replication in resting CD4+ T cells by reducing dNTP concentrations needed for reverse transcription. Baldauf *et al.*[3] show that HIV infection of resting CD4+ T cells (left) is blocked by the SAMHD1 restriction factor early in the viral life cycle by limiting the amounts of dNTPs, which are needed to reverse transcribe genomic RNA (purple) into a cDNA copy (red). When they engineered HIV-1 virions to contain Vpx (normally present in HIV-2 but not HIV-1) (middle), they found that Vpx orchestrates the proteosomal degradation of SAMHD1, dNTP concentrations rise and reverse transcription, integration of the viral cDNA into the chromosome and transcription of HIV genes occurs. However, an unknown downstream block in these cells interferes with release of virions. In activated CD4+ T cells (right), despite high expression of SAMHD1, dNTP concentrations are elevated enough to support reverse transcription, and the viral life cycle goes to completion with release of infectious virus.

T cells is about 25% of that in Vpx-untreated activated CD4+ T cells from the same donor. The residual advantage to HIV-1 in activated T cells is probably explained by the greater nuclear abundance of transcription factors, such as NFAT, FOS, JUN and nuclear factor-κB, in activated T cells that are also required to turn on the HIV-1 LTR. However, viral reverse transcription, integration and transcription is not the whole story. The authors could not detect viral production in resting CD4+ T cells infected with Vpx-containing HIV-1; thus, unknown Vpx-insensitive blocks to HIV production occur at a later stage in the viral life cycle. It is unclear whether this might also be the case in myeloid cells. Although two studies have found that Vpx-treated monocyte-derived dendritic cells are more efficient at transmitting the virus to activated CD4+ T cells in *in vitro* co-culture[11,13], it is uncertain whether cell-free viruses were produced by the infected dendritic cells.

With this new study by Baldauf *et al.*[3], SAMHD1 is becoming an increasingly important host restriction factor for HIV-1 in both myeloid cells and resting CD4+ T cells. During HIV-1's evolution from primate lentiviruses, the accessory gene that counters SAMHD1 (*vpx*) was lost. Do loss of *vpx* and persistent SAMHD1 expression and the corresponding limit to infection in myeloid cells and resting CD4+ T cells provide an advantage to HIV-1? It would seem so. Although the simian immunodeficiency virus strain $SIV_{mac}239$, which lacks *vpx*, is slightly less pathogenic than the wild type SIV virus in rhesus monkeys[12], in humans, HIV-1 (which lacks *vpx*) is much more pathogenic than HIV-2 (which resembles macaque SIV and contains *vpx*). Although these findings are at first counterintuitive, the answer to why HIV-1 has lost *vpx* may lie in avoiding triggering an antiviral innate immune response in SAMHD1-restricted cells. When dendritic cells are infected with HIV-1 supplemented with Vpx, expression of interferon-β, a cytokine that orchestrates a global antiviral response, is induced[11,13]. It is not clear how Vpx-mediated degradation of SAMHD1 leads to interferon induction in myeloid cells. HIV-1 reverse transcripts also trigger interferon production in T cells and macrophages when another AGS-linked gene, *TREX1*, is knocked out (in mice) or inactivated (in human cells)[14]. Trex1 is a cytosolic DNase that digests excess nonproductive HIV reverse transcripts to avoid triggering interferon responses in activated CD4+ T cells and macrophages. Mutations in both *TREX1* and *SAMHD1* are linked to AGS, and both enzymes target HIV-1 reverse transcription: SAMHD1 controls DNA synthesis (via dNTP concentrations), whereas Trex1 controls degradation of reverse transcripts, much like a kitchen sink analogy in which SAMHD1 controls the faucet and Trex1 controls the drain. Therefore, HIV-1 may take advantage of both molecules to achieve an optimal viral cDNA concentration to promote viral transmission while evading innate immunity. Further studies are needed to understand whether and how HIV-1 restriction might enable HIV to avoid triggering antiviral innate immunity and how this might enhance viral transmission and infection.

COMPETING FINANCIAL INTERESTS
The authors declare no competing financial interests.

1. Zack, J.A. *et al. Cell* **61**, 213–222 (1990).
2. Plesa, G. *et al. J. Virol.* **81**, 13938–13942 (2007).
3. Baldauf, H.-M. *et al. Nat. Med.* **18**, 1682–1687 (2012)
4. Rice, G. *et al. Nat. Genet.* **41**, 829–832 (2009).
5. Laguette, N. *et al. Nature* **474**, 654–657 (2011).
6. Hrecka, K. *et al. Nature* **474**, 658–661 (2011).
7. Lahouassa, H. *et al. Nat. Immunol.* **13**, 223–228 (2012).
8. Berger, A. *et al. PLoS Pathog.* **7**, e1002425 (2011).
9. Hofmann, H. *et al. J Virol.* published online, doi:10.1128/JVI.01657-12 (2012).
10. Laguette, N. *et al. Cell Host Microbe* **11**, 205–217 (2012).
11. Sunseri, N., O'Brien, M., Bhardwaj, N. & Landau, N.R. *J. Virol.* **85**, 6263–6274 (2011).
12. Gibbs, J.S. *et al. J. Virol.* **69**, 2378–2383 (1995).
13. Manel, N. *et al. Nature* **467**, 214–217 (2010).
14. Yan, N., Regalado-Magdos, A.D., Stiggelbout, B., Lee-Kirsch, M.A. & Lieberman, J. *Nat. Immunol.* **11**, 1005–1013 (2010).

Waking up HSCs: a new role for E-selectin

Malcolm A S Moore

Two anatomical niches for hematopoietic stem cells (HSCs) have been reported in the bone marrow, but a distinct function for each of these niches has remained unclear. A new role in stem cell proliferation has now been identified for the adhesion molecule E-selectin expressed by bone marrow endothelial cells at the vascular niche (pages 1651–1657).

A prerequisite for HSC function is the ability to travel through the bloodstream and home to the bone marrow. These circulating HSCs develop low-affinity contacts with the cell adhesion molecules E- and P-selectin on the endothelium in a process called rolling that precedes firm adhesion via ICAM-1 and VECAM-1 (ref. 1). Upon egress from the vasculature, HSCs reside in, or adjacent to, specialized microenvironments in the bone marrow[2,3]. The endothelial or perivascular niche is adjacent to bone marrow endothelial sinuses, and its perivascular stromal cells produce the HSC chemoattractant CXCL12, whereas the endothelium provides the HSC survival and proliferation-inducing factor c-Kit ligand (also known as stem cell factor)[2,3] (**Fig. 1**). The majority of HSCs are quiescent for prolonged periods, and only a minority undergoes asymmetric division to produce one HSC and one non–self-renewing, transit-amplifying progenitor cell[4].

In this issue of *Nature Medicine*, Winkler *et al.*[5] describe a new role for E-selectin expressed exclusively by endothelial cells of the vascular niche, showing that this molecule is a key regulator of HSC proliferation. Mice deficient in either the E- or P-selectin gene (*Sele*$^{-/-}$ or *Selp*$^{-/-}$ mice) show mild phenotypes, but mice lacking both selectins have extreme leukocytosis, marked extramedullary hematopoiesis and a lack of leukocyte rolling and die of opportunistic bacterial infections due to low leukocyte extravasation at sites of inflammation[6]. Winkler *et al.*[5] have now demonstrated increased HSC quiescence and self-renewal potential in *Sele*$^{-/-}$ mice and in wild-type mice given an E-selectin antagonist, GMI-1070.

The authors determined HSC proliferation by measuring BrdU incorporation into DNA during S phase. In wild-type mice, BrdU labeled 50% of HSCs in 3.3 d, whereas it took 9.5 d to label HSCs to the same extent in *Sele*$^{-/-}$ mice. BrdU has some HSC toxicity that could trigger their proliferation, leading to an underestimate of the number of quiescent cells[4]. Nevertheless, Winkler *et al.*[5] found that this HSC proliferation was suppressed in the absence of E-selectin. The authors then used three assays to determine HSC cell cycle status, confirming that loss of E-selectin increases HSC quiescence. Using a long-term competitive repopulation assay, they showed that sixfold more HSCs survived treatment with hydroxyurea, an S-phase–specific cytotoxic drug, in *Sele*$^{-/-}$ compared to wild-type mice. This slower cell cycling and higher frequency of quiescent HSCs when E-selectin is absent was unexpected, because, at least in the periphery, P- and E-selectins are largely redundant in function[1]. The authors detected E-selectin only in CD31$^+$ endothelial cells, and the expression of E-selectin was 16-fold higher in the endothelium of vasculature near the interface with the endosteal region compared to the central sinusoidal vasculature (**Fig. 1**). There was a marked increase in E-selectin–expressing endothelial cells in this endosteal region during recovery from irradiation. Despite differences in HSC proliferation between E-selectin–deficient and wild-type mice, there was no difference in their total femoral HSC numbers. Using reciprocal HSC transplantation, Winkler *et al.*[5] showed that the proliferative effect was not cell autonomous but was due to E-selectin binding to receptors on HSCs.

High-dose or repeated rounds of chemotherapy or irradiation can eventually exhaust the self-renewal capacity of the HSC pool, leading to prolonged bone marrow suppression and life-threatening neutropenia in people being treated for cancer. Therefore, Winkler *et al.*[5] investigated the role of E selectin in protection from chemotherapy- or irradiation-induced HSC damage. In *Sele*$^{-/-}$ mice, more HSCs survived after a single injection of the antimetabolite 5-flurouracil compared to in wild-type mice. With consecutive rounds of cytotoxic treatment, the *Sele*$^{-/-}$ mice were clearly more resistant and survived a median of 82 d longer than wild-type mice. Similarly, the *Sele*$^{-/-}$ mice showed greater HSC survival after treatment with the alkylating agent cyclophosphamide than wild-type mice. The *Sele*$^{-/-}$ mice also showed accelerated recovery of peripheral leukocytes after nonlethal

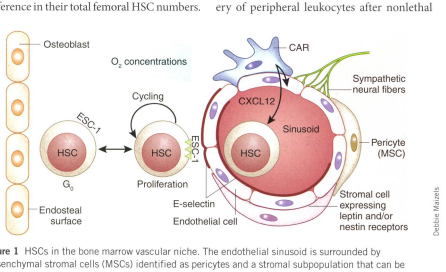

Figure 1 HSCs in the bone marrow vascular niche. The endothelial sinusoid is surrounded by mesenchymal stromal cells (MSCs) identified as pericytes and a stromal subpopulation that can be further identified by their expression of nestin and/or leptin receptors. CAR cells are MSCs characterized by high expression of the chemokine CXCL12, which is a chemoattractant for CXCR4-expressing HSCs. Sympathetic neural fibers also connect with the niche and may provide negative proliferative signals. E-selectin is expressed exclusively on the endothelial cells of the niche and can bind HSCs expressing an appropriate ligand. ESC-1 is shown here as a candidate ligand, the binding of which to E-selectin is required for circulating HSCs to attach and roll on the sinusoidal endothelium before their firm attachment and egress. In addition, Winkler *et al.*[5] now show that the attachment to E-selectin–expressing endothelium induces HSC proliferation, self-renewal and chemo- and radiosensitivity. HSCs close to the bone endosteal surface are in a hypoxic environment and are in a quiescent state. The extent of migration of these quiescent HSCs into the proliferation-inducing environment of the E-selectin–expressing vasculature niche is dependent on the demand for production of mature blood cells.

Malcolm A.S. Moore is in the Cell Biology Program, Memorial Sloan-Kettering Cancer Center, New York, New York, USA.
e-mail: m-moore@ski.mskcc.org

irradiation compared with wild-type mice. These studies support the authors' conclusion that E-selectin has an unexpected additional role as a crucial component of the endothelium of the vascular niche that induces HSC proliferation, self-renewal and chemo- and radiosensitivity.

The mechanism behind E-cadherin–mediated regulation of HSC proliferation remains obscure. Further investigation into the E-selectin ligands expressed on HSCs and their function upon E-selectin binding are required. Several E-selectin ligands have been identified on hematopoietic cells and on leukemia cells and a variety of solid tumor types[1]. Although diverse proteins seem to function as E-selectin ligands, the core species of these ligands are decorated with sialofucosylated carbohydrates such as sialyl Lewis X and sialidated glycosphingolipids (which have recently been recognized as E-selectin ligands)[1]. Winkler *et al.*[5] found that treatment of mouse HSCs with 1-phenyl-2-palmitoyl-3-morpholino-1-propanol (PPMP), a potent inhibitor of the glucosylceramide synthetase involved in the synthesis of glycosphingolipids, reduced their E-selectin binding.

The authors excluded most of the canonical E-selectin ligands in their search for one that was expressed in the endothelial niche and that specifically suppressed HSC proliferation. In an attempt to characterize noncanonical E-selectin receptors, they undertook 'pull-down' proteomic studies with E-selectin–coated magnetic beads but could not detect any of the candidate E-selectin ligands CD43, CD65, CD147 or death receptor 3 (also known as TNFRSF25) in these pull-downs. However, they did identify the canonical E-selectin ligand 1 (ESL-1), a part of the E-selectin receptor-ligand signaling complex[1,7], in these assays. The authors do not propose a mechanism to account for the HSC proliferation that may result from binding of ESL-1 to E-selectin. It will be of interest to investigate this further in light of a study showing that ESL-1 regulates transforming growth factor-β (TGF-β)[8]. TGF-β is one of the most potent inhibitors of HSC proliferation, and neutralization of TGF-β releases HSCs from quiescence (reviewed in refs. 9,10). TGF-β downmodulates receptors for a number of cytokines known to stimulate HSC proliferation[10]. It is synthesized as an inactive precursor (proTGF-β) that undergoes a cleavage and maturation process in the Golgi apparatus in a process involving latent TGF-β–binding protein 3 (LTBP3)[8]. Gain of ESL-1 in the Golgi region, or knockdown of LTBP3, decreases TGF-β signaling[8]. The mechanism involves ESL-1 binding to proTGF-β, resulting in inhibition of furin-mediated maturation of proTGF-βl, which leads to decreased extracellular amounts of bioactive TGF-β[8]. *Esl1*$^{-/-}$ mice show increased mature TGF-β, increased intraosseous TGF-β signaling and decreased proliferation of chondrocytes with development of chondroplasia[8]. The link between ESL-1 and TGF-β may explain the authors' observation on E-selectin stimulation of HSC proliferation[5], and additional studies in this area using the *Esl1*$^{-/-}$ mouse model should be informative in this respect.

The authors suggest that the aberrant glycosylation and expression of *de novo* E-selectin ligands is characteristic of many tumor cells and could aid their homing and engraftment into the bone marrow. Their findings imply that interaction of tumor cells with endothelium expressing E-selectin might stimulate tumor growth and proliferation, as metastasis frequently involves endothelial E-selectin binding to tumor E-selectin ligands, which, in turn, may induce tumor cell proliferation. They also point out that chemotherapy-induced myelosuppression remains a clinical problem and that reducing this dose-limiting side effect would translate to less infection, less need for support with blood products and less need for hospitalization of patients treated for cancer with chemotherapy. The use of an E-selectin antagonist such as GMI-1070 might also be of therapeutic value in preventing metastasis from primary breast or prostate tumor sites to the blood marrow and would inhibit tumor cell and HSC proliferation. This would protect HSCs from damage by cell-cycle–specific chemotherapy. However, on the negative side, such a strategy could equally promote tumor stem cell dormancy and protection from chemotherapy that targets cycling tumor cells, a possibility that will need to be investigated.

COMPETING FINANCIAL INTERESTS
The author declares competing financial interests: details are available at http://www.nature.com/doifinder/10.1038/nm.2992.

1. Zarbock, A., Ley, K., McEver, R.P. & Hidalgo, A. *Blood* **118**, 6743–6751 (2011).
2. Ding, L., Saunders, T.L., Enikolopov, G. & Morrison, S.J. *Nature* **481**, 457–462 (2012).
3. Méndez-Ferrer, S. *et al. Nature* **466**, 829–834 (2010).
4. Wilson, A. *et al. Cell* **135**, 1118–1129 (2008).
5. Winkler, I.G. *et al. Nat. Med.* **18**, 1651–1657 (2012).
6. Frenette, P.S., Mayadas, T.N., Rayburn, H., Hynes, R.O. & Wagner, D.D. *Cell* **84**, 563–574 (1996).
7. Miyazaka, Y. *et al. Biochem. J.* **440**, 33–41 (2011).
8. Yang, T. *et al. J. Clin. Invest.* **120**, 2474–2485 (2010).
9. Blank, U. & Karlsson, S. *Leukemia* **25**, 1379–1388 (2011).
10. Fortunel, N.O., Hatzfeld, A. & Hatzfeld, J.A. *Blood* **96**, 2022–2036 (2000).

Protective immunity from a germinal center sanctuary

Harriet L Robinson & Rama Rao Amara

A new study provides mechanistic insights into how live attenuated simian immunodeficiency virus (SIV) vaccines (LAVs) can protect monkeys from infection with pathogenic SIV. The authors show that replicating LAVs stimulate a protective immune response from a safe haven in the germinal centers of lymph nodes (pages 1673–1681).

For the past 20 years, LAVs have been known to be capable of preventing the acquisition of viral infection after challenge with highly pathogenic SIV[1]. However, the mechanisms of LAV-mediated protection have not been clear[2]. In this issue of *Nature Medicine*, Fukazawa *et al.*[3] find that virus-specific T cells in lymph nodes, but not in blood, correlate with protection from SIV (**Fig. 1**). Notably, the germinal centers of lymph nodes seemed to provide a refuge for replicating LAV. The level of LAV replication in germinal centers correlated with the numbers of protective T cells in the lymph node. These results reveal a novel sanctuary from which replicating LAV can stimulate protective T cell responses in its host.

LAVs, although too risky for use in humans, have proven to be the most effective vaccines for controlling high-dose intravenous virus challenges in nonhuman primate models. To identify the immune correlates for

Harriet L. Robinson is at Geovax, Smyrna, Georgia, USA. Rama Rao Amara is at the Emory Vaccine Center, Yerkes National Primate Research Center, Emory University, Atlanta, Georgia, USA.
e-mail: hrobinson@geovax.com or ramara@emory.edu

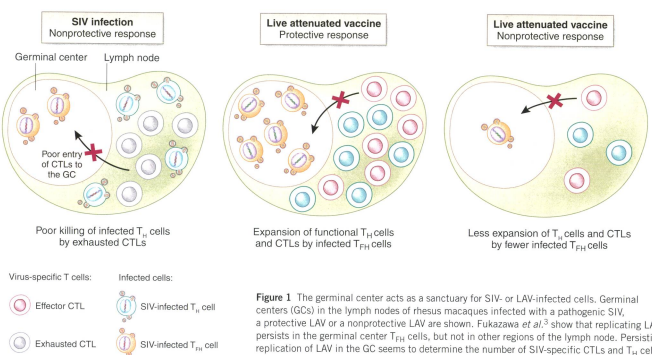

Figure 1 The germinal center acts as a sanctuary for SIV- or LAV-infected cells. Germinal centers (GCs) in the lymph nodes of rhesus macaques infected with a pathogenic SIV, a protective LAV or a nonprotective LAV are shown. Fukazawa *et al.*[3] show that replicating LAV persists in the germinal center T_{FH} cells, but not in other regions of the lymph node. Persisting replication of LAV in the GC seems to determine the number of SIV-specific CTLs and T_H cells in the non-GC regions of the lymph node. This sanctuary for the replicating LAV reflects poor trafficking of the CTLs to germinal centers. In infections with the nonattenuated SIV, the CTLs become exhausted and hence poorly clear the virus-infected T_H cells in the extra-GC regions of the lymph node.

LAV-mediated protection, Fukazawa *et al.*[3] studied a cohort of 32 rhesus macaques infected with one of five LAVs that differed in their degree of protection. To test for correlates of protection, the authors measured 11 immune predictors (eight for T cell responses and three for antibody responses) versus three categories of protection: completely protected, partially protected and unprotected. Completely protected macaques showed no evidence of acquisition of infection by the challenge virus. Partially protected macaques showed high viral loads that were transiently controlled and that then re-emerged as the virus underwent immunological escape and T cells became exhausted. Unprotected macaques had levels of virus replication indistinguishable from those of unvaccinated control macaques.

The authors' exhaustive analyses of antiviral immunity revealed a strong association between protection and the numbers and function of SIV-specific cytotoxic T cells (CTLs) and T helper (T_H) cells in the lymph nodes of the macaques (**Fig. 1**). Fukazawa *et al.*[3] found that SIV-specific T cells in the blood did not show a significant association with protection. SIV-specific antibodies (neutralizing and antibody-dependent cell-mediated cytotoxicity activities) showed a trend toward being associated with protection. The authors also analyzed gene expression profiles in whole lymph nodes and did not find a role for innate immunity in protection, although these analyses will also need to be done on purified cell populations from lymph nodes.

Fukazawa *et al.*[3] then turned their attention to the germinal centers of lymph nodes, where they found that the LAVs replicated in the germinal center follicular helper T (T_{FH}) cells that support antibody maturation[4]. The extent of replication of the LAVs in germinal centers correlated with the number of virus-specific T cells in lymph nodes, which in turn correlated with protection. Viral replication in germinal centers represents a unique mechanism by which chronic viral infections can evade antiviral CTLs, which traffic poorly to germinal centers[5,6]. These results highlight a new mechanism by which LAVs persist despite the presence of effector CTLs capable of preventing acquisition of a highly pathogenic infection.

It will be important to understand the factors that target LAVs to T_{FH} cells in the germinal center. Are these cells infected in the T cell zone before they migrate to germinal centers? Or does virus that has been trapped by antibodies on follicular dendritic cells infect T_{FH} cells? What receptors mediate the entry of either free or antibody-trapped virus into T_{FH} cells, which do not express high amounts of the CCR5 co-receptor? Do viruses replicating in the germinal center maintain functional effector T cell responses in the lymph node by infecting cells outside of the germinal center?

Recently, there has been renewed interest in combining drugs and vaccines to achieve a 'functional cure' for HIV (long-term control of virus infection in the absence of drugs)[8]. The results from the study by Fukazawa *et al.*[3] suggest that CTLs may not be able to clear an immunodeficiency virus infection once the virus has gained entry to the germinal center. Studies have shown that the reservoirs of HIV in HIV-infected individuals treated with highly active antiretroviral therapy (HAART) are localized in T_H cells that express high levels of the programmed death-1 (PD-1) receptor[9]. Among T_H cells, T_{FH} cells in the germinal center express the highest amounts of PD-1. Thus, germinal centers may also serve as a refuge for viral reservoirs during HAART. Given this, CTL-based therapies for eradication may have to target the elicited CTLs to germinal centers, or non–CTL-based therapies will need to be used to kill persisting infections in germinal centers.

The study by Fukazawa *et al.*[3] is a major step forward in understanding how LAVs prevent the acquisition of SIV in nonhuman primate models. It also reveals that germinal centers are a heretofore underappreciated reservoir for the persistence of immunodeficiency viruses in the presence of an active CTL response.

COMPETING FINANCIAL INTERESTS
The authors declare no competing financial interests.

1. Daniel, M.D., Kirchhoff, F., Czajak, S.C., Sehgal, P.K. & Desrosiers, R.C. *Science* **258**, 1938–1941 (1992).
2. Koff, W.C. *et al. Nat. Immunol.* **7**, 19–23 (2006).
3. Fukazawa, Y. *et al. Nat. Med.* **18**, 1673–1681 (2012).
4. Crotty, S. *Annu. Rev. Immunol.* **29**, 621–663 (2011).
5. Hong, J., Amancha, P., Rogers, K., Ansari, A. & Villinger, F. *J. Immunol.* **188**, 3247–3256 (2012).
6. Vojnov, L. *et al. PLoS ONE* **6**, e23515 (2011).
7. Heath, S.L., Tew, J.G., Tew, J.G., Szakal, A.K. & Burton, G.F. *Nature* **377**, 740–744 (1995).
8. International AIDS Society Scientific Working Group on HIV Cure *et al. Nat. Rev. Immunol.* **12**, 607–614 (2012).
9. Chomont, N. *et al. Nat. Med.* **15**, 893–900 (2009).

A sweet surprise for HIV broadly neutralizing antibodies

Johannes P M Langedijk & Hanneke Schuitemaker

The production of cross-reactive neutralizing antibodies is the ultimate goal in HIV vaccine development, but no immunogen other than HIV itself has been able to elicit this type of humoral immunity. In natural HIV infections, these antibodies take several years to develop. A new study sheds light on what may be causing this delay in neutralizing antibody development (pages 1688–1692).

The HIV-1 envelope spike, composed of gp120 and gp41 trimers, is extremely variable, which challenges the design of a vaccine that needs to protect against the majority of, if not all, circulating HIV-1 strains. The only conserved protein surfaces on the envelope spike that can be targeted by broadly neutralizing antibodies are the relatively recessed receptor-binding site and a transiently exposed hydrophobic membrane-proximal external region (MPER) at the base of the spike's stem. The remaining surface of the spike is highly variable, hidden by conformational masking or shielded by carbohydrates that make up more than half of the molecular weight of the envelope molecule. Interestingly, these carbohydrates, which are usually considered immunologically silent self antigens that shield the protein surface, are in fact a major component of the epitope of a recently discovered new class of very potent and broadly neutralizing antibodies against HIV[1,2]. These antibodies recognize the high-mannose component of two specific, closely spaced carbohydrates in combination with a small patch of protein surface and can be grouped into antibodies that mainly bind the glycan at position 160 of the envelope molecule and those that bind the glycan at position 332 (refs. 3,4). Notably, these glycan-based epitopes seem to be even more commonly recognized by antibodies in HIV-infected people than the established targets CD4bs and MPER.

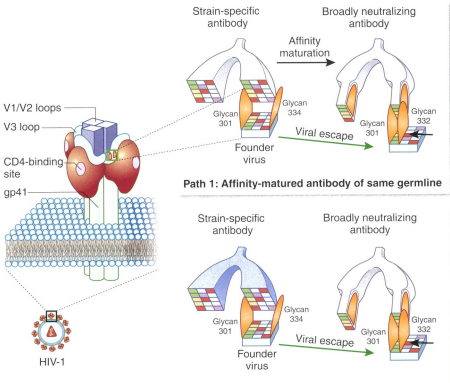

Figure 1 A new pathway for evolution of HIV-1 broadly neutralizing antibodies. Broadly neutralizing antibodies can take several years to develop after natural infection by HIV. This may be due to the time-consuming process of affinity maturation (path 1) or the necessity to generate completely new antibodies (path 2) as a result of the initial absence of an epitope on the founder virus. The data of Moore *et al.*[9] imply that the emergence of a glycan at position 332 in the HIV-1 envelope spike, which allows the virus to escape the initial antibody response, creates a new epitope for a broadly neutralizing antibody. This knowledge may subsequently be applied to develop heterologous prime–boost regimens in vaccination strategies against HIV. The left images in paths 1 and 2 show the variable epitope, consisting of a large protein surface with many different amino acids (indicated as different colors), and the images on the right show the glycan canyon that is created by the glycan shift from position 334 to 332, resulting in a conserved epitope with a small protein surface fenced by two conserved high-mannose glycans in orange. Complementary antibodies are shown in the context of the different HIV-1 epitopes.

Johannes P.M. Langedijk and Hanneke Schuitemaker are at Crucell Holland BV, Leiden, The Netherlands. Hanneke Schuitemaker is also at the Academic Medical Center of the University of Amsterdam, Amsterdam, The Netherlands.
e-mail: hlangedi@its.jnj.com or hschuite@its.jnj.com

The higher than initially expected prevalence of broadly neutralizing antibodies in HIV-infected individuals[5–7] has sparked optimism of the possibility of making a vaccine that can elicit them. However, the time it takes for HIV-infected people to develop these antibodies (which can be up to years[8]) poses a big hurdle to HIV vaccine development. The article by Moore *et al.*[9] in this issue of *Nature Medicine* may shed some light into why the process of developing broadly neutralizing antibodies takes so long. The authors describe an HIV evolutionary pathway in which viral escape from a first antibody response that is directed against an epitope in the viral envelope C3 region is mediated through a shift of an envelope glycan from position 334 to position 332 (**Fig. 1**). This creates a new epitope that subsequently elicits the production of broadly neutralizing antibodies by the host immune response. Therefore, the escape viral variant with the relocated glycan, not the founder virus, is responsible for eliciting a broadly neutralizing antibody response.

The new data of Moore *et al.*[9] can be better understood in the context of the cocrystal structure of PGT128, a glycan-dependent broadly neutralizing antibody against HIV-1, in complex with the HIV-1 envelope gp120 outer domain[4]. This structure indicates that recognition of the HIV-1 envelope by PGT128 requires two closely spaced glycans at positions 301 and 332 at the base of the third variable domain (V3) in gp120, which form a glycan canyon that can be penetrated by the long CDR3 region of this antibody[4] (**Fig. 1**). The HIV-1 escape mutation described by Moore *et al.*[9] shifts an N-linked glycan from position 334 to position 332. This reshapes the epitope from one that binds an HIV strain-specific antibody with a relatively large footprint on the variable protein surface of the spike into one with a glycan canyon with enough non-selfness for immune recognition and a smaller protein surface, thus creating a new conserved viral epitope (**Fig. 1**). Interestingly, Moore *et al.*[9] discovered that there is a similar evolutionary path for the creation of the highly conserved glycan 160–based epitope of HIV-1. They found that the appearance of virus variants with the 332 glycan later in infection is common among HIV-1 clade C viruses, although not all patients can mount a broadly neutralizing immune response to that epitope. This implies that there are still unknown factors that influence whether broadly neutralizing antibodies will develop or not.

The identification of this HIV evolutionary pathway that drives the breadth of the host humoral immune response may provide new clues for the development of vaccine regimens. Although it is not known whether the first type-specific antibodies and the subsequent broadly neutralizing antibodies in the HIV-infected patients studied by Moore *et al.*[9] were from the same germ line, the pathway that they describe may indicate that affinity maturation of the first type-specific antibody is driven by the HIV-1 escape variant, affecting the broadly neutralizing antibody specificity. Their results could also imply that heterologous prime–boost regimens using different HIV envelope epitopes may be required to elicit broadly neutralizing humoral immunity. The absence of the 332 glycan in a substantial proportion of HIV-1 clade C founder viruses may suggest that a vaccine containing only this epitope will have insufficient efficacy. Therefore, the inclusion of other HIV-1 epitopes, for instance, an epitope that includes the glycan at position 160, should be considered, because this epitope is relatively conserved among founder viruses. Finally, similar evolutionary studies on virus–host interactions in HIV-infected individuals who developed different broadly neutralizing antibody specificities will be required to obtain a more complete picture of potential heterologous prime–boost vaccine regimens that may be used to elicit protective broadly neutralizing antibodies.

COMPETING FINANCIAL INTERESTS
The authors declare no competing financial interests.

1. Walker, L.M. *et al. Science* **326**, 285–289 (2009).
2. Walker, L.M. *et al. Nature* **477**, 466–470 (2011).
3. McLellan, J.S. *et al. Nature* **480**, 336–343 (2011).
4. Pejchal, R. *et al. Science* **334**, 1097–1103 (2011).
5. Euler, Z. *et al. J. Virol.* **86**, 2045–2055 (2012).
6. Simek, M.D. *et al. J. Virol.* **83**, 7337–7348 (2009).
7. Doria-Rose, N.A. *et al. J. Virol.* **84**, 1631–1636 (2010).
8. Euler, Z. *et al. J. Infect. Dis.* **201**, 1045–1053 (2010).
9. Moore, P.L. *et al. Nat. Med.* **18**, 1688–1692 (2012).

A sirtuin link between metabolism and heart disease

Keith A Webster

The sirtuins (SIRTs) have gained preeminence for their roles in the response to caloric restriction and the regulation of aging and lifespan. A new study now identifies gene promoters that bind the transcription factor AP1 as targets for silencing by SIRT6, providing possible links between SIRT6 deficiency and dysregulation of insulin-like growth factor signaling, hypertrophic cardiomyopathy and heart failure (pages 1643–1650).

The SIRTs are a family of class III histone deacetylases (HDACs), distinguished from other HDAC classes by their requirement for nicotinamide adenine dinucleotide (NAD) in the deacetylation reaction. SIRTs can catalyze deacetylation of histone and nonhistone lysines. The requirement for NAD constitutes an ancient and evolutionarily conserved mechanism that may link the expression of SIRT-regulated genes with metabolism and nutritional state[1].

SIRTs were first discovered in yeast, in which an extra copy of *SIR2* was shown to extend lifespan by 50%, whereas its deletion shortened lifespan[1]. In worms (*Caenorhabditis elegans*) and flies (*Drosophila melanogaster*) the respective SIR2 homologs seemed to similarly regulate lifespan, and in worms this regulation was found to be mediated by DAF-16, a homolog of human Forkhead (FOXO) transcription factors that regulate stress-related genes, apoptotic factors, antioxidants and metabolism[2,3]. Regulation of glucose homeostasis is a recurring theme linking SIRTs with caloric restriction, aging and lifespan throughout evolution. Daf2, an insulin-like receptor that regulates PI3K, also regulates DAF-16 and is downregulated by Sir2 or caloric restriction[4].

Compelling evidence now implicates each of the mammalian nuclear SIRTs 1, 6 and 7 in the regulation of aging, with links to metabolism, caloric restriction and, especially in the case of SIRT6, glucose homeostasis and the insulin

Keith A. Webster is in the Department of Molecular and Cellular Pharmacology and the Vascular Biology Institute at the University of Miami Miller School of Medicine, Miami, Florida, USA.
e-mail: kwebster@med.miami.edu

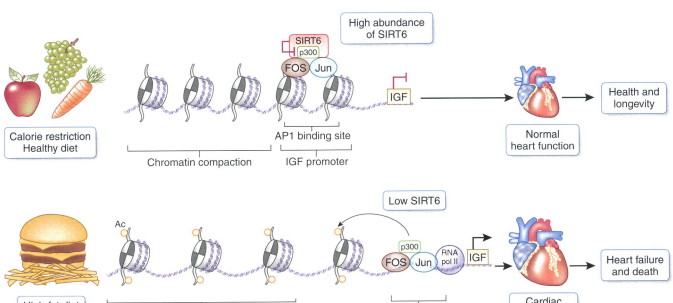

Figure 1 Derepression of IGF signaling–related genes and hypertrophic cardiomyopathy by SIRT6 deficiency. Sundaresan *et al.*[7] provide evidence to suggest that in healthy individuals SIRT6 suppresses IGF signaling–related genes by binding and silencing expression from AP1-dependent promoters, and this contributes to metabolic homeostasis and the maintenance of a healthy heart. Low expression of SIRT6 possibly caused by a high-fat diet, sedentary lifestyle and/or genetics results in reduced SIRT6 silencing, and overexpression of IGF and possibly also of other AP1-dependent genes, thus promoting cardiomyopathy, heart failure and early death. Ac, acetylated H3K9.

and insulin-like growth factor (IGF) signaling pathways[5,6]. In this issue of *Nature Medicine*, Sundaresan *et al.*[7] now directly link SIRT6 with heart disease, which is currently the main determinant of human lifespan in Western populations. Their work shows that SIRT6 selectively downregulates multiple components of the IGF pathway in mouse hearts by binding the transcription factor c-Jun and directing its deacetylase activity selectively to gene promoters with binding sites for the transcription factor Fos/Jun (AP1). The authors show that SIRT6 expression is decreased in failing human hearts, and, in parallel transgenic mouse models, they present plausible evidence that SIRT6 deficiency–induced chronic activation of the IGF signaling pathway and its effectors promotes hypertrophic cardiomyopathy, adverse cardiac remodeling and heart failure (**Fig. 1**).

SIRT6-deficient mice show the most severe phenotype of all SIRT gene knockouts, with premature aging that includes features of osteoporosis, spinal curvature, absence of subcutaneous fat and severe metabolic imbalance, lymphopenia and acute onset hypoglycemia that results in death of mice within 1 month of age[2]. In contrast, transgenic overexpression of *Sirt6* protects mice against the adverse consequences of a high-fat diet, including the 'metabolic syndrome' (characterized by obesity, insulin resistance, elevated serum triglycerides and cholesterol), which is commonly considered a forerunner of cardiovascular disease[6].

SIRT6 selectively targets and deacetylates histone H3 lysine 9 (H3K9), and before the study by Sundaresan *et al.*[7] three SIRT6-specific targets had been identified that contribute to metabolic dysfunction and aging. The first targets to be discovered were H3K9 sites on human telomeres, at which deacetylation by SIRT6 was required to prevent telomere-dependent genome instability and premature senescence[8]. Subsequently, it was shown that the RELA subunit of the transcription factor NF-κB selectively bound SIRT6, thus directing its deacetylase function to the chromatin of NF-κB–dependent genes and resulting in their silencing[9]. More recently, SIRT6 was shown to bind and exert similar control over HIF1-α–regulated genes, and increased expression of genes encoding products such as glucose transporters and glycolytic enzymes in *Sirt6*-knockout mice substantially accounted for their hypoglycemia phenotype and premature death[10].

The studies by Sundaresan *et al.*[7] identify a new cardiomyopathy phenotype of SIRT6-deficient mice and shed additional light on the targets and mechanism of action of SIRT6 that may be relevant to heart disease and, consequently to life span, if the results extend to humans. Using *Sirt6*-knockout mice that survive up to 1 year of age (due to backcrossing the original 129sv strain with Black Swiss/FVB mice), the authors showed that these mice age more rapidly compared with wild-type mice on the same background and develop classical symptoms of hypertrophic cardiomyopathy (HCM), with contractile dysfunction, chamber dilation and, ultimately, heart failure. To confirm that SIRT6 has a heart-selective role, the authors showed that cardiac-specific deletion of *Sirt6* conferred the same cardiomyopathy as whole-body knockout of *Sirt6*. The *Sirt6*-knockout phenotype includes defects in mitochondrial structure and organization, increased apoptosis and overexpression of fetal cardiac genes, typical of classical HCM. Sundaresan *et al.*[7] then showed that SIRT6-overexpressing transgenic mice were protected from HCM that was either driven pharmacologically or caused by pressure overload.

The authors attribute the cardiomyopathy in *Sirt6*-knockout mice to overactivity of the IGF–Akt pathway caused by SIRT6 deficiency. Whereas acute activation of this pathway is known to be protective in the setting of acute myocardial infarction, there is also evidence that chronic IGF–Akt overactivity mediates hypertrophic growth[11]. Sundaresan *et al.*[7] found that the hearts of *Sirt6*-knockout mice had elevated levels of the pathway members IGF-1R, InsR, Akt, GSK3 and IGF-2 and increased activities of multiple signaling components and downstream effectors, including

eIF4E, S6P and p70S6K. They found no hypoglycemia and no changes in the expression of NF-κB– or HIF-1α–dependent genes in these mice. Nicotinamide, a sirtuin inhibitor, and PQ401, a partially selective inhibitor of IGF signaling, both rescued the cardiomyopathy in *Sirt6*-knockout mice, supporting direct roles for SIRT6 and the IGF pathway in heart disease.

To define the underlying mechanism, the authors used chromatin immunoprecipitation assays to show that SIRT6 binds the promoters of IGF-related genes, and they found that H3K9 at these sites was hypoacetylated in *Sirt6*-knockout mice. Using *in silica* analyses, they revealed that AP1-binding sites are common to multiple IGF-responsive gene promoters, implicating these as candidate targets for SIRT6. Indeed, the results confirm that the AP1 component c-Jun is a binding partner for SIRT6, allowing its deacetylase activity to be selectively delivered to AP1 sites of IGF-related genes in the heart and theoretically allowing the complex to bind and fine-tune all promoters with active AP1-binding sites. Knockdown of c-Jun decreased the association of SIRT6 with IGF-associated genes, and inhibition of AP1 downregulated the expression of the same genes in the *Sirt6*-knockout mice.

If the results of Sundaresan *et al.*[7] extrapolate to the human heart, SIRT6 may be a new susceptibility marker for HCM and, possibly, a therapeutic target. The regulation of SIRT6 and dysregulation during HCM becomes an important issue. Clearly, energy state and diet could have roles because SIRT6 expression is responsive to caloric restriction. Interestingly, SIRT1 is also regulated by caloric restriction and can bind and activate the *SIRT6* promoter, possibly amplifying the response to caloric restriction, diet or both[12]. AP1 is now the third SIRT6-regulated transcription factor to be identified, and, along with NF-κB and HIF-1α, it also regulates major stress response pathways. It may also be pertinent that the opposing histone acetyltransferase activity for SIRT6 at genomic sites that bind these transcription factors is the adaptor protein p300/CREB-binding protein (CBP), which is known to have a major role in HCM. This may be a coincidence or there may be a selective regulatory relationship between SIRT6 and p300/CBP, a possibility that deserves further investigation.

COMPETING FINANCIAL INTERESTS
The author declares no competing financial interests.

1. Ralser, M. *et al. Front. Pharmacol.* **3**, 32 (2012).
2. Haigis, M.C. & Guarente, L.P. *Genes Dev.* **20**, 2913–2921 (2006).
3. Oellerich, M.F. & Potente, M. *Circ. Res.* **110**, 1238–1251 (2012).
4. Herndon, L.A. *et al. Nature* **419**, 808–814 (2002).
5. Xiao, C. *et al. J. Biol. Chem.* **285**, 36776–36784 (2010).
6. Kanfi, Y. *et al. Aging Cell* **9**, 162–173 (2010).
7. Sundaresan, N.R. *et al. Nat. Med.* **18**, 1643–1650 (2012).
8. Michishita, E. *et al. Nature* **452**, 492–496 (2008).
9. Kawahara, T.L. *et al. Cell* **136**, 62–74 (2009).
10. Zhong, L. *et al. Cell* **140**, 280–293 (2010).
11. Chu, C.H. *et al. Endocrinology* **150**, 2723–31 (2009).
12. Kim, H.S. *et al. Cell Metab.* **12**, 224–236 (2010).

Small airways, big challenge: measuring the unseen?

Salman Siddiqui & Omar S Usmani

An imaging technique adapted to differentiate between chronic obstructive pulmonary disease phenotypes can identify small-airway pathophysiology, locate the disease and potentially track disease progression. This approach may be used as a biomarker to identify the small-airway lesion in chronic obstructive pulmonary disease, at an individual level in the clinic (pages 1711–1715).

Chronic obstructive pulmonary disease (COPD) is a progressive lung disease that is projected to be the third largest global cause of mortality by the year 2030 (ref. 1). Its diagnosis has conventionally been based on physiological pulmonary function tests that document the presence of airflow limitation that is not fully reversible[2] and is characterized by at least two distinct processes in the small airways of the lung. First, there is destruction of alveolar sacs that leads to alveolar airspace enlargement (emphysema), causing a loss of functional surface area for gas exchange, and second, there is a narrowing and eventually an obliteration of the lumen of small airways due to remodeling of the airway wall (bronchiolitis).

It is not currently possible to distinguish clearly between bronchiolitis and emphysema on the basis of physiological pulmonary function tests that are conventionally used to diagnose COPD, as both processes are associated with airway obstruction and occur synchronously (albeit to variable degrees) in individual patients. Therefore, a simple biomarker that measures emphysema and functionally relevant bronchiolitis would be an important advance and allow for more detailed noninvasive pathological phenotyping of COPD, thus increasing the phenotypic granularity of COPD[3].

In this issue of *Nature Medicine*, Galban *et al.*[4] describe a new computed tomography (CT)-based imaging approach to assess differences in COPD phenotypes in a well-defined cohort of patients with COPD. They identify 'functional small-airways disease' (FSAD) in COPD and thus characterize and quantify the missing link in the COPD paradigm—intraparenchymal small-airway obliteration and damage that is distinct from emphysema. Identifying functional disease in the small airways of individuals with COPD may be a powerful biomarker of disease progression, allowing screening of early disease in at-risk populations and a better understanding of the immunopathogenesis of both emphysema and small airways disease, which are currently poorly understood.

The authors provide tantalizing evidence from imaging suggesting that small-airway obliteration and narrowing precedes the onset of emphysema in COPD[4]. In support of this concept, a recent study demonstrated by imaging lung tissue in COPD (using micro-CT) that small-airway obliteration may well precede the onset of emphysema[5]. These observations suggest that accurately diagnosing and developing appropriate treatments to target the small airways may be important in attenuating the emphysematous lung damage that occurs in COPD. This is a major challenge, as the small airways, conventionally defined as airways less than 2 mm in diameter, are notoriously

Salman Siddiqui is at the Institute for Lung Health, Department of Infection, Immunity and Inflammation, University of Leicester & Glenfield Hospital, Leicester, UK. Omar S. Usmani is at the National Heart and Lung Institute, Imperial College London & Royal Brompton Hospital, Airways Disease Section, London, UK.
e-mail: salman95@yahoo.com

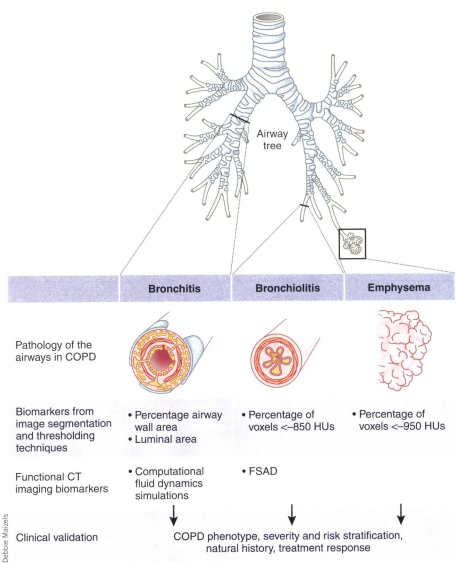

Figure 1 Pathological phenotypes of COPD and imaging biomarkers. Galban *et al.*[4] use a new imaging technique that can track pairs of individual voxels—small lung elements that contain a composite of lung tissue (both alveolar tissue and small-airway wall tissue), microvasculature and gas—between CT scans acquired during inspiration and expiration. Functional disease in intraparenchymal small airways can be identified, allowing discrimination between emphysema voxels on an expiratory CT scan and voxels that trap gas as a result of small-airway dysfunction and damage. The parametric response map generated produces a unique signature that provides spatial and quantitative information on the degree of 'normal lung', 'emphysematous lung damage' and functional small airways disease (FSAD) in COPD. These techniques allow functional properties to be derived from static CT imaging. HU, Hounsfield unit.

difficult to study *in vivo* because their cross-sectional area is smaller than the spatial resolution of conventional imaging techniques for the lungs, such as CT[6].

The observations of Galban *et al.*[4] resulted from assessing the small-airway signature in individuals across the spectrum of COPD severity at a single point in time, and, as the authors point out, the results will need to be confirmed with longitudinal studies. This is particularly pertinent as, for the same degree of physiological airflow limitation, people with COPD were shown to have very different degrees of FSAD and emphysema. One could therefore speculate that the FSAD regions of the lung may be salvageable and treatable lung tissue that has not progressed to complete obliteration and emphysema.

Another key observation was that although imaging biomarkers of both FSAD and emphysema were strongly associated with physiological indices of airflow limitation, only FSAD was associated with exacerbations of COPD[4], which are a major cause of mortality and healthcare use[7]. Identification of the FSAD phenotype may therefore be an important strategy in identifying patients at risk of future exacerbations. In contrast, emphysema—unlike FSAD—was strongly associated with breathlessness and walking distance, suggesting that these two histopathological processes seen in COPD may account for different aspects of the clinical expression of the disease.

The CT-based imaging approach described by Galban *et al.*[4], called parametric response mapping (PRM), uses state-of-the-art image registration techniques to track changes in individual three-dimensional volume elements (voxels) that make up the visual image between inspiratory and expiratory CT scans (**Fig. 1**). Conventionally, CT scans have been used to characterize emphysema at total lung capacity (fully inflated lung volumes), which correlates histopathologically with the extent of emphysema[8] and relates closely to clinically important COPD outcomes and lung function tests that assess airflow limitation[9]. More recently, CT scans acquired during expiration have been used to characterize the amount of 'air trapping' in the lung using thresholding techniques similar to those described for emphysema, as the small airways are prone to closure and gas trapping that seems to be a fundamental process[10].

However, unlike emphysema, the histopathological surrogate of air trapping on CT imaging in COPD has yet to be defined and may be either closure or narrowing of small airways at low lung volumes, altered lung perfusion or gas remaining in emphysematous airspaces. By extending a technique originally described to spatially register magnetic resonance diffusion images in cancer studies[11], the current study is a major advance in our ability to measure disease in the small airways of patients with COPD. The power of the PRM technique lies in its ability to globally assess all voxels in the lung parenchyma that are functionally abnormal due to small-airways disease while excluding emphysema voxels, generating a unique signature quantifying both the degree and spatial localization of normal lung parenchyma, functionally abnormal small-airway parenchyma and emphysematous lung.

Future studies will be required to correlate FSAD with histopathological bronchiolar remodeling in COPD. Galban *et al.*[4] extended the ability of CT modality imaging to be used as a functional rather than static image tool in COPD, extending the panel of putative imaging biomarkers that can be derived from CT. Further work will be required to progress toward regulatory approval with these biomarkers, including phantom studies to assess the impact of scanner and image acquisition parameters upon measurement accuracy and larger clinical studies to show clinical validity

by linking biomarkers to disease severity, natural history and treatment response (**Fig. 1**).

There is now an expanding toolbox of imaging techniques, including hyperpolarized helium-3 and xenon-129 noble gas magnetic resonance imaging, giving spatial insight into small-airways disease to assess peripheral lung ventilation, airway diffusion and acinar microstructure[12,13]. Ultimately, the small airways represent a unique challenge for pulmonary medicine as the pathophysiological processes described occur at very small length scales[14] and are intrinsically coupled to large-airway function and airway wall and lung tissue mechanics. Indeed, small-airways disease may be related to processes operating at even smaller scales, such as cellular automata describing the interactions of immune, inflammatory and structural cells and genetic and epigenetic modifications. Understanding how these disparate length scales interact to cause disease and dysfunction in the small airways and contribute to the heterogeneous disorder that is COPD will undoubtedly require a systems approach. Reassuringly, the respiratory community has risen to this challenge, having formed large-scale consortia[15,16] to answer these complex questions for the benefit of individuals with disabling chronic conditions such as COPD.

COMPETING FINANCIAL INTERESTS
The authors declare no competing financial interests.

1. Decramer, M., Janssens, W. & Miravitlles, M. *Lancet* **379**, 1341–1351 (2012).
2. Global Strategy for the Diagnosis. Management and Prevention of COPD, Global Initiative for Chronic Obstructive Lung Disease (GOLD) 2011. Published online at http://www.goldcopd.org/guidelines-global-strategy-for-diagnosis-management.html (21 February 2011).
3. Agustí, A. & Vestbo, J. *Am. J. Respir. Crit. Care Med.* **184**, 507–513 (2011).
4. Galbán, C.J. *et al. Nat. Med.* **18**, 1711–1715 (2012).
5. McDonough, J.E. *et al. N. Engl. J. Med.* **365**, 1567–1575 (2011).
6. Usmani, O.S. & Barnes, P.J. *Ann. Med.* **44**, 146–156 (2012).
7. Holguin, F. *et al. Chest* **128**, 2005–2011 (2005).
8. Gevenois, P.A. *et al. Am. J. Respir. Crit. Care Med.* **154**, 187–192 (1996).
9. Martinez, C.H. *et al. Thorax* **67**, 399–406 (2012).
10. Venegas, J.G. *et al. Nature* **434**, 777–782 (2005).
11. Galbán, C.J. *et al. Nat. Med.* **15**, 572–576 (2009).
12. Butler, J.P. *et al. N. Engl. J. Med.* **367**, 244–247 (2012).
13. Marshall, H. *et al. Thorax* **67**, 613–617 (2012).
14. Bayat, S. *J. Appl. Physiol.* **113**, 851–852 (2012).
15. Politi, A.Z. *et al. J. Theor. Biol.* **266**, 614–624 (2010).
16. Brightling, C.E., Gupta, S., Gonem, S. & Siddiqui, S. *Clin. Exp. Allergy* **42**, 638–649 (2012).

Defeating dengue: a challenge for a vaccine

Dengue poses a substantial clinical problem, with the four serotypes of dengue viruses infecting 50–100 million people per year and approximately half the world's population estimated to be at risk. As there is no specific treatment for dengue, the development of an effective vaccine will be an important measure for controlling this disease. A phase 2b trial testing a recombinant live, attenuated tetravalent dengue–yellow fever chimeric virus vaccine in Thai schoolchildren of 4–11 years of age has recently been reported[1]. The vaccine showed an overall efficacy of 30.2%, and one or more doses of the vaccine reduced the incidence of disease caused by the DENV3 and DENV4 dengue virus serotypes by 80–90%, with less reduction of disease caused by DENV1; however, there was no efficacy against DENV2. We asked three experts to comment on the results of this trial and how they might influence the landscape of dengue vaccine development.

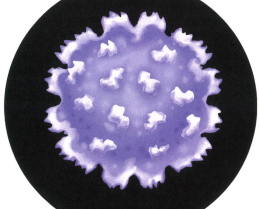

Mark Giles/Science Source

Michael S Diamond

There are four serotypes of dengue virus, and infection with one serotype induces adaptive immune responses that are believed to provide durable immunity against re-infection by the same serotype. However, a second infection with a different serotype increases the relative risk of developing severe disease, possibly because poorly neutralizing cross-reactive antibodies from the primary infection enhance infection of the second dengue virus serotype in cells expressing Fcγ receptors[2]. Thus, the goal of dengue virus vaccine development is to produce a balanced protective antibody response against all four serotypes and avoid an incomplete immune response that theoretically could facilitate pathogenesis[3].

The much-anticipated results of a phase 2b trial with a live, attenuated tetravalent dengue virus vaccine show that, surprisingly, the vaccine prevented only 30.2% of febrile dengue virus infections[1]. Although the incidence of DENV3 and DENV4 cases was reduced by 80–90%, the vaccine was less effective (~60%) against DENV1 and had no efficacy against DENV2. The low overall efficacy was skewed by a high number of DENV2 infections during the trial.

Why was there a lack of efficacy of the vaccine against DENV2 although neutralization titers were higher against DENV2 compared to DENV1 and DENV3? The authors suggest that future work should measure the neutralizing activity of serum on myeloid cells (which are dengue virus targets *in vivo*) that express Fcγ receptors instead of the currently used fibroblast cells[1]. Other possible explanations could be that the neutralization assay used cannot ascertain whether there were four balanced serotype-specific responses compared to less protective cross-reactive responses; that the circulating DENV2 strain was of a different genotype than the DENV2 strain used for vaccine formulation and subsequent neutralization assays and,

Eva Harris

The four dengue virus serotypes (DENV1–4) cause the most prevalent arthropod-borne viral disease of humans worldwide, yet the mechanisms by which the host immune response provides either protection from or enhancement of a subsequent infection with a different dengue virus serotype are poorly understood, and this has been a major hindrance in dengue vaccine development. The existence of four distinct serotypes—in essence, four different viruses—complicates matters further, as exemplified by the fact that the tetravalent dengue vaccine did not protect against DENV2 in the first proof-of-concept dengue vaccine efficacy trial[1]. Various reasons may explain this lack of protection[1,5], and several crucial points emerge from the trial results.

First, there is an urgent need for more in-depth immunological studies of vaccine recipients as well as of natural dengue virus infections, using samples from prospective cohort studies from documented first, second and third dengue virus infections before a subsequent symptomatic versus inapparent dengue virus infection. Second, an integrated analysis of B and T cell responses is necessary that focuses on diverse effector functions

1. Sabchareon, A. *et al.* Protective efficacy of the recombinant, live-attenuated, CYD tetravalent dengue vaccine in Thai schoolchildren: a randomised, controlled phase 2b trial. *Lancet* published online, doi:10.1016/S0140-6736(12)61428-7 (2012).
2. Halstead, S.B. Pathogenesis of dengue: challenges to molecular biology. *Science* **239**, 476–481 (1988).
3. Murphy, B.R. & Whitehead, S.S. Immune response to dengue virus and prospects for a vaccine. *Annu. Rev. Immunol.* **29**, 587–619 (2011).
4. Pierson, T.C., Fremont, D.H., Kuhn, R.J. & Diamond, M.S. Structural insights into the mechanisms of antibody-mediated neutralization of flavivirus infection: implications for vaccine development. *Cell Host Microbe* **4**, 229–238 (2008).
5. Halstead, S.B. Dengue vaccine development: a 75% solution? *Lancet* published online, doi:10.1016/S0140-6736(12)61510-4 (2012).
6. Kraus, A.A., Messer, W., Haymore, L.B. & de Silva, A.M. Comparison of plaque- and flow cytometry-based methods for measuring dengue virus neutralization. *J. Clin. Microbiol.* **45**, 3777–3780 (2007).
7. Libraty, D.H. *et al.* Differing influence of viral burden and immune activation on disease severity in secondary dengue virus infection. *J. Infect. Dis.* **185**, 1213–1221 (2002).
8. Stephens, H.A. *et al.* HLA-A and B associations in secondary dengue virus infections correlate with disease severity and the infecting viral serotype in ethnic Thais. *Tissue Antigens* **60**, 309–318 (2002).
9. Guirakhoo, F. *et al.* Recombinant chimeric yellow fever-dengue type 2 vaccine is immunogenic and protective in nonhuman primates. *J. Virol.* **74**, 5477–5485 (2000).
10. Endy, T.P. *et al.* Relationship of preexisting dengue virus (DV) neutralizing antibody levels to viremia and severity of disease in a prospective cohort study of DV infection in Thailand. *J. Infect. Dis.* **189**, 990–1000 (2004).

thus, may not have been inhibited efficiently by vaccine-induced antibodies; that the neutralization test used did not account for other factors that modulate antibody inhibition, including virus maturation and interactions with complement[4]; or that the induction of protective but non-neutralizing antibodies and the role of T cell responses were not considered.

"One final consideration is how much protection is needed to control epidemics of severe disease, which requires sequential infection by multiple serotypes."

Although the results of this trial[1] were unexpected, they provide an opportunity for establishing better immune correlates of protection. The challenge will be to determine which of the explanations above account for the failure of the vaccine against DENV2. One final consideration is how much protection is needed to control epidemics of severe disease, which requires sequential infection by multiple serotypes. Would a vaccine that reduces infection of three serotypes be sufficient? An ongoing phase 3 efficacy study with more than 30,000 subjects may provide answers to this question. Then, we can decide whether 75% is closer to half-full or half-empty.

Professor, Departments of Medicine, Molecular Microbiology and Pathology & Immunology, Washington University School of Medicine, St. Louis, Missouri, USA.

COMPETING FINANCIAL INTERESTS
The author declares competing financial interests: details are available at http://www.nature.com/doifinder/10.1038/nm.2997.

that may contribute synergistically to protection. These include the role of complement, the contribution of type-specific versus cross-reactive neutralizing antibodies, antibody-dependent cell-mediated cytotoxicity and viral inhibition, B cell magnitude and breadth, and the epitope repertoire, magnitude, frequency, human leukocyte antigen restriction and multifunctionality of $CD8^+$ T cell responses. Third, for neutralization assays to be predictive, a more relevant human monocytic cell line that is susceptible to infection by mature and partially immature dengue virus virions and that expresses Fcγ receptors, which can mediate antibody-dependent uptake of dengue virus immune complexes, should be used (for example, the, U937-DC-SIGN line)[6]. Fourth, it will be crucial to study the pre- and post-vaccination immune responses at the individual level in relation to outcome and thus design vaccine trials such that preimmunization blood samples from all subjects are available for future study.

In sum, the results from this proof-of-concept vaccine efficacy trial highlight the crucial need to improve understanding of the immune response to natural dengue virus infections and vaccine candidates and to identify robust correlates of protection.

Professor, Division of Infectious Diseases and Vaccinology, and Director, Center for Global Public Health, School of Public Health, University of California–Berkeley, Berkeley, California, USA.

COMPETING FINANCIAL INTERESTS
The author declares no competing financial interests.

Francis A Ennis

Dengue virus infections are a major cause of morbidity and severe illness in tropical regions. The development of a safe, effective vaccine to provide protection against severe dengue by any of the four dengue virus serotypes is an important goal. The risk for more serious infection is increased during secondary dengue virus infections[2], indicating that residual immune responses to the first infecting virus do not protect against other dengue virus serotypes and that cross-reactive immune responses sensitize some individuals for more serious illness by a second virus. Factors such as the host immune genotype, the numbers of preexisting cross-reactive T cells and the concentrations of cross-reactive antibodies probably contribute to this increased risk[7,8].

"Although higher serum concentrations of dengue virus-neutralizing antibodies correlate with a decreased risk of illness, such immune correlates do not necessarily reflect protective mechanisms."

These factors make the development of a safe and effective tetravalent dengue virus vaccine a complex challenge. The recent study by Sabchareon *et al.*[1] offers some promise for a live, attenuated chimeric tetravalent dengue virus. Their results showed that the vaccine induced only modest protection against DENV1, DENV3 and DENV4 and none against DENV2, the major cause of dengue illness during this study. Future sequencing of DENV2 isolates from ill study subjects should determine the relevance of the vaccine DENV2 to circulating DENV2. A single dose of a monovalent YFV–DENV2 vaccine has been shown to protect monkeys against wild-type DENV2 challenge[9]. Testing the tetravalent dengue virus described by Sabchareon *et al.*[1] for protection in nonhuman primates against a subsequent DENV2 challenge, analogous to this human clinical trial, may be warranted. Unlike other viral infections such as measles or mumps, dengue virus infections can occur in the presence of naturally acquired neutralizing antibodies[10]. Standard and research-based antibody assays using all available preinfection sera might provide insights into the failure of this tetravalent dengue virus to protect some individuals from dengue. Although higher serum concentrations of dengue virus-neutralizing antibodies correlate with a decreased risk of illness[10], such immune correlates do not necessarily reflect protective mechanisms. Further research into dengue vaccine development should be stimulated by the unexpected results of this trial[1], which is nevertheless an important step forward in the quest for a safe, effective dengue vaccine.

Professor of Medicine, University of Massachusetts Medical School, Worcester, Massachusetts, USA.

COMPETING FINANCIAL INTERESTS
The author declares no competing financial interests.

Before epilepsy unfolds

There is increasing interest in understanding how epilepsy initiates and how to thwart the establishment of the disease. Many questions remain open as to what targets may the best for preventing epilepsy and whether any common triggering pathway exists to treat this complex malady. In 'Bedside to Bench', Rod C. Scott and Gregory Holmes discuss alternative therapies to treat neonatal seizures to prevent chronic cognitive impairment and brain developmental problems, which can lead to epilepsy later in life. Increasing inhibitory signals in the developing brain may be useful in dampening brain hyperexcitability—and enhanced susceptibility for seizures—and blocking epilepsy development in children. In 'Bench to Bedside', Annamaria Vezzani argues how the mTOR pathway may be a potential target for blocking epileptogenesis. The role of mTOR in seizures in early life and progression of established disease raises the possibility that mTOR could be a common mediator involved in epilepsy at different stages of disease initiation and progression. Given the lack of current antiepileptic drugs to prevent seizures in children and to block epileptogenesis, developing new disease-modifying therapies remains a priority.

■ BEDSIDE TO BENCH

Opening up the potassium door in neonatal seizures

Rod C Scott & Gregory L Holmes

The highest incidence of seizures in humans is in the first month of life[1]. Because of the birthing process, infants are at risk for a number of brain injuries such as trauma, hypoxic-ischemic insults, intracranial hemorrhages and infection; frequently associated with seizures. In addition, a large number of pathological processes occurring in neonates, such as congenital brain malformations and genetic channelopathies, may also result in seizures. Despite advances in the care of sick neonates, and although the outcome after neonatal seizures is greatly influenced by the etiology of the seizures, there are concerns that these seizures may contribute to brain damage, cognitive impairments and the high incidence of epilepsy in affected children when they are older[2]. It is therefore essential that both clinical and basic scientists continue to work together to understand how seizures and associated cognitive impairments occur, to define new therapeutic strategies that prevent seizures and subsequent development of epilepsy and to test them in the clinical setting.

It is widely accepted that seizures in a vulnerable neonatal population should be treated[3]. Yet this treatment has changed little over the last 50 years, with most clinicians using phenobarbital or phenytoin—a GABA agonist and a sodium channel blocker, respectively—as first-line therapies, despite well-conducted human studies showing that both drugs are incompletely effective[4]. In addition to this poor efficacy, animal data also indicate that both drugs can lead to apoptosis when administered to developing rats[5].

Given the lack of efficacy and safety of these drugs in neonates, there is a need for new molecular targets. Recent clinical studies on newborns with benign familial neonatal convulsions may provide a clue. These newborns begin having seizures between days 2 and 8 of life and remit by 16 months[6,7], with very little residual cognitive impairment. This syndrome results from mutations in *KCNQ2* and *KCNQ3*, which encode the voltage-gated potassium channels Kv7.2 and Kv7.3, which are expressed in the brain. The gene products form heteromultimeric channels that mediate the M current, a slowly activating, noninactivating potassium current that serves to inhibit neuronal firing. Mouse models of human *KCNQ2* and *KCNQ3* mutations show early-life seizures and reduced amplitude and increased deactivation kinetics of the M current[8].

Now Weckhuysen *et al.*[9] show that a mutation in one of these potassium channels may not be quite so benign. The authors studied a cohort of 80 infants and young children with unexplained neonatal or early infantile epileptic encephalopathies to identify mutations in *KCNQ2* and *KCNQ3*. All of the patients had onset of seizures within the first 3 months of life followed by slowing of psychomotor development. Remarkably, a full 10% of the patients had heterozygous functional variants in *KCNQ2* that were deemed likely to be pathological mutations. The mutations in this cohort were not benign and resulted in severe seizures that were medically intractable and had an unfavorable developmental course. Therefore, disruptions in Kv7.2 lead to differing phenotypes, although the reasons for this remain obscure.

This study has raised two important questions with respect to the role of potassium channels in neonates with seizures[9]— why a genetic mutation of potassium channels results in the very broad spectrum of cognitive impairments observed across clinical studies and whether targeting potassium channels with antiepileptic drugs will be a more successful strategy than current therapies in the treatment of neonatal seizures.

The mutations identified[9] overlap with the mutations found in benign neonatal familial convulsions pedigrees, suggesting that the mutations have differing effects on the neural systems underpinning cognition. The cognitive impairment may be a function of seizures, but both groups of individuals have frequent early-onset seizures yet the cognitive outcomes are vastly different. Therefore, there may be a direct relationship between abnormalities in the potassium channel and cognition. Although knockout models may provide insight into the role of potassium channels in cognition, the use of heterologous *in vitro* expression systems or transgenic models could shed light into channel kinetics and the effect on cognitive systems between mutations associated with good or poor outcomes, potentially leading to important mechanistic insights.

Rod C. Scott is at University College London, Institute of Child Health, London, UK, and the Geisel School of Medicine at Dartmouth, Hanover, New Hampshire, USA. Gregory L. Holmes is at the Geisel School of Medicine at Dartmouth, Hanover, New Hampshire, USA.
e-mail: gregory.l.holmes@dartmouth.edu

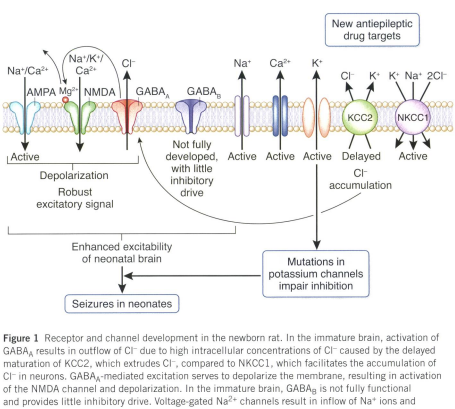

Figure 1 Receptor and channel development in the newborn rat. In the immature brain, activation of $GABA_A$ results in outflow of Cl^- due to high intracellular concentrations of Cl^- caused by the delayed maturation of KCC2, which extrudes Cl^-, compared to NKCC1, which facilitates the accumulation of Cl^- in neurons. $GABA_A$-mediated excitation serves to depolarize the membrane, resulting in activation of the NMDA channel and depolarization. In the immature brain, $GABA_B$ is not fully functional and provides little inhibitory drive. Voltage-gated Na^{2+} channels result in inflow of Na^+ ions and depolarization, whereas outflow of K^+ ions is mediated by voltage-gated K^+ channels, resulting in hyperpolarization, which is therefore the main source of inhibition in the immature brain. Enhancing K^+ current with antiepileptic drugs that target this channel could potentially be efficacious in stopping seizures in neonates.

The clinical observation that seizures associated with potassium channel mutations begin during the neonatal period and can result in severe epilepsy in infants suggests that potassium channels play a crucial part in inhibition in neonates. Notably, it raises the possibility that the potassium channel may be targeted for treating epilepsy, given the limited success of current clinical strategies.

In neonates, potassium channels provide one of the few sources of inhibition in a brain that is heavily weighted toward excitability. The enhanced excitability of the immature brain compared to the mature brain is related to the sequential development and expression of essential signaling pathways. First, excitatory signaling is more robust in infants due to glutamate receptor subunit configuration, in which the predominant NMDA receptor glutamate-binding subunit is the NR2B subunit. These units have reduced magnesium sensitivity, resulting in high excitability. Second, in immature rodents and immature human brain, α-amino-3-hydroxyl-5-methyl-4-isoxazole-propionate (AMPA) receptors, a non-NMDA–type glutamate receptor that mediates fast synaptic transmission, are calcium permeable because they lack the GLuR2 subunit, resulting also in greater excitability and an increased likelihood of seizures in the immature brain. During the first few weeks of life there is enhanced excitation due to an overabundance of these two types of receptors. Third, GABA, which in the adult brain is the primary inhibitory neurotransmitter, exerts a paradoxical excitatory action during the early postnatal period[10] upon activation owing to a large intracellular concentration of chloride in immature neurons[11] (**Fig. 1**) that results in an efflux of negatively charged chloride ions, leading to neuronal excitation rather than inhibition. Finally, the high input resistance of immature neurons also facilitates the generation of action potentials and synchronized activities. Both the tonic and phasic components of the potassium channel–dependent M current are required to keep this enhanced excitation in check.

The immature brain's high susceptibility for seizures can therefore be explained by the morphological and physiological events occurring during early life: the depolarizing effect of GABA and the overexpression of AMPA and NMDA receptors with a composition that enhances excitability of neuronal networks places potassium channels as one of the main means of inhibition in the developing brain[12]. The work of Weckhuysen *et al.*[9] provides further support for the concept that potassium channels have an important role in inhibition in the developing brain and that mutations in these channels can result in severe epilepsy.

The findings kick the ball back to the basic neuroscientists. Understanding how the seven unique mutations reported by Weckhuysen *et al.*[9] alter potassium M currents and cause such a severe phenotype could lead to new therapeutics. Recently, retigabine (also known as ezogabine), a drug that acts as an activator of neuronally expressed KCNQ channels[13–16], has been approved to treat partial seizures in adults. As potassium currents provide much of the inhibition in neonatal neurons, potassium channels could be a new and clinically useful target for the treatment of neonatal seizures. Although animal data are limited, ezogabine has already been found to be particularly efficacious in treating seizures in immature rats[17,18]. Animal and clinical studies are clearly warranted to determine whether drugs enhancing potassium channel openings will be safe and well tolerated, given that these channels are not confined to the brain.

Physicians treating neonatal seizures are still using inefficacious drugs that have substantial side effects. A drug that aims for a new target, potassium channels, which seem to play a key part in inhibition in the neonatal brain, and that would be effective and safe would have an enormous clinical impact by reducing seizure-related morbidity and mortality in a vulnerable population.

COMPETING FINANCIAL INTERESTS
The authors declare competing financial interests: details are available at http://www.nature.com/doifinder/10.1038/nm.2987.

1. Lanska, M.J. & Lanska, D.J. *Neuroepidemiology* **15**, 117–125 (1996).
2. Ronen, G.M., Buckley, D., Penney, S. & Streiner, D.L. *Neurology* **69**, 1816–1822 (2007).
3. Glass, H.C. *et al. J. Pediatr.* **155**, 318–323 (2009).
4. Painter, M.J. *et al. N. Engl. J. Med.* **341**, 485–489 (1999).
5. Bittigau, P. *et al. Proc. Natl. Acad. Sci. USA* **99**, 15089–15094 (2002).
6. Singh, N.A. *et al. Brain* **126**, 2726–2737 (2003).
7. Singh, N.A. *et al. Nat. Genet.* **18**, 25–29 (1998).
8. Singh, N.A. *et al. J. Physiol. (Lond.)* **586**, 3405–3423 (2008).
9. Weckhuysen, S. *et al. Ann. Neurol.* **71**, 15–25 (2012).
10. Ben-Ari, Y., Gaiarsa, J.L., Tyzio, R. & Khazipov, R. *Physiol. Rev.* **87**, 1215–1284 (2007).
11. Dzhala, V.I. *et al. Nat. Med.* **11**, 1205–1213 (2005).
12. Ben-Ari, Y. & Holmes, G.L. *Lancet Neurol.* **5**, 1055–1063 (2006).
13. Miceli, F., Soldovieri, M.V., Martire, M. & Taglialatela, M. *Curr. Opin. Pharmacol.* **8**, 65–74 (2008).
14. Schenzer, A. *et al. J. Neurosci.* **25**, 5051–5060 (2005).
15. Large, C.H. *et al. Epilepsia* **53**, 425–436 (2012).
16. Gunthorpe, M.J., Large, C.H. & Sankar, R. *Epilepsia* **53**, 412–424 (2012).
17. Sankar, R. *et al. Epilepsia* **51** (suppl. 3), 39–42 (2010).
18. Mazarati, A., Wu, J., Shin, D., Kwon, Y.S. & Sankar, R. *Epilepsia* **49**, 1777–1786 (2008).

BENCH TO BEDSIDE

Finding the epileptogenesis switch

Annamaria Vezzani

One unmet clinical need in epilepsy therapy is to arrest epileptogenesis induced by different precipitating events such as brain injury, gene mutation or undefined causes. This requires the discovery of drugs targeting key etiopathogenic mechanisms underlying the disease's onset and progression. Modeling of epileptogenesis has shown this is a dynamic and progressive process altering cellular connectivity and inducing molecular changes in neurons, glia and endothelial cells of the blood-brain barrier that precede the first clinical seizure. Research for new epilepsy therapies is faced with the vital question of whether the different precipitating events trigger overlapping mechanisms of epileptogenesis, as their identification would permit the development of broad-spectrum, etiology-independent drugs.

A putative pathophysiologic mechanism of epileptogenesis shared by different forms of the disease and its associated comorbidities is the brain perturbation of the mammalian target of the rapamycin (mTOR) signaling cascade (**Fig. 1**). mTOR is a serine/threonine kinase that is sensitive to the macrolide antibiotic rapamycin and is activated in response to various environmental stimuli[1]. Activation of mTOR regulates cerebral cortical development[2] and synaptic function and plasticity and promotes processes such as protein synthesis and degradation, gene transcription and cytoskeletal modifications[1–3] that are instrumental for the cellular and molecular changes occurring during epileptogenesis.

The tumor suppressor genes *Tsc1* and *Tsc2* (tuberous sclerosis 1 and 2), which encode hamartin and tuberin, and their upstream regulators phosphatase and tensin homolog (*Pten*), Ste20-related kinase adaptor α, and neurofibromin 1 are crucial negative modulators of mTOR. Mutations of these genes in humans result in mTOR hyperactivity and pathologic cellular alterations, with high comorbidity with epilepsy[3]. The identification of *Tsc1* and *Tsc2* mutations as causative factors of tuberous sclerosis complex (TSC) drew special attention to the possibility of mTOR dysfunction in epileptogenesis, given that about 80% of people with TSC develop epilepsy[2]. mTOR signaling is enhanced in cortical tubers, pathological brain lesions of TSC, and in the regions of cytoarchitectural abnormalities of other forms of developmental brain malformations associated with intractable seizures[2].

The possible link between mTOR and epileptogenesis was strengthened by the development of mouse models with conditional inactivation of the *Tsc1*, *Tsc2* or *Pten* genes in astrocytes, neurons or both, which had mTOR overactivation, hypertrophy of brain cells, spontaneous seizures and premature death[2,3]. Astrocytes proliferation, neuronal cell dispersion and mossy fiber sprouting, key features of epileptogenesis, were also reported in these mice[2,3]. Focal tuber-like lesions were reproduced when the *Tsc1* gene was conditionally ablated in embryonic mouse neurons at precise developmental time points[4,5]. Rapamycin prevented or reduced mTOR activation–related neuropathology and the ensuing seizures in these mice. These beneficial effects, however, were reversible some weeks after drug washout, except when repeated pulse treatment was adopted[6].

The therapeutic effects of mTOR inhibition may not come as a surprise in genetic disorders caused by mTOR hyperactivation; however, the inhibition also affected epileptogenesis in models of acquired forms of epilepsy, such as temporal lobe epilepsy (TLE). In TLE models, convulsant drugs such as kainic acid or pilocarpine are used to precipitate self-sustained seizures lasting for several hours (that is, status epilepticus), which precedes the development of epileptogenesis over the following week, resulting in chronic recurrent seizures. A rapid and transient mTOR activation was described in the rat hippocampus and neocortex after kainic acid–induced status epilepticus, and a second wave of hippocampal mTOR induction occurred during epileptogenesis, persisting after epilepsy onset[7]. The mTOR target phosphorylated ribosomal protein S6 was induced after status epilepticus in neurons and reactive astrocytes, as also detected in sclerotic human TLE hippocampi[8]. Rapamycin treatment before kainic acid abolished mTOR activation without affecting status epilepticus and reduced cell loss, neurogenesis and mossy fiber sprouting evolving during epileptogenesis. The onset of spontaneous seizures was postponed and their frequency greatly reduced. If rapamycin treatment was initiated after status epilepticus and then continued, the second wave of mTOR activation was inhibited and mossy fiber sprouting and the frequency of spontaneous seizures were reduced, but cell loss and neurogenesis were not affected[7]. These data suggest that mTOR involvement in the various aspects of epileptogenesis may vary depending on the time elapsed from the initial precipitating injury (that is, status epilepticus) and that earlier intervention to block its activation may be more effective.

Some controversy emerged, however, when rapamycin was administered after pilocarpine-induced status epilepticus in mice[9]—hypertrophy of the dentate gyrus of the hippocampus, which may be in part determined by enlargement of granule cells, and mossy fiber sprouting were reduced, but other neuropathological alterations and spontaneous seizures were not affected. Granule cell hypertrophy was associated with mTOR activation also in human mTLE and may affect cell susceptibility to synaptic inputs contributing to hyperexcitability[8]. These divergent findings between TLE models suggest that the degree to which mTOR contributes to epileptogenesis may depend on the nature of the initial brain injury. Blockade of mTOR hyperactivation may expand its therapeutic potential beyond the epileptogenesis phase, as therapeutic effects of chronic rapamycin or its analogs were observed also in epileptic animals after the disease was established[10,11].

In the context of childhood epilepsy, mTOR activation plays a part in models of infantile spasms—a form of seizure that is often found in disorders associated with mTOR dysfunction. Rapamycin reduced spasms in immature rats[12]; suppression of the spasms using a pulse protocol was lasting after drug withdrawal, in agreement with lack of seizure relapse with intermittent protocols in mutant mice[6]. These studies underline the importance of the rapamycin treatment protocol design for efficient and lasting seizure inhibition.

A noteworthy finding is the lack of effect of rapamycin on the generation of other types of recurrent seizures arising after spasms, suggesting a lack of antiepileptogenic effects in this model. However, rapamycin rescued the cognitive functions and exploratory ability, which are compromised in mice with spasms[12], reminiscent of neurodevelopmental comorbidities in human infants. These behavioral deficits were also described in genetic models of mTOR hyperactivity, also in the absence of seizures.

Annamaria Vezzani is in the Department of Neuroscience, Mario Negri Institute for Pharmacological Research, Milano, Italy.
e-mail: annamaria.vezzani@marionegri.it

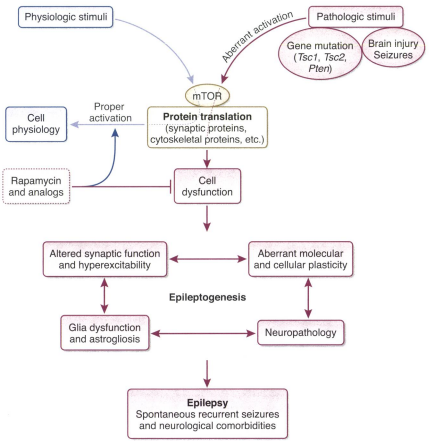

Figure 1 Pathophysiological cascade of mTOR-dependent events leading to epilepsy development. mTOR overactivation contributes to the generation of seizures by promoting maladaptive molecular and cellular changes, which occur in epileptogenesis after injury and prior epilepsy onset. Pathologic activation of mTOR may also contribute to some neurological abnormalities underlying epilepsy comorbidities such as cognitive deficits and autism[2,3]. The balance in favor of cell physiology can be reestablished by using rapamycin or its analogs.

In a neonatal rat model of hypoxia-induced seizures[13], neuronal mTOR hyperactivity was implicated in the subacute increase in seizure susceptibility, development of later life epilepsy and altered social behavior. Thus, mTOR might be a common mediator in the interaction between early life seizures, development of epilepsy and neurodevelopmental comorbidities, possibly by altering cell connectivity in the brain during crucial developmental windows.

Experimental findings have encouraged translation to the clinical setting, where antiseizure activity of mTOR inhibition was studied in people with TSC and intractable epilepsy[14–16]. One case report described seizure reduction in a 10-year-old girl with TSC using a 10-month treatment protocol with rapamycin[14]. A phase 2 prospective open-label trial enrolling 28 individuals with TSC between 3 and 34 years of age showed marked reduction of a type of tumor that arises in the brain of individuals with TSC with 6-month treatment with the mTOR inhibitor everolimus. Seizure frequency was monitored as a secondary endpoint in 16 subjects and was shown to be significantly decreased in nine subjects, whereas one person had seizures worsening[15]. A subsequent preliminary report from a combined phase 1/2 clinical trial assessed seizures as the primary endpoint and showed a minimum 25% seizure reduction in 15 out of 17 TSC-affected individuals, with nine subjects showing a greater than 50% decrease and one person showing seizure worsening[16].

Unfortunately, the paradoxical exacerbation of mTOR inhibition on neurotoxicity has also emerged in preclinical studies[17], suggesting this treatment may not be indicated in some circumstances. Antiepileptogenic trials have not been designed yet, as there are several potential obstacles. For example, optimal treatment protocols need to be designed to maximize the therapeutic effects while reducing potential adverse effects, including immunosuppression, growth inhibition and alterations in brain development. Animal studies indicate that such protocols may differ in genetic disorders and acquired epilepsies, or in pediatric and adult populations. In addition, the lack of biomarkers to predict epileptogenesis means it is not possible to select the high-risk population for treatment among the affected individuals.

In spite of these evident barriers, the wide range of beneficial effects of mTOR inhibition in various epileptogenesis models (including traumatic brain injury) calls for further investigation to promote clinical translation. Additional preclinical research will also be needed to clarify the master regulators of epileptogenesis, their response to upstream epileptogenic stimuli and the downstream effector pathways and targets. This knowledge would help in developing new antiepileptogenic, disease-modifying therapies to prevent or even cure the disease.

COMPETING FINANCIAL INTERESTS
The author declares no competing financial interests.

1. Han, J.M. & Sahin, M. *FEBS Lett.* **585**, 973–980 (2011).
2. Crino, P.B. *Trends Mol. Med.* **17**, 734–742 (2011).
3. Galanopoulou, A.S. *et al. Epilepsia* **53**, 1119–1130 (2012).
4. Meziane, D.M. *et al. J. Clin. Invest.* **121**, 1596–1607 (2011).
5. Meikle, L. *et al. J. Neurosci.* **27**, 5546–5558 (2007).
6. Sunnen, C.N. *et al. Epilepsia* **52**, 2065–2075 (2011).
7. Zheng, L.-H. *et al. J. Neurosci.* **29**, 6964–6972 (2009).
8. Sha, L.-Z. *et al. PLoS ONE* **7**, e39152 (2012).
9. Buckmaster, P.S. & Lew, F.H. *J. Neurosci.* **31**, 2337–2347 (2011).
10. Kwon, C.-H. *et al. Proc. Natl. Acad. Sci. USA* **100**, 12923–12928 (2003).
11. Huang, X. *et al. Neurobiol. Dis.* **40**, 193–199 (2010).
12. Raffo, E. *Neurobiol. Dis.* **43**, 322–329 (2011).
13. Talos, D.M. *et al. PLoS ONE* **7**, e35885 (2012).
14. Muncy, J. *et al. J. Child Neurol.* **24**, 477 (2009).
15. Krueger, D.A. *et al. N. Engl. J. Med.* **363**, 1801–1811 (2012).
16. Ryther, R.C.C. & Wong, M. *Curr. Neurol. Neurosci. Rep.* **12**, 410–418 (2012).
17. Zeng, L.-H. *et al. Cell Cycle* **9**, 2281–2285 (2010).

■ METABOLISM

An obesity hub

Dysregulation of thermogenesis and inflammation are linked to obesity. A new study in mice shows that a receptor commonly expressed in fat cells controls both programs and functions in a cell-autonomous manner (*Cell* **151**, 96–110).

Li Ye *et al.* used a chemical screen to identify proteins in white adipocytes that increase expression of the gene encoding Pgc1α in these cells, as this reflects activation of the thermogenic program. TRPV4, a calcium-permeable ion channel that is highly expressed in white fat cells, was found to negatively regulate Pgc1α and oxidative metabolism in these cells. Inhibition of TRPV4 increased expression of the gene encoding uncoupling protein 1 (UCP1) and other mitochondrial genes, which caused 'browning' of adipocytes and boosted respiration. Interestingly, this inhibition also dampened proinflammatory pathways, which decreased the expression of chemokines and cytokines and their secretion from fat cells. Mice lacking TRPV4 showed an improved metabolic profile; they were protected from diet-induced obesity owing to increased energy expenditure and had improved insulin sensitivity as a result of reduced inflammation in adipose tissue.

Although the authors found that TRPV4 antagonists could improve glucose tolerance in obese mice, which suggested that they might have potential for treating obesity and type 2 diabetes, further research should investigate the effects of TRPV4 inhibition in other tissues where this channel is expressed.—*CP*

■ IMMUNOLOGY

$CD8^+$ T cells mediate elite control

Elite controllers are rare individuals who are infected with HIV-1 yet maintain low to undetectable levels of virus in their blood and have no disease. Many of these people express specific major histocompatibility complex (MHC) class I alleles, which suggests that viral control is mediated by $CD8^+$ T cells. David Watkins and his colleagues now report that in a monkey model of elite control of simian immunodeficiency virus (SIV) infection, $CD8^+$ T cells targeting just three epitopes in the SIV Vif and Nef proteins correlate with control of virus replication (*Nature* doi:10.1038/nature11443).

In these authors' model of elite control—rhesus macaques expressing the MHC class I molecule Mamu-B*08 and infected with a highly pathogenic SIV—Mamu-B*08–restricted $CD8^+$ T cells recognizing three SIV epitopes (two in Vif and one in Nef) have been shown to predominate the T cell response. Watkins and his colleagues have now assessed the importance of these $CD8^+$ T cell responses by vaccinating Mamu-B*08+ macaques with vectors encoding or not encoding the three immunodominant SIV epitopes and subsequently challenging the macaques intrarectally with high doses of pathogenic SIVmac239. They found that all macaques vaccinated with the immunodominant T cell epitopes robustly controlled virus early in infection and showed higher post-infection T cell responses specific for two of the epitopes, Vif RL9 and Nef RI10, than the macaques vaccinated with nonimmunodominant SIV epitopes. In particular, cytotoxic T cells recognizing Nef RL10 were associated with viral control during the chronic phase of infection. A surge in viremia in two macaques vaccinated with the immunodominant epitopes during chronic phase was associated with escape of the immunodominant epitopes, further underlining their importance in T cell maintenance of viral control. This study will encourage further investigation of the relevant mechanisms and increase the potential for targeted vaccines to induce $CD8^+$ T cell mediated control of HIV infection.—*AF*

BONE

Regulating bone remodeling

Increased osteoclast activity is implicated in a number of bone loss conditions; thus, targeting bone resorption by osteoclasts could be a potential therapeutic avenue for these pathologies. A new study shows that the adenosine diphosphate (ADP) receptor P2RY12 regulates osteoclast function and can be therapeutically targeted in mouse models of bone loss (*J. Clin. Invest.* 122, 3579–3592).

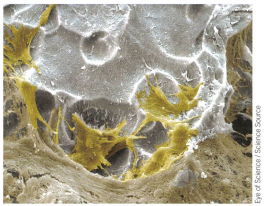

Eye of Science / Science Source

ADP is known to increase osteoclast activity, so Xinming Su *et al.* decided to examine the role of P2RY12 in osteoclasts. Mice lacking P2RY12 showed decreased osteoclast activity *in vivo* and were partially protected from age-related bone loss. Bone marrow macrophages from *P2ry12*$^{-/-}$ mice could be differentiated *ex vivo* into mature osteoclasts, but these osteoclasts showed reduced resorption function and could not be stimulated by ADP to increase bone resorption.

The authors then tested the susceptibility of *P2ry12*$^{-/-}$ mice to various types of pathological bone loss and found that they were less susceptible than wild-type mice to arthritis-associated, tumor-associated and ovariectomy-induced bone loss. Su *et al.* also showed that clopidogrel, which inhibits P2RY12 and is a US Food and Drug Administration–approved antiplatelet drug, could partially protect wild-type mice from pathological bone loss.

Although there are currently no prospective data on the effects of clopidogrel on bone in patients being treated with this drug, clinical studies to evaluate this aspect may be useful to better assess the potential for therapeutically targeting P2RY12 in bone loss conditions.—*MS*

■ NEUROSCIENCE

Growth factor can shrink reward responses

A recent paper in *Science* (**338**, 124–128) shows that brain-derived neurotrophic factor (BDNF) can reduce the behavioral response to morphine exposure in mice.

Conditioned place preference (CPP) is a commonly used way to measure reward. In this task, animals tend to spend more time in a place they associate with having received a drug of abuse. Ja Wook Koo *et al.* found that chronic administration of morphine to mice led to the reduced expression of BDNF in the ventral tegmental area (VTA), a key component of the brain's reward circuits. Knocking down BDNF expression in the VTA enabled morphine to increase the excitability of dopamine neurons in this brain region and potentiate CPP. By contrast, applying BDNF in the VTA markedly suppressed CPP. Directly stimulating dopamine terminals from the VTA

in the nucleus accumbens, a major VTA target and another key reward component, reversed the suppressive effect of BDNF on morphine reward.

Downstream from BDNF, the team found that several genes were involved in mediating its effects. Reducing the expression of the transcription factor Sox11 in the nucleus accumbens increased CPP, and overexpressing the immediate early gene *Gadd45g* in the same brain region further enhanced the effect of morphine.

This very thorough study indicates that BDNF has a nuanced role in the brain's response to drugs of abuse, as the opposite effect—a strengthened effect of cocaine after BDNF administration—had previously been reported. The cellular specificity and downstream mechanisms that account for these different effects have yet to be fully elucidated.—*JCL*

■ AUTOIMMUNITY

IL-26: inducing inflammation

A recent study identifies the interleukin-10 (IL-10) cytokine family member IL-26 as a key upstream mediator of the inflammatory cascade in rheumatoid arthritis (*PLoS Biol.* **10**, e1001395).

IL-26 has previously been shown to be overexpressed in Crohn's disease, which suggests that it may be involved in the pathogenesis of chronic inflammatory disorders. Murielle Corvaisier *et al.* investigated this cytokine in human rheumatoid arthritis and found that it is overexpressed in the serum and synovial fluid from patients with rheumatoid arthritis compared with healthy subjects. IL-26 was constitutively expressed by the synovial cells in rheumatoid arthritis joints, and its production was upregulated by IL-1β and IL-17A, both of which are known to be involved in rheumatoid arthritis pathogenesis.

The authors then found that IL-26 induced the expression of proinflammatory cytokines and chemokines by cultured myeloid cells. As rheumatoid arthritis is characterized by T helper type 1 (T_H1) and T_H17 inflammatory responses, they then investigated whether IL-26 can influence the type of T_H response induced. Using coculture experiments, the authors found that, via secretion of IL-1β, IL-26–treated monocytes can induce the polarization of memory $CD4^+$ T cells into T_H17 cells.

The authors suggest that IL-26 could be a potential therapeutic target in rheumatoid arthritis and that its role should also be investigated in other inflammatory disorders.—*MS*

■ CARDIOVASCULAR DISEASES

Degradation relieves the pressure

Drugs that activate the nuclear hormone receptor peroxisome proliferator–activated receptor γ (PPAR-γ) lower blood pressure, whereas dominant-negative mutations in the gene encoding PPAR-γ cause hypertension. Helping to explain these effects, Christopher Pelham *et al.* uncover a new mechanism by which PPAR-γ controls vasoconstriction and blood pressure (*Cell Metab.* **16**, 462–472).

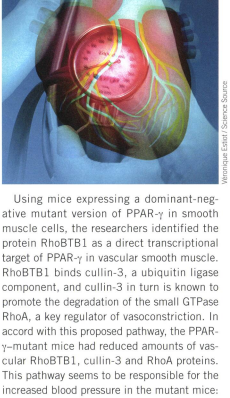

Veronique Estel / Science Source

Using mice expressing a dominant-negative mutant version of PPAR-γ in smooth muscle cells, the researchers identified the protein RhoBTB1 as a direct transcriptional target of PPAR-γ in vascular smooth muscle. RhoBTB1 binds cullin-3, a ubiquitin ligase component, and cullin-3 in turn is known to promote the degradation of the small GTPase RhoA, a key regulator of vasoconstriction. In accord with this proposed pathway, the PPAR-γ–mutant mice had reduced amounts of vascular RhoBTB1, cullin-3 and RhoA proteins. This pathway seems to be responsible for the increased blood pressure in the mutant mice: for example, treatment of wild-type mice with an inhibitor of cullin-3 function raised both vascular RhoA protein amounts and blood pressure, but the inhibitor did not further increase blood pressure in the PPAR-γ–mutant mice.

The antihypertensive function of cullin-3 uncovered in this study may also shed light on the recent discovery that mutations in the gene encoding cullin-3 cause hypertension in humans.—*MB*

Written by Michael Basson, Alison Farrell, Juan Carlos López, Carolina Pola and Meera Swami

New from NPG

Melanomas resist T-cell therapy through inflammation-induced reversible dedifferentiation

Landsberg, J. *et al. Nature* doi:10.1038/nature11538 (10 October).

A new study provides mechanistic insights into how tumors can acquire resistance to adoptive cell cytotoxic T cell therapy. The authors show that in a mouse melanoma model, resistance occurs through the reversible loss of melanocytic antigens on melanoma cells, which is triggered by inflammation. They identify the proinflammatory cytokine tumor necrosis factor-α as a key factor that induces this dedifferentiation of the melanoma cells.

***De novo* gene mutations highlight patterns of genetic and neural complexity in schizophrenia**

Xu, B. *et al. Nat. Genet.* doi:10.1038/ng.2446 (3 October).

By sequencing the exomes of individuals with schizophrenia and of their unaffected parents, the authors find that the individuals with schizophrenia have a greater number of *de novo* mutations that cause protein-coding changes than would be expected. In addition, they identify four candidate genes that have recurrent alterations in individuals with schizophrenia.

The kinase TBK1 controls IgA class switching by negatively regulating noncanonical NF-kB signalling

Jin, J. *et al. Nat. Immunol.* doi:10.1038/ni.2423 (30 September).

The authors identify the B cell regulatory molecule TBK1 as a key regulator of antibody class switching to immunoglobulin A (IgA). They show that mice lacking TBK1 expression in their B cells produce higher serum amounts of IgA and autoantibodies and develop kidney disease as a result of renal accumulation of autoimmune IgA complexes.

Divergent roles of ALS-linked protein FUS/TLS and TDP-43 intersect in processing long pre-mRNAs

Lagier-Tourenne, C. *et al. Nat. Neurosci.* doi:10.1038/nn.3230 (30 September).

The authors identified common mRNA targets regulated by two amyotrophic lateral sclerosis (ALS)-associated proteins, FUS/TLS and TDP-43. These common targets were transcribed from genes with very long introns that encode proteins important in neuronal integrity. The amounts of several of these proteins were reduced in ALS neurons, and the authors suggest that dysregulation of FUS/TLS or TDP-43 can elicit a common pathogenic pathway in ALS.

PERSPECTIVE

nature medicine

Chromoanagenesis and cancer: mechanisms and consequences of localized, complex chromosomal rearrangements

Andrew J Holland & Don W Cleveland

Next-generation sequencing of DNA from human tumors or individuals with developmental abnormalities has led to the discovery of a process we term chromoanagenesis, in which large numbers of complex rearrangements occur at one or a few chromosomal loci in a single catastrophic event. Two mechanisms underlie these rearrangements, both of which can be facilitated by a mitotic chromosome segregation error to produce a micronucleus containing the chromosome to undergo rearrangement. In the first, chromosome shattering (chromothripsis) is produced by mitotic entry before completion of DNA replication within the micronucleus, with a failure to disassemble the micronuclear envelope encapsulating the chromosomal fragments for random reassembly in the subsequent interphase. Alternatively, locally defective DNA replication initiates serial, microhomology-mediated template switching (chromoanasynthesis) that produces local rearrangements with altered gene copy numbers. Complex rearrangements are present in a broad spectrum of tumors and in individuals with congenital or developmental defects, highlighting the impact of chromoanagenesis on human disease.

Karyotype abnormalities comprise numerical and structural alterations in chromosomes and are defining features of the cancer cell genome. Structural rearrangements in chromosomes are caused by erroneous repair of DNA double-strand breaks and include deletions, duplications, inversions and translocations. Recurrent translocations are common in hematological malignancies, in which they have been shown to drive tumorigenesis through the creation of fusion genes derived from portions of two normal genes joined together[1]. In addition, rearrangements also contribute to disruption of tumor suppressor genes and amplification of oncogenes.

The advent of high-throughput DNA sequencing has enabled the interrogation of the cancer genome in unprecedented detail. Catalogs of the somatic mutations present in cancer cells are rapidly appearing (for example, http://www.sanger.ac.uk/genetics/CGP/Census/). Sequencing of both ends of the same DNA fragment (known as paired-end sequencing) reduces alignment ambiguities when matching short sequence reads to the reference genome. Paired-end sequencing of millions of genomic fragments from a single tumor can map genome-wide chromosomal rearrangements. Its use has recently brought considerable attention to the effect of structural chromosomal changes on cancer development[2–4] and uncovered an unexpected phenomenon in which tens to hundreds of rearrangements occur within one or a handful of genomic regions[5]. Sequencing of DNA from individuals with developmental abnormalities has identified constitutive chromosomes with similarly complex, localized rearrangements[6–9].

Two mechanisms have been proposed to provoke such rearrangements in a single event. The first is a cellular crisis termed chromothripsis[5] (from the Greek 'chromo' for chromosomes and 'thripsis,' for shattering). The second is local rearrangements with altered gene copy numbers produced by serial, microhomology-mediated template switching during DNA replication, termed chromoanasynthesis[8] ('chromo' for chromosomes and 'anasynthesis,' for reconstitution). Evidence to date suggests that chromothripsis is the probable mechanism underlying most of the rearrangements identified in cancer. Nevertheless, recognizing that at least two mechanisms produce complex, localized rearrangements, we propose the word chromoanagenesis ('chromo' for chromosomes and 'anagenesis,' for rebirth) to describe this class of chromosomal rearrangement that is independent of the provoking mechanism.

Here we discuss the evidence supporting the view that chromoanagenesis occurs as a one-off cellular event that may contribute to the initiation and development of human cancer. We outline the mechanisms that have been proposed to create highly localized complex genomic rearrangements, including provocative recent work suggesting that chromoanagenesis is initiated by a chromosome mis-segregation error, producing a micronucleus in which the localized shattering and religation take place in two subsequent cell cycles. We also describe how similarly complex rearrangements with copy number changes can be driven by cellular stress during DNA replication, resulting in replication fork collapse which initiates microhomology-mediated template switching.

A one-off cellular cataclysm

Three primary lines of evidence indicate that many of the localized chromosomal rearrangements observed in cases of chromoanagenesis do not arise from a progressive series of independent rearrangements; rather, they occur in a single catastrophic event[5].

Ludwig Institute for Cancer Research and Department of Cellular and Molecular Medicine, University of California San Diego, La Jolla, California, USA. Correspondence should be addressed to A.J.H. (a1holland@ucsd.edu) and D.W.C. (dcleveland@ucsd.edu).

Received 15 May; accepted 1 October; published online 7 November 2012; doi:10.1038/nm.2988

First, in cancer cells the chromosome rearrangements primarily alternate between two copy number states. The lower copy number state represents heterozygous deletion of a DNA fragment and the higher copy state indicates retention of a DNA piece (**Fig. 1**). The higher copy number state does not always result from two copies of a DNA fragment, as tumors are often aneuploid (containing an abnormal number of chromosomes). Progressive models with sequential chromosomal translocations predict substantially more than two copy number states[5]. Second, heterozygosity is preserved in multiple separate regions with higher copy number states in which DNA fragments have been retained. Regions in which heterozygosity is maintained can be encompassed within an area spanned by multiple additional rearrangements that have the orientation of deletions, duplications and inversions[5]. If a deletion occurred early in a successive series of rearrangements, then heterozygosity would be permanently eliminated between the breakpoints. Thus, for a progressive model to explain chromoanagenesis, deletion events could only occur late in the sequence of rearrangements, a scenario that seems unlikely given the number of rearrangements involved in chromoanagenesis[5]. In contrast, alternating regions of heterozygosity (retention of a DNA fragment) and loss of heterozygosity (loss of a DNA fragment) inevitably result from rearrangements that are caused by a one-off cataclysmic event proposed to occur during chromothripsis (**Fig. 1**). Third and finally, in tumors in which chromoanagenesis has occurred, the chromosomal breakpoints cluster to a greater degree than expected from sequential independent rearrangements[5].

Overall, it is therefore likely that most of the rearrangements present in the chromoanagenesis found in cancer cells occur in a single catastrophic event arising from chromosome pulverization followed by the rejoining of chromosomal fragments in a random order (**Fig. 1**). The idea that cancer genomes evolve in rapid bursts is in line with the evolutionary theory of punctuated equilibrium originally proposed by Eldredge and Gould in 1972, which posits that species undergo little alteration for most of their evolutionary history, with rare events leading to rapid evolutionary shifts that can result in the creation of a new species[10]. Similarly, creating many alterations in a single genomic event increases the probability that large adaptive leaps can be achieved, which may be advantageous in the severe genetic or environmental pressures encountered in tumors.

Even if it is accepted that multiple complex rearrangements can occur in a single event, the high frequency of genome changes in cancer cells firmly suggests additional rearrangements can also be expected before or after chromoanagenesis, consistent with the widely held view that genomic changes in many cancers accumulate from a progressive series of errors. Indeed, some regions of rearranged chromosomes alternate between two and three copy number states, which suggests that a partial duplication of the rearranged chromosome occurs after chromoanagenesis takes place[5]. Alternatively, if an initiating event created massive DNA double-strand breaks simultaneously on both genetically identical sister chromatids of a replicated chromosome, then the random stitching together of chromosome fragments could lead to a duplication of specific chromosomal fragments in the rearranged sister chromatids[11].

Solitary confinement: locked away in a micronucleus

Since its discovery, the most perplexing feature of chromoanagenesis is how chromosomal rearrangements can be limited to a very small subset of chromosomes, often a single chromosome or chromosome arm. What event(s) causes this massive damage and how can it be highly localized to distinct genomic regions? A very surprising

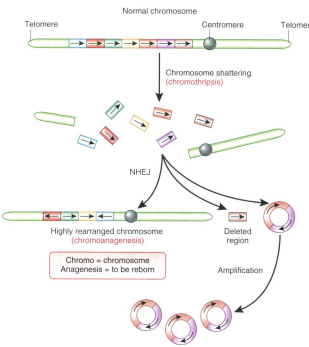

Figure 1 Mechanism for the creation of complex chromosomal rearrangements by NHEJ after chromosome shattering. Chromothripsis results in the shattering of one or a few chromosomes (or a chromosome arm), leading to the simultaneous creation of many double-strand breaks. Most of the shattered fragments are stitched back together through NHEJ, leading to chromoanagenesis: the creation of a chromosome with complex, highly localized chromosomal rearrangements. The rearranged chromosome contains two copy number states: a high copy number state for each religated fragment and a low copy number state for fragments that were not reincorporated and therefore lost. Broken DNA fragments may also be joined together to form circular, extrachromosomal double minute chromosomes that often harbor oncogenes and are frequently amplified, resulting in a dramatically increased copy number of DNA fragments on these chromosomes.

mechanism was identified in early 2012: chromosome shattering may arise from an error in mitotic chromosome segregation that leads to the production of a micronucleus[12].

During normal mitosis, the replicated genetic information is divided equally into the two new daughter nuclei such that each cell receives a single copy of each duplicated chromosome. Errors in chromosome segregation during mitosis result in the production of aneuploid cells. Aneuploidy is a hallmark of cancer and has been widely proposed to have a role in the initiation and development of tumors[13,14]. Although aneuploidy and structural alterations in chromosomes have often been thought to arise independently of one another, recent evidence has shown that these two chromosomal aberrations can be mechanistically linked.

Most tumor cells do not possess a stably aneuploid genome; rather, they have a continually changing karyotype driven by high rates of chromosome gain and loss during division, a phenomenon known as chromosomal instability[15]. Live-cell imaging experiments have revealed that chromosomally unstable tumor cells show an increase in the number of chromosomes that lag in the middle of the spindle during anaphase[16,17]. One or both copies of such lagging chromosomes often do not reach the two major chromosome masses at the poles of the cells before nuclear envelope reassembly, and consequently

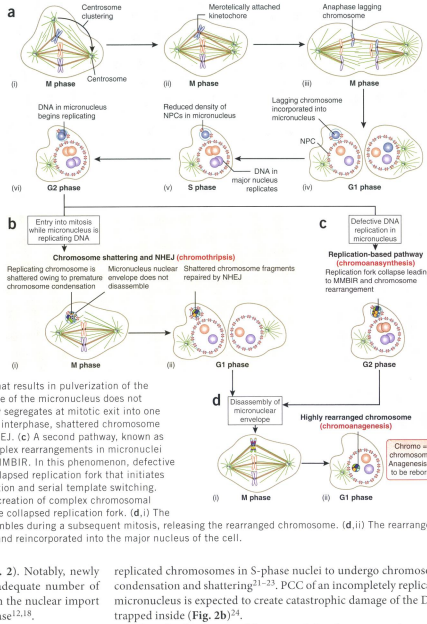

Figure 2 Mitotic errors produce micronuclei and subsequent chromoanagenesis. (**a**,i) Cells with extra centrosomes form multi-polar mitotic spindles. In many instances centrosomes coalesce into two groups before anaphase. (**a**,ii) Centrosome clustering increases the frequency of merotelic attachments, in which a duplicated chromosome attaches through its kinetochore to microtubules arising from both mitotic spindle poles[21,52]. (**a**, iii) If not corrected before anaphase, merotelically attached chromosomes may lag in the middle of the mitotic spindle. (**a**, iv) Lagging chromosomes are sometimes excluded from both daughter nuclei and instead form a micronucleus in one of the daughter cells in the subsequent interphase. (**a**) Micronuclei often contain fewer nuclear pore complexes (NPCs) (v), impairing nuclear import and delaying DNA replication of chromosome(s) in the micronucleus (vi). Chromoanagenesis (the creation of complex, localized chromosomal rearrangements) can arise in micronuclei through two distinct mechanisms. (**b**,i) The predominant pathway, known as chromothripsis[5], involves chromosome shattering after mitotic entry while the micronucleus is still replicating its DNA. The incompletely replicated micronuclear DNA undergoes premature chromosome condensation that results in pulverization of the trapped chromosome(s). Often the nuclear envelope of the micronucleus does not disassemble and the intact micronucleus randomly segregates at mitotic exit into one of the daughter cells. (**b**,ii) During the subsequent interphase, shattered chromosome pieces within the micronucleus are repaired by NHEJ. (**c**) A second pathway, known as chromoanasynthesis[8], leads to the creation of complex rearrangements in micronuclei through a replication-based mechanism, such as MMBIR. In this phenomenon, defective DNA replication in the micronucleus leads to a collapsed replication fork that initiates microhomology-dependent priming of DNA replication and serial template switching. MMBIR can result in chromoanagenesis, with the creation of complex chromosomal rearrangements at genomic regions surrounding the collapsed replication fork. (**d**,i) The micronucleus nuclear envelope eventually disassembles during a subsequent mitosis, releasing the rearranged chromosome. (**d**,ii) The rearranged chromosome is segregated on the mitotic spindle and reincorporated into the major nucleus of the cell.

they form a self-contained micronucleus (**Fig. 2**). Notably, newly formed micronuclei frequently possess an inadequate number of nuclear pores and consequently show defects in the nuclear import of some components in the subsequent interphase[12,18].

Reduced nuclear import has several consequences for the chromatin sequestered inside micronuclei. First, micronuclei show defective DNA damage response signaling, resulting in defective and/or delayed repair of induced DNA damage[12,19,20]. Second, DNA replication in micronuclei is delayed compared with that in the major nucleus, with some micronuclei still replicating DNA when the major nucleus is in G2 phase (**Fig. 2a**)[12]. Third, entry into mitosis while the micronucleus is undergoing DNA replication produces massive DNA double-strand breaks in the micronuclear DNA[12].

Pulverizing chromosomes within a micronucleus

The most plausible mechanism for the observed chromosomal pulverization that characterizes chromothripsis is entry into mitosis before the completion of DNA replication within a micronucleus, resulting in breaks in the incompletely replicated micronuclear DNA during premature chromosome condensation (PCC). PCC was originally described in classic cell fusion experiments and occurs when cyclin-dependent kinase activity in a mitotic cell induces incompletely replicated chromosomes in S-phase nuclei to undergo chromosome condensation and shattering[21–23]. PCC of an incompletely replicated micronucleus is expected to create catastrophic damage of the DNA trapped inside (**Fig. 2b**)[24].

Although it has been widely assumed that the micronuclear envelope will dissemble in mitosis, allowing the chromosome(s) contained within to spill into the cytoplasm of the mitotic cell, this is not what happens for many micronuclei. Indeed, disassembly of the micronuclear envelope frequently fails at the onset of the subsequent mitosis, with the intact micronucleus randomly segregating at mitotic exit into one of the daughter cells[12]. Persistence of a micronucleus into interphase of the second cell cycle after its initial formation provides a plausible mechanism for isolating the chromosomal fragments generated as a result of PCC so that they may subsequently be repaired by ligation (in a random order) (**Fig. 2b**). For the subset of micronuclei for which the nuclear membrane does disassemble, the fragments of pulverized chromosomes (nearly all of which lack centromeres and microtubule attachment sites) will be unable to be segregated and may be lost or may form *de novo* micronuclei at mitotic exit.

How a micronucleus escapes nuclear envelope disassembly during mitosis is unresolved, but the reduced density of nuclear pores may result in reduced incorporation of several key envelope constituents

that are phosphorylated by mitotic cyclin-dependent kinases to promote nuclear envelope breakdown. Eventually, however, further cycling of the cell will yield micronuclear envelope disassembly when it enters a subsequent mitosis, releasing the rearranged chromosome into the mitotic cytoplasm and allowing its conventional mitotic segregation with the main mitotic chromosome mass (**Fig. 2d**). The mis-segregation of chromosomes into micronuclei provides a plausible route through which whole chromosome mis-segregation can promote chromosome breaks and subsequent rearrangement, thereby mechanistically coupling events leading to the acquisition of numerical and structural chromosomal alterations. In addition, this pathway also offers an explanation for how the DNA breaks acquired during chromothripsis may be circumscribed to one or a small number of chromosomes—those trapped within a micronucleus[12]. Thus, an initial error in chromosome segregation during mitosis is likely to be one key event in the initiation of chromoanagenesis. As such it will now be of interest to look for evidence of chromothripsis in the tumors formed in mice that have been genetically manipulated to exhibit chromosomal instability and aneuploidy[25].

Alternative proposals for chromosome shattering

It should be noted that at present the mechanisms responsible for chromothripsis remain controversial. In addition to chromosome shattering caused by mitotic entry with incompletely replicated DNA, three additional proposals have been put forward to explain how localized chromosome shattering may result in complex, localized rearrangements. We propose that each of these mechanisms is made more plausible if one imparts the formation of micronuclei as a means to either spatially localize DNA damage or contain the chromosome fragments created by this damage so that they may be religated to produce chromosomal rearrangements.

To explain the confined nature of the DNA damage created during chromothripsis, an initial proposal was that localized double-strand DNA breaks were induced by free radicals or ionizing radiation during mitosis[5], when chromosomes are highly compacted and DNA damage signaling is suppressed[26]. The formation at mitotic exit of a micronucleus containing the damaged chromosome fragments would provide a means to constrain the fragments produced so as to facilitate their religation into a rearranged chromosome characteristic of chromoanagenesis.

Telomere dysfunction has also been proposed as a cause of chromothripsis[5]. Continued proliferation of somatic cells in the absence of telomerase activity leads to the progressive attrition of telomeres. Eventually, telomere-shortening exposes uncapped chromosome ends that are prone to fusion, which creates a dicentric chromosome with two microtubule attachment sites on each sister chromatid. If these sites attach to opposite spindle poles during mitosis, the resulting chromosome will become highly stretched during anaphase. As chromothripsis seems to occur in a single catastrophic cellular event, one possibility is that the bridging chromosome undergoes massive localized genomic damage at the cleavage furrow during cytokinesis[27]. A more attractive explanation, however, is that the lagging dicentric chromosome does not incorporate into the major nucleus of either daughter cell and instead forms a micronucleus. Therefore, telomerase deficiency could promote chromothripsis indirectly, by disrupting chromosome segregation and leading to the production of micronuclei. The examination of telomerase-deficient mouse models for evidence of extensive localized genomic rearrangements will be an important test of whether telomere dysfunction can promote chromothripsis.

Finally, chromothriptic chromosome shattering has been suggested to result from an aborted attempt at apoptosis[28]. Whereas apoptosis has traditionally been considered as an irreversible cascade that, once initiated, irrevocably leads to cell death, recent evidence has clearly shown that initial apoptotic events can be reversed if the initiating stimulus is removed[29]. Reversal of apoptosis has been termed anastasis (Greek for 'rising to life'), and it can occur after measurable DNA damage, allowing cells to acquire permanent genetic changes that facilitate transformation[29]. Anastasis promotes an increase in numerical and structural chromosomal alterations as well as an increase in micronuclei formation[29]. Reversal of apoptosis after the initiation of DNA damage and chromosome fragmentation may lead to the religation of chromosome fragments and the production of chromosomal rearrangements[30,31]. In the tumor microenvironment, apoptosis can be initiated by various stresses, including chemotherapy, ionizing radiation, hypoxia and nutrient deprivation. This raises the possibility that these transient stress stimuli could induce an aborted apoptosis that initiates the DNA damage responsible for chromothripsis. As in the other proposed mechanisms, if anastasis occurred specifically within a micronucleus, DNA damage would be confined to the chromosome(s) trapped inside[32]. It will be of interest to establish whether anastasis can initiate chromothripsis and the development of complex chromosomal rearrangements in cultured cells.

After shattering: weaving together chromosomal fragments

Most of the breakpoints of the reassembled chromosomes created by chromothripsis in human cancers show either a lack of homology or areas of microhomology, pointing toward nonhomologous end joining (NHEJ) as the predominant mechanism that stitches the shattered chromosomes back together after extensive double-strand breaks (**Fig. 1**)[5,33,34]. NHEJ can occur at any point in the cell cycle and often occurs at regions of microhomology that are 1–4 nucleotides in length[35]. NHEJ occurs in a series of steps[35]. First, the Ku protein heterodimer (Ku70/Ku80) is recruited to both ends of the DNA at the site of a double-strand break. Ku recruits a complex of the protein artemis and the DNA-dependent protein kinase catalytic subunit involved in processing the ends of DNA breaks. As a final step, the ligase IV complex (comprising DNA ligase IV and its cofactor XRCC4) is recruited by Ku and ligates the adjacent DNA ends, thereby repairing the double-strand break. Ligation of incorrect ends though NHEJ can lead to chromosomal translocations. The random reassembly by NHEJ of many simultaneously created chromosome fragments can account for the majority of the chromosomal translocations created during chromoanagenesis in cancer cells.

Constitutional rearrangements from a slip-up in DNA replication

In contrast to the chromosome shattering and NHEJ found in cancer cells, some instances of chromoanagenesis contain complex constitutional chromosomal rearrangements carrying a signature with microhomology at the ends of rearranged segments indicative of a DNA replication-based mechanism as the causative agent[8,9] (**Box 1**). These rearrangements are associated with congenital or developmental abnormalities and contain multiple duplications and triplications, neither of which can be readily explained by a mechanism involving the NHEJ-mediated repair of many simultaneously created double-strand breaks.

The most persuasive evidence for rearrangements from DNA replication-based mechanisms, including fork-stalling and template switching (FoSTes)[36] and microhomology-mediated break-induced

BOX 1 Germline chromothripsis contributes to human disease

Complex genomic rearrangements consist of at least two breakpoint junctions and are associated with various congenital or developmental abnormalities. In contrast to rearrangements generated by cancer chromoanagenesis, which arise in differentiated somatic cells, constitutional rearrangements occur in the germ line or very early in embryonic development. Several recent studies have revealed that some people with inherited genetic defects have complex constitutional chromosomal rearrangements that strongly resemble the somatic rearrangements found in cancer chromoanagenesis. Analysis of a family trio identified a complex series of *de novo* chromosomal rearrangements occurring in a child with congenital abnormalities[6]. These rearrangements clustered in small genomic regions on three chromosomes (chromosomes 1, 4 and 10) and bore the hallmarks of chromoanagenesis. An additional study of 17 individuals with developmental and congenital abnormalities revealed four with inherited chromoanagenesis-like rearrangements in a single chromosome (involving chromosomes 1 or 9 in one person each and chromosome 22 in two additional people)[8].

High-resolution analysis of the breakpoints in 52 patients with cytogenetically defined chromosomal abnormalities identified at least two additional cases of constitutional complex genomic rearrangements that share similarities with the rearrangements identified in cancer chromoanagenesis[7]. The genomic rearrangements involved two or three chromosomes (chromosome 5 and X or chromosomes 3, 5 and 7) and showed few losses and gains of DNA segments. The largely dosage-balanced state (in which genes or DNA sequences are present in the correct copy number) observed in these multichromosome constitutional rearrangements is distinct from the more extensive copy number changes frequently observed in cancer chromoanagenesis[5] and from some other individuals with constitutional chromoanagenesis involving only a single chromosome[8]. Dosage alterations may be favored in cancer cells owing to a loss of tumor suppressor genes, whereas the more balanced chromosomal translocations observed in complex genomic rearrangements may reflect a selection for rearrangements that are compatible with organismal viability. Indeed, less-complex rearrangements are expected for heritable disorders, because massive constitutional rearrangements would be expected to be lethal during development.

In an effort to determine the mechanism responsible for the creation of constitutional complex chromosomal rearrangements, a recent study analyzed the breakpoints in ten individuals with congenital abnormalities[9]. The rearrangements consisted of between 3 and 24 inter- and intrachromosomal breakpoints with features similar to those observed in cancer chromoanagenesis. Eight of the individuals had rearrangements that probably arose through the creation of multiple simultaneous double-strand DNA breaks followed by non-homologous repair (as originally proposed for chromothripsis in cancer cells[5]). However, two other individuals had a genetic signature at the junctions of rearrangements that was most consistent with the idea that these arrangements arose through defective DNA replication, which led to serial template switching (chromoanasynthesis)[9] (**Box 2**).

replication (MMBIR)[37], is from sequencing of breakpoint junctions, which reveals areas of microhomologies and templated insertions (54–1542 bps)[8]. MMBIR may occur when a replication fork collapses after encountering a nick in the template strand (**Box 2**). Breakage of a replication fork then promotes microhomology-dependent priming of DNA replication and serial template switching, resulting in complex chromosomal rearrangements surrounding the site of the collapsed fork[8] (**Fig. 3**). Oncogene-induced DNA replication stress can cause cellular senescence and may provide an additional source of collapsed replication forks that trigger MMBIR[38,39]. In FoSTes, rearrangements seem to arise as a result of a stalled replication fork coupled with a consecutive series of long-range replication fork template switches (**Fig. 3**).

Replication-based mechanisms do not necessarily require micronuclei to explain the formation of complex localized chromosomal rearrangements. Indeed, the organization of chromosomes into distinct territories within a cell's nucleus may help bias microhomology-dependent template switching to sequences on a single or small subset of chromosomes that are in close proximity in three-dimensional space. Nevertheless, micronuclei often show defective DNA replication[12] and the partitioning of a chromosome into a micronucleus would provide an elegant explanation for how aberrant DNA replication could be restricted to one or a few spatially isolated chromosomes (**Fig. 2c**).

Although FoSTes and MMBIR offer a plausible route for the generation of complex copy number variations and an explanation for how multiple copy number changes may arise in some germline cases of chromoanagenesis[8,9] (**Boxes 1** and **2**), it should also be noted that inspection of breakpoints in several additional cases of constitutional structural rearrangements bear similarity to what is predicted by local chromosome shattering followed by NHEJ[6,9]. Thus, although the weight of evidence supports a mechanism of massive chromosomal breakage followed by NHEJ to explain the complex genomic rearrangements observed in many cancers[5,33,34], there seem to be at least two distinct mechanisms responsible for the chromoanagenesis-like rearrangements associated with genomic disorders[6,8,9].

Chromoanagenesis in human cancer

The multiple, localized, chromosome rearrangements characteristic of chromoanagenesis occur in many different types of cancers with an overall frequency of ~2–3% (refs. 5,33,34,40–44). The frequency of chromoanagenesis is elevated in specific tumor types, including ~25% of bone cancers[5] and ~18% of late-stage neuroblastomas[44]. Moreover, chromoanagenesis is widespread in primary and metastatic colorectal cancer[34] and there is a striking association between mutations in *TP53* (encoding the p53 protein) and chromoanagenesis in sonic hedgehog–induced medulloblastoma (SHH-MB) and acute myeloid leukemia (AML)[33]. Notably, chromoanagenesis has been associated with poor survival in a variety of tumor types[33,43,44], but further studies will be required to define the incidence and consequence of chromoanagenesis across a larger set of human cancers.

In the vast majority of cases it is probable that chromoanagenesis creates genomic alterations that do not produce any advantages or lead to a substantial reduction in cellular fitness. As a result, the occurrence of chromoanagenesis in cancer is likely to be considerably higher than the ~3% that has been observed, with most cases of chromoanagenesis expected not to provide a selectable advantage and to escape clinical detection. However, in rare circumstances chromoanagenesis may lead to the creation of one or more

BOX 2 Replication-based mechanisms that lead to complex chromosomal rearrangements

The insertion of short sequences at breakpoint junctions that are 'templated' from nearby genomic regions provides evidence of a DNA replication–associated mechanism for chromosomal rearrangements. Such a mechanism (chromoanasynthesis) has been proposed to account for some examples of complex constitutional chromosomal rearrangements[8,9] (**Box 1**). Two related mechanisms have been proposed for these genomic alterations. The first, known as fork-stalling and template switching (FoSTes), occurs when a replication fork stalls at a DNA lesion, allowing the lagging strand of the replication fork to disengage and switch to an area of microhomology on a neighboring replication fork[36]. The two replication forks will be in physical proximity, but they may be separated by large stretches of DNA sequence. DNA synthesis would initiate temporarily at this second site before the nascent strand disengages again and invades an additional replication fork. This process may repeat multiple times, leading to serial template switching before completion of DNA synthesis on the original template.

The second mechanism is known as microhomology-mediated break-induced replication (MMBIR) and is initiated when a replication fork collapses upon encountering a nick in the template strand[37]. This process creates a DNA double-strand break in one arm of the replication fork; however, as there is not an additional DNA end to be used in double-strand break repair, the 5′ end of the broken arm is resected to leave a 3′ single-stranded DNA overhang, which invades a DNA sequence with microhomology to the single stranded 3′ end. The 3′ end primes DNA synthesis and establishes a replication fork. The extended arm eventually separates from the template and the 3′ end re-invades an additional region to repeat the process. Eventually, a switch occurs to the original genomic region and replication continues to the chromosome end.

FoSTes and MMBIR can result in complex genomic rearrangements surrounding the site of the original defective replication fork. Serial template switching can lead to the insertion of specific DNA sequences from distinct genomic regions that lie in close proximity in three-dimensional space and can also explain the increases in copy number (duplications and triplications) observed in some cases of complex constitutional chromosomal rearrangements[8]. For example, duplication can occur when a template switch occurs to a DNA sequence that lies behind (relative to the direction of the fork) the location where the replication fork collapsed[37].

cancer-causing lesions in a single catastrophic event, thereby providing an advantage for cellular growth.

One key route through which chromosome shattering and religation by NHEJ could promote aberrant cellular proliferation is by facilitating oncogene amplification through the creation of small, circular fragments of DNA that lack centromeres and telomeres and frequently harbor oncogenes (**Fig. 4a**). These extrachromosomal fragments are known as double minute chromosomes and are often present at many copies per cell[45]. During chromothripsis it is postulated that individual chromosomes (or portions of them) are initially broken into many pieces and randomly reassembled by NHEJ. Although many of the pieces are stitched back together in random order to produce a highly rearranged chromosome, some fragments may also be joined together to create a circular double minute (**Fig. 4a**), the amplification of which can be selected for if it confers a growth advantage[5,33]. One example of such a rearrangement is exemplified in one small-cell lung cancer cell line that was found to contain a double minute chromosome (carrying the *MYC* oncogene) created by the fusion of several segments of chromosome 8 that were absent from a rearranged copy of chromosome 8 generated by chromoanagenesis[5].

A second potential route by which chromoanagenesis could create cancer-causing mutations is through the loss or disruption of tumor suppressor genes (**Fig. 4b**). For example, in one chordoma, chromosome shattering facilitated the loss of chromosomal fragments that contained, or led to rearrangements that directly disrupted, each of three tumor suppressor genes (F-box and WD repeat-containing 7 *(FBXW7)*, Werner Syndrome, RecQ helicase-like *(WRN)* and cyclin-dependent kinase inhibitor 2A *(CDKN2A))*[5]. In addition, in colorectal cancer the breakpoints generated by chromothripsis have been found to affect several known cancer-causing genes (notch 2, *(NOTCH2)*, exonuclease 1 *(EXO1)* and myeloid/lymphoid or mixed-lineage leukemia 3 *(MLL3))*[34]. The rearrangements created by chromoanagenesis

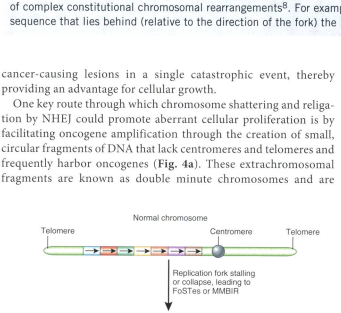

Figure 3 Mechanism for complex chromosomal rearrangements as a result of FoSTes and MMBIR. FoSTes occurs when a replication fork stalls at a DNA lesion, whereas MMBIR is initiated after replication fork collapse. FoSTes and MMBIR lead to microhomology-dependent priming of DNA replication and serial template switching, which can lead to chromoanagenesis. In addition to the deletion and retention of DNA fragments, FoSTes and MMBIR can also lead to duplication and triplication of DNA sequences. Therefore, FoSTes and MMBIR can result in more than two copy number states on the rearranged chromosome. Modified from ref. 53. DSB, double-strand break.

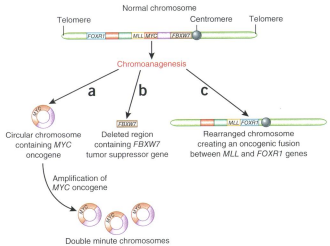

Figure 4 Chromoanagenesis may create oncogenic lesions. The complex chromosomal rearrangements created by chromoanagenesis can be oncogenic. (**a**) Initial chromosomal shattering followed by rejoining by NHEJ may create circular fragments of DNA harboring oncogenes such as *MYC*. Amplification of these extrachromosomal double minute chromosomes can provide a growth advantage. Other pieces of a shattered chromosome may be joined together to create a highly rearranged chromosome. (**b**) Chromoanagenesis can lead to the loss or disruption of regions containing tumor suppressor genes such as *FBXW7*. (**c**) Rearrangements may also create oncogenic fusion genes by joining the coding sequence two normal genes together, for example, the fusion of the *MLL* and the forkhead box R1 (*FOXR1*) genes.

often affect only a single allele of a tumor suppressor gene and the other copy of the gene is retained, implying that the second intact allele may be inactivated epigenetically. Alternatively, the affected gene may act as a haploinsufficient tumor suppressor, as has been shown for the tumor suppressor *FBXW7* (refs. 46,47).

Finally, the chromosome shattering and religation characteristic of chromoanagenesis can generate oncogenic fusion genes by joining the coding portions of two genes in the same orientation (**Fig. 4c**). For example, chromoanagenesis in medulloblastoma tumors leads to recurrent translocations that fuse *PVT1* (a non–protein coding gene) to the *MYC* proto-oncogene, resulting in *MYC* amplification[42].

Chromoanagenesis: an early or late event in human tumors?

Although chromoanagenesis can sculpt the cancer genome, leading to the creation of potentially oncogenic lesions, it is notable that it has yet to be formally shown that the genetic abnormalities that arise as a consequence of chromoanagenesis act, either individually or in combination, to drive tumorigenesis. The handful of studies reported so far have analyzed chromoanagenesis by sampling a single and relatively late stage in tumor development; thus, it remains unsettled at which stage during tumor evolution chromoanagenesis occurs. Chromoanagenesis often occurs after *TP53* mutations in patients with AML or SHH-MB[33], whereas in neuroblastoma chromoanagenesis has been identified in 18% of late-stage cancers but is absent in early stage tumors[44]. These observations argue that chromoanagenesis may be a relatively late event, at least in the development of these types of cancer. In the future it will be important to do longitudinal studies in animal models or human cancer patients to establish whether chromoanagenesis is an early initiating event or a later event that only occurs after additional defects, such as *TP53* mutations, have been acquired.

Stayin' alive

It is remarkable that a cell can survive the catastrophic events of chromoanagenesis that arise either after replication fork collapse in chromoanasynthesis or after tens to hundreds of DNA breaks accompanying chromothripsis. This suggests that that acquired defects in DNA damaging signaling cascades may set the stage for tolerating the massive DNA damage that can trigger chromoanagenesis. Whole-genome sequencing coupled with microarray analysis has uncovered a striking association between chromoanagenesis and both germline and somatic inactivation of the *TP53* tumor suppressor gene[33,41,42]. There is a considerable enrichment for chromoanagenesis in samples from people affected by AML with *TP53* mutations[33]. In one study, chromoanagenesis was observed in all ten of the SHH-MB samples with *TP53* mutations, but was not observed in SHH-MBs with an intact *TP53* gene[33]. An independent study found that chromoanagenesis in Group 3 medulloblastomas (one of the four main medulloblastoma subgroups) is associated with loss of the *TP53* gene[42]. Other medulloblastoma subtypes rarely show chromoanagenesis (including WNT-subtype medulloblastomas harboring mutated *TP53*), indicating that the link between p53 mutation and chromoanagenesis is dependent on the tumor type[33,42].

Germline mutations of *TP53* in people with SHH-MB occur before chromoanagenesis, suggesting that *TP53* mutations may either predispose cells to DNA damage or allow cellular survival after it. Indeed, p53 has an important role in promoting cell cycle arrest, apoptosis or senescence in response to DNA damage[48]. Analysis of early T cell precursor acute lymphoblastic leukemia has also hinted at a link between mutations in genes involved in DNA repair and chromoanagenesis[40]. Two neuroblastoma tumors with evidence of chromoanagenesis were also found to contain mutations in genes functioning in the Fanconi anemia–DNA damage response pathway, indicating that lesions that attenuate DNA damage signaling pathways may have a general role in facilitating the survival of cells that undergo events that initiate chromosome shattering[44].

Clinical implications of chromoanagenesis

It is clear that chromoanagenesis has the capacity to create novel genetic alterations that can potentially drive tumor progression. Indeed, chromoanagenesis has been associated with poor survival in AML[33], neuroblastoma[44] and multiple myeloma[43]. In AML the association between chromoanagenesis and poor survival is independent of patient age and leukemia karyotype classification, raising the possibility that this distinctive genetic alteration may be a useful prognostic marker for predicting disease outcome or therapeutic responsiveness[33]. However, in neuroblastoma, chromoanagenesis has only been observed in late-stage patients (stage 3–4) who have a poorer outcome than those with early-stage tumors[44]. Therefore, the prognostic value of chromoanagenesis will probably depend upon the cancer type and will be sensitive to when during tumor evolution chromoanagenesis occurs as well as to what additional genetic events (such as *TP53* mutations) predispose to chromoanagenesis. In addition to its role in shaping cancer genomes, chromoanagenesis has also been reported to create complex constitutional genomic rearrangements, which probably contribute to congenital or developmental defects (**Box 1**). Clearly, more work will be needed in larger patient cohorts to determine the full clinical implications arising from chromoanagenesis.

Li-Fraumeni syndrome patients with heterozygous germline mutations in *TP53* show an increased incidence of chromoanagenesis in SHH-MB and possibly also in other Li-Fraumeni syndrome–associated malignancies[33]. The use of DNA-damaging

agents and ionizing radiation in cancer therapy may induce chromosome shattering, especially through an initial mis-segregation of a damaged chromosome. Comparing the genomes of primary tumors with those that relapse after therapy will provide important insights into whether chromoanagenesis can be induced by specific therapeutic regimes and whether this may contribute to the emergence of resistance in the primary tumor.

Looking forward

Given the large number of genomic alterations occurring in a single event, chromoanagenesis could allow the rapid development of new phenotypes that facilitate tumor initiation, progression and the evolution of resistance to drug therapy. For a more complete understanding of the role of chromoanagenesis in tumorigenesis, it will now be necessary to establish the point at which chromoanagenesis occurs during the clonal evolution of a tumor. In addition, establishing which types of tumors show the highest incidence of chromoanagenesis will aid in the discovery of additional cooperating genetic alterations that facilitate the initiation of—or response to—chromoanagenesis. Such studies will also need to determine whether chromoanagenesis is more common in tumors with specific DNA damage signaling defects and to establish whether there is tissue-type or tumor-type context specificity in the mechanisms leading to chromoanagenesis.

Along with variation in the genetic makeup of individual tumors, emerging evidence points to the existence of considerable intratumoral genetic heterogeneity[49,50]. Establishing what fraction of cells in a given tumor possess complex chromosomal rearrangements and how this subpopulation evolves over time is now an important next step in understanding subclonal tumor architecture and the context-specific factors that determine tumor development after chromoanagenesis.

ACKNOWLEDGMENTS

We apologize to all whose work was not cited because of space restrictions. This work was supported by a grant (GM29513) from the US National Institutes of Health to D.W.C., who receives salary support from the Ludwig Institute for Cancer Research. A.J.H. is supported by a Leukemia & Lymphoma Society special fellowship.

COMPETING FINANCIAL INTERESTS

The authors declare no competing financial interests.

Published online at http://www.nature.com/doifinder/10.1038/nm.2988.
Reprints and permissions information is available online at http://www.nature.com/reprints/index.html.

1. Mitelman, F., Johansson, B. & Mertens, F. The impact of translocations and gene fusions on cancer causation. *Nat. Rev. Cancer* **7**, 233–245 (2007).
2. Stephens, P.J. *et al.* Complex landscapes of somatic rearrangement in human breast cancer genomes. *Nature* **462**, 1005–1010 (2009).
3. Campbell, P.J. *et al.* Identification of somatically acquired rearrangements in cancer using genome-wide massively parallel paired-end sequencing. *Nat. Genet.* **40**, 722–729 (2008).
4. Campbell, P.J. *et al.* The patterns and dynamics of genomic instability in metastatic pancreatic cancer. *Nature* **467**, 1109–1113 (2010).
5. Stephens, P.J. *et al.* Massive genomic rearrangement acquired in a single catastrophic event during cancer development. *Cell* **144**, 27–40 (2011).
6. Kloosterman, W.P. *et al.* Chromothripsis as a mechanism driving complex *de novo* structural rearrangements in the germline. *Hum. Mol. Genet.* **20**, 1916–1924 (2011).
7. Chiang, C. *et al.* Complex reorganization and predominant non-homologous repair following chromosomal breakage in karyotypically balanced germline rearrangements and transgenic integration. *Nat. Genet.* **44**, 390–397 (2012).
8. Liu, P. *et al.* Chromosome catastrophes involve replication mechanisms generating complex genomic rearrangements. *Cell* **146**, 889–903 (2011).
9. Kloosterman, W.P. *et al.* Constitutional chromothripsis rearrangements involve clustered double-stranded DNA breaks and nonhomologous repair mechanisms. *Cell Rep.* **1**, 648–655 (2012).
10. Eldredge, N. & Gould, S.J. Punctuated equilibria: an alternative to phyletic gradualism. *Models in Paleobiol.* **82**, 82–115 (1972).
11. Chen, J.M., Ferec, C. & Cooper, D.N. Transient hypermutability, chromothripsis and replication-based mechanisms in the generation of concurrent clustered mutations. *Mutat. Res.* **750**, 52–59 (2012).
12. Crasta, K. *et al.* DNA breaks and chromosome pulverization from errors in mitosis. *Nature* **482**, 53–58 (2012).
13. Gordon, D.J., Resio, B. & Pellman, D. Causes and consequences of aneuploidy in cancer. *Nat. Rev. Genet.* **13**, 189–203 (2012).
14. Holland, A.J. & Cleveland, D.W. Losing balance: the origin and impact of aneuploidy in cancer. *EMBO Rep.* **13**, 501–514 (2012).
15. Lengauer, C., Kinzler, K.W. & Vogelstein, B. Genetic instability in colorectal cancers. *Nature* **386**, 623–627 (1997).
16. Thompson, S.L. & Compton, D.A. Examining the link between chromosomal instability and aneuploidy in human cells. *J. Cell Biol.* **180**, 665–672 (2008).
17. Gascoigne, K.E. & Taylor, S.S. Cancer cells display profound intra- and interline variation following prolonged exposure to antimitotic drugs. *Cancer Cell* **14**, 111–122 (2008).
18. Hoffelder, D.R. *et al.* Resolution of anaphase bridges in cancer cells. *Chromosoma* **112**, 389–397 (2004).
19. Terradas, M., Martin, M., Hernandez, L., Tusell, L. & Genesca, A. Nuclear envelope defects impede a proper response to micronuclear DNA lesions. *Mutat. Res.* **729**, 35–40 (2012).
20. Terradas, M., Martin, M., Tusell, L. & Genesca, A. DNA lesions sequestered in micronuclei induce a local defective-damage response. *DNA Repair (Amst.)* **8**, 1225–1234 (2009).
21. Rao, P.N. & Johnson, R.T. Mammalian cell fusion: studies on the regulation of DNA synthesis and mitosis. *Nature* **225**, 159–164 (1970).
22. Johnson, R.T. & Rao, P.N. Mammalian cell fusion: induction of premature chromosome condensation in interphase nuclei. *Nature* **226**, 717–722 (1970).
23. Sperling, K. & Rao, P.N. The phenomenon of premature chromosome condensation: its relevance to basic and applied research. *Humangenetik* **23**, 235–258 (1974).
24. Meyerson, M. & Pellman, D. Cancer genomes evolve by pulverizing single chromosomes. *Cell* **144**, 9–10 (2011).
25. Holland, A.J. & Cleveland, D.W. Boveri revisited: chromosomal instability, aneuploidy and tumorigenesis. *Nat. Rev. Mol. Cell Biol.* **10**, 478–487 (2009).
26. Zhang, W., Peng, G., Lin, S.Y. & Zhang, P. DNA damage response is supressed by the high cyclin-dependent kinase 1 activity in mitotic mammalian cells. *J. Biol. Chem.* **286**, 35899–35905 (2011).
27. Janssen, A., van der Burg, M., Szuhai, K., Kops, G.J. & Medema, R.H. Chromosome segregation errors as a cause of DNA damage and structural chromosome aberrations. *Science* **333**, 1895–1898 (2011).
28. Tubio, J.M. & Estivill, X. Cancer: When catastrophe strikes a cell. *Nature* **470**, 476–477 (2011).
29. Tang, H.L. *et al.* Cell survival, DNA damage and oncogenic transformation following a transient and reversible apoptotic response. *Mol. Biol. Cell* **23**, 2240–2252 (2012).
30. Stanulla, M., Wang, J., Chervinsky, D.S., Thandla, S. & Aplan, P.D. DNA cleavage within the MLL breakpoint cluster region is a specific event which occurs as part of higher-order chromatin fragmentation during the initial stages of apoptosis. *Mol. Cell. Biol.* **17**, 4070–4079 (1997).
31. Stanulla, M., Chhalliyil, P., Wang, J., Jani-Sait, S.N. & Aplan, P.D. Mechanisms of MLL gene rearrangement: site-specific DNA cleavage within the breakpoint cluster region is independent of chromosomal context. *Hum. Mol. Genet.* **10**, 2481–2491 (2001).
32. Terradas, M., Martin, M., Tusell, L. & Genesca, A. Genetic activities in micronuclei: is the DNA entrapped in micronuclei lost for the cell? *Mutat. Res.* **705**, 60–67 (2010).
33. Rausch, T. *et al.* Genome sequencing of pediatric medulloblastoma links catastrophic DNA rearrangements with *TP53* mutations. *Cell* **148**, 59–71 (2012).
34. Kloosterman, W.P. *et al.* Chromothripsis is a common mechanism driving genomic rearrangements in primary and metastatic colorectal cancer. *Genome Biol.* **12**, R103 (2011).
35. Lieber, M.R. The mechanism of double-strand DNA break repair by the nonhomologous DNA end-joining pathway. *Annu. Rev. Biochem.* **79**, 181–211 (2010).
36. Lee, J.A., Carvalho, C.M. & Lupski, J.R.A. DNA replication mechanism for generating nonrecurrent rearrangements associated with genomic disorders. *Cell* **131**, 1235–1247 (2007).
37. Hastings, P.J., Ira, G. & Lupski, J.R. A microhomology-mediated break-induced replication model for the origin of human copy number variation. *PLoS Genet.* **5**, e1000327 (2009).
38. Bartkova, J. *et al.* Oncogene-induced senescence is part of the tumorigenesis barrier imposed by DNA damage checkpoints. *Nature* **444**, 633–637 (2006).
39. Di Micco, R. *et al.* Oncogene-induced senescence is a DNA damage response triggered by DNA hyper-replication. *Nature* **444**, 638–642 (2006).
40. Zhang, J. *et al.* The genetic basis of early T-cell precursor acute lymphoblastic leukaemia. *Nature* **481**, 157–163 (2012).
41. Wu, C. *et al.* Poly-gene fusion transcripts and chromothripsis in prostate cancer. *Genes Chromosom. Cancer* doi:10.1002/gcc.21999 (2012).

42. Northcott, P.A. *et al.* Subgroup-specific structural variation across 1,000 medulloblastoma genomes. *Nature* **488**, 49–56 (2012).
43. Magrangeas, F., Avet-Loiseau, H., Munshi, N.C. & Minvielle, S. Chromothripsis identifies a rare and aggressive entity among newly diagnosed multiple myeloma patients. *Blood* **118**, 675–678 (2011).
44. Molenaar, J.J. *et al.* Sequencing of neuroblastoma identifies chromothripsis and defects in neuritogenesis genes. *Nature* **483**, 589–593 (2012).
45. Wahl, G.M. The importance of circular DNA in mammalian gene amplification. *Cancer Res.* **49**, 1333–1340 (1989).
46. Mao, J.H. *et al. Fbxw7/Cdc4* is a p53-dependent, haploinsufficient tumour suppressor gene. *Nature* **432**, 775–779 (2004).
47. Kemp, Z. *et al. CDC4* mutations occur in a subset of colorectal cancers but are not predicted to cause loss of function and are not associated with chromosomal instability. *Cancer Res.* **65**, 11361–11366 (2005).
48. Kastan, M.B. & Bartek, J. Cell-cycle checkpoints and cancer. *Nature* **432**, 316–323 (2004).
49. Gerlinger, M. *et al.* Intratumor heterogeneity and branched evolution revealed by multiregion sequencing. *N. Engl. J. Med.* **366**, 883–892 (2012).
50. Yap, T.A., Gerlinger, M., Futreal, P.A., Pusztai, L. & Swanton, C. Intratumor heterogeneity: seeing the wood for the trees. *Sci. Transl. Med.* **4**, 127ps110 (2012).
51. Ganem, N.J., Godinho, S.A. & Pellman, D. A mechanism linking extra centrosomes to chromosomal instability. *Nature* **460**, 278–282 (2009).
52. Silkworth, W.T., Nardi, I.K., Scholl, L.M. & Cimini, D. Multipolar spindle pole coalescence is a major source of kinetochore mis-attachment and chromosome mis-segregation in cancer cells. *PLoS ONE* **4**, e6564 (2009).
53. Maher, C.A. & Wilson, R.K. Chromothripsis and human disease: piecing together the shattering process. *Cell* **148**, 29–32 (2012).

BRIEF COMMUNICATIONS

nature medicine

Identification of the molecular basis of doxorubicin-induced cardiotoxicity

Sui Zhang[1], Xiaobing Liu[2,3], Tasneem Bawa-Khalfe[1], Long-Sheng Lu[2], Yi Lisa Lyu[4], Leroy F Liu[4] & Edward TH Yeh[1,2]

Doxorubicin is believed to cause dose-dependent cardiotoxicity through redox cycling and the generation of reactive oxygen species (ROS). Here we show that cardiomyocyte-specific deletion of *Top2b* (encoding topoisomerase-IIβ) protects cardiomyocytes from doxorubicin-induced DNA double-strand breaks and transcriptome changes that are responsible for defective mitochondrial biogenesis and ROS formation. Furthermore, cardiomyocyte-specific deletion of *Top2b* protects mice from the development of doxorubicin-induced progressive heart failure, suggesting that doxorubicin-induced cardiotoxicity is mediated by topoisomerase-IIβ in cardiomyocytes.

Doxorubicin is still widely used in modern cancer treatments despite the advent of targeted therapy[1,2], but dose-dependent cardiotoxicity often limits its clinical use. Doxorubicin's cellular target is topoisomerase-II (Top2) (ref. 3). Doxorubicin binds both DNA and Top2 to form the ternary Top2-doxorubicin-DNA cleavage complex, which triggers cell death. There are two Top2 enzymes: Top2α and Top2β. Top2α, a known marker of cell proliferation, is overexpressed in tumors but is not detectable in quiescent tissues[4,5]. Top2α is thus thought to be the molecular basis of doxorubicin's anticancer activity.

Doxorubicin has been postulated to induce cardiotoxicity through redox cycling and ROS generation[6]. This ROS hypothesis, however, has been tempered by a series of studies in which treatment with a ROS scavenger failed to prevent cardiac toxicity caused by doxorubicin[7,8]. Thus, an alternative hypothesis is needed to explain doxorubicin-induced cardiotoxicity.

Adult mammalian cardiomyocytes express Top2β but no detectable Top2α[4]. Top2β is also a target for doxorubicin, and the Top2β-doxorubicin-DNA ternary cleavage complex can induce DNA double-strand breaks (DSBs), leading to cell death[9]. We hypothesized that Top2β may directly contribute to the development of doxorubicin-induced cardiomyopathy. In support of this hypothesis, Top2β-deleted mouse embryonic fibroblasts have been shown to be resistant to doxorubicin-induced cell death[9]. However, it is unknown whether Top2β is required for doxorubicin-induced cardiotoxicity or how the effects of doxorubicin on Top2β might lead to cardiac dysfunction.

To investigate the role of Top2β in doxorubicin-induced cardiac toxicity, we established a mouse model with cardiomyocyte-specific deletion of *Top2b* (α-MHC-MerCreMer-*Top2b*$^{flox/flox}$ mice). We crossed mice carrying a *loxP*-flanked *Top2b* allele (*Top2b*$^{flox/flox}$)[10] with mice carrying a myosin heavy chain promoter and a fusion protein containing Cre and mutated estrogen receptor (α-MHC-MerCreMer)[11]. The resulting α-MHC-MerCreMer-*Top2b*$^{flox/flox}$ mice were viable, fertile and normal in size, and did not display any gross physical or behavioral abnormalities (data not shown). We achieved cardiomyocyte-specific Cre induction by treating mice with tamoxifen (25 mg per kilogram of body weight by gavage, once a day for 5 consecutive days). Two weeks after the final dose of tamoxifen, we harvested the mouse hearts. We confirmed deletion of Top2β from cardiomyocytes by staining heart sections with an antibody to Top2β. Top2β protein was readily detectable in the nuclei of heart sections from a representative untreated α-MHC-MerCreMer-*Top2b*$^{flox/flox}$ (*Top2b*$^{+/+}$) mouse (**Supplementary Fig. 1a**). However, heart sections from tamoxifen-treated α-MHC-MerCreMer-*Top2b*$^{flox/flox}$ (*Top2b*$^{Δ/Δ}$) mice showed a marked reduction in the number of Top2β-positive nuclei. A reduction in Top2β expression was also detectable in whole–heart cell lysates by western blot analysis (**Supplementary Fig. 1b**). Because Cre expression is driven by a cardiomyocyte-specific promoter, endothelial cells and other stromal cells in the *Top2b*$^{Δ/Δ}$ mouse would still express Top2β. Top2β is apparently not required for normal homeostasis of adult hearts, as *Top2b*$^{Δ/Δ}$ mice survived for more than 10 months with no apparent pathology and with preserved ejection fractions (data not shown).

We used microarray-based Ingenuity Pathways Analysis (IPA) to study the effect of doxorubicin treatment in *Top2b*$^{+/+}$ and *Top2b*$^{Δ/Δ}$ mouse hearts in an unbiased way. We treated mice with doxorubicin (25 mg per kilogram of body weight by intraperitoneal injection (i.p.)) and killed them 16 h later. We prepared cardiomyocytes from excised hearts and extracted mRNA for microarray analysis. IPA of microarray data based on expression changes (>1.5-fold) in 59,306 genes upon doxorubicin treatment identified perturbation (mainly activation) of genes in the tumor suppressor protein p53 and β-adrenergic signaling pathways in *Top2b*$^{+/+}$ but not *Top2b*$^{Δ/Δ}$ cardiomyocytes (**Fig. 1a**, **Supplementary Fig. 2a** and **Supplementary Table 1**). We found no difference between *Top2b*$^{+/+}$ and *Top2b*$^{Δ/Δ}$ cardiomyocytes from untreated mice. Of particular note is that *Top2b*$^{+/+}$ cardiomyocytes from mice treated with doxorubicin showed a 200-fold upregulation of *Trp53inp1*, a p53-inducible gene that regulates apoptosis[12] (**Supplementary Fig. 2b**). We also observed increases in transcripts of *Apaf1*, *Bax* and *Fas*, genes important in the apoptotic pathway[13] (**Supplementary Fig. 2c**). Upregulation of *Trp53inp1*, *Apaf1*, *Bax*, *Mdm2* and *Fas* occurred in cardiomyocytes from doxorubicin-treated

[1]Department of Cardiology, The University of Texas MD Anderson Cancer Center, Houston, Texas, USA. [2]Texas Heart Institute at St. Luke's Episcopal Hospital, Houston, Texas, USA. [3]Department of Vascular Surgery, Ninth People's Hospital, Shanghai Jiao Tong University School of Medicine, Shanghai, China. [4]Department of Pharmacology, University of Medicine and Dentistry of New Jersey—Robert Wood Johnson Medical School, Piscataway, New Jersey, USA. Correspondence should be addressed to E.T.H.Y. (etyeh@mdanderson.org).

Received 6 June; accepted 7 August; published online 28 October 2012; doi:10.1038/nm.2919

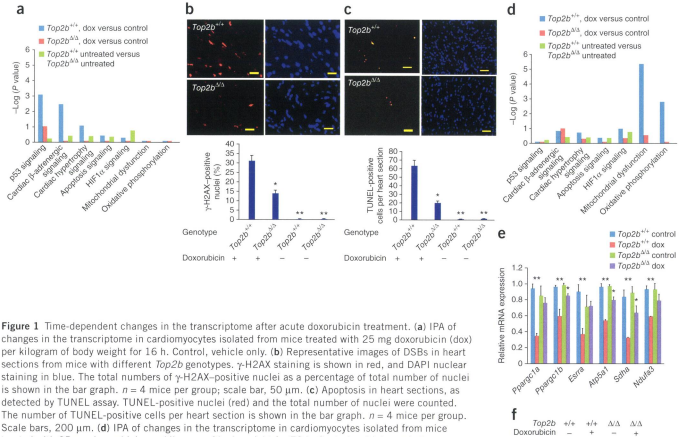

Figure 1 Time-dependent changes in the transcriptome after acute doxorubicin treatment. (**a**) IPA of changes in the transcriptome in cardiomyocytes isolated from mice treated with 25 mg doxorubicin (dox) per kilogram of body weight for 16 h. Control, vehicle only. (**b**) Representative images of DSBs in heart sections from mice with different *Top2b* genotypes. γ-H2AX staining is shown in red, and DAPI nuclear staining in blue. The total numbers of γ-H2AX–positive nuclei as a percentage of total number of nuclei is shown in the bar graph. $n = 4$ mice per group; scale bar, 50 μm. (**c**) Apoptosis in heart sections, as detected by TUNEL assay. TUNEL-positive nuclei (red) and the total number of nuclei were counted. The number of TUNEL-positive cells per heart section is shown in the bar graph. $n = 4$ mice per group. Scale bars, 200 μm. (**d**) IPA of changes in the transcriptome in cardiomyocytes isolated from mice treated with 25 mg doxorubicin per kilogram of body weight for 72 h. Control, vehicle control. (**e**) Quantitative RT-PCR validation of changes in the expression of selected genes involved in mitochondrial biogenesis and function. $n = 3$ mice per group. The mRNA expression levels of each gene were calculated by $2^{-\Delta\Delta Ct}$ (comparative threshold cycle; see Online Methods). Expression was normalized to mouse *Gapdh*. (**f**) Western blot analysis of Ndufa3, Atp5a and Sdha in mitochondria isolated from cardiomyocytes of the indicated genotypes. Cox4i1 was used as a loading control. One-way analysis of variance was used to determine statistical significance. $^*P < 0.05$; $^{**}P < 0.001$; error bars, mean ± s.e.m. (**b**,**c**,**e**).

Top2b$^{+/+}$ mice but not in cardiomyocytes from doxorubicin-treated *Top2b*$^{\Delta/\Delta}$ mice. This finding is consistent with the previous observation that doxorubicin and Top2β form a DNA ternary cleavage complex to induce DNA DSBs, leading to cell death[9].

We confirmed activation of the DNA damage response pathway in the heart by immunostaining for the DSB marker γ-H2AX[14]. The number of DSBs caused by doxorubicin was reduced by 60% in hearts from *Top2b*$^{\Delta/\Delta}$ compared to *Top2b*$^{+/+}$ mice (**Fig. 1b**). Furthermore, after acute doxorubicin treatment, there were 70% fewer apoptotic nuclei in the hearts of *Top2b*$^{\Delta/\Delta}$ as compared to *Top2b*$^{+/+}$ mice (**Fig. 1c**). Thus, Top2β expression correlates with the effects of doxorubicin on the transcriptome, DSBs and apoptosis in cardiomyocytes.

To gain further insight into the pathogenesis of doxorubicin-induced cardiotoxicity, we repeated the transcriptome analysis 72 h after doxorubicin exposure in cardiomyocytes of the treated mice. The IPA of microarray data based on expression changes (>1.5-fold) of 59,306 genes after doxorubicin treatment identified perturbation (mainly repression) in mitochondrial function and oxidative phosphorylation pathways in *Top2b*$^{+/+}$ cardiomyocytes but not in *Top2b*$^{\Delta/\Delta}$ cardiomyocytes (**Supplementary Table 2**). We found no difference between cardiomyocytes from untreated *Top2b*$^{+/+}$ and *Top2b*$^{\Delta/\Delta}$ mice. The IPA profile after doxorubicin treatment for 72 h was dramatically shifted compared to that observed after treatment for 16 h (**Fig. 1a**,**d**). Early activation of the p53 pathway was followed by repression of genes involved in mitochondrial dysfunction and oxidative phosphorylation pathways in *Top2b*$^{+/+}$ but not *Top2b*$^{\Delta/\Delta}$ cardiomyocytes (**Fig. 1a**,**d** and **Supplementary Table 2**). Both *Ppargc1a* and *Ppargc1b*, encoding the transcriptional coactivators PGC-1α and PGC-1β, were downregulated by 50% in *Top2b*$^{+/+}$ but not *Top2b*$^{\Delta/\Delta}$ hearts after doxorubicin treatment for 72 h. This was confirmed by quantitative PCR analysis of *Ppargc1a* and *Ppargc1b* transcripts (**Fig. 1e**). *Esrra*, a downstream target of PGC-1α, was also downregulated in doxorubicin-treated *Top2b*$^{+/+}$ but not *Top2b*$^{\Delta/\Delta}$ cardiomyocytes (**Fig. 1e**). Consistent with the crucial role exerted by PGC-1α and PGC-1β in mitochondrial biogenesis[15,16], the abundance of transcripts of genes involved in the electron transport chain, such as *Ndufa3* (encoding NADH dehydrogenase 1-α subcomplex, 3), *Sdha* (encoding succinate dehydrogenase complex II, subunit A) and *Atp5a1* (encoding ATP synthase subunit α (Atp5a)), was downregulated more strongly in doxorubicin-treated *Top2b*$^{+/+}$ cardiomyocytes than in doxorubicin-treated *Top2b*$^{\Delta/\Delta}$ cardiomyocytes (**Fig. 1e**). These effects were confirmed by measurements of protein abundance (**Fig. 1f**). Thus, in the presence of Top2β, doxorubicin decreases the transcription of genes involved in the regulation of mitochondrial biogenesis and function.

We next tested whether these effects on gene expression would have functional effects on mitochondria. We used JC-1, a lipophilic

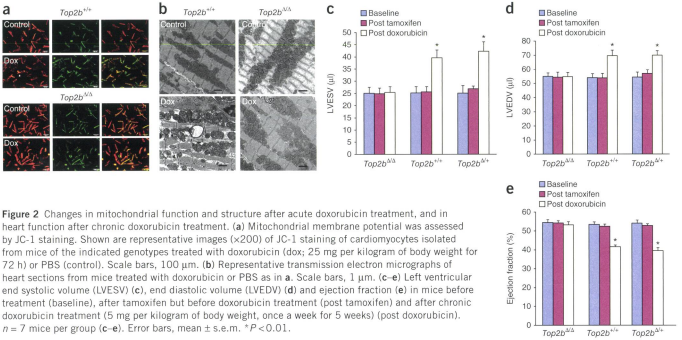

Figure 2 Changes in mitochondrial function and structure after acute doxorubicin treatment, and in heart function after chronic doxorubicin treatment. (**a**) Mitochondrial membrane potential was assessed by JC-1 staining. Shown are representative images (×200) of JC-1 staining of cardiomyocytes isolated from mice of the indicated genotypes treated with doxorubicin (dox; 25 mg per kilogram of body weight for 72 h) or PBS (control). Scale bars, 100 μm. (**b**) Representative transmission electron micrographs of heart sections from mice treated with doxorubicin or PBS as in **a**. Scale bars, 1 μm. (**c**–**e**) Left ventricular end systolic volume (LVESV) (**c**), end diastolic volume (LVEDV) (**d**) and ejection fraction (**e**) in mice before treatment (baseline), after tamoxifen but before doxorubicin treatment (post tamoxifen) and after chronic doxorubicin treatment (5 mg per kilogram of body weight, once a week for 5 weeks) (post doxorubicin). $n = 7$ mice per group (**c**–**e**). Error bars, mean ± s.e.m. *$P < 0.01$.

fluorochrome, to evaluate the status of the mitochondrial membrane potential in isolated cardiomyocytes. The monomeric form of JC-1 has an emission maximum of 529 nm (green), whereas JC-1 aggregates, which form at higher concentrations, have an emission maximum of 590 nm (red). The red/green fluorescence ratio is dependent on mitochondrial membrane potential but independent of the shape, density and size of mitochondria. We found that the red fluorescence was markedly reduced in doxorubicin-treated cardiomyocytes from $Top2b^{+/+}$ but not $Top2b^{\Delta/\Delta}$ mice (**Fig. 2a**). The FACS-based red/green ratio was 0.82 ± 0.12 in mitochondria from doxorubicin-treated $Top2b^{+/+}$ mice and 2.79 ± 0.43 in untreated $Top2b^{+/+}$ controls (s.e.m.; $n = 3$ mice per group). The red/green ratio in mitochondria from $Top2b^{\Delta/\Delta}$ mice was 2.09 ± 0.06 (doxorubicin-treated) versus 2.72 ± 0.18 (untreated control, $n = 3$). These results indicate that mitochondria fail to maintain their membrane potential in doxorubicin-treated $Top2b^{+/+}$ mice but not in doxorubicin-treated $Top2b^{\Delta/\Delta}$ cardiomyocytes. By electron microscopy, we observed marked mitochondrial damage and vacuolization in doxorubicin-treated $Top2b^{+/+}$ mouse hearts but minimal ultrastructural changes in similarly treated $Top2b^{\Delta/\Delta}$ hearts (**Fig. 2b**). We confirmed these ultrastructural changes by direct measurement of the oxygen consumption rate of cardiomyocytes *in vitro*. This rate was substantially reduced in cardiomyocytes from doxorubicin-treated $Top2b^{+/+}$ but not $Top2b^{\Delta/\Delta}$ mice (**Supplementary Fig. 3a**). Thus, Top2β is required for doxorubicin-induced ultrastructural and functional changes in cardiomyocyte mitochondria.

The functional and structural changes in mitochondria that occurred after doxorubicin exposure suggest that ROS generation is a result of changes in the transcriptome rather than redox cycling of doxorubicin as previously suggested. We next investigated generation of ROS in the hearts of doxorubicin-treated $Top2b^{+/+}$ and $Top2b^{\Delta/\Delta}$ mice. We detected ROS generation using dihydroethidium (DHE). Doxorubicin-induced ROS were reduced by 70% in the hearts of $Top2b^{\Delta/\Delta}$ as compared to $Top2b^{+/+}$ mice (**Supplementary Fig. 3b,c**), indicating that ROS generation is also dependent on Top2β.

To test the potential clinical relevance of the Top2β mouse model, we tested the effect of chronic administration of doxorubicin on left ventricular ejection fraction as measured by cardiac magnetic resonance imaging (MRI)[17]. Before Cre induction, we performed cardiac MRI scans of each mouse to record the baseline ejection fraction. We carried out cardiomyocyte-specific Cre induction by treating mice with tamoxifen. Two weeks after the final dose of tamoxifen, we performed another cardiac MRI scan to confirm that cardiac function had not been affected by the tamoxifen treatment. We began doxorubicin treatment (5 mg per kilogram of body weight, i.p., once a week for 5 weeks) 7 d after the second MRI scan. Two weeks after the final dose of doxorubicin, we performed a third MRI scan (**Supplementary Fig. 4a**).

End systolic and end diastolic volumes as determined by cardiac MRI were markedly increased in $Top2b^{+/+}$ and $Top2b^{+/\Delta}$ but not $Top2b^{\Delta/\Delta}$ mice after chronic doxorubicin exposure (**Fig. 2c**,**d**). Baseline ejection fractions were 53% in all three groups (**Fig. 2e**). Tamoxifen treatment did not significantly affect ejection fractions in any of the three groups, suggesting that Top2β is not required for the normal function of adult hearts. After 5 weeks of doxorubicin treatment, $Top2b^{+/+}$ and $Top2b^{+/\Delta}$ mice showed decreases in ejection fraction from 53% to 43%, whereas $Top2b^{\Delta/\Delta}$ mice showed no change in ejection fraction. These results indicate that Top2β is required for doxorubicin to induce a reduction in ejection fraction, a clinical hallmark of doxorubicin-induced cardiomyopathy.

We also studied hearts after 5 weeks of doxorubicin treatment. In doxorubicin-treated $Top2b^{+/+}$ mice, the abundance of transcripts of genes involved in mitochondrial biogenesis was decreased, ROS levels and fibrosis were increased and ultrastructural changes in mitochondria were observed; these effects were less severe in doxorubicin-treated $Top2b^{\Delta/\Delta}$ hearts (**Supplementary Fig. 4b**–**e**). Thus, Top2β-dependent cardiac pathology is similar in acute and chronic treatment models.

Our results suggest that doxorubicin-induced cardiotoxicity is not solely due to redox cycling of doxorubicin. Specifically, our findings implicate Top2β as an essential driver of doxorubicin-induced cardiotoxicity. In the presence of Top2β, doxorubicin activates the DNA response and apoptosis pathways and triggers a marked alteration in the transcriptome that selectively affects oxidative phosphorylation and mitochondrial biogenesis in cardiomyocytes. Our results also

provide an alternative explanation for the classical observation that doxorubicin causes both structural and functional mitochondrial abnormalities[18]. These effects could be due to downregulation of both *Ppargc1a* and *Ppargc1b*, which are crucial for mitochondrial biogenesis and function. Because inhibition or poisoning of Top2β by Top2-directed anticancer drugs (for example, doxorubicin) leads to activation of the DNA damage response, it is possible that DNA damage responses activate p53 to suppress *Ppargc1* transcription, leading to defective mitochondrial biogenesis and metabolic failure[19]. It is also possible that doxorubicin-mediated inhibition or poisoning of Top2β could suppress transcription in a p53-independent manner. Top2β has been shown to be recruited to hormone promoters to regulate transcription[20]. Indeed, we found that Top2β in the presence of doxorubicin bound avidly to the promoters of *Ppargc1a* and *Ppargc1b* in both mouse atrial cardiomyocyte cells (HL-1) and isolated adult mouse cardiomyocytes (**Supplementary Fig. 5**). The binding of the Top2β-doxorubicin complex to the promoters of *Ppargc1a* and *Ppargc1b* is likely to be responsible for blocking transcription, but definitive evidence for this will require additional studies. Taken together, these results indicate that *Top2b* is required to initiate the entire cardiotoxicity cascade.

The implications of our findings are twofold. First, drugs that specifically target the Top2α isozyme, but not Top2β, should be less cardiotoxic and, hence, more useful clinically. This conclusion is based on the assumption that Top2β does not contribute significantly to doxorubicin's tumoricidal activity. Second, patients with higher expression of Top2β in cardiomyocytes may be more susceptible to doxorubicin-induced cardiotoxicity. These predictions can be tested in animals and humans.

METHODS

Methods and any associated references are available in the online version of the paper.

Accession codes. Microarray data have been deposited in the Gene Expression Omnibus (GEO) database with the accession code GSE40289.

Note: Supplementary information is available in the online version of the paper.

ACKNOWLEDGMENTS

We thank C.H. Ren for expert technical assistance and F.M. Lin and H. Dou for conducting studies on mitochondria DNA. W.C. Claycomb (Louisiana State University Health Science Center) provided HL-1 cells. This study is supported by the Cancer Prevention Research Institute of Texas and McNair Medical Institute (E.T.H.Y.), US National Institutes of Health grant CA102463 (to L.F.L.), the New Jersey Commission on Cancer Research Grant 06-2419-CCR-EO, US Department of Defense Idea Award W81XWH-07-1-0407 and Concept Award W81XWH06-1-0514 (to Y.L.L.).

AUTHOR CONTRIBUTIONS

E.T.H.Y. and L.F.L. conceived the project. S.Z., X.L., T.B.-K., L.-S.L. and Y.L.L. performed experiments and data analysis. E.T.H.Y. and S.Z. wrote the manuscript with editorial input from L.F.L. and Y.L.L.

COMPETING FINANCIAL INTERESTS

The authors declared no competing financial interests.

Published online at http://www.nature.com/doifinder/10.1038/nm.2919.
Reprints and permissions information is available online at http://www.nature.com/reprints/index.html.

1. Yeh, E.T. & Bickford, C.L. *J. Am. Coll. Cardiol.* **53**, 2231–2247 (2009).
2. Force, T. & Kolaja, K.L. *Nat. Rev. Drug Discov.* **10**, 111–126 (2011).
3. Tewey, K.M., Rowe, T.C., Yang, L., Halligan, B.D. & Liu, L.F. *Science* **226**, 466–468 (1984).
4. Capranico, G., Tinelli, S., Austin, C.A., Fisher, M.L. & Zunino, F. *Biochim. Biophys. Acta* **1132**, 43–48 (1992).
5. Lyu, Y.L. *et al. Mol. Cell. Biol.* **26**, 7929–7941 (2006).
6. Singal, P.K. & Iliskovic, N. *N. Engl. J. Med.* **339**, 900–905 (1998).
7. Myers, C. *et al. Semin. Oncol.* **10**, 53–55 (1983).
8. Martin, E. *et al. Toxicology* **255**, 72–79 (2009).
9. Lyu, Y.L. *et al. Cancer Res.* **67**, 8839–8846 (2007).
10. Lyu, Y.L. & Wang, J.C. *Proc. Natl. Acad. Sci. USA* **100**, 7123–7128 (2003).
11. Sohal, D.S. *et al. Circ. Res.* **89**, 20–25 (2001).
12. Okamura, S. *et al. Mol. Cell* **8**, 85–94 (2001).
13. Ogasawara, J. *et al. Nature* **364**, 806–809 (1993).
14. Plesca, D., Mazumder, S. & Almasan, A. *Methods Enzymol.* **446**, 107–122 (2008).
15. Arany, Z. *et al. Proc. Natl. Acad. Sci. USA* **103**, 10086–10091 (2006).
16. Lai, L. *et al. Genes Dev.* **22**, 1948–1961 (2008).
17. Wang, J. *et al. Circ. Res.* **106**, 1904–1911 (2010).
18. Wallace, K.B. *Pharmacol. Toxicol.* **93**, 105–115 (2003).
19. Sahin, E. *et al. Nature* **470**, 359–365 (2011).
20. Ju, B.G. *et al. Science* **312**, 1798–1802 (2006).

nature medicine

The sirtuin SIRT6 blocks IGF-Akt signaling and development of cardiac hypertrophy by targeting c-Jun

Nagalingam R Sundaresan[1], Prabhakaran Vasudevan[2], Lei Zhong[3], Gene Kim[4], Sadhana Samant[1], Vishwas Parekh[2], Vinodkumar B Pillai[1], P V Ravindra[1], Madhu Gupta[5], Valluvan Jeevanandam[1], John M Cunningham[2], Chu-Xia Deng[6], David B Lombard[7], Raul Mostoslavsky[3] & Mahesh P Gupta[1]

Abnormal activation of insulin-like growth factor (IGF)-Akt signaling is implicated in the development of various diseases, including heart failure. However, the molecular mechanisms that regulate activation of this signaling pathway are not completely understood. Here we show that sirtuin 6 (SIRT6), a nuclear histone deacetylase, functions at the level of chromatin to directly attenuate IGF-Akt signaling. SIRT6-deficient mice developed cardiac hypertrophy and heart failure, whereas SIRT6 transgenic mice were protected from hypertrophic stimuli, indicating that SIRT6 acts as a negative regulator of cardiac hypertrophy. SIRT6-deficient mouse hearts showed hyperactivation of IGF signaling–related genes and their downstream targets. Mechanistically, SIRT6 binds to and suppresses the promoter of IGF signaling–related genes by interacting with c-Jun and deacetylating histone 3 at Lys9 (H3K9). We also found reduced SIRT6 expression in human failing hearts. These findings disclose a new link between SIRT6 and IGF-Akt signaling and implicate SIRT6 in the development of cardiac hypertrophy and failure.

Heart failure is the leading contributor of human morbidity and mortality in the developed world[1]. Although a number of risk factors have been recognized for heart failure, the molecular mechanisms contributing to the initiation of heart failure are incompletely understood[2]. Recent studies have demonstrated that heart failure can be prevented or reverted, at least in experimental models, by caloric restriction, a dietary regimen that limits calorie intake[3–5].

The health benefits of calorie restriction are thought to be mediated by a family of NAD-dependent deacetylases called sirtuins. The mammalian genome encodes seven ubiquitously expressed sirtuin isoforms (SIRT1–SIRT7), which are emerging as key regulators of a myriad of biological functions, ranging from cell growth to lifespan extension[6]. Among the sirtuins, SIRT6, a chromatin-associated deacetylase, is considered to have a leading role in regulating genomic stability, cellular metabolism, stress response and aging[7–12]. SIRT6 deacetylates H3K9 and acts as a transcriptional co-repressor of NF-κB and hypoxia inducible factor-1α (HIF-1α) target genes in a tissue- and context-dependent manner[8,10,13]. SIRT6-deficient mice show severe hypoglycemia and a multisystemic accelerated aging phenotype and die at around 26 d after birth[12]. The hypoglycemia of SIRT6-deficient mice seems to result from increased activity of HIF-1α target genes and increased glucose uptake by multiple organs[13,14]. However, neither correction of hypoglycemia by feeding mice with glucose nor reduced NF-κB signaling could completely rescue the lethality of SIRT6-deficient mice, suggesting that additional mechanisms must contribute to the mutant phenotype of SIRT6-deficient mice[8,14].

Mammalian aging and aging-associated diseases have been shown to be associated with dysregulation of IGF-Akt signaling[15]. In the heart, although short-term activation of IGF-Akt signaling promotes physiologic growth, sustained hyperactivation leads to the development of pathologic hypertrophy and heart failure[16,17]. Although much is known about the positive activators of this pathway, very little is known about the endogenous negative regulators, which might have potential to block the IGF-Akt pathway and protect the heart from developing heart failure.

In this study, we show that SIRT6 directly controls IGF-Akt signaling at the level of chromatin through c-Jun, a stress-responsive transcription factor, and deacetylation of H3K9. Our findings also demonstrate that SIRT6 deficiency induces hyperactivation of IGF-Akt signaling, which culminates in the development of cardiac hypertrophy and heart failure in mice.

RESULTS

Loss of SIRT6 induces cardiac hypertrophy and failure

To study the role of SIRT6 in the development of heart failure, we first analyzed SIRT6 expression in failing human hearts and in mouse hearts in which we had induced hypertrophy by either surgically creating transverse aortic constriction (TAC) or infusing the hypertrophic agonists

[1]Department of Surgery, Committee on Cellular and Molecular Physiology, University of Chicago, Chicago, Illinois, USA. [2]Department of Pediatrics, Committee on Developmental Biology, University of Chicago, Chicago, Illinois, USA. [3]The Massachusetts General Hospital Cancer Center, Harvard Medical School, Boston, Massachusetts, USA. [4]Department of Medicine, Section of Cardiology, University of Chicago, Chicago, Illinois, USA. [5]Department of Physiology and Biophysics, University of Illinois at Chicago, Chicago, Illinois, USA. [6]National Institute of Diabetes, Digestive and Kidney Diseases, US National Institutes of Health, Bethesda, Maryland, USA. [7]Department of Pathology and Institute of Gerontology, University of Michigan, Ann Arbor, Michigan, USA. Correspondence should be addressed to M.P.G. (mgupta@surgery.bsd.uchicago.edu).

Received 2 April; accepted 29 August; published online 21 October 2012; doi:10.1038/nm.2961

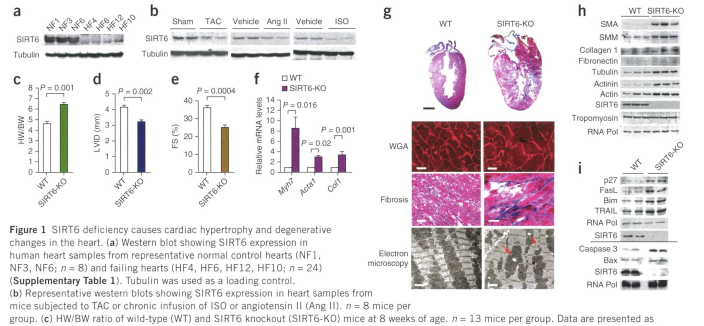

Figure 1 SIRT6 deficiency causes cardiac hypertrophy and degenerative changes in the heart. (**a**) Western blot showing SIRT6 expression in human heart samples from representative normal control hearts (NF1, NF3, NF6; $n = 8$) and failing hearts (HF4, HF6, HF12, HF10; $n = 24$) (**Supplementary Table 1**). Tubulin was used as a loading control. (**b**) Representative western blots showing SIRT6 expression in heart samples from mice subjected to TAC or chronic infusion of ISO or angiotensin II (Ang II). $n = 8$ mice per group. (**c**) HW/BW ratio of wild-type (WT) and SIRT6 knockout (SIRT6-KO) mice at 8 weeks of age. $n = 13$ mice per group. Data are presented as means ± s.d. (**d**,**e**) Left ventricular internal diameter (LVID; $n = 7$ mice per group) and fractional shortening (FS; $n = 10$ mice per group) of WT and SIRT6 knockout mice at 8 weeks of age as determined by echocardiography. Data are presented as means ± s.d. (**f**) mRNA levels of the indicated genes in heart samples of WT and SIRT6 knockout mice. $n = 6$ mice per group. Data are presented as the mean ± s.d. For **c**–**f**, Student's t test was used to calculate the P values. (**g**) Whole-heart sections stained with H&E showing concentric hypertrophy in SIRT6 knockout hearts (top row; scale bar, 2 mm); left ventricular muscle sections stained with wheat germ agglutinin (WGA) to demarcate cell boundaries (second row; scale bars, 10 μm) or Masson's trichrome to detect fibrosis (third row; scale bars, 40 μm); and electron micrographs showing vacuolization (red arrows) and degeneration of mitochondria in SIRT6 knockout hearts (bottom row; scale bars, 1 μm). (**h**,**i**) Representative western blots showing the expression of the indicated fibrosis markers, cytoskeletal proteins and apoptotic markers in WT and SIRT6 knockout hearts. $n = 6$ per group. The line between the blots indicates two different gels. RNA Pol, RNA polymerase; SMA, α-smooth muscle actin; SMM, smooth muscle myosin.

isoproterenol (ISO) or angiotensin-II (Ang-II). In both human and mouse hearts, SIRT6 amounts were markedly reduced compared to control hearts (**Fig. 1a**,**b** and **Supplementary Table 1**), suggesting that SIRT6 deficiency is associated with the development of cardiac hypertrophy and failure. To test whether SIRT6 deficiency contributes to heart disease, we analyzed hearts of SIRT6 whole-body knockout mice. SIRT6 knockout mice on an inbred genetic (129sv) background die at around 26 d of age[12], whereas SIRT6 knockout mice on crossbred genetic backgrounds survive for up to 1 year[14]. We therefore analyzed crossbred SIRT6 knockout mice(129sv/C57BL6) for this study. These crossbred SIRT6 knockout mice spontaneously developed concentric cardiac hypertrophy at around 8–12 weeks of age with a significantly increased heart weight to body weight (HW/BW) ratio, reduced left ventricular internal diameter and reduced fractional shortening (**Fig. 1c**–**e**). SIRT6 knockout hearts also showed increased expression of cardiac fetal genes, increased cardiomyocyte size and interstitial fibrosis (**Fig. 1f**,**g**). These hearts also showed severe degenerative changes, including aggregation and vacuolization of mitochondria (**Fig. 1g**). SIRT6 knockout hearts also expressed higher levels of aging-associated cytoskeleton proteins[18] such as actin, actinin and tubulin; fibrotic markers such as α-smooth muscle actin, myosin, collagen-1 and fibronectin; and apoptotic markers such as caspase 3, Bax, TRAIL, Bim, FasL and p27 (**Fig. 1h**,**i**), which are signs of a failing heart.

To test whether a partial reduction in SIRT6 expression, as seen in human failing hearts (**Supplementary Fig. 1a**), could be sufficient to induce heart failure, we analyzed the hearts of *SIRT6*$^{+/-}$ heterozygous mice. Young *SIRT6*$^{+/-}$ mice showed no noticeable cardiac defects; however, at around 6 months of age, they spontaneously developed characteristics of pathologic cardiac hypertrophy, such as increased HW/BW and heart weight to tibia length (HW/TL) ratios, increased cardiomyocyte size and interstitial fibrosis (**Supplementary Fig. 1b**–**d**), suggesting that reduced expression of SIRT6 can contribute to the development of cardiac hypertrophy.

To study the cardiac-specific effects of SIRT6, we used a tamoxifen-inducible α-myosin heavy chain (α-MHC)-Cre system to delete SIRT6 in the hearts of adult mice (**Supplementary Fig. 2**). Cardiac-specific deletion of SIRT6 resulted in a significantly increased HW/TL ratio, increased left ventricular wall thickness, increased cardiomyocyte cross-sectional area and induction of interstitial fibrosis (**Fig. 2a**–**c**). Echocardiography of these mice revealed significantly reduced cardiac contractile function (**Fig. 2d**). In addition, cardiac-specific SIRT6-deleted hearts had increased expression of fetal genes and cell death markers (**Fig. 2e**,**f**). We obtained similar results by analyzing hearts of mice in which SIRT6 was deleted both in the skeletal and cardiac muscles by use of the MCK-Cre system (N.R.S., D.B.L. and M.P.G., unpublished data). These data demonstrate that SIRT6 is an endogenous negative regulator of cardiac hypertrophy.

SIRT6 activation blocks development of cardiac hypertrophy

We first examined the effect of SIRT6 overexpression in an *in vitro* model of cardiomyocyte hypertrophy. We infected neonatal rat cardiomyocytes with either a control vector or a vector expressing SIRT6 (**Supplementary Fig. 3a**,**b**). SIRT6-overexpressing cells had a dampened hypertrophic response to phenylephrine treatment based on analysis of protein synthesis, atrial natriuretic factor (ANF) release from nuclei and sarcomere organization, which are hallmarks of cardiomyocyte hypertrophy (**Fig. 3a**,**b**). These results indicate an antihypertrophic effect of SIRT6 in cardiomyocytes.

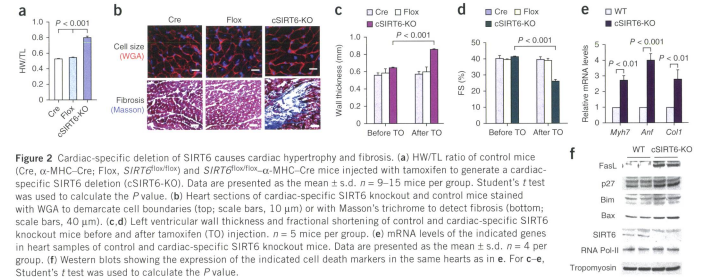

Figure 2 Cardiac-specific deletion of SIRT6 causes cardiac hypertrophy and fibrosis. (**a**) HW/TL ratio of control mice (Cre, α-MHC–Cre; Flox, *SIRT6*$^{flox/flox}$) and *SIRT6*$^{flox/flox}$–α-MHC–Cre mice injected with tamoxifen to generate a cardiac-specific SIRT6 deletion (cSIRT6-KO). Data are presented as the mean ± s.d. $n = 9$–15 mice per group. Student's t test was used to calculate the P value. (**b**) Heart sections of cardiac-specific SIRT6 knockout and control mice stained with WGA to demarcate cell boundaries (top; scale bars, 10 μm) or with Masson's trichrome to detect fibrosis (bottom; scale bars, 40 μm). (**c**,**d**) Left ventricular wall thickness and fractional shortening of control and cardiac-specific SIRT6 knockout mice before and after tamoxifen (TO) injection. $n = 5$ mice per group. (**e**) mRNA levels of the indicated genes in heart samples of control and cardiac-specific SIRT6 knockout mice. Data are presented as the mean ± s.d. $n = 4$ per group. (**f**) Western blots showing the expression of the indicated cell death markers in the same hearts as in **e**. For **c**–**e**, Student's t test was used to calculate the P value.

To evaluate the antihypertrophic effects of SIRT6 *in vivo*, we generated cardiac-specific SIRT6 transgenic mice (**Supplementary Fig. 3c**). At baseline, SIRT6 transgenic mice had no noticeable cardiac abnormalities. We induced cardiac hypertrophy in these mice by either surgically creating TAC or infusing ISO into the abdomen. Nontransgenic mice subjected to TAC for 4 weeks developed massive cardiac hypertrophy, as indicated by an increased HW/TL ratio, increased left ventricular wall thickness and decreased fractional shortening (**Fig. 3c**–**e**). These changes were accompanied by an increased cardiomyocyte cross-sectional area and induction of fibrosis (**Fig. 3f**,**g**). Notably, the hearts of SIRT6 transgenic mice did not undergo similar pathological growth after being subjected to TAC (**Fig. 3c**–**g**). We found similar cardioprotective effects of SIRT6 overexpression in the ISO model of cardiac hypertrophy (**Supplementary Fig. 3d**–**g**). These data indicate that SIRT6 overexpression is capable of blocking the development of pathologic cardiac hypertrophy.

SIRT6 antagonizes IGF signaling

SIRT6 knockout mice on the 129Sv genetic background develop severe hypoglycemia and hypoinsulinemia, which is mediated through alterations in HIF-1α activity[13,14]. To test whether such metabolic changes contribute to the cardiac phenotype we observed

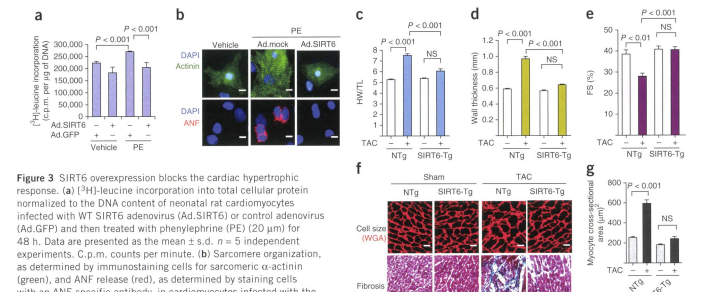

Figure 3 SIRT6 overexpression blocks the cardiac hypertrophic response. (**a**) [^{3}H]-leucine incorporation into total cellular protein normalized to the DNA content of neonatal rat cardiomyocytes infected with WT SIRT6 adenovirus (Ad.SIRT6) or control adenovirus (Ad.GFP) and then treated with phenylephrine (PE) (20 μm) for 48 h. Data are presented as the mean ± s.d. $n = 5$ independent experiments. C.p.m. counts per minute. (**b**) Sarcomere organization, as determined by immunostaining cells for sarcomeric α-actinin (green), and ANF release (red), as determined by staining cells with an ANF-specific antibody, in cardiomyocytes infected with the indicated adenoviruses (Ad.mock indicates empty vector) and stimulated with phenylephrine. DAPI stain marks the position of nuclei. Scale bars, 10 μm. (**c**) HW/TL ratios in nontransgenic (NTg) and SIRT6 transgenic (SIRT6-Tg) mice subjected to sham or to TAC treatment for 4 weeks. Data are presented as the mean ± s.d. $n = 8$ mice per group. (**d**,**e**) Left ventricular wall thickness and fractional shortening, as measured by echocardiography, of the same hearts as in **c**. $n = 6$ mice per group. For **c**–**e**, one-way analysis of variance (ANOVA) was applied to calculate the P value. (**f**) Heart sections of nontransgenic and SIRT6 transgenic mice subjected to sham or TAC treatment and stained with WGA to demarcate cell boundaries (top; scale bars, 10 μm) or Masson's trichrome to detect fibrosis (bottom; scale bars, 40 μm). (**g**) Quantification of myocyte cross-sectional area in nontransgenic and SIRT6 transgenic mice subjected to sham or to TAC treatment. Data are presented as the mean ± s.d. $n = 5$ mice per group. Student's t test was used to calculate the P value. NS, not significant.

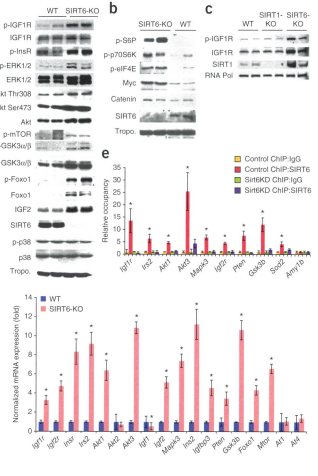

Figure 4 SIRT6 is a negative regulator of IGF signaling. (**a**) Representative western blots showing increased expression and phosphorylation of IGF signaling–related proteins in SIRT6 knockout hearts compared to WT control hearts. The expression of p38 and tropomyosin (tropo.) were not changed in these hearts and were therefore used as loading controls. $n = 6$ mice per group. The antibodies used for detecting ERK and GSK3 recognized the ERK1/2 and GSK3α/β isoforms, respectively. The 'p-' prefix indicates the phosphorylated form. (**b**) Representative western blots showing increased expression of transcription and translation factors in SIRT6 knockout hearts. $n = 6$ mice per group. (**c**) Representative western blots showing expression of IGF1R, p-IGF1R and SIRT1 in heart lysates of WT, SIRT1 knockout and SIRT6 knockout mice. $n = 3$ mice per group. (**d**) Real-time PCR analysis of IGF signaling–related genes in heart samples of WT and SIRT6 knockout mice. $n = 6$ mice per group. (**e**) ChIP analysis to detect SIRT6 binding to the promoters of the indicated genes performed with a SIRT6-specific antibody or IgG control antibody in WT or SIRT6 knockdown (Sirt6KD) cardiomyocytes. The occupancy of SIRT6 to promoters is shown relative to background signals with IgG control antibody. $n = 4$ independent experiments. Data are presented as the mean ± s.d. Student's t test was applied to calculate the P value. $^*P < 0.001$.

in SIRT6-deficient mice, we analyzed myocardial glucose uptake, serum insulin and blood glucose concentrations and the expression of HIF-1α target glycolytic genes, previously shown to be regulated by SIRT6. We found no change in glucose uptake in the hearts of SIRT6 knockout mice (**Supplementary Fig. 4a**). We also noted no statistically significant variation in blood glucose or insulin concentrations in these mice (**Supplementary Fig. 4b,c**). Western blot analysis revealed that expression of the HIF-1α target genes *PFK1*, *TPI1* and *GAPDH* were unchanged in SIRT6 knockout hearts (**Supplementary Fig. 4d**). In addition, we found no noticeable changes in the expression of mitochondrial superoxide dismutase 2 (MnSOD) and glutathione *S*-transferase (GST), which have previously been shown to be targeted by the transcription factor NF-κB (**Supplementary Fig. 4d**). These findings indicate that the development of heart failure in SIRT6 knockout mice is not mediated by alterations in either systemic glucose homeostasis or activation of HIF-1α or NF-κB signaling in the heart.

We next tested whether effects on IGF-Akt signaling might underlie the cardiac phenotype of SIRT6 knockout mice. SIRT6 knockout hearts had substantially increased amounts of proteins (and/or phosphoproteins) related to this pathway, including IGF1 receptor (IGF1R), insulin receptor (InsR), extracellular signal-regulated kinase 1 (ERK1)/ERK2, Akt, forkhead box O1 (Foxo1), glycogen synthase kinase 3 (GSK3) and IGF2 (**Fig. 4a** and **Supplementary Fig. 4e**). The amount of membrane-bound IGF2 was also increased in SIRT6 knockout hearts (**Supplementary Fig. 4f**). We also noted that failing human hearts had higher amounts of IGF1R and phosphorylated Akt expression compared to controls; similarly, hypertrophic mouse hearts in the TAC and ISO models had increased expression of these proteins compared to control hearts (**Supplementary Fig. 4g,h**). Additionally, SIRT6 knockout hearts showed increased expression of transcription and translation factors acting downstream of IGF signaling, including Myc, β-catenin, eukaryotic translation initiation factor 4E (eIF4E), S6P and p70S6K (**Fig. 4b**). However, SIRT6 knockout hearts did not show increased expression of p38 or tropomyosin, which served as loading controls (**Fig. 4a,b**). Conversely, the expression and phosphorylation of IGF signaling–related proteins were attenuated in SIRT6-overexpressing transgenic hearts (**Supplementary Fig. 5a**). These data indicate that induction of cardiac hypertrophy in SIRT6-deficient hearts might be related to hyperactivation of IGF-Akt signaling–related proteins.

Because SIRT6-deficient mice develop a multiorgan aging phenotype, we asked whether the effect of SIRT6 on IGF signaling is limited to the heart or is a more widespread phenomenon. We first analyzed the effects of nicotinamide (NAM), a general inhibitor of sirtuins, and trichostatin A (TSA), a class I and II histone deacetylase (HDAC) inhibitor. Treatment with NAM, but not TSA, increased the expression and phosphorylation of IGF1R in three different cells (adult mouse cardiac fibroblasts and 3T3L and Cos7 cells) analyzed, indicative of the involvement of a sirtuin in IGF1R activation (**Supplementary Fig. 5b**). We next analyzed the effects of SIRT6 deficiency in mouse embryonic fibroblasts (MEFs). As in the heart, SIRT6 knockout MEFs showed hyperactivation of IGF signaling–related proteins (**Supplementary Fig. 5c**). SIRT6 knockdown in 293T cells using retroviral vectors targeting SIRT6 had a similar effect (**Supplementary Fig. 5d**). To confirm these findings, we performed a reconstitution experiment in which we re-expressed SIRT6 in SIRT6 knockout cells. Re-expression of wild-type SIRT6, but not a SIRT6 mutant lacking deacetylase activity, attenuated IGF1R activation in SIRT6 knockout MEFs (**Supplementary Fig. 5e**), indicating that SIRT6-dependent regulation of IGF signaling is not limited to the heart. We also tested whether deficiency of other sirtuins present in the nucleus, such as SIRT1, can activate IGF1R. However, IGF1R activation occurred in SIRT6 knockout but not in SIRT1 knockout hearts (**Fig. 4c**). We have recently shown that Akt membrane localization and activation are under the control of SIRT1 (ref. 19). SIRT6 knockout hearts, in which Akt was activated, showed markedly increased expression of SIRT1 (**Fig. 4c**), which might be needed for mediating Akt activation in these hearts. Taken together, these findings indicate that SIRT6 has a central role in regulating IGF-Akt signaling.

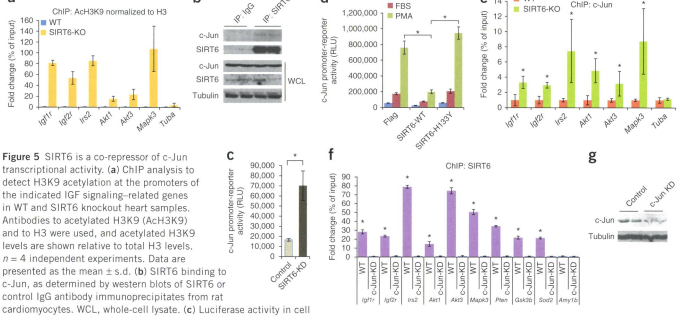

Figure 5 SIRT6 is a co-repressor of c-Jun transcriptional activity. (**a**) ChIP analysis to detect H3K9 acetylation at the promoters of the indicated IGF signaling–related genes in WT and SIRT6 knockout heart samples. Antibodies to acetylated H3K9 (AcH3K9) and to H3 were used, and acetylated H3K9 levels are shown relative to total H3 levels. $n = 4$ independent experiments. Data are presented as the mean ± s.d. (**b**) SIRT6 binding to c-Jun, as determined by western blots of SIRT6 or control IgG antibody immunoprecipitates from rat cardiomyocytes. WCL, whole-cell lysate. (**c**) Luciferase activity in cell extracts from control or SIRT6 knockdown (SIRT6-KD) 293T cells transfected with a c-Jun–dependent luciferase reporter plasmid. $n = 5$ independent experiments. Data are presented as the mean ± s.d. RLU, relative light units. Student's t test was applied to calculate the P value, $^*P < 0.001$. (**d**) Luciferase activity in rat cardiomyocytes cotransfected with the c-Jun–dependent luciferase reporter plasmid and plasmids expressing WT SIRT6 (SIRT6-WT) or mutant SIRT6 (SIRT6-H133Y); the cells were serum starved overnight and induced with FBS or with the c-Jun activator phorbol 12-myristate 13-acetate (PMA). $n = 8$ independent experiments. Data are presented as the mean ± s.d. ANOVA was applied to calculate the P value. $^*P < 0.001$. (**e**) ChIP analysis using a c-Jun–specific antibody to detect c-Jun occupancy at promoters of IGF signaling–related genes in WT or SIRT6 knockout mouse heart homogenates. $n = 4$ independent experiments. Data are presented as the mean ± s.d. $^*P < 0.001$ compared to WT (Student's t test). (**f**) ChIP analysis using a SIRT6-specific antibody to detect SIRT6 occupancy at the promoters of the indicated genes in control (WT) and c-Jun knockdown (c-Jun-KD) rat cardiomyocytes. SIRT6 occupancy at the promoters is shown relative to the background signal with IgG control antibody. $^*P < 0.001$ (Student's t test). $n = 4$ independent experiments. Data are presented as the mean ± s.d. (**g**) Western blots showing c-Jun knockdown in rat cardiomyocytes.

SIRT6 blocks IGF signaling by deacetylating H3K9

Because SIRT6 is a chromatin-associated deacetylase, we posited that it could directly influence the expression of IGF signaling–related genes by modifying chromatin. To test this hypothesis, we used available microarray data from the skeletal muscle of SIRT6 knockout mice[13]. The results of a clustering analysis using these data suggested that SIRT6 deficiency substantially increased the expression of key IGF signaling–related genes, including *Igf2*, *Igf2r*, *Foxo1*, *Igf1r*, *Mapk3*, *Pten*, *Gsk3*, *Irs2*, *Akt3* and *Ins2* (**Supplementary Fig. 6a**), whereas the expression of other such genes, including *Ins1* and *Igf1*, was down regulated (**Supplementary Fig. 6b**). To test whether similar changes also take place in the heart, we performed real-time PCR. In SIRT6 knockout hearts, the mRNA levels of key IGF signaling–related genes, including *Igf1r*, *Igf2r*, *Insr*, *Irs2*, *Akt1*, *Akt3*, *Igf2*, *Mapk3*, *Ins2*, *Igfbp3*, *Pten*, *Gsk3b*, *Foxo1* and *Mtor*, were significantly upregulated, whereas *Igf1* was downregulated (**Fig. 4d**). The expression of *Akt2*, an IGF signaling–related gene, and *At1* and *At4*, which are unrelated to IGF signaling, were unchanged (**Fig. 4d**), indicating that SIRT6 deficiency specifically induces certain IGF signaling genes rather than nonspecifically activating the cellular transcription machinery. By chromatin immunoprecipitation (ChIP), we found that SIRT6 binds to promoters of IGF signaling–related genes in cardiomyocytes, and knockdown of SIRT6 reduced its binding to these promoters (**Fig. 4e** and **Supplementary Fig. 6c**), indicating the specificity of SIRT6 binding to these genes.

SIRT6 deacetylates H3K9 and thereby regulates gene expression by modifying chromatin structure[10]. We therefore asked whether SIRT6 deficiency results in increased H3K9 acetylation in the promoters of upregulated IGF signaling–related genes. ChIP analysis revealed increased acetylation of H3K9 in SIRT6-deficient cells compared to wild-type control cells (**Fig. 5a** and **Supplementary Fig. 7a**). However, acetylation of H3K14 was not increased, which served as a negative control (**Supplementary Fig. 7b,c**). These data demonstrate that SIRT6 directly suppresses the expression of key IGF signaling–related genes by deacetylating H3K9 at their promoters.

SIRT6 suppresses the transcriptional activity of c-Jun

To search for a transcription factor that could be targeted by SIRT6 and that might regulate the expression of IGF signaling–related genes, we performed an *in silico* analysis and identified an evolutionarily conserved c-Jun binding site in the promoters of IGF signaling–related genes (**Supplementary Fig. 8**). c-Jun is a stress-responsive subunit of the AP-1 transcription factor[20]. Supporting the potential role of c-Jun in SIRT6 function, we found marked changes in the expression levels of well-known AP-1 target genes in SIRT6 knockout skeletal muscle based on the available microarray data[13] (**Supplementary Fig. 9a**). We found that SIRT6 was bound to AP-1 target genes by ChIP analysis (**Supplementary Fig. 9 b**) and that SIRT6 physically interacts with c-Jun in cardiomyocytes (**Fig. 5b** and **Supplementary Fig. 10a**), consistent with the idea that SIRT6 is a regulator of c-Jun–dependent gene transcription. We next tested the effect of SIRT6 on the transcriptional activity of c-Jun, as assessed by a luciferase reporter assay using a reporter construct carrying multiple c-Jun binding sites. This assay indicated that SIRT6 knockdown

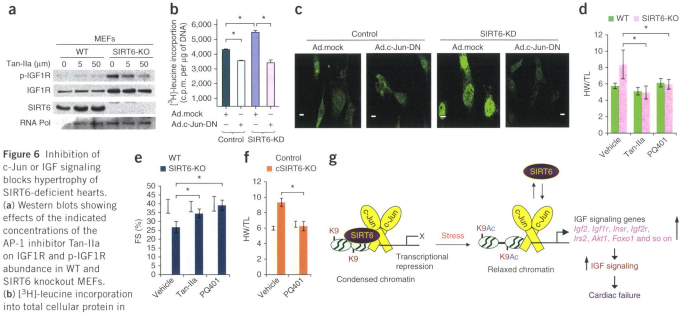

Figure 6 Inhibition of c-Jun or IGF signaling blocks hypertrophy of SIRT6-deficient hearts. (**a**) Western blots showing effects of the indicated concentrations of the AP-1 inhibitor Tan-IIa on IGF1R and p-IGF1R abundance in WT and SIRT6 knockout MEFs. (**b**) [3H]-leucine incorporation into total cellular protein in control and SIRT6 knockdown neonatal rat cardiomyocytes infected with control (Ad.mock) or c-Jun dominant-negative (Ad.c-Jun-DN) adenovirus vectors. Data are presented as the mean ± s.d. $n = 6$–8 independent experiments. $^*P < 0.001$ (Student's t test). (**c**) Confocal imaging of ANF in the same group of cardiomyocytes as in **b**. Scale bars, 10 μm. (**d**,**e**) HW/TL ratio (**d**) and fractional shortening (FS) (**e**) of WT and SIRT6 knockout mice injected with vehicle, the AP-1 inhibitor Tan-IIa or the IGF1R inhibitor PQ401 for 2 weeks. $n = 6$–9 mice per group. Data are presented as the mean ± s.d. $^*P < 0.001$ (ANOVA). (**f**) HW/TL ratio of control (*Sirt6*$^{flox/flox}$) and cardiac-specific SIRT6 knockout mice injected with vehicle or the IGF1R inhibitor PQ401 for 2 weeks. $n = 6$ mice per group. Data are presented as the mean ± s.d. $^*P < 0.001$ (Student's t test). (**g**) Under normal conditions, SIRT6 inhibits the expression of IGF signaling–related genes by deacetylating histones and repressing c-Jun activity, thereby restraining IGF signaling. Under pathological stress, cardiac SIRT6 expression is reduced, leading to increased acetylation of H3K9 (K9Ac) at the promoters of IGF signaling genes and c-Jun–mediated transcriptional activation. Increased expression of multiple IGF-Akt signaling–related genes leads to the development of cardiac hypertrophy, fibrosis and heart failure.

enhanced the transcriptional activity of endogenous c-Jun (**Fig. 5c** and **Supplementary Fig. 10b**). Moreover, wild-type SIRT6, but not a catalytic mutant (H133Y SIRT6), attenuated the transcriptional activity of c-Jun (**Fig. 5d** and **Supplementary Fig. 10c**), suggesting that the deacetylase activity of SIRT6 is needed for attenuating c-Jun–dependent gene transcription. As assessed by ChIP analysis using a c-Jun–specific antibody, c-Jun was bound to the promoters of IGF signaling–related genes and loss of SIRT6 enhanced the binding of c-Jun to target promoters (**Fig. 5e** and **Supplementary Fig. 10d**,**e**), indicating that the enhanced transcriptional activity of c-Jun in SIRT6-deficient cells contributes to the increased expression of IGF signaling–related genes.

We next asked whether loss of c-Jun affects the occupancy of SIRT6 at promoters of IGF signaling–related genes. Knockdown of c-Jun significantly reduced SIRT6 occupancy at these promoters (**Fig. 5f**,**g** and **Supplementary Fig. 10f**), indicating that SIRT6 is specifically recruited to these promoters by forming a complex with c-Jun.

Inhibition of c-Jun or IGF-Akt signaling blocks cardiac hypertrophy

Having shown that SIRT6 deficiency activates c-Jun–dependent transcription, we next asked whether inhibition of c-Jun could block the hypertrophy of SIRT6-deficient cardiomyocytes. Inhibition of c-Jun in SIRT6 knockout MEFs by treating them with an AP-1–specific inhibitor, tanshinone IIa (Tan-IIa)[21], for 24 h led to decreased expression and phosphorylation of IGF1R in a concentration-dependent manner (**Fig. 6a**). The compound did not have this effect in wild-type cells (**Fig. 6a**). We next inhibited c-Jun function using an adenovirus expressing a dominant-negative version of c-Jun, which, when infected into cardiomyocytes, blocked the activity of endogenous c-Jun (**Supplementary Fig. 11a**). The hypertrophic response of SIRT6-deficient cardiomyocytes, as measured by [3H]-leucine incorporation into total cellular protein, expression of ANF and sarcomere reorganization, was completely blocked by c-Jun inhibition (**Fig. 6b**,**c** and **Supplementary Fig. 11b**,**c**). These effects were associated with reduced phosphorylation of IGF1R and reduced mRNA expression of key IGF signaling–related genes, such as *Igf2*, *Igf1r* and *Irs2* (**Supplementary Fig. 11d**,**e**), suggesting that the hypertrophy of SIRT6-deficient cardiomyocytes can be attributed to the increased transcriptional activity of c-Jun. Confirming these findings, we found that Tan-IIa treatment also blocked the hypertrophic response of SIRT6-deficient cardiomyocytes (**Supplementary Fig. 12a**,**b**). Administration of Tan-IIa to SIRT6 knockout mice blocked the cardiac hypertrophic response *in vivo* (**Fig. 6d**,**e** and **Supplementary Fig. 13a**–**c**), and this effect was associated with inhibition of *Igf2* and fetal gene expression (**Supplementary Fig. 13d**). These data demonstrate that SIRT6 deficiency induces cardiac hypertrophy through hyperactivation of c-Jun.

To obtain evidence that cardiac hypertrophy of SIRT6-deficient cells results from c-Jun–dependent hyperactivation of IGF-Akt signaling, we performed a series of rescue experiments using specific inhibitors of IGF-Akt signaling. Treatment of SIRT6-deficient cardiomyocytes with PQ401, a pharmacological inhibitor of IGF signaling, significantly ($P < 0.001$) blocked hypertrophy of cardiomyocytes (sarcomeric reorganization, ANF release, protein synthesis and NFAT (nuclear factor of activated T cells) promoter activity) (**Supplementary Fig. 12b**–**e**). Knockdown of IGF1R expression using siRNA had similar effects (**Supplementary Fig. 14a**–**e**). An Akt inhibitor, Akt-v (triciribine)[19], also blocked the hypertrophic

response of SIRT6-deficient cardiomyocytes (**Supplementary Fig. 12b,d–f**). To test whether inhibition of IGF signaling could block the cardiac hypertrophy of SIRT6 knockout mice *in vivo*, we treated these mice with PQ401 for 14 d. PQ401 treatment of SIRT6 knockout mice prevented the increase in the HW/TL ratio and the cross-sectional area of cardiomyocytes, with significant improvement in contractile function, which was associated with reduced activation of IGF-Akt signaling (**Fig. 6d,e** and **Supplementary Fig. 15a–c**). Treatment of cardiac-specific SIRT6-deleted mice with PQ401 had similar effects (**Fig. 6f** and **Supplementary 15d,e**). From these studies, we conclude that hyperactivation of IGF-Akt signaling contributes to the development of cardiac hypertrophy and heart failure in SIRT6-deficient mice.

DISCUSSION

In this study, we identify a direct link between two evolutionarily conserved nutrient-sensitive signaling pathways, the insulin/IGF and sirtuin pathways, which are widely implicated in pathophysiological conditions. Our data show that IGF signaling–related genes are negatively regulated by SIRT6 at the level of chromatin. SIRT6 deficiency enhanced H3K9 acetylation and augmented the promoter binding and transcriptional activity of c-Jun, which resulted in hyperactivation of multiple IGF signaling–related genes and the development of cardiac hypertrophy and failure.

Hyperactivation of signaling by insulin and the IGF family of growth factors has been implicated in the pathophysiology of many diseases, including cancer[22], diabetes[23], obesity[23], musculoskeletal disease[24] and neurodegenerative disease[25]. Dysregulation of insulin/IGF signaling has been also reported in human end-stage failing hearts[26]. In SIRT6-deficient hearts, most of the key components of insulin/IGF signaling pathways, including IGF1R, InsR, IGF2R, IGF2, IRS2, MAPK3 and Akt, were overexpressed, but IGF1 was not. In fact, IGF1 expression was downregulated in SIRT6 knockout hearts, consistent with previous reports in which low circulating IGF1 concentrations were found in SIRT6 knockout mice[12–14]. We also found increased amounts of membrane-bound IGF2 in SIRT6 knockout hearts, suggesting that membrane-associated IGF2 might drive constant IGF signaling, contributing to the development of cardiac hypertrophy, despite low cardiac expression of IGF1. IGF2 acts on multiple receptors, including, IGF1R, IGF2R and InsR, to promote the development of pathologic cardiac hypertrophy and tumorigenesis[27,28]. Consistent with our data, transgenic mice overexpressing IGF2 have cardiac structural changes that reflect heart failure[29]. We found that PTEN mRNA, a suppressor of IGF signaling, was modestly upregulated in SIRT6 knockout cardiomyocytes, raising the question of why increased PTEN expression was unable to block hyperactive IGF signaling in SIRT6 knockout hearts. From these studies, we deduce that SIRT6 has a major role in regulating the expression of IGF signaling–related genes and that dysregulation of this pathway might contribute to the pathophysiology of several diseases, including heart failure.

Mechanistically, SIRT6 blocks the expression of IGF signaling–related genes through its ability to suppress the transcriptional activity of c-Jun (**Fig. 6g**). c-Jun is a subunit of the transcription factor AP-1, which regulates cell proliferation, differentiation and apoptosis[20]. c-Jun is involved in the development of the embryonic heart[30], whereas in the adult heart, c-Jun activation leads to hypertrophy and subsequent failure[31–36]. Transgenic mice with whole-body c-Jun overexpression develop tumors of multiple organs leading to death of the mice[29]. Elevated expression of c-Jun has also been reported during aging[37]. Growth factors and oxidative stress promote the transcriptional activity of c-Jun, whereas dietary restriction antagonizes it[37,38]. In our *in silico* analysis, we found evolutionarily conserved c-Jun binding sites in several insulin/IGF signaling–related gene promoters, suggesting that these genes are probably regulated by a c-Jun–dependent transcription mechanism. Consistent with this, a previous report has shown that c-Jun has a crucial role in the regulation of *Igf2* expression[6]. In addition to IGF signaling–related genes, it is also possible that other c-Jun targets participate in the development of pathologic cardiac hypertrophy in SIRT6 knockout mice. In particular, as we found increased expression of many proapoptotic and prohypertrophic genes in SIRT6 knockout hearts (*Trail*, *Bim*, *P27*, *Myc* and *Ctnnb1* (β-catenin)), a role of these factors in the cardiac hypertrophy of these mice cannot be excluded. However, inhibition of IGF signaling was sufficient to block the cardiac hypertrophic response in SIRT6 knockout mice, suggesting that IGF signaling has a major role in this response. Notably, we did not find upregulation of previously identified HIF-1α–targeted glycolytic genes, suggesting that SIRT6 deficiency–induced cardiac failure is not mediated through HIF-1α.

The expression of IGF2 is also regulated by genomic imprinting[28]. In the present study, two different findings argue against the loss of genomic imprinting as the cause of *Igf2* activation in SIRT6 knockout cells. First, other genes that were upregulated in SIRT6 knockout cells, such as *Igf1r*, *Akt*, *Gsk3* and *Mapk3*, are not controlled by genomic imprinting. Second, *IGF2* activation was blocked by inhibiting c-Jun. Thus, it seems that activation of c-Jun is the mechanism responsible for SIRT6-mediated activation of IGF signaling–related genes and the development of cardiac hypertrophy.

In many previous studies, lifespan extension in response to caloric restriction has been linked with the activation of sirtuins and a reduction in IGF-Akt signaling[4,6]. Among the seven members of the sirtuin family, SIRT1, SIRT3 and SIRT6 have been shown to be activated in response to caloric restriction[39–41]. However, recent studies have shown that SIRT1 deacetylates and activates Akt and thereby promotes cardiac hypertrophy and tumorigenesis in mice[42], casting doubt on the idea that SIRT1 promotes longevity. The activation of SIRT3 has been linked to an extension of lifespan in humans[28]. Although, the underlying mechanism of the antiaging effect of SIRT3 is not known, growing evidence suggests that SIRT3 might promote longevity by facilitating mitochondrial function[42] and blocking cellular oxidative stress[43]. Our data show that the SIRT6 sirtuin directly controls IGF-Akt signaling, supporting the idea that SIRT6 is capable of promoting longevity. Consistent with our findings, it was recently reported that SIRT6-overexpressing transgenic male mice that had an extended lifespan had reduced IGF signaling[44]. From these studies, it can be concluded that SIRT6 has an important role in controlling pro-growth and pro-aging IGF-Akt signaling in mammals.

Other HDACs, particularly class II HDACs, are capable of blocking the cardiac hypertrophic response. These HDACs function by shuttling in and out of the nucleus as needed to protect the heart from hypertrophic stimuli[45]. This mechanism does not apply to the negative regulatory effects of SIRT6, as we found no evidence of SIRT6 export from the nucleus during the hypertrophy of cardiomyocytes. Instead, SIRT6 levels were substantially reduced in failing human and mouse hearts in which IGF-Akt signaling was hyperactivated, suggesting that loss of SIRT6 contributes to the development of heart failure. This finding raises the possibility that low levels of SIRT6 expression might be a risk factor for heart failure in humans. In summary, this study demonstrates that the nuclear sirtuin SIRT6 directly

controls the expression of insulin/IGF-Akt signaling–related genes at the level of chromatin and, hence, the development of cardiac hypertrophy and heart failure.

METHODS

Methods and any associated references are available in the online version of the paper.

Note: Supplementary information is available in the online version of the paper.

ACKNOWLEDGMENTS

We thank F. Alt, Harvard Medical School, for providing SIRT6 knockout mice, E. Verdin, University of California, San Francisco, for providing Flag-SIRT6 wild-type and mutant plasmids, F. VanGool, Institut de Biologie, Universite Libre de Bruxelles, Gosselies, Belgium, for providing mouse-SIRT6 expression plasmid and K. Chua, Stanford University, for providing SIRT6 retroviral vectors and SIRT6 knockout MEFs. The α-MHC promoter vector used to make cardiac-specific SIRT6 transgenic mice was provided by J. Robbins, University of Cincinnati. This study was supported by US National Institutes of Health grants RO1 HL-117041, HL-83423 and 111455 to M.P.G. N.R.S. was supported by a postdoctoral fellowship from the American Heart Association.

AUTHOR CONTRIBUTIONS

N.R.S. and M.P.G. designed the study and wrote the manuscript. N.R.S. performed the majority of experiments. P.V. performed the ChIP experiments. L.Z. analyzed tissue microarray data. G.K. did echocardiography of mice. S.S. analyzed human samples and performed electron microscopy. V.P. performed *in silico* analysis and identified c-Jun target genes. V.B.P. performed experiments with IGF1R inhibitors. P.V.R. generated transgenic mice and did *in vitro* hypertrophy experiments. M.G. analyzed cardiac fetal gene program and cell death markers. V.J. provided human cardiac tissue samples during surgery. J.M.C. planned and supervised ChIP experiments. C.-X.D. provided *Sirt6*^{loxP} mice. D.B.L. provided heart samples from SIRT6-MCK-Cre mice and participated in discussing experiments. R.M. provided microarray data and discussed the whole study multiple times. M.P.G. coordinated with different investigators, supervised the whole study and generated the final draft of the manuscript.

COMPETING FINANCIAL INTERESTS

The authors declare no competing financial interests.

Published online at http://www.nature.com/doifinder/10.1038/nm.2961.
Reprints and permissions information is available online at http://www.nature.com/reprints/index.html.

1. Lloyd-Jones, D. *et al.* Heart disease and stroke statistics—2010 update: a report from the American Heart Association. *Circulation* **121**, e46–e215 (2010).
2. Donmez, G. & Guarente, L. Aging and disease: connections to sirtuins. *Aging Cell* **9**, 285–290 (2010).
3. Kahn, A.J. Development, aging, and life duration: effects of nutrient restriction. *Am. J. Clin. Nutr.* **25**, 822–828 (1972).
4. Fontana, L., Partridge, L. & Longo, V.D. Extending healthy life span—from yeast to humans. *Science* **328**, 321–326 (2010).
5. Weiss, E.P. & Fontana, L. Caloric restriction: powerful protection for the aging heart and vasculature. *Am. J. Physiol. Heart Circ. Physiol.* **301**, H1205–H1219 (2011).
6. Haigis, M.C. & Guarente, L.P. Mammalian sirtuins—emerging roles in physiology, aging, and calorie restriction. *Genes Dev.* **20**, 2913–2921 (2006).
7. Kanfi, Y. *et al.* SIRT6 protects against pathological damage caused by diet-induced obesity. *Aging Cell* **9**, 162–173 (2010).
8. Kawahara, T.L. *et al.* SIRT6 links histone H3 lysine 9 deacetylation to NF-κB-dependent gene expression and organismal life span. *Cell* **136**, 62–74 (2009).
9. Kim, H.S. *et al.* Hepatic-specific disruption of SIRT6 in mice results in fatty liver formation due to enhanced glycolysis and triglyceride synthesis. *Cell Metab.* **12**, 224–236 (2010).
10. Michishita, E. *et al.* SIRT6 is a histone H3 lysine 9 deacetylase that modulates telomeric chromatin. *Nature* **452**, 492–496 (2008).
11. Michishita, E., Park, J.Y., Burneskis, J.M., Barrett, J.C. & Horikawa, I. Evolutionarily conserved and nonconserved cellular localizations and functions of human SIRT proteins. *Mol. Biol. Cell* **16**, 4623–4635 (2005).
12. Mostoslavsky, R. *et al.* Genomic instability and aging-like phenotype in the absence of mammalian SIRT6. *Cell* **124**, 315–329 (2006).
13. Zhong, L. *et al.* The histone deacetylase Sirt6 regulates glucose homeostasis via Hif1α. *Cell* **140**, 280–293 (2010).
14. Xiao, C. *et al.* SIRT6 deficiency results in severe hypoglycemia by enhancing both basal and insulin-stimulated glucose uptake in mice. *J. Biol. Chem.* **285**, 36776–36784 (2010).
15. Holzenberger, M. *et al.* IGF-1 receptor regulates lifespan and resistance to oxidative stress in mice. *Nature* **421**, 182–187 (2003).
16. Matsui, T. *et al.* Phenotypic spectrum caused by transgenic overexpression of activated Akt in the heart. *J. Biol. Chem.* **277**, 22896–22901 (2002).
17. Matsui, T., Nagoshi, T. & Rosenzweig, A. Akt and PI 3-kinase signaling in cardiomyocyte hypertrophy and survival. *Cell Cycle* **2**, 220–223 (2003).
18. Kostin, S., Hein, S., Arnon, E., Scholz, D. & Schaper, J. The cytoskeleton and related proteins in the human failing heart. *Heart Fail. Rev.* **5**, 271–280 (2000).
19. Sundaresan, N.R. *et al.* The deacetylase SIRT1 promotes membrane localization and activation of Akt and PDK1 during tumorigenesis and cardiac hypertrophy. *Sci. Signal.* **4**, ra46–ra58 (2011).
20. Hess, J., Angel, P. & Schorpp-Kistner, M. AP-1 subunits: quarrel and harmony among siblings. *J. Cell Sci.* **117**, 5965–5973 (2004).
21. Chiu, Y.C. *et al.* Peptidoglycan enhances IL-6 production in human synovial fibroblasts via TLR2 receptor, focal adhesion kinase, Akt, and AP-1–dependent pathway. *J. Immunol.* **183**, 2785–2792 (2009).
22. Gallagher, E.J. & LeRoith, D. The proliferating role of insulin and insulin-like growth factors in cancer. *Trends Endocrinol. Metab.* **21**, 610–618 (2010).
23. Gatenby, V.K. & Kearney, M.T. The role of IGF-1 resistance in obesity and type 2 diabetes-mellitus-related insulin resistance and vascular disease. *Expert Opin. Ther. Targets* **14**, 1333–1342 (2010).
24. Glass, D.J. PI3 kinase regulation of skeletal muscle hypertrophy and atrophy. *Curr. Top. Microbiol. Immunol.* **346**, 267–278 (2010).
25. Freude, S., Schilbach, K. & Schubert, M. The role of IGF-1 receptor and insulin receptor signaling for the pathogenesis of Alzheimer's disease: from model organisms to human disease. *Curr. Alzheimer Res.* **6**, 213–223 (2009).
26. Haq, S. *et al.* Differential activation of signal transduction pathways in human hearts with hypertrophy versus advanced heart failure. *Circulation* **103**, 670–677 (2001).
27. Chu, C.H. *et al.* Activation of insulin-like growth factor II receptor induces mitochondrial-dependent apoptosis through Goq and downstream calcineurin signaling in myocardial cells. *Endocrinology* **150**, 2723–2731 (2009).
28. Chua, B.H. & D'Amore, P.A. IGF2 epigenetic regulation and role in development and disease. *Cytokine Growth Factor Rev.* **19**, 111–120 (2008).
29. Zaina, S. *et al.* Shortened life span, bradycardia, and hypotension in mice with targeted expression of an Igf2 transgene in smooth muscle cells. *Endocrinology* **144**, 2695–2703 (2003).
30. Eferl, R. *et al.* Functions of c-Jun in liver and heart development. *J. Cell Biol.* **145**, 1049–1061 (1999).
31. Schunkert, H., Jahn, L., Izumo, S., Apstein, C.S. & Lorell, B.H. Localization and regulation of c-fos and c-jun protooncogene induction by systolic wall stress in normal and hypertrophied rat hearts. *Proc. Natl. Acad. Sci. USA* **88**, 11480–11484 (1991).
32. Iwaki, K., Sukhatme, V.P., Shubeita, H.E. & Chien, K.R. α- and β-adrenergic stimulation induces distinct patterns of immediate early gene expression in neonatal rat myocardial cells. fos/jun expression is associated with sarcomere assembly; Egr-1 induction is primarily an α 1–mediated response. *J. Biol. Chem.* **265**, 13809–13817 (1990).
33. Takemoto, Y. *et al.* Increased JNK, AP-1 and NF-κB DNA binding activities in isoproterenol-induced cardiac remodeling. *J. Mol. Cell. Cardiol.* **31**, 2017–2030 (1999).
34. Nadruz, W. Jr., Corat, M.A., Marin, T.M., Guimaraes Pereira, G.A. & Franchini, K.G. Focal adhesion kinase mediates MEF2 and c-Jun activation by stretch: role in the activation of the cardiac hypertrophic genetic program. *Cardiovasc. Res.* **68**, 87–97 (2005).
35. Reiss, K. *et al.* ANG II receptors, c-myc, and c-jun in myocytes after myocardial infarction and ventricular failure. *Am. J. Physiol.* **264**, H760–H769 (1993).
36. Freire, G., Ocampo, C., Ilbawi, N., Griffin, A.J. & Gupta, M. Overt expression of AP-1 reduces α myosin heavy chain expression and contributes to heart failure from chronic volume overload. *J. Mol. Cell. Cardiol.* **43**, 465–478 (2007).
37. Kim, H.J. *et al.* Modulation of redox-sensitive transcription factors by calorie restriction during aging. *Mech. Ageing Dev.* **123**, 1589–1595 (2002).
38. Jung, K.J. *et al.* Effect of short term calorie restriction on pro-inflammatory NF-κB and AP-1 in aged rat kidney. *Inflamm. Res.* **58**, 143–150 (2009).
39. Cohen, H.Y. *et al.* Calorie restriction promotes mammalian cell survival by inducing the SIRT1 deacetylase. *Science* **305**, 390–392 (2004).
40. Kanfi, Y. *et al.* Regulation of SIRT6 protein levels by nutrient availability. *FEBS Lett.* **582**, 543–548 (2008).
41. Hirschey, M.D. *et al.* SIRT3 regulates mitochondrial fatty-acid oxidation by reversible enzyme deacetylation. *Nature* **464**, 121–125 (2010).
42. Sundaresan, N.R. *et al.* The deacetylase SIRT1 promotes membrane localization and activation of Akt and PDK1 during tumorigenesis and cardiac hypertrophy. *Sci. Signal.* **4**, ra46 (2011).
43. Sundaresan, N.R. *et al.* Sirt3 blocks the cardiac hypertrophic response by augmenting Foxo3a-dependent antioxidant defense mechanisms in mice. *J. Clin. Invest.* **119**, 2758–2771 (2009).
44. Kanfi, Y. *et al.* The sirtuin SIRT6 regulates lifespan in male mice. *Nature* **483**, 218–221 (2012).
45. Zhang, C.L. *et al.* Class II histone deacetylases act as signal-responsive repressors of cardiac hypertrophy. *Cell* **110**, 479–488 (2002).

nature medicine

Vascular niche E-selectin regulates hematopoietic stem cell dormancy, self renewal and chemoresistance

Ingrid G Winkler[1], Valérie Barbier[1], Bianca Nowlan[2], Rebecca N Jacobsen[2,3], Catherine E Forristal[2], John T Patton[4], John L Magnani[4] & Jean-Pierre Lévesque[2,3]

The microenvironment, or niche, surrounding a stem cell largely governs its cellular fate. Two anatomical niches for hematopoietic stem cells (HSCs) have been reported in the bone marrow, but a distinct function for each of these niches remains unclear. Here we report a new role for the adhesion molecule E-selectin expressed exclusively by bone marrow endothelial cells in the vascular HSC niche. HSC quiescence was enhanced and self-renewal potential was increased in E-selectin knockout (*Sele*$^{-/-}$) mice or after administration of an E-selectin antagonist, demonstrating that E-selectin promotes HSC proliferation and is a crucial component of the vascular niche. These effects are not mediated by canonical E-selectin ligands. Deletion or blockade of E-selectin enhances HSC survival threefold to sixfold after treatment of mice with chemotherapeutic agents or irradiation and accelerates blood neutrophil recovery. As bone marrow suppression is a severe side effect of high-dose chemotherapy, transient blockade of E-selectin is potentially a promising treatment for the protection of HSCs during chemotherapy or irradiation.

HSCs reside in the bone marrow and generate the cells needed to replenish the blood and immune system. This process requires tight regulation, with instructions provided by cues within specific local microenvironments (niches). At least two anatomical HSC niches have been described in the bone marrow: an endosteal or osteoblastic niche within 2–3 cell diameters from the bone–bone marrow interface[1–5] and an endothelial or (peri-)vascular niche adjacent to bone marrow endothelial sinuses[6–9]. Whether these two anatomically defined niches have separate functions, and the degree to which factors at these niches control HSC behavior, is under intense investigation[10]. The identification of functional components unique to each of these niches would greatly contribute to these investigations.

Endothelial selectins are cell adhesion molecules that are expressed at the vascular HSC niche to which hematopoietic stem and progenitor cells (HSPCs) adhere. The selectins are a family of three cell adhesion molecules with well-characterized roles in leukocyte homing. E-selectin (endothelial selectin) and P-selectin (platelet selectin) are typically expressed by endothelial cells at sites of injury or inflammation, enabling leukocytes with counter-receptors to roll on the activated vasculature[11]. Consistent with this function, leukocytes in mice deficient for both E- and P-selectin (or their functional receptors) have severely impaired leukocyte migration[12,13]. However P- and E-selectin are constitutively expressed on bone marrow endothelium[14–16], aiding the homing and engraftment of circulating HSPCs[17,18]. Here we demonstrate an additional role for E-selectin in steady-state hematopoiesis. We show that E-selectin on the bone marrow vasculature directly induces HSC proliferation and chemosensitivity at the expense of HSC self renewal.

RESULTS

HSCs cycle slower when E-selectin is absent in mice

To determine whether the absence of endothelial selectins alters HSC quiescence, we first measured HSC turnover in wild-type (WT) and E-selectin knockout (*Sele*$^{-/-}$) mice by BrdU incorporation *in vivo*. BrdU is a thymidine analog that is incorporated into genomic DNA during the S phase of cell division. After BrdU administration, we harvested bone marrow cells from the mice and measured the percentage of phenotypic Lin$^-$Kit$^+$Sca1$^+$ (LKS$^+$) CD34$^-$ HSCs[19] that had incorporated BrdU. The percentage of HSCs incorporating BrdU steadily increased over time, with 50% of the HSCs in WT mice incorporating BrdU and entering S phase by 3.3 d *in vivo* (**Fig. 1a–c**). HSC turnover was markedly reduced in *Sele*$^{-/-}$ mice and in mice with knockout alleles of both P- and E-selectin (*Selp*$^{-/-}$ *Sele*$^{-/-}$); these mice required ~9.5 d for 50% of their HSCs to be BrdU$^+$ (2.8-fold slower than WT) (**Fig. 1a–c**). Notably, this reduced HSC turnover was specific to E-selectin knockout mice, as HSC cycling in P-selectin knockout (*Selp*$^{-/-}$) mice was similar to that in WT mice (**Fig. 1c**). We also observed these differences in HSC turnover using other phenotypic markers of HSCs (**Supplementary Fig. 1**). These results show that E-selectin, but not P-selectin, acts in the bone marrow to accelerate HSC turnover.

Slower HSC cycling *in vivo* would suggest increased quiescence and greater self-renewal potential. We confirmed this by three independent assays: cell-cycle analysis, hydroxyurea S-phase suicide assay and rhodamine 123 (Rho) efflux. Cell-cycle analyses using an antibody to Ki-67, a nuclear marker of cell cycling, showed that 30% more HSCs were quiescent (in the G0 phase) in *Sele*$^{-/-}$ mice compared to WT mice (**Fig. 1d,e**). We confirmed this result using the hydroxyurea *in vivo* suicide assay[20].

[1]Stem Cells and Cancer Group, Mater Medical Research Institute, South Brisbane, Queensland, Australia. [2]Stem Cell Biology Group, Mater Medical Research Institute, South Brisbane, Queensland, Australia. [3]University of Queensland, School of Medicine, Brisbane, Queensland, Australia. [4]GlycoMimetics Inc., Gaithersburg, Maryland, USA. Correspondence should be addressed to I.G.W. (iwinkler@mmri.mater.org.au) or J.-P.L. (jplevesque@mmri.mater.org.au).

Received 12 June; accepted 12 September; published online 21 October 2012; doi:10.1038/nm.2969

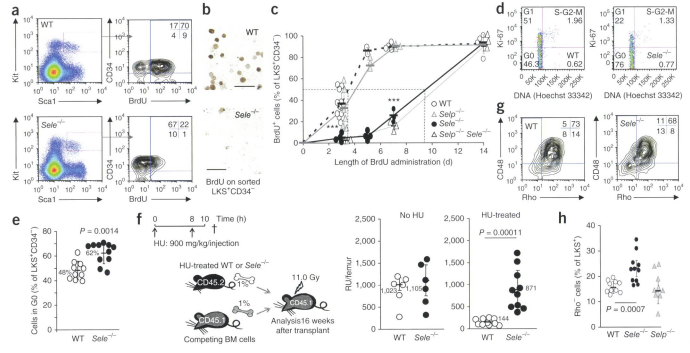

Figure 1 HSC quiescence is increased in E-selectin knockout (*Sele*$^{-/-}$) mice. (**a**–**c**) HSC turnover measured by BrdU incorporation in mice of the indicated genotypes continuously administered BrdU. At set periods of time, the percentage of BrdU incorporation in phenotypic HSCs was measured. (**a**) Dot plot showing the LKS$^+$ gate within Lin$^-$ bone marrow cells (left). BrdU after 3 d of incorporation and CD34 expression on gated LKS$^+$ cells from representative mice (right). Inserted quadrants show percentages of cells in each quadrant of the dot plots. (**b**) Cytospins of sorted HSCs (LKS$^+$CD34$^-$) stained for BrdU incorporation after 5 d of BrdU administration. Scale bar, 50 μm. (**c**) Percentage of bone marrow LKS$^+$CD34$^-$ HSCs that incorporated BrdU over time. Data are pooled from four separate experiments. ***$P < 0.001$. (**d**,**e**) Cell-cycle analysis of LKS$^+$CD34$^-$ HSCs. (**d**) Typical dot plots of DNA content (Hoechst 33342) plotted versus Ki-67 nuclear antigen staining. The cell-cycle phases were defined as G0 (Ki-67$^-$ and 2*n* DNA), G1 (Ki-67$^+$ and 2*n* DNA) and S-G2-M (Ki-67$^+$ and DNA >2*n*). (**e**) Percentage of LKS$^+$CD34$^-$ HSC in phase G0 (quiescence). (**f**) HSC quiescence in *Sele*$^{-/-}$ and WT mice as measured by hydroxyurea (HU) *in vivo* suicide assay. Data shows the number of surviving reconstituting units (RU) per femur after injection with HU or no HU control. (**g**,**h**) Rhodamine efflux by HSCs. (**g**) Contour plot showing Rho efflux and CD48 staining on gated bone marrow LKS$^+$ cells from representative mice. (**h**) Percentage of bone marrow LKS$^+$ cell able to efflux Rho. Data are pooled from three separate experiments. Each symbol in **c**,**e**,**f** and **h** represents data for one mouse. All statistical significance was calculated by nonparametric Mann-Whitney test. All data are shown as the mean ± s.d.

We injected hydroxyurea, an S phase–specific cytotoxic drug, into *Sele*$^{-/-}$ or WT mice and then tested the bone marrow of these mice in long-term competitive repopulation (LT-CR) transplant assays to quantify the number of surviving HSCs. We found sixfold more surviving HSCs (expressed as reconstituting units[21] per femur) in *Sele*$^{-/-}$ compared to WT mice (**Fig. 1f**), confirming that a higher frequency of HSCs are quiescent when E-selectin is absent. Lastly, we measured Rho fluorescence to assess HSC numbers. Rho is a vital fluorescent dye effluxed by long-term repopulating HSCs with highest engraftment potential, similarly to Hoechst 33342 dye efflux by side-population cells[22]. The amount of Rho efflux was higher in HSCs from *Sele*$^{-/-}$ mice compared to those from WT or *Selp*$^{-/-}$ mice (**Fig. 1g**,**h**). Collectively these data confirm that E-selectin at the vascular niche induces HSC cycling.

Despite differences in HSC quiescence, the total number of HSCs per femur was not significantly different between *Sele*$^{-/-}$ and WT mice, as measured by either limiting dilution LT-CR transplant assay or phenotypic analysis (**Supplementary Fig. 2**). This result shows that the effects of an E-selectin–deficient microenvironment on HSCs are qualitative (a greater proportion of HSCs being quiescent with heightened self renewal), not quantitative.

HSC proliferation induced by E-selectin is cell extrinsic

To confirm that the increased HSC quiescence in *Sele*$^{-/-}$ mice is extrinsic to the HSCs (that is, microenvironmentally mediated), we generated fetal liver transplantation chimeras using fetal liver cells from WT and *Sele*$^{-/-}$ embryos and established long-term chimerism after transplantation into WT or *Sele*$^{-/-}$ adult recipients. When transplanted into *Sele*$^{-/-}$ recipients, WT HSCs showed 2.5-fold less turnover. In contrast, both WT and *Sele*$^{-/-}$ HSCs showed normal turnover when transplanted into WT recipients (**Fig. 2**).

We next confirmed that, within the bone marrow, E-selectin is expressed exclusively by endothelial cells. We detected E-selectin RNA transcripts only in sorted bone marrow endothelial cells and not in any other hematopoietic or stromal cell populations tested (**Fig. 3a**). Overall, the amount of E-selectin mRNA was 16-fold higher in the bone marrow endosteal region as compared to the central bone marrow (**Fig. 3b**). Flow cytometry showed a similar enrichment of E-selectin–expressing endothelial cells in the endosteal region as compared to the central bone marrow (**Fig. 3c**), suggesting that the vasculature expressing E-selectin is enriched near the interface with bone. Furthermore, the number of E-selectin–positive endothelial cells increased 18-fold at the endosteum during the recovery phase from irradiation, when surviving HSCs must cycle to regenerate hematopoiesis (**Supplementary Fig. 3**). Together these data confirm that E-selectin expressed by endothelial cells at the HSC vascular niche accelerates HSC proliferation, and that this effect is extrinsically mediated by the bone marrow microenvironment.

Absence of E-selectin enhances HSC chemoresistance

Bone marrow suppression and life-threatening neutropenia can follow cytotoxic chemotherapy, and direct chemotherapy-induced damage

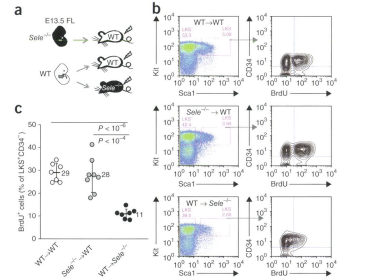

Figure 2 The effect of E-selectin on HSC turnover is mediated by the bone marrow microenvironment. (**a**) Model showing the establishment of transplantation chimeras using fetal liver cells from WT C57BL/6 or *Sele*$^{-/-}$ embryos at embryonic day 13.5 (E13.5 FL) that were transplanted into lethally irradiated WT or *Sele*$^{-/-}$ adult recipients. HSC turnover in these transplantation chimeras was tested 20 weeks after transplant, at which time they were treated with BrdU for 3 d. (**b**) Flow cytometry dot plot gating for LKS$^+$ cells (left) and contour plots of BrdU incorporation and CD34 expression in gated LKS$^+$ cells (right). (**c**) Percentage of bone marrow LKS$^+$CD34$^-$ HSCs that incorporated BrdU. Each dot represents a single mouse. Bars are the mean ± s.d. All statistical significance was calculated by nonparametric Mann-Whitney test.

to HSCs is a contributing factor. Although HSCs can undergo self renewal, high-dose or repeated rounds of chemotherapy or irradiation can eventually exhaust the self-renewal capacity of the HSC pool, leading to prolonged bone marrow suppression and cytopenia. To test whether the relatively quiescent HSCs in *Sele*$^{-/-}$ mice are more resistant to chemotherapy, we explored several models, including HSC survival after a single round of treatment with the antimetabolite 5-fluorouracil (5-FU) or repeated rounds of treatment with the alkylating agent cyclophosphamide (CYP), which also has immunomodulatory properties. We intraperitoneally administered each of these two cytotoxic drugs to WT and *Sele*$^{-/-}$ mice and determined the number of surviving HSCs by LT-CR transplant assays. Indeed, 2.6-fold more HSCs, measured as reconstitution units (RU) per femur, survived a single injection of 5-FU in *Sele*$^{-/-}$ mice (356 ± 123 (mean ± s.d.) RU per femur) compared to WT mice (133 ± 57 RU per femur; **Fig. 4a**). This difference was more pronounced when the mice were treated with four rounds of CYP (one round every 2 weeks): HSCs in *Sele*$^{-/-}$ mice showed an almost eight-fold greater survival compared to those in WT mice (1 in 52 of the initial reconstitution units per femur survived in WT mice compared to 1 in 9 in *Sele*$^{-/-}$ mice) (**Fig. 4a**).

To test whether these effects on HSC survival would result in enhanced survival of the mice, we intraperitoneally administered 5-FU once every 10 d (150 mg per kg body weight) to cohorts of WT or *Sele*$^{-/-}$ mice and monitored them for survival. In this assay, *Sele*$^{-/-}$ mice showed significantly more resistance to repeated rounds of chemotherapy, with a median survival time exceeding 140 d, compared to a median survival time of 58 d in WT mice (**Fig. 4b**).

Faster blood recovery after irradiation of *Sele*$^{-/-}$ mice

We next investigated whether peripheral leukocyte counts would also recover faster after stress in *Sele*$^{-/-}$ mice. Intensive high-dose chemotherapy in human patients typically results in prolonged leukopenia with pronounced neutropenia. Mice, however, showed only a short drop in the number of blood leukocytes after cytotoxic injection (**Fig. 5**). In contrast, we found that 9.0 Gy split-dose irradiation was not lethal in C57BL/6 mice but did induce prolonged leucopenia; under these conditions, WT mice required 28 d for their blood leukocyte numbers to return to the minimum normal threshold of 4,000 blood leukocytes per microliter. Blood leukocyte recovery was significantly accelerated in *Sele*$^{-/-}$ mice after irradiation (**Fig. 4c**).

E-selectin antagonist also increases HSC chemoresistance

To be clinically useful, the benefits of enhanced HSC chemoresistance and faster leukocyte recovery after treatment need to be achievable by transient administration of an E-selectin antagonist. GMI-1070 is a small synthetic glycomimetic that blocks binding of E-selectin to its receptors[23]. GMI-1070 has >50-fold higher selectivity for E-selectin than P- or L-selectin and is currently in phase 2 clinical trials for a separate indication, sickle-cell crisis[23].

We intraperitoneally administered GMI-1070 or saline to WT mice for 18–25 d and analyzed its effects on HSCs. We used a long period of GMI-1070 administration (bi-daily for 18–25 d), as recent studies have suggested that true HSCs cycle very infrequently in bone marrow, once every 35 d or more[24,25]; thus, a prolonged period of drug administration may be needed to alter HSC turnover. Administration of GMI-1070 to WT mice delayed HSC cycling, with 37% less BrdU incorporation after a 3 d BrdU pulse (**Fig. 5a**), and increased the proportion of Rho-effluxing HSCs 44% compared to saline-administered controls (**Fig. 5a**). Therefore GMI-1070 was efficacious at reducing

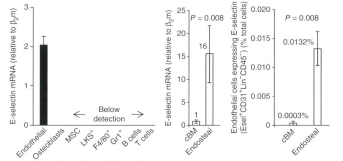

Figure 3 E-selectin–expressing endothelial cells are enriched in the endosteal region. (**a**) E-selectin mRNA expression relative to β_2-microglobulin (β_2m) in the specified bone marrow cell populations sorted from WT mice and subjected to qRT-PCR. MSC, mesenchymal stromal cells. Data are the mean ± s.d. (**b**) E-selectin mRNA expression relative to β_2-microglobulin (β_2m) in RNA extracts from central bone marrow (cBM) and endosteal regions of the femur. Data are mean ± s.d. from 3–4 mice per group. The data were normalized such that E-selectin mRNA expression in cBM was set to a value of 1. (**c**) The frequency of CD45$^-$Lin$^-$CD31$^+$ endothelial cells expressing E-selectin (Esel), as determined by flow cytometry of bone marrow cells collected from central bone marrow and endosteum stained with mouse E-selectin–specific antibody. Data are mean ± s.d. from four mice per group. All statistical significance was calculated by nonparametric Mann-Whitney test.

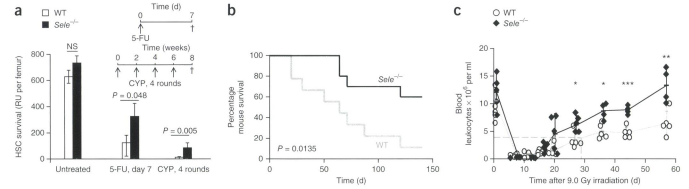

Figure 4 HSCs from *Sele*$^{-/-}$ mice are chemoresistant and radioresistant. (**a**) Long-term reconstitution units (RU) 16 weeks after transplant in competitive repopulation transplant assays performed using bone marrow from donor WT or *Sele*$^{-/-}$ mice, either untreated, after 7 d of treatment with a single dose of 5-FU or after treatment with four rounds of CYP. NS, not significant. Data are the mean ± s.d. (**b**) Mouse survival in mice injected with 5-FU once every 10 d. (**c**) Blood leukocyte recovery in WT and *Sele*$^{-/-}$ mice irradiated with 9.0 Gy. Each dot represents data for a single mouse. Bars are the mean ± s.d. for each time point. $^*P < 0.05$, $^{**}P < 0.01$, $^{***}P < 0.001$. All statistical significance was calculated by nonparametric Mann-Whitney test.

HSC proliferation despite the fact that GMI-1070 is bioactive for only 2 h in the serum after each bi-daily injection (when at a serum concentration of >10 μg ml^{-1}) (data not shown).

Although pretreatment with the E-selectin antagonist induced HSC quiescence, it did not increase HSC number per femur by either phenotypic analysis or LT-CR transplant assay in primary recipients (**Fig. 5b**). To further explore whether HSC self renewal was affected, we performed serial bone marrow transplantations. Serial transplantation is used to rapidly age HSCs, as extensive HSC self renewal is required to repopulate the whole hematopoietic system in each successive recipient. The use of serial bone marrow transplantation in the mouse mimics the gradual decline in HSC function over a lifetime in transplanted patients. When donor mice had been pretreated with saline, blood chimerism declined with each serial transplant, consistent with a gradual decline in HSC function, as previously reported[26]. In sharp contrast, there was a steady increase in reconstitution potential when the donor bone marrow was derived from mice pretreated with GMI-1070 (**Fig. 5b**). In tertiary transplant recipients, the number of reconstitution units per femur was 3.3-fold higher if the original donor had been pretreated for 25 d with GMI-1070 (1,036 ± 261 compared to 309 ± 143 CD45.2$^+$ RU per femur for saline-injected donors). These results show that transient pretreatment with the E-selectin antagonist *in vivo* significantly increases the self-renewal capacity of HSCs.

HSC quiescence may confer resistance to cytotoxic chemotherapy or radiotherapy. Indeed, when donor mice were administered a single dose of 5-FU and bone marrow transplanted in an LT-CR assay, we found that 2.9-fold more HSC survived if 5-FU donors had also been pretreated with GMI-1070 compared to 5-FU alone (**Fig. 5c**). Thus, transient administration of an E-selectin antagonist almost exactly mimics the increased HSC chemoresistance of *Sele*$^{-/-}$ mice (**Fig. 4a**).

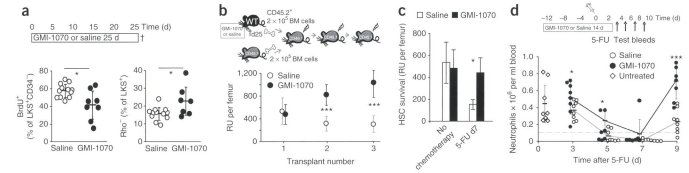

Figure 5 Administration of a small, synthetic E-selectin antagonist enhances HSC quiescence, chemoresistance, self-renewal capacity and blood leukocyte recovery after chemotherapy. (**a**) Diagram showing the timecourse of the experiment in which WT mice were administered the E-selectin antagonist GMI-1070 or saline for 18–25 d (top). Percentage of BrdU incorporation in gated bone marrow LKS$^+$CD34$^-$ HSCs (bottom left) and percentage of gated bone marrow LKS$^+$ cells able to efflux Rho (Rho$^-$) (bottom right). Data were pooled from two independent experiments. (**b**) The number of long-term competitive reconstitution units (RU) per CD45.2$^+$ donor femur in a serial-transplantation assay in which 200,000 CD45.2$^+$ bone marrow (BM) cells from GMI-1070–treated or saline-treated mice were transplanted into lethally irradiated congenic recipients together with an equal number of competing CD45.1$^+$ bone marrow cells. At 25 weeks after primary transplants, 10% of the pooled femoral bone marrow was transplanted into secondary and then tertiary recipients each at 16 weeks after transplant. Data are the mean ± s.d. $n = 8$–10 recipients per group. (**c**) HSC survival measured by competitive long-term reconstitution assays 7 d after a single injection of 5-FU or saline in donor mice performed using pooled bone marrow from mice pretreated with GMI-1070 or saline. One percent of the femoral bone marrow was injected into recipients together with 200,000 congenic competing bone marrow cells. Data are mean ± s.d. of the calculated number of long-term reconstitution units per femur. There were four donors and eight recipients per treatment group. (**d**) Blood CD11b$^+$Gr1^{bright} neutrophil recovery measured by flow cytometry in GMI-1070–pretreated or control mice administered a single dose of 5-FU, as indicated. $^*P < 0.05$, $^{***}P < 0.001$. Each symbol in **a** and **d** represents data from a single mouse, and all data are the mean ± s.d. All statistical significance was calculated by nonparametric Mann-Whitney test.

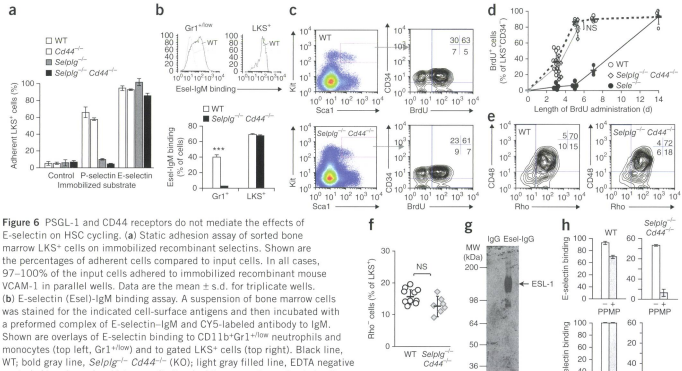

Figure 6 PSGL-1 and CD44 receptors do not mediate the effects of E-selectin on HSC cycling. (**a**) Static adhesion assay of sorted bone marrow LKS+ cells on immobilized recombinant selectins. Shown are the percentages of adherent cells compared to input cells. In all cases, 97–100% of the input cells adhered to immobilized recombinant mouse VCAM-1 in parallel wells. Data are the mean ± s.d. for triplicate wells. (**b**) E-selectin (Esel)-IgM binding assay. A suspension of bone marrow cells was stained for the indicated cell-surface antigens and then incubated with a preformed complex of E-selectin–IgM and CY5-labeled antibody to IgM. Shown are overlays of E-selectin binding to CD11b+Gr1$^{+/low}$ neutrophils and monocytes (top left, Gr1$^{+/low}$) and to gated LKS+ cells (top right). Black line, WT; bold gray line, *Selplg*$^{-/-}$ *Cd44*$^{-/-}$ (KO); light gray filled line, EDTA negative control. Also shown is a histogram (bottom) of the percentage of gated cells that bound E-selectin–IgM. Data are the mean ± s.d. $n = 6$ mice per group. ***$P < 0.001$. (**c**) Three-day BrdU incorporation plotted relative to CD34 expression in gated LKS+ cells in WT and *Selplg*$^{-/-}$*Cd44*$^{-/-}$ mice. Inserted quadrants show percentages of cells in each quadrant of the dot plots. (**d**) Timecourse of BrdU incorporation in gated bone marrow LKS+CD34− cells. Bars are the mean ± s.d. NS, not significant. (**e**) Rho efflux by HSCs. Contour plot showing Rho efflux plotted against CD48 staining on gated bone marrow LKS+ cells from representative WT and *Selplg*$^{-/-}$ *Cd44*$^{-/-}$ mice. (**f**) Percentage of bone marrow LKS+ cells able to efflux Rho. (**g**) E-selectin pulldown experiments. Lysates of Lin−Kit+ cells from *Selplg*$^{-/-}$ *Cd44*$^{-/-}$ mice were incubated with recombinant mouse E-selectin–hulgG1–Fc (Esel-IgG) or control (IgG)-coated beads, pulled down, eluted with EDTA and western blotted with a rabbit antibody to ESL-1. MW, molecular weight. (**h**) Binding of LKS+ cells from WT and *Selplg*$^{-/-}$ *Cd44*$^{-/-}$ mice to recombinant human E-selectin–IgM (top histograms) and P-selectin–IgM (bottom histograms) after an overnight incubation with or without PPMP, as measured by flow cytometry. Data are the mean ± s.d. (triplicate wells, three repeats). Each symbol in **d** and **f** represents data from a single mouse. All statistical significance was determined by nonparametric Mann-Whitney test.

Short-term administration of GMI-1070 in mice also accelerated the recovery of blood neutrophils after 5-FU treatment (**Fig. 5d**). Therefore, transient pretreatment with an E-selectin antagonist not only increases the proportion of HSCs that are able to survive chemotherapy but also accelerates blood leukocyte recovery afterward.

Noncanonical E-selectin ligands mediate HSC proliferation

We have previously demonstrated that adhesion of human and mouse HSPCs to E- and P-selectin alters HSPC behavior *in vitro*[27,28]. P-selectin glycoprotein ligand-1 (PSGL-1, also called CD162), the best-characterized selectin ligand, binds to both P- and E-selectin and is expressed by HSPCs, as well as by mature myeloid cells[27–30]. However, absence of PSGL-1 did not prevent LKS+ HSPC adherence to E-selectin (**Fig. 6a,b**), even though the adhesion of mature Gr1+ myeloid cells to E-selectin was abrogated (**Fig. 6b**). Similarly, the absence of both PSGL-1 (*Selplg*$^{-/-}$) and the sialylated CD44 glycoform HCELL (*Cd44*$^{-/-}$), another canonical E-selectin ligand expressed by HSPCs and mature leukocytes[30,31], did not prevent HSPC binding to E-selectin in static-adhesion and flow cytometry–based assays (**Fig. 6a,b**). Furthermore, HSCs from *Selplg*$^{-/-}$ *Cd44*$^{-/-}$ mice incorporated BrdU at the same rate as did HSCs from WT mice (**Fig. 6c,d**) and did not show a significant difference in the number of Rho-negative cells (**Fig. 6e,f**), indicating that noncanonical ligands on HSCs mediate E-selectin–induced HSC proliferation.

To characterize E-selectin ligands on HSPCs, we used E-selectin–coated magnetic beads in pulldown experiments with lysates of Lin−Kit+ HSPCs from *Selplg*$^{-/-}$ *Cd44*$^{-/-}$ mice and looked for the presence of candidate E-selectin ligands by western blotting. Antibodies to CD43, endoglycan or CD147 (ref. 32) did not detect these candidate E-selectin ligands in pulldowns from HSPC extracts (data not shown). However, we did detect E-selectin ligand-1 (ESL-1), which most likely forms part of the E-selectin ligand signaling complex[33–35] (**Fig. 6g**). We did not detect any other candidate E-selectin ligands, such as CD65 (by flow cytometry) or death receptor 3 (ref. 36) (by quantitative RT-PCR (qRT-PCR)) on LKS+ HSPCs.

Human neutrophils express both glycoprotein and glycosphingolipid E-selectin ligands[37]. We next investigated whether mouse HSCs also express E-selectin–binding cell-surface glycosphingolipid ligands. We incubated mouse bone marrow HSPCs overnight in the presence of 18 μM 1-phenyl-2-palmitoyl-3-morpholino-1-propanol (PPMP), a potent inhibitor of the glucosylceramide synthetase that is involved in the synthesis of glycosphingolipids[38]. PPMP treatment reduced E-selectin binding by 88% in *Selplg*$^{-/-}$ *Cd44*$^{-/-}$ HSPCs and 30% in WT HSPCs (**Fig. 6h**). PSGL-1 glycoprotein binding to P-selectin was unaltered by PPMP treatment, showing the specificity of this treatment for glycosphingolipid ligands (**Fig. 6h**).

Together these results suggest that, in the absence of both PSGL-1 and CD44/HCELL, glycosphingolipids are major E-selectin ligands

on mouse HSPCs. Furthermore, as cell-surface glycosphingolipids are reported to be potent adhesion and signaling molecules (forming the glycosynapse[39,40]), such glycosphingolipids may be involved in transducing E-selectin–mediated signaling from endothelial cells forming the vascular niche to HSCs.

DISCUSSION

Here we report that E-selectin expressed on the bone marrow vasculature is a potent driver of HSC proliferation *in vivo*. Furthermore, we found that transient administration of a small synthetic E-selectin antagonist blocks proliferative signaling by the vascular HSC niche, promoting HSC quiescence, HSC self renewal and increased survival after treatment with chemotherapeutic agents *in vivo*.

Environmental cues are crucial regulators of normal and malignant stem-cell behavior. Far from being homogenous, bone marrow tissue contains a mosaic of microenvironments, each of which provides a unique set of instructions regulating or reinforcing cell fate. The most potent and quiescent HSCs are enriched near osteoblasts lining the endosteal bone surface[1–4,24] and in poorly perfused areas of the bone marrow[41], leading to the hypothesis that unique factors and cues at these niches actively maintain HSC quiescence and self-renewal capacity. By inference, HSCs located outside these specialized niches may commit to hematopoietic lineages and lose stem-cell potential in the absence of osteoblastic cues. We now show that the adhesion molecule E-selectin is a crucial component of the vascular HSC niche that actively induces HSC proliferation. E-selectin deficiency or antagonism leads to HSC quiescence, a greater capacity to self renew and enhanced chemoresistance. Our findings challenge the current assumption that factors unique to the osteoblastic niche alone maintain HSC dormancy and self renewal and are supported by recent evidence showing a key role for Kit ligand expressed by endothelial cells in HSC maintenance[10]. Indeed it seems that in the absence of a specific E-selectin–mediated proliferative signal, greater numbers of HSC remain quiescent.

That HSC proliferation seems to be regulated by E-selectin but not P-selectin is surprising, as both endothelial selectins are largely redundant in function in the periphery, and *Sele*$^{-/-}$ mice have no obvious phenotype and have normal blood indices[42,43]. Intravital imaging studies on mouse calvariae have suggested that E-selectin is expressed mainly on bone marrow sinusoidal vasculature, whereas P-selectin is present on larger blood vessels[16]. Thus, it seems that these two endothelial selectins may be expressed in distinct, possibly nonoverlapping locations in the bone marrow and have distinct functional roles in this tissue. Furthermore, we found that the expression of E-selectin is greatly increased during the recovery phase after irradiation when HSCs divide to reconstitute hematopoiesis, supporting the notion that E-selectin promotes HSC proliferation in regenerating or inflamed bone marrow.

The identity of the E-selectin ligand involved in regulating HSC cycling in the bone marrow remains uncertain. None of the canonical E-selectin ligands tested had an effect on HSCs; however, the involvement of ESL-1 cannot be excluded, as we detected it in E-selectin pulldowns from HPSC cell lysates. ESL-1 is a glycoprotein of the Golgi apparatus, but in cell culture, its expression may be redirected to the cell-surface plasma membrane after post-translational modifications, such as the addition of a glycosylphosphatidylinositol anchor[44,45]. Notably, inhibition of sphingolipid glycosylation reduced the E-selectin binding of *Selplg*$^{-/-}$ *Cd44*$^{-/-}$ HSCs by 88%, suggesting that glycosphingolipids may also be important E-selectin ligands on HSCs. To our knowledge, glycosphingolipid E-selectin ligands have not previously been reported on normal adult stem cells. It is tempting to speculate that such glycosphingolipid E-selectin ligands might be involved in cell signaling only when HSCs are already in close physical contact with E-selectin at the vascular niche.

Aberrant glycosylation is characteristic of many tumor cells and is a frequent early marker of oncogenic transformation[46]. The *de novo* expression of E-selectin ligands on tumor cells is thought to aid their homing and engraftment into the bone marrow[47–49]. Our findings suggest that the acquisition of E-selectin ligands by tumor cells may also influence subsequent tumor cell proliferation and tumor growth.

Finally, chemotherapy-induced bone marrow suppression remains a clinical problem. Reducing the myelosuppressive effect of chemotherapy could result in less infection and less of a requirement for blood product and hospital support. Our study of how the vascular niche regulates stem-cell behavior suggests a new approach to alleviate these potentially life-threatening complications of chemotherapy.

METHODS

Methods and any associated references are available in the online version of the paper.

Note: *Supplementary information is available in the online version of the paper.*

ACKNOWLEDGMENTS

The authors wish to thank R. Wadley for assistance with cell sorting, P. Frenette (Albert Einstein College of Medicine, New York) for providing selectin knockout mice, B. Furie (Beth Israel Deaconess Medical Center, Harvard Medical School, Boston) for *Selplg*$^{-/-}$ mice, T. Mak (Ontario Cancer Institute, Toronto) for *Cd44*$^{-/-}$ mice, D. Vestweber (Max Planck Institute of Molecular Biomedicine, Münster, Germany) for antibody to ESL-1, K. Snapp (Northwestern University, Chicago) for selectin-IgM constructs and L. Purton, C. Walkley and C. Bonder for helpful discussions. This work was supported by project grants 350406 and 543706 (I.G.W. and J.-P.L.) and Career Development Fellowships 488817 and APP1033736 (I.G.W.) from the National Health and Medical Research Council of Australia, a Senior Research Fellowship from the Cancer Council of Queensland (J.-P.L.) and a research contract with GlycoMimetics Inc to generate the data in **Figure 5**.

AUTHOR CONTRIBUTIONS

I.G.W. initiated, conceived of, designed and supervised research, wrote the manuscript, performed experiments and analyzed data. V.B., B.N., R.N.J. and C.E.F. performed experiments and analyzed data. J.T.P. and J.L.M. contributed vital new reagents and commented on the research direction. J.-P.L. initiated the study, supervised research direction and experiments, performed some experiments and edited the manuscript. All authors discussed and commented on the manuscript.

COMPETING FINANCIAL INTERESTS

The authors declare competing financial interests: details are available in the online version of the paper.

Published online at http://www.nature.com/doifinder/10.1038/nm.2969.
Reprints and permissions information is available online at http://www.nature.com/reprints/index.html.

1. Arai, F. *et al.* Tie2/angiopoietin-1 signaling regulates hematopoietic stem cell quiescence in the bone marrow niche. *Cell* **118**, 149–161 (2004).
2. Xie, Y. *et al.* Detection of functional haematopoietic stem cell niche using real-time imaging. *Nature* **457**, 97–101 (2009).
3. Köhler, A. *et al.* Altered cellular dynamics and endosteal location of aged early hematopoietic progenitor cells revealed by time-lapse intravital imaging in long bones. *Blood* **114**, 290–298 (2009).
4. Lo Celso, C. *et al.* Live-animal tracking of individual haematopoietic stem/progenitor cells in their niche. *Nature* **457**, 92–96 (2009).
5. Lévesque, J.P., Helwani, F.M. & Winkler, I.G. The endosteal 'osteoblastic' niche and its role in hematopoietic stem cell homing and mobilization. *Leukemia* **24**, 1979–1992 (2010).
6. Kiel, M.J. *et al.* SLAM family receptors distinguish hematopoietic stem and progenitor cells and reveal endothelial niches for stem cells. *Cell* **121**, 1109–1121 (2005).
7. Sugiyama, T., Kohara, H., Noda, M. & Nagasawa, T. Maintenance of the hematopoietic stem cell pool by CXCL12-CXCR4 chemokine signaling in bone marrow stromal cell niches. *Immunity* **25**, 977–988 (2006).

8. Méndez-Ferrer, S. *et al.* Mesenchymal and haematopoietic stem cells form a unique bone marrow niche. *Nature* **466**, 829–834 (2010).
9. Butler, J.M. *et al.* Endothelial cells are essential for the self-renewal and repopulation of Notch-dependent hematopoietic stem cells. *Cell Stem Cell* **6**, 251–264 (2010).
10. Ding, L., Saunders, T.L., Enikolopov, G. & Morrison, S.J. Endothelial and perivascular cells maintain haematopoietic stem cells. *Nature* **481**, 457–462 (2012).
11. Kansas, G.S. Selectins and their ligands: current concepts and controversies. *Blood* **88**, 3259–3287 (1996).
12. Frenette, P.S., Mayadas, T.N., Rayburn, H., Hynes, R.O. & Wagner, D.D. Susceptibility to infection and altered hematopoiesis in mice deficient in both P- and E-selectins. *Cell* **84**, 563–574 (1996).
13. Maly, P. *et al.* The α(1,3)fucosyltransferase Fuc-TVII controls leukocyte trafficking through an essential role in L-, E-, and P-selectin ligand biosynthesis. *Cell* **86**, 643–653 (1996).
14. Jacobsen, K., Kravitz, J., Kincade, P.W. & Osmond, D.G. Adhesion receptors on bone marrow stromal cells: *in vivo* expression of vascular cell adhesion molecule-1 by reticular cells and sinusoidal endothelium in normal and γ-irradiated mice. *Blood* **87**, 73–82 (1996).
15. Schweitzer, K.M. *et al.* Constitutive expression of E-selectin and vascular cell adhesion molecule-1 on endothelial cells of hematopoietic tissues. *Am. J. Pathol.* **148**, 165–175 (1996).
16. Sipkins, D.A. *et al. In vivo* imaging of specialized bone marrow endothelial microdomains for tumour engraftment. *Nature* **435**, 969–973 (2005).
17. Hidalgo, A., Weiss, L.A. & Frenette, P.S. Functional selectin ligands mediating human CD34+ cell interactions with bone marrow endothelium are enhanced postnatally. *J. Clin. Invest.* **110**, 559–569 (2002).
18. Katayama, Y. *et al.* PSGL-1 participates in E-selectin–mediated progenitor homing to bone marrow: evidence for cooperation between E-selectin ligands and α4 integrin. *Blood* **102**, 2060–2067 (2003).
19. Osawa, M., Hanada, K., Hamada, H. & Nakauchi, H. Long-term lymphohematopoietic reconstitution by a single CD34-low/negative hematopoietic stem cell. *Science* **273**, 242–245 (1996).
20. Lord, B.I., Dexter, T.M., Clements, J.M., Hunter, M.A. & Gearing, A.J. Macrophage-inflammatory protein protects multipotent hematopoietic cells from the cytotoxic effects of hydroxyurea *in vivo*. *Blood* **79**, 2605–2609 (1992).
21. Purton, L.E. & Scadden, D.T. Limiting factors in murine hematopoietic stem cell assays. *Cell Stem Cell* **1**, 263–270 (2007).
22. Hüttmann, A., Liu, S.L., Boyd, A.W. & Li, C.L. Functional heterogeneity within rhodamine123(lo) Hoechst33342(lo/sp) primitive hemopoietic stem cells revealed by pyronin Y. *Exp. Hematol.* **29**, 1109–1116 (2001).
23. Chang, J. *et al.* GMI-1070, a novel pan-selectin antagonist, reverses acute vascular occlusions in sickle cell mice. *Blood* **116**, 1779–1786 (2010).
24. Wilson, A. *et al.* Hematopoietic stem cells reversibly switch from dormancy to self-renewal during homeostasis and repair. *Cell* **135**, 1118–1129 (2008).
25. Catlin, S.N., Busque, L., Gale, R.E., Guttorp, P. & Abkowitz, J.L. The replication rate of human hematopoietic stem cells *in vivo*. *Blood* **117**, 4460–4466 (2011).
26. Purton, L.E. *et al.* RARγ is critical for maintaining a balance between hematopoietic stem cell self-renewal and differentiation. *J. Exp. Med.* **203**, 1283–1293 (2006).
27. Lévesque, J.P. *et al.* PSGL-1–mediated adhesion of human hematopoietic progenitors to P-selectin results in suppression of hematopoiesis. *Immunity* **11**, 369–378 (1999).
28. Winkler, I.G., Snapp, K.R., Simmons, P.J. & Levesque, J.-P. Adhesion to E-selectin promotes growth inhibition and apoptosis of human and murine hematopoietic progenitor cells independent of PSGL-1. *Blood* **103**, 1685–1692 (2004).
29. Eto, T., Winkler, I., Purton, L.E. & Levesque, J.P. Contrasting effects of P-selectin and E-selectin on the differentiation of murine hematopoietic progenitor cells. *Exp. Hematol.* **33**, 232–242 (2005).
30. Dimitroff, C.J., Lee, J.Y., Rafii, S., Fuhlbrigge, R.C. & Sackstein, R. CD44 is a major E-selectin ligand on human hematopoietic progenitor cells. *J. Cell Biol.* **153**, 1277–1286 (2001).
31. Katayama, Y., Hidalgo, A., Chang, J., Peired, A. & Frenette, P.S. CD44 is a physiological E-selectin ligand on neutrophils. *J. Exp. Med.* **201**, 1183–1189 (2005).
32. Zarbock, A., Ley, K., McEver, R.P. & Hidalgo, A. Leukocyte ligands for endothelial selectins: specialized glycoconjugates that mediate rolling and signaling under flow. *Blood* **118**, 6743–6751 (2011).
33. Hidalgo, A., Peired, A.J., Wild, M.K., Vestweber, D. & Frenette, P.S. Complete identification of E-selectin ligands on neutrophils reveals distinct functions of PSGL-1, ESL-1, and CD44. *Immunity* **26**, 477–489 (2007).
34. Zöllner, O. & Vestweber, D. The E-selectin ligand-1 is selectively activated in Chinese hamster ovary cells by the α(1,3)-fucosyltransferases IV and VII. *J. Biol. Chem.* **271**, 33002–33008 (1996).
35. Wild, M.K., Huang, M.C., Schulze-Horsel, U., van der Merwe, P.A. & Vestweber, D. Affinity, kinetics, and thermodynamics of E-selectin binding to E-selectin ligand-1. *J. Biol. Chem.* **276**, 31602–31612 (2001).
36. Gout, S., Morin, C., Houle, F. & Huot, J. Death receptor-3, a new E-Selectin counter-receptor that confers migration and survival advantages to colon carcinoma cells by triggering p38 and ERK MAPK activation. *Cancer Res.* **66**, 9117–9124 (2006).
37. Nimrichter, L. *et al.* E-selectin receptors on human leukocytes. *Blood* **112**, 3744–3752 (2008).
38. Sandvig, K., Garred, O., van Helvoort, A., van Meer, G. & van Deurs, B. Importance of glycolipid synthesis for butyric acid–induced sensitization to shiga toxin and intracellular sorting of toxin in A431 cells. *Mol. Biol. Cell* **7**, 1391–1404 (1996).
39. Todeschini, A.R., Dos Santos, J.N., Handa, K. & Hakomori, S.I. Ganglioside GM2-tetraspanin CD82 complex inhibits met and its cross-talk with integrins, providing a basis for control of cell motility through glycosynapse. *J. Biol. Chem.* **282**, 8123–8133 (2007).
40. Todeschini, A.R. & Hakomori, S. Functional role of glycosphingolipids and gangliosides in control of cell adhesion, motility and growth, through glycosynaptic microdomains. *Biochim. Biophys. Acta* **1780**, 421–433 (2008).
41. Winkler, I.G. *et al.* Positioning of bone marrow hematopoietic and stromal cells relative to blood flow *in vivo*: serially reconstituting hematopoietic stem cells reside in distinct nonperfused niches. *Blood* **116**, 375–385 (2010).
42. Labow, M.A. *et al.* Characterization of E-selectin–deficient mice: demonstration of overlapping function of the endothelial selectins. *Immunity* **1**, 709–720 (1994).
43. Kunkel, E.J. & Ley, K. Distinct phenotype of E-selectin–deficient mice: E-selectin is required for slow leukocyte rolling *in vivo*. *Circ. Res.* **79**, 1196–1204 (1996).
44. Steegmaier, M., Borges, E., Berger, J., Schwarz, H. & Vestweber, D. The E-selectin–ligand ESL-1 is located in the Golgi as well as on microvilli on the cell surface. *J. Cell Sci.* **110**, 687–694 (1997).
45. Miyaoka, Y. *et al.* Retention in the Golgi apparatus and expression on the cell surface of CfrESl-1/Glg-1/MG-160 are regulated by two distinct mechanisms. *Biochem. J.* **440**, 33–41 (2011).
46. Hakomori, S. Tumor malignancy defined by aberrant glycosylation and sphingo(glyco)lipid metabolism. *Cancer Res.* **56**, 5309–5318 (1996).
47. Gout, S., Tremblay, P.L. & Huot, J. Selectins and selectin ligands in extravasation of cancer cells and organ selectivity of metastasis. *Clin. Exp. Metastasis* **25**, 335–344 (2008).
48. Tremblay, P.L., Auger, F.A. & Huot, J. Regulation of transendothelial migration of colon cancer cells by E-selectin–mediated activation of p38 and ERK MAP kinases. *Oncogene* **25**, 6563–6573 (2006).
49. Dimitroff, C.J. *et al.* Identification of leukocyte E-selectin ligands, P-selectin glycoprotein ligand-1 and E-selectin ligand-1, on human metastatic prostate tumor cells. *Cancer Res.* **65**, 5750–5760 (2005).

nature medicine

Angiogenesis induced by CNS inflammation promotes neuronal remodeling through vessel-derived prostacyclin

Rieko Muramatsu[1,2], Chisato Takahashi[1,2], Shuzo Miyake[1,2], Harutoshi Fujimura[3], Hideki Mochizuki[2,4] & Toshihide Yamashita[1,2]

Angiogenesis is a prominent feature of central nervous system (CNS) disease and has roles in both the continued promotion of inflammation and the subsequent repair processes. Here we report that prostacyclin (or prostaglandin I_2 (PGI_2)) derived from new vessels promotes axonal remodeling of injured neuronal networks after CNS inflammation. In a localized model of experimental autoimmune encephalomyelitis (EAE), new vessels formed around the inflammatory lesion, followed by sprouting of adjacent corticospinal tract (CST) fibers. These sprouting fibers formed a compensatory motor circuit, leading to recovery of motor function. Capillary endothelial cell–derived prostacyclin bound to its receptor, the type I prostaglandin receptor (IP receptor), on CST neurons, promoting sprouting of CST fibers and contributing to the repair process. Inhibition of prostacyclin receptor signaling impaired motor recovery, whereas the IP receptor agonist iloprost promoted axonal remodeling and motor recovery after the induction of EAE. These findings reveal an important function of angiogenesis in neuronal rewiring and suggest that prostacyclin is a promising molecule for enhancing functional recovery from CNS disease.

CNS inflammation leads to the disruption of intricate neural networks, causing deficits in motor, sensory, cognitive and other functions[1]. However, these deficits are often followed by limited, but substantial, spontaneous recovery, suggesting that plasticity in remnant neuronal networks compensates for lost functions[2]. In multiple sclerosis, immune-mediated axonal damage is responsible for neurological deficits[3,4]. This axonal damage involves focal degeneration of axons with intact myelin sheaths[5]. In the EAE model of multiple sclerosis, a motor function deficit persists because of substantial loss of axons along the CST, a descending motor tract that connects cortical layer V neurons with spinal targets[6,7]. This deficit is frequently followed by partial recovery, which is associated with spontaneous remodeling of CST axons[8]. However, the molecular mechanisms by which restorative neuronal remodeling is promoted are unknown.

Inflammatory mediators have the potential to remodel the vascular network, suggesting that inflammation may promote angiogenesis[9]. Angiogenesis is a prominent feature of several CNS conditions, including multiple sclerosis, brain tumors, epilepsy and stroke[10,11]. Because neovascularization is thought to pathologically contribute to the development of inflammatory disorders, targeting angiogenesis has been considered beneficial in delaying the course of disease[12]. Designing therapies targeting the angiogenic process is problematic because new blood vessels have roles in wound healing and repair processes, as well as chronic inflammation. Moreover, the vascular niche provides trophic factors for neurons[13]; therefore, new blood vessels induced by inflammation may affect neuronal function.

Prostacyclin (prostaglandin I_2, PGI_2) is one such trophic factor that is synthesized by vascular endothelial and smooth muscle cells[14]. Prostacyclin also inhibits platelet aggregation and is a potent vasodilator[14]. In the present study, we show that prostacyclin derived from new vessels enhances axonal remodeling and promotes functional recovery in EAE.

RESULTS

Compensatory neural circuit formation after localized EAE

We used a localized model of EAE[8,15], which is characterized by the formation of anatomically defined lesions in the spinal cord. We targeted the inflammatory lesion to the dorsal thoracic spinal cord at thoracic levels 3 and 4 (Th3 and Th4), resulting in injury to the bilateral dorsal CST and other dorsal and lateral tract systems (**Supplementary Fig. 1a**)[2,8,15]. Histological evaluation of the spinal cords revealed severe but single focal inflammatory lesions in these mice (**Supplementary Fig. 1b**) that were characterized by the presence of $CD4^+$ and $CD11b^+$ mononuclear inflammatory cells (**Supplementary Fig. 1c**) and focal demyelination (**Supplementary Fig. 1d**). Anterograde tracing revealed that the dorsal CSTs were disrupted at the level of the lesion, resulting in the disappearance of the CSTs below the level of the lesion (**Supplementary Fig. 1e**). Severe hindlimb paresis was followed by partial spontaneous recovery up to day 21 after induction (**Supplementary Fig. 1f**). The hindlimb-placing response, which strongly depends on corticospinal tract integrity, showed a similar pattern of recovery (**Supplementary Fig. 1g**).

[1]Department of Molecular Neuroscience, Graduate School of Medicine, Osaka University, Suita, Osaka, Japan. [2]Japan Science and Technology Agency, Core Research for Evolutional Science and Technology, Tokyo, Japan. [3]Toneyama National Hospital, Toyonaka, Osaka, Japan. [4]Department of Neurology, Graduate School of Medicine, Osaka University, Suita, Osaka, Japan. Correspondence should be addressed to T.Y. (yamashita@molneu.med.osaka-u.ac.jp).

Received 31 May; accepted 17 August; published online 7 October 2012; doi:10.1038/nm.2943

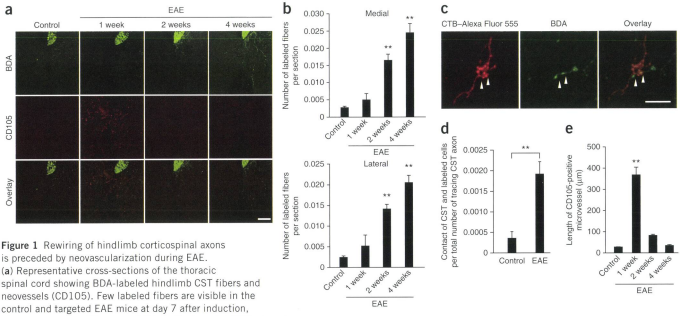

Figure 1 Rewiring of hindlimb corticospinal axons is preceded by neovascularization during EAE. (**a**) Representative cross-sections of the thoracic spinal cord showing BDA-labeled hindlimb CST fibers and neovessels (CD105). Few labeled fibers are visible in the control and targeted EAE mice at day 7 after induction, whereas numerous fibers are visible in the targeted EAE mice at days 14 and 28. Expression of CD105 (marker for proliferating endothelial cells) was induced on day 7. Scale bar, 100 μm. (**b**) Quantitative analysis of the thoracic spinal cord innervations of hindlimb CST fibers. Values represent the mean ± s.e.m. (control: $n = 7$; EAE day 7: $n = 6$; EAE day 14: $n = 6$; EAE day 28: $n = 6$). $^{**}P < 0.01$ using Scheffe's test. (**c**) Thoracic spinal cord cross-section at day 28 after EAE with anterograde labeling of hindlimb CST (BDA) and retrograde tracing of long propriospinal neurons (Alexa Fluor 555–conjugated CTB). Arrowheads indicate the contact positions. Scale bar, 20 μm. (**d**) Quantitative analysis of the contact between labeled CST collaterals and long propriospinal neurons. Values represent the mean ± s.e.m. ($n = 6$ per group). $^{**}P < 0.01$ using Student's t test. (**e**) Quantitative analysis of **a** showing that the length of CD105-positive blood vessels per section (control: $n = 7$; EAE day 7: $n = 6$; EAE day 14: $n = 6$; EAE day 28: $n = 6$). $^{**}P < 0.01$ using Scheffe's test.

Because the recovery of hindlimb motor performance is thought to be caused partly by reorganization of the damaged CST[2,8,15], we further analyzed the events caused by targeted EAE. Although we found only a few biotinylated dextran amine (BDA)-labeled sprouting fibers of the hindlimb CSTs in the thoracic spinal cords of non-EAE control mice (number of collaterals per section: medial, 0.0027; lateral, 0.0024), the number of labeled sprouting fibers in the spinal cords of EAE mice one segment above the lesion increased at 14 and 28 d after lesion (collaterals per section at 14 d: medial, 0.0165; lateral, 0.0142; 28 d: medial, 0.0245; lateral, 0.0205; **Fig. 1a**,**b** and **Supplementary Fig. 1h**,**i**). This increase did not start until 7 d after the lesion was induced (collaterals per section at 7 d: medial, 0.0049; lateral, 0.0051; **Fig. 1a**,**b**). We hypothesized that these sprouting fibers formed a compensatory neuronal network by making functional connections with propriospinal neurons that project intersegmentally to the motor neurons, as has been demonstrated previously after thoracic spinal cord injury[16–18]. To label thoracic propriospinal neurons, we injected Alexa Fluor 555–conjugated cholera toxin subunit B (CTB; a retrograde tracer) into the gray matter of the spinal cords at lumbar levels 1 and 2 (L1 and L2) of control and EAE mice. Two weeks after tracer injection, the number of contacts between BDA-labeled CST collaterals and the cell bodies of the propriospinal neurons labeled with CTB in the spinal cord one segment above the lesion were increased compared with control mice (number of contacts between the CST and CTB-labeled cells: EAE, 0.0025; control, 0.0004; **Fig. 1c**,**d**).

To test the role of thoracic propriospinal neurons above the lesion in mediating functional recovery, we ablated these neurons by infusing *N*-methyl-D-aspartic acid (NMDA) into the gray matter in the segment above the targeted lesion. Motor function recovered over the course of 28 d after EAE induction. However, 3 d after the infusion of NMDA into EAE mice, hindlimb-placing scores and motor recovery were impaired, as compared to control mice without EAE that had received an infusion of NMDA (**Supplementary Fig. 2a**,**b**). The reductions in number of neurons, amount of myelin and lesion length in the spinal cord induced by NMDA injection were comparable between EAE and control mice (**Supplementary Fig. 2c**–**h**). These results show that the CST collaterals formed new connections with the lumbar spinal cord through the propriospinal pathway. The time course of this reorganization is associated closely with that of motor recovery after EAE induction. Thus, these findings provide an anatomical basis for the recovery of motor function and neuronal remodeling during the course of targeted EAE.

Angiogenesis precedes CST reorganization

During the development of the nervous system, axons are guided by attractive and repulsive cues in the extracellular matrix[19]. However, the neuronal network formed as a result of EAE differs from the developmentally formed locomotor network, suggesting that the molecules and mechanisms involved may also differ[2]. Inflammatory processes in several diseases can induce angiogenesis[20]. Thus, we measured the extent of new vessel formation by immunostaining for CD105 (endoglin), a marker of angiogenesis that is expressed in the brains of patients with multiple sclerosis[21]. Seven days after the induction of EAE, the length of CD105-positive capillaries increased markedly around the focal lesions in the spinal cords of EAE mice (368.5 μm per section) compared with control mice (28.2 μm per section; **Fig. 1a**,**e** and **Supplementary Fig. 3a**) and then decreased to the baseline level and remained there at 2 weeks after induction. The lengths of CD31 (PECAM-1)-positive endothelial cells increased in the inflammatory lesions at 1 week after EAE induction and remained elevated for up to 4 weeks (**Supplementary Fig. 3b**,**c**). We observed colocalization of CD105 with some of the CD31-positive

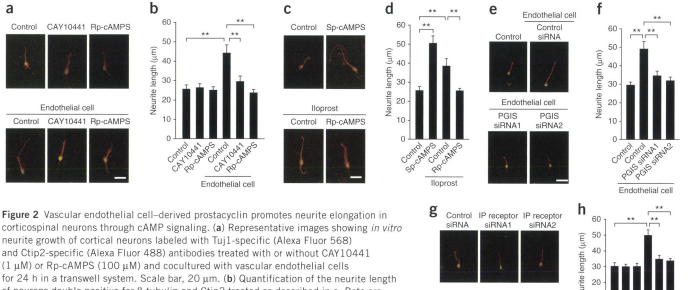

Figure 2 Vascular endothelial cell–derived prostacyclin promotes neurite elongation in corticospinal neurons through cAMP signaling. (**a**) Representative images showing *in vitro* neurite growth of cortical neurons labeled with Tuj1-specific (Alexa Fluor 568) and Ctip2-specific (Alexa Fluor 488) antibodies treated with or without CAY10441 (1 μM) or Rp-cAMPS (100 μM) and cocultured with vascular endothelial cells for 24 h in a transwell system. Scale bar, 20 μm. (**b**) Quantification of the neurite length of neurons double positive for β-tubulin and Ctip2 treated as described in **a**. Data are means ± s.e.m. $^{**}P < 0.01$ using Scheffe's test. $n = 49$–78 neurons per group. (**c**) Representative images of cortical neurons preincubated with or without Rp-cAMPS (cAMP antagonist; 100 μM) and then cultured with iloprost (1 μM; IP receptor agonist) for 24 h. Sp-cAMPS is a cAMP agonist (100 μM). Scale bar, 20 μm. (**d**) Quantification of neurite length of neurons double positive for β-tubulin and Ctip2 treated as described in **c**. Data are means ± s.e.m. $^{**}P < 0.01$ using Scheffe's test. $n = 49$–60 neurons. (**e**) Representative images of cortical neurons cocultured with or without vascular endothelial cells that were transfected with PGIS siRNA. Scale bar, 20 μm. (**f**) Quantification of neurite length of the neurons double positive for β-tubulin and Ctip2 treated as described in **e**. Data are means ± s.e.m. $^{**}P < 0.01$ using Scheffe's test. $n = 36$–82 neurons. (**g**) Representative images of cortical neurons transfected with IP receptor siRNA or control siRNA and cocultured with vascular endothelial cells. Scale bar, 20 μm. (**h**) Quantification of neurite length of the neurons double positive for β-tubulin and Ctip2 treated as described in **g**. Data are means ± s.e.m. $^{**}P < 0.01$ using Scheffe's test. $n = 50$–65 neurons.

endothelial cells (**Supplementary Fig. 3d**). We used CD105 as a marker for angiogenesis because it was coexpressed with Ki67 in capillaries (**Supplementary Fig. 3e**). These results suggest that the increase in the density of vascular endothelial cells was caused by the increase in the density of the new vessels. The kinetics of these findings reveal that new vessel formation was followed by reorganization of the CST.

Prostacyclin promotes axonal elongation

The results described above prompted us to investigate whether the newly formed blood vessels secrete factors that promote axonal sprouting, resulting in reorganization of the neuronal network. Therefore, we next explored whether vascular endothelial cells promote neurite growth *in vitro*. We prepared vascular endothelial cells and cortical neurons from mouse brains and cocultured them in a transwell system for 24 h to prevent contact between the different cell types and measured neurite length of neurons that were positive for Tuj1, a class III β-tubulin, and COUP transcription factor interacting protein 2 (Ctip2, also known as Bcl11B), a marker of subcortically projecting neurons including those in the CST. Notably, neurite length increased when cocultured with vascular endothelial cells as compared with control neurons cultured without endothelial cells (control, 27.91 μm; coculture, 45.26 μm; **Fig. 2a**,**b**). These results suggest that a diffusible factor or factors secreted from brain endothelial cells may promote neurite outgrowth in corticospinal neurons.

To identify the soluble factor(s) responsible for this effect, we focused on vasoconstrictor peptides, including endothelin[22]. By ELISA, we detected a stable metabolite of prostacyclin, 6-keto prostaglandin F1 α (6-keto–PGF1-α) in the medium of cultured endothelial cells (20.6 ng per ml in 10^6 cells) from control mice after 1 d *in vitro*. We did not detect 6-keto–PGF1-α in the supernatants from cultures of cortical neurons (data not shown). The prostacyclin receptor (IP receptor) is a G protein–coupled receptor that is primarily coupled to the activation of adenylate cyclase, which catalyzes the formation of 3′,5′ cyclic adenosine monophosphate (cAMP)[14], a key messenger for axon regeneration[23,24]. Treatment of neurons with the IP receptor antagonist CAY10441 abrogated the effect of endothelial cells on neurite growth (coculture, 45.26 μm; CAY10441, 30.71 μm; **Fig. 2a**,**b**). These results suggest that vascular endothelial cells promote neurite elongation through the IP receptor.

Because the binding of prostacyclin to the IP receptor increases the amount of cAMP, we investigated whether the elevation in intracellular cAMP in neurons was required for neurite elongation. We found that treatment of neurons with Rp-cAMPS, an antagonist of cAMP, inhibited endothelial cell–induced neurite elongation (coculture, 45.26 μm; Rp-cAMPS, 26.84 μm; **Fig. 2a**,**b**). Conversely, treatment of neurons with iloprost, an IP receptor agonist, promoted neurite elongation in a cAMP-dependent manner (vehicle-treated control, 27.91 μm; iloprost, 42.14 μm; iloprost and Rp-cAMPS, 26.90 μm; **Fig. 2c**,**d**). We confirmed that treatment with Sp-cAMPS, an agonist of cAMP, enhanced neurite elongation (vehicle-treated control, 27.91 μm; iloprost, 50.45 μm; **Fig. 2c**,**d**).

To assess whether prostacyclin released from vascular endothelial cells was responsible for the observed effect on neurite elongation, we transfected endothelial cells with two different prostacyclin synthase (PGIS) siRNAs, siRNA1 and siRNA2 (**Supplementary Fig. 4a**)

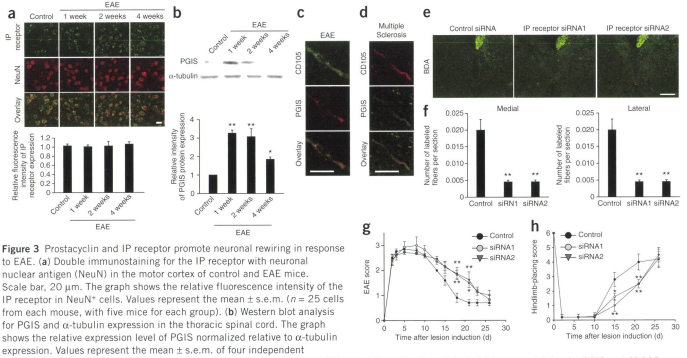

Figure 3 Prostacyclin and IP receptor promote neuronal rewiring in response to EAE. (**a**) Double immunostaining for the IP receptor with neuronal nuclear antigen (NeuN) in the motor cortex of control and EAE mice. Scale bar, 20 μm. The graph shows the relative fluorescence intensity of the IP receptor in NeuN$^+$ cells. Values represent the mean ± s.e.m. ($n = 25$ cells from each mouse, with five mice for each group). (**b**) Western blot analysis for PGIS and α-tubulin expression in the thoracic spinal cord. The graph shows the relative expression level of PGIS normalized relative to α-tubulin expression. Values represent the mean ± s.e.m. of four independent experiments. $^*P < 0.05$, $^{**}P < 0.01$ using one-way analysis of variance (ANOVA) followed by Tukey's test. (**c**) Immunostaining for PGIS and CD105 in the spinal cord after EAE. Scale bar, 10 μm. (**d**) Immunostaining for CD105 and PGIS in autopsy spinal cord samples from individuals with multiple sclerosis. Scale bar, 10 μm. (**e**) Representative sections of the thoracic spinal cord showing BDA-labeled sprouting fibers of the CST 14 d after EAE induction. Scale bar, 100 μm. (**f**) Quantitative analysis of hindlimb CST fiber innervation in the thoracic spinal cord 14 d after EAE induction. $^{**}P < 0.01$ using one-way ANOVA followed by Scheffe's test. Values are represented as mean ± s.e.m. (control: $n = 7$; IP receptor siRNA1: $n = 6$; IP receptor siRNA2: $n = 6$). (**g**,**h**) Quantification of EAE scores (**g**) and hindlimb-placing scores (**h**) in EAE mice treated with control siRNA or siRNA directed against the IP receptor (siRNA1 and siRNA2). Values are represented as mean ± s.e.m. $^*P < 0.05$, $^{**}P < 0.01$ using one-way ANOVA followed by Bonferroni's test.

and found that, when these were cocultured with neurons, silencing of PGIS inhibited neurite elongation (control siRNA, 49.07 μm; PGIS siRNA1, 34.55 μm; PGIS siRNA2, 31.91 μm; **Fig. 2e,f**). When we knocked down IP receptor expression in the cortical neurons (**Supplementary Fig. 4b**), vascular endothelial cell–induced neurite elongation was completely inhibited (control siRNA, 49.81 μm; IP receptor siRNA1, 34.79 μm; IP receptor siRNA2, 33.78 μm; **Fig. 2g,h**). Therefore, prostacyclin derived from vascular endothelial cells promotes neurite outgrowth of corticospinal neurons *in vitro* through the IP receptor and activation of adenylate cyclase.

The IP receptor is crucial for motor recovery from EAE

We investigated whether prostacyclin signaling promotes neuronal remodeling and motor recovery in EAE mice. Immunohistochemical analysis revealed that the majority of the neurons in layer V of the hindlimb motor cortex expressed IP receptor before and after the induction of EAE (**Fig. 3a**). Glial fibrillary acidic protein (GFAP)-positive astrocytes in the motor cortex expressed the IP receptor at very low levels (**Supplementary Fig. 5a**). We found an increase in PGIS and 6-keto–PGF1-α expression in the lesioned tissues (**Fig. 3b** and **Supplementary Fig. 5b**), with expression of PGIS primarily in the CD105-positive neovessels (**Fig. 3c**) but not in neurons or astrocytes in the spinal cord (**Supplementary Fig. 5c**). Although PGIS was also expressed in CD31$^+$ as well as in platelet-derived growth factor receptor-α (PDGFR-α)-positive cells in the spinal cord, the levels of their expressions in each cell were unchanged on day 7 after the induction of EAE (**Supplementary Fig. 5c,d**). The level of PGIS in CD31$^+$ vascular endothelial cells was comparable between control and EAE spinal cords (**Supplementary Fig. 5e**), suggesting that the increase in PGIS expression after EAE induction was caused by the increase in neovessel formation and the upregulation of PGIS in these vessels. Moreover, we observed weak expression of cyclooxygenase 2 (COX-2) in the focal EAE lesions of the spinal cord (**Supplementary Fig. 5f**). We also detected PGIS expression in CD105-positive cells in brain and spinal cord autopsy samples obtained from three individuals with multiple sclerosis (**Fig. 3d**).

To investigate whether the activation of IP receptor is required for motor recovery from EAE-induced paresis, we knocked down expression of the IP receptor *in vivo* by transfecting neurons in layer V of the hindlimb motor cortices with IP receptor siRNA1 or siRNA2 in EAE mice (**Supplementary Fig. 6a–d**). This enabled us to specifically block the IP receptor in CST neurons while investigating the effects in the spinal cord. *In vivo* transfection of IP receptor siRNAs decreased the formation of CST collaterals in response to focal EAE lesions (IP receptor siRNA1: medial, 0.0045; lateral, 0.0042; IP receptor siRNA2: medial, 0.0045; lateral, 0.0043) compared with control siRNA transfection at 14 d after induction of EAE (control siRNA: medial, 0.0200; lateral, 0.0190; **Fig. 3e**,**f** and **Supplementary Fig. 6e**). Spontaneous recovery of motor function was delayed by knockdown of the IP receptor by siRNA (**Fig. 3g**,**h**). This effect of IP receptor knockdown on axonal remodeling was not caused by increased dieback of the CST, which is immunoreactive for protein kinase C γ (PKC-γ, a marker of the CST), rostral to the lesion (**Supplementary Fig. 6f**,**g**). Of note, in the cervical spinal cord, a location distal to the lesion, the formation of CST collaterals increased in EAE, and this increase was not abolished by transfection of IP receptor siRNA

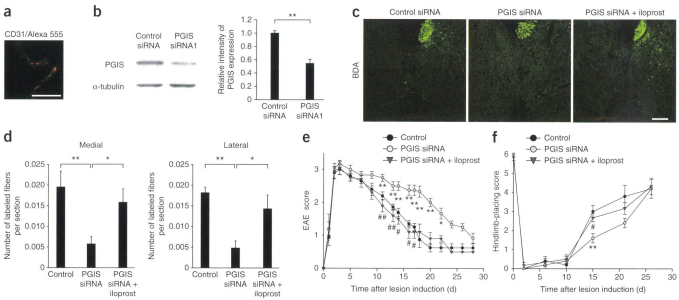

Figure 4 Knockdown of PGIS in vascular endothelial cells delays recovery of motor function in EAE. (**a**) Representative image of a brain section immunostained for CD31 (Alexa Fluor 488) in mice transfected with Alexa Fluor 555–labeled oligonucleotides showing that transfection of the oligonucleotide into the endothelial cells succeeded *in vivo*. Scale bar, 20 μm. (**b**) Expression of PGIS in capillary endothelial cells in the brain after transfection with PGIS siRNA. The graph shows the relative intensity of the PGIS bands relative to α-tubulin. Values are represented as mean ± s.e.m. $^{**}P < 0.01$ using one-way ANOVA followed by Student's *t* test. (**c**) Representative cross-sections of the thoracic spinal cord showing BDA-labeled sprouting fibers of the CST 14 d after the induction of EAE. Scale bar, 100 μm. (**d**) Quantitative analysis of hindlimb CST fiber innervation in the thoracic spinal cord 14 d after EAE induction. Values represent the mean ± s.e.m. (control: $n = 5$; PGIS siRNA: $n = 7$; PGIS siRNA plus iloprost: $n = 6$). $^{*}P < 0.05$, $^{**}P < 0.01$ using one-way ANOVA followed by Scheffe's test. (**e**,**f**) Quantification of EAE scores (**e**) and hindlimb-placing scores (**f**) in EAE mice treated as indicated. Values are represented as mean ± s.e.m. (control siRNA: $n = 6$; PGIS siRNA: $n = 6$; PGIS siRNA plus iloprost: $n = 6$). $^{*}P < 0.05$, $^{**}P < 0.01$ compared to control, $^{\#}P < 0.05$, $^{\#\#}P < 0.01$ compared to PGIS siRNA using one-way ANOVA followed by Bonferroni's test.

(**Supplementary Fig. 6b**,**i**), suggesting these plastic changes in CST remodeling in this remote area are induced through a mechanism that is independent of the IP receptor. These results suggest the IP receptor is required for CST reorganization around the EAE lesion, as well as for one phase of functional recovery after induction of focal EAE.

Prostacyclin drives motor recovery and CST reorganization

To assess the role of prostacyclin expressed in vascular endothelial cells, we inhibited PGIS expression in vascular endothelial cells (**Fig. 4a**,**b**) by intravenous injection of PGIS siRNA. This procedure achieved selective suppression of PGIS expression in $CD31^+$ cells but not in PDGFR-α^+ cells in the spinal cord (**Supplementary Fig. 7a**,**b**). Indeed, we did not observe the transfected fluorescent oligonucleotide in PDGFR-α^+–cells (**Supplementary Fig. 7c**). CST collateral formation was reduced on day 14 after EAE induction when endothelial vascular cells were transfected with PGIS siRNA at days 0 and 7 (medial, 0.0058; lateral, 0.0048) as compared to transfection of EAE mice with the control siRNA (medial, 0.0200; lateral, 0.0182; **Fig. 4c**,**d** and **Supplementary Fig. 7d**). Recovery of motor function was delayed by PGIS knockdown in endothelial cells (**Fig. 4e**,**f**). The effect of PGIS knockdown on CST reorganization and recovery of motor function was attenuated by intrathecal treatment with the IP receptor agonist iloprost on the day after EAE induction (PGIS siRNA: medial, 0.0058; lateral, 0.0048; PGIS siRNA plus iloprost: medial, 0.0159; lateral, 0.0143; **Fig. 4c**–**f**). None of the treatments (PGIS siRNA or iloprost) affected vascular formation compared to EAE plus control siRNA in the spinal cord (**Supplementary Fig. 7e**,**f**). These data show that prostacyclin expressed by vascular endothelial cells is required for reorganization of the CST and functional recovery after EAE.

IP receptor agonist promotes motor recovery

We next tested whether IP receptor activation promoted recovery after EAE. We delivered iloprost intrathecally into the thoracic spinal cord using osmotic minipumps starting on the day of EAE induction. Treatment with iloprost significantly increased the number of BDA-labeled sprouting CST fibers at day 14 after induction (medial, 0.0243; lateral, 0.0230) compared to treatment with a vehicle control (medial, 0.0172; lateral, 0.0158; **Fig. 5a**,**b** and **Supplementary Fig. 8a**). This treatment did not alter PGIS expression in the lesioned tissues 7 d after EAE induction (**Fig. 5c**). EAE scores and spontaneous recovery of motor function were accelerated by iloprost treatment (**Fig. 5d**,**e**).

To obtain additional electrophysiological evidence regarding rewiring of the injured CST, we measured cortical-evoked cord dorsum potentials (CDPs) at 14 d after induction of EAE. The results showed that the connection from the cerebral cortex to the CST below the EAE lesion was facilitated by iloprost treatment (**Fig. 5f**,**g**). Consistent with the siRNA results, treatment with CAY10441, an IP receptor antagonist, significantly decreased the number of BDA-labeled sprouting CST fibers at 14 d after EAE induction (medial, 0.0063; lateral, 0.0063) compared to treatment with the vehicle control (**Fig. 5a**,**b**). Spontaneous recovery of motor function and reconnection of the injured CST as measured by CDPs were also prevented by treatment with CAY10441 (**Fig. 5d**–**g**). Oligodendrocytes in the spinal cord only faintly expressed the IP receptor (**Supplementary Fig. 8b**). Neither iloprost nor CAY10441 had an effect on myelination, axonal damage or the formation of new vessels in the spinal cord at 14 d after EAE induction (**Supplementary Fig. 8c**–**f**) and did not alter the accumulation of $CD4^+$ or $CD11b^+$ cells in the spinal cord at 7 d after induction (**Supplementary Fig. 8c**,**d**).

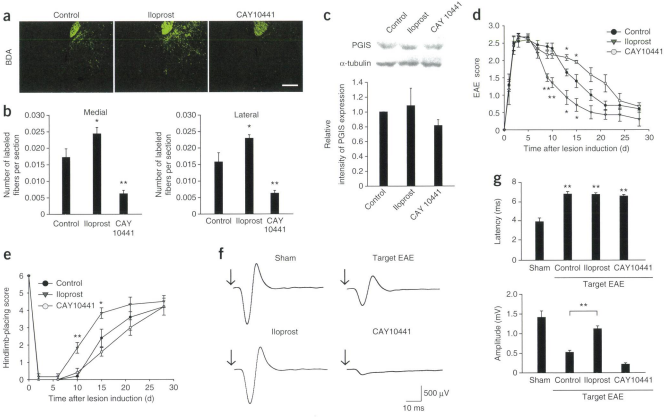

Figure 5 Treatment with iloprost improves the EAE-induced deficit in motor function. (**a**) Representative cross-sections of the thoracic spinal cord showing BDA-labeled sprouting fibers of the CST 14 d after the induction of EAE and treatment with iloprost or CAY10441. Scale bar, 100 μm. (**b**) Quantitative analysis of hindlimb CST fiber innervation in the thoracic spinal cord 14 d after EAE induction. Values are represented as mean ± s.e.m. (control: $n = 6$; iloprost: $n = 5$; CAY10441: $n = 6$). $^{*}P < 0.05$, $^{**}P < 0.01$ using one-way ANOVA followed by Scheffe's test. (**c**) Western blot analysis and relative quantification of PGIS expression in target lesions of the thoracic spinal cord obtained from each group of mice. Values are represented as mean ± s.e.m. ($n = 3$). (**d**,**e**) Quantification of EAE scores (**d**) and hindlimb-placing scores (**e**) in EAE mice treated with iloprost or CAY10441. Values are represented as mean ± s.e.m. (control: $n = 6$; iloprost: $n = 5$; CAY10441: $n = 6$). $^{*}P < 0.05$, $^{**}P < 0.01$ using one-way ANOVA followed by Bonferroni's test. (**f**) Representative sample traces of cortical evoked potentials below the lesion in each group of mice. Arrows indicate the times of cortical stimulation. (**g**) The average latencies and amplitudes of cortical evoked potentials from the experiments in **f**. Values are represented as mean ± s.e.m. (sham: $n = 6$, control: $n = 6$; iloprost: $n = 5$; CAY10441: $n = 6$). $^{**}P < 0.01$ using one-way ANOVA followed by Scheffe's test.

Treatment with either iloprost or CAY10441 did not alter T cell responses to antigen in a proliferation assay compared with vehicle-treated controls (**Supplementary Fig. 9a**). Moreover, we observed no differences in the concentration of various cytokines in the spinal cord tissue or the amount secreted by T cells obtained from vehicle-, iloprost- or CAY10441-treated mice stimulated with myelin basic protein (MBP) (**Supplementary Fig. 9b,c**). These results suggest that iloprost or CAY10441 did not affect inflammation.

DISCUSSION

Our present findings suggest that soluble factors released from the vascular endothelium promote axonal rewiring and functional recovery in EAE. Treatment with iloprost does not reduce the clinical onset of EAE in rats[25], suggesting the IP receptor is not involved in the development of EAE and prostacyclin and its receptor do not have a major role in regulating inflammation in EAE. Supporting this notion, our *in vitro* experiments revealed that prostacyclin does not modulate T cell proliferation or cytokine production from re-stimulated T cells *in vitro*. In addition, because prostacyclin is secreted by new vessels, which are formed as a result of inflammation, prostacyclin may act specifically during the remission phase of EAE. In this context, we describe a new role for prostacyclin.

During development, peripheral sympathetic axons are guided by endothelin secreted from the external carotid artery[26], suggesting that axonal guidance is influenced by endothelium-derived factors during development of the peripheral nervous system. In contrast, a close association of axons and blood vessels had not been observed in the CNS, suggesting this type of navigation was PNS specific and restricted to development. Our present findings reveal an unexpected function of blood vessels in the adult CNS in response to injury. Prostacyclin may be associated with other types of CNS disease, as neovascularization also occurs in brain tumors, epilepsy and stroke. *In vivo* imaging has suggested a role of new vessels in influencing sprouting of injured axons in response to spinal cord injury[27]. Blood vessel density is increased within 2 weeks after spinal cord injury, and these vessels seem to exert a growth-stimulating action on dorsal root ganglia[27]. Thus, the mechanism we identified here may be relevant to other CNS diseases that disrupt neuronal networks in adults. Taken together, our *in vitro* and *in vivo* findings show that prostacyclin is secreted from neovessels formed as a result of CNS inflammation. By signaling through the IP receptor expressed on neurons, this promotes neuronal remodeling and the formation of a compensatory motor neuronal network that contributes to the recovery of hindlimb motor function after EAE.

METHODS

Methods and any associated references are available in the online version of the paper.

Note: Supplementary information is available in the online version of the paper.

ACKNOWLEDGMENTS

The authors are grateful to N. Takakura, H. Kidoya and M. Ueno for helpful comments and M. Niwa and S. Nakagawa for technical advice on culturing of endothelial cells. This work was supported by a Grant-in-Aid for Scientific Research on Innovative Areas (23122512) from the Japan Society for the Promotion of Sciences to R.M. and the Core Research for Evolutional Science and Technology from Japan Science and Technology Agency to T.Y.

AUTHOR CONTRIBUTIONS

R.M. performed all experiments, with the exception of the portions indicated below. C.T. supported immunohistochemical analyses. C.T. and S.M. helped with *in vitro* experiments. H.M. and H.F. provided the autopsy samples from individuals with multiple sclerosis. R.M. and T.Y. designed the experiments. T.Y. coordinated and directed the project and wrote the manuscript.

COMPETING FINANCIAL INTERESTS

The authors declare no competing financial interests.

Published online at http://www.nature.com/doifinder/10.1038/nm.2943.
Reprints and permissions information is available online at http://www.nature.com/reprints/index.html.

1. Lucas, S.M., Rothwell, N.J. & Gibson, R.M. The role of inflammation in CNS injury and disease. *Br. J. Pharmacol.* **147**, S232–S240 (2006).
2. Harel, N.Y. & Strittmatter, S.M. Can regenerating axons recapitulate developmental guidance during recovery from spinal cord injury? *Nat. Rev. Neurosci.* **7**, 603–616 (2006).
3. Hauser, S.L. & Oksenberg, J.R. The neurobiology of multiple sclerosis: genes, inflammation, and neurodegeneration. *Neuron* **52**, 61–76 (2006).
4. Trapp, B.D. & Nave, K.A. Multiple sclerosis: an immune or neurodegenerative disorder? *Annu. Rev. Neurosci.* **31**, 247–269 (2008).
5. Nikić, I. *et al.* A reversible form of axon damage in experimental autoimmune encephalomyelitis and multiple sclerosis. *Nat. Med.* **17**, 495–499 (2011).
6. DeLuca, G.C., Ebers, G.C. & Esiri, M.M. Axonal loss in multiple sclerosis: a pathological survey of the corticospinal and sensory tracts. *Brain* **127**, 1009–1018 (2004).
7. Black, J.A., Liu, S., Hains, B.C., Saab, C.Y. & Waxman, S.G. Long-term protection of central axons with phenytoin in monophasic and chronic-relapsing EAE. *Brain* **129**, 3196–3208 (2006).
8. Kerschensteiner, M. *et al.* Remodeling of axonal connections contributes to recovery in an animal model of multiple sclerosis. *J. Exp. Med.* **200**, 1027–1038 (2004).
9. Jackson, J.R., Seed, M.P., Kircher, C.H., Willoughby, D.A. & Winkler, J.D. The codependence of angiogenesis and chronic inflammation. *FASEB J.* **11**, 457–465 (1997).
10. Fokman, J. & Brem, H. Angiogenesis and inflammation. in *Inflammation: Basic Principles and Clinical Correlates.* 2nd edn., 821–839 (Raven Press, New York, 1992).
11. Kirk, S., Frank, J.A. & Karlik, S. Angiogenesis in multiple sclerosis: is it good, bad or an epiphenomenon? *J. Neurol. Sci.* **217**, 125–130 (2004).
12. Costa, C., Incio, J. & Soares, R. Angiogenesis and chronic inflammation: cause or consequence? *Angiogenesis* **10**, 149–166 (2007).
13. Carmeliet, P. Blood vessels and nerves: common signals, pathways and diseases. *Nat. Rev. Genet.* **4**, 710–720 (2003).
14. Vane, J.R. & Botting, R.M. Pharmacodynamic profile of prostacyclin. *Am. J. Cardiol.* **75**, 3A–10A (1995).
15. Buddeberg, B.S. *et al.* Behavioral testing strategies in a localized animal model of multiple sclerosis. *J. Neuroimmunol.* **153**, 158–170 (2004).
16. Bareyre, F.M. *et al.* The injured spinal cord spontaneously forms a new intraspinal circuit in adult rats. *Nat. Neurosci.* **7**, 269–277 (2004).
17. Courtine, G. *et al.* Recovery of supraspinal control of stepping via indirect propriospinal relay connections after spinal cord injury. *Nat. Med.* **14**, 69–74 (2008).
18. Menétrey, D., de Pommery, J. & Roudier, F. Propriospinal fibers reaching the lumber enlargement in the rat. *Neurosci. Lett.* **58**, 257–261 (1985).
19. Tessier-Lavigne, M. & Goodman, C.S. The molecular biology of axon guidance. *Science* **274**, 1123–1133 (1996).
20. Kirk, S.L. & Karlik, S.J. VEGF and vascular changes in chronic neuroinflammation. *J. Autoimmun.* **21**, 353–363 (2003).
21. Holley, J.E., Newcombe, J., Whatmore, J.L. & Gutowski, N.J. Increased blood vessel density and endothelial cell proliferation in multiple sclerosis cerebral white matter. *Neurosci. Lett.* **470**, 65–70 (2010).
22. Uesugi, N., Muramatsu, R. & Yamashita, T. Endothelin promotes neurite elongation by a mechanism dependent on c-Jun N-terminal kinase. *Biochem. Biophys. Res. Commun.* **383**, 509–512 (2009).
23. Snider, W.D., Zhou, F.Q., Zhong, J. & Markus, A. Signaling the pathway to regeneration. *Neuron* **35**, 13–16 (2002).
24. Hannila, S.S. & Filbin, M.T. The role of cyclic AMP signaling in promoting axonal regeneration after spinal cord injury. *Exp. Neurol.* **209**, 321–332 (2008).
25. Jung, S., Donhauser, T., Toyka, K.V. & Hartung, H.P. Propentofylline and iloprost suppress the production of TNF-α by macrophages but fail to ameliorate experimental autoimmune encephalomyelitis in Lewis rats. *J. Autoimmun.* **10**, 519–529 (1997).
26. Makita, T., Sucov, H.M., Gariepy, C.E., Yanagisawa, M. & Ginty, D.D. Endothelins are vascular-derived axonal guidance cues for developing sympathetic neurons. *Nature* **452**, 759–763 (2008).
27. Dray, C., Rougon, G. & Debarbieux, F. Quantitative analysis by *in vivo* imaging of the dynamics of vascular and axonal networks in injured mouse spinal cord. *Proc. Natl. Acad. Sci. USA* **106**, 9459–9464 (2009).

nature medicine

Immunomodulatory glycan LNFPIII alleviates hepatosteatosis and insulin resistance through direct and indirect control of metabolic pathways

Prerna Bhargava[1], Changlin Li[2], Kristopher J Stanya[1], David Jacobi[1,3], Lingling Dai[1,4], Sihao Liu[1], Matthew R Gangl[1], Donald A Harn[2] & Chih-Hao Lee[1]

Parasitic worms express host-like glycans to attenuate the immune response of human hosts. The therapeutic potential of this immunomodulatory mechanism in controlling the metabolic dysfunction that is associated with chronic inflammation remains unexplored. We demonstrate here that administration of lacto-N-fucopentaose III (LNFPIII), a Lewis^x-containing immunomodulatory glycan found in human milk and on parasitic helminths, improves glucose tolerance and insulin sensitivity in diet-induced obese mice. This effect is mediated partly through increased interleukin-10 (Il-10) production by LNFPIII-activated macrophages and dendritic cells, which reduces white adipose tissue inflammation and sensitizes the insulin response of adipocytes. Concurrently, LNFPIII treatment upregulates nuclear receptor subfamily 1, group H, member 4 (Fxr-α, also known as Nr1h4) to suppress lipogenesis in the liver, conferring protection against hepatosteatosis. At the signaling level, the extracellular signal-regulated kinase (Erk)-activator protein 1 (Ap1) pathway seems to mediate the effects of LNFPIII on both inflammatory and metabolic pathways. Our results suggest that LNFPIII may provide new therapeutic approaches to treat metabolic diseases.

The metabolic syndrome is often associated with obesity and is a major medical and economic concern worldwide. Nutrient surplus is one of the main factors that contribute to the obesity pandemic, as well as to increased metabolic burdens on the mitochondria and the endoplasmic reticulum, leading to subcellular organelle dysfunction[1]. Chronic inflammation is often observed in states of obesity and is a common outcome of these metabolic stresses and a key contributor to the pathologies that are associated with metabolic diseases, such as insulin resistance, type 2 diabetes, atherosclerosis and nonalcoholic fatty liver diseases. Although the features of chronic metabolic-related inflammation (or meta-inflammation) differ from those of acute inflammatory responses to exogenous insults, studies have shown that several pathogen-sensing mechanisms of innate immunity are negative regulators of insulin sensitivity[1]. For example, pattern-recognition receptors and downstream effectors (such as Toll-like receptor-4 (Tlr4), IκB kinase β (Ikk-β), Ikk-ε, tumor necrosis factor α (Tnf-α) and double-stranded RNA-dependent protein kinase) have been shown to be activated by high-fat feeding and induce metabolic diseases[2–6]. In addition, activation of the nucleotide-binding domain, leucine-rich-containing family, pyrin domain-containing-3 (Nlrp3) inflammasome, possibly in response to lipid metabolites (for example, fatty acids or ceramides)[7,8], results in the cleavage of pro-caspase-1 (pro-Casp-1) and release of mature Il-1β, which causes insulin resistance[7,8].

Resident macrophages and lymphocytes in metabolic tissues, such as white adipose tissue (WAT) and liver, are believed to have important roles in meta-inflammation[9–13]. For example, obesity triggers the appearance of proinflammatory macrophages in the WAT, where they are histologically presented as crown-like structures (CLS)[14,15]. These so-called 'classically activated' (or M1) macrophages are partly responsible for the low-grade, chronic inflammation that is associated with metabolic dysregulation[1]. In contrast, adipose-resident macrophages from lean individuals have an 'alternatively activated' (or M2) phenotype[16], which functions to repair damage inflicted by pro-inflammatory M1 signals[17]. Studies have identified several sources of T helper type 2 (T_H2) cytokines (for example, Il-4 and Il-13) within WAT that mediate alternative activation[10,13,18]. Depletion of T_H2 cytokine–producing cells or the downstream mediators in macrophages leads to insulin resistance[10,13,19]. In contrast, increased T_H2 cytokine production, as in helminth infection, improves glucose homeostasis[18]. Although it remains unclear how T_H2-biased, anti-inflammatory immune responses improve metabolic homeostasis, overexpression of the anti-inflammatory cytokine Il-10 has been shown to improve insulin sensitivity[20].

The ability to drive T_H2-type and anti-inflammatory responses during helminth infection has been associated with decreased damage to host tissues, prolonging host survival[21]. During infection with *Schistosoma mansoni*, parasite eggs trapped in host tissues,

[1]Department of Genetics and Complex Diseases, Division of Biological Sciences, Harvard School of Public Health, Boston, Massachusetts, USA. [2]Department of Infectious Diseases, College of Veterinary Medicine, University of Georgia, Athens, Georgia, USA. [3]Centre Hospitalier Régional Universitaire de Tours, Service de Medecine Interne–Nutrition, INSERM U1069, Université François Rabelais, Tours, France. [4]Pharmacogenetics Research Institute, Institute of Clinical Pharmacology, Central South University, Changsha, Hunan, China. Correspondence should be addressed to C.-H.L. (clee@hsph.harvard.edu) or D.A.H. (dharn@uga.edu).

Received 29 May; accepted 30 August; published online 28 October 2012; doi:10.1038/nm.2962

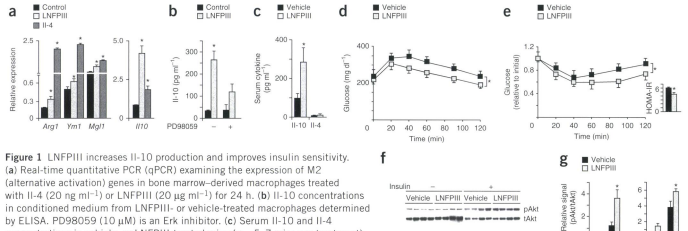

Figure 1 LNFPIII increases Il-10 production and improves insulin sensitivity. (**a**) Real-time quantitative PCR (qPCR) examining the expression of M2 (alternative activation) genes in bone marrow–derived macrophages treated with Il-4 (20 ng ml^{-1}) or LNFPIII (20 $\mu g\ ml^{-1}$) for 24 h. (**b**) Il-10 concentrations in conditioned medium from LNFPIII- or vehicle-treated macrophages determined by ELISA. PD98059 (10 μM) is an Erk inhibitor. (**c**) Serum Il-10 and Il-4 concentrations in vehicle- or LNFPIII-treated mice ($n = 5–7$ mice per treatment). (**d**,**e**) GTT (**d**) and ITT (**e**) in vehicle- and LNFPIII-treated mice. The inset in **e** shows the HOMA-IR. (**f**) Western blot analyses examining insulin-stimulated Akt phosphorylation in WAT from vehicle- and LNFPIII-treated mice (from four individual mice per treatment). pAkt, phosphorylated Akt; tAkt, total Akt. (**g**) The relative signal of pAkt to tAkt in WAT with or without insulin injection quantified by densitometry using the western signals in **f** or by ELISA-based assays. All values are expressed as means ± s.e.m. For *in vitro* assays, the mean and s.e.m. were determined from 3–4 biological replicates for a representative experiment. Experiments were repeated three times. *In vivo* studies were reproduced in three mouse cohorts ($n = 5–7$ mice per treatment). Insulin signaling was examined in two of the three cohorts. $^*P < 0.05$ (LNFPIII or Il-4 compared to vehicle control).

such as the liver, are the main stimuli for T_H2 cytokine production in mice[22]. Injection of a saline-soluble homogenate of eggs (soluble egg antigen, SEA) is sufficient to induce T_H2 biasing of the immune response[23]. Subsequently, it was shown that glycans and glycoproteins found in SEA, such as the $Lewis^X$-containing LNFPIII, GalNAcβ1–4GlcNAc (LacdiNAc), fucosylated LacdiNAc and omega-1 (a T2 RNase), are capable of mediating immunomodulatory activity[24–27]. Notably, LNFPIII is one of the major sugars found in postpartum human milk and is thought to have a similar protective immunomodulatory effect in the fetus[28,29]. These observations suggest that during coevolution with human hosts, *S. mansoni* parasites expressing immunomodulatory glycans were able to escape detection and had a developmental advantage. In fact, macrophages treated with LNFPIII show a T_H2 cytokine–independent, M2-like phenotype characterized by the expression of the M2 markers arginase 1 (Arg1) and chitinase 3-like 3 (Ym1, also known as Chi3l3)[30]. LNFPIII and other helminth-derived glycans induce Il-10 production[31], upregulate T regulatory cell numbers[32] and inhibit bacterial lipopolysaccharide–induced inflammatory responses[31].

The mechanisms through which LNFPIII exerts these anti-inflammatory activities remain poorly characterized. It has been shown that LNFPIII signals through several C-type lectin receptors[33] and Tlr4 (ref. 34), which leads to the activation of Erk. Although helminth infections polarize the immune response toward the T_H2 type, studies have shown that it reduces, rather than exacerbates, the incidence of allergic responses, possibly because of the anti-inflammatory activity of Il-10 (ref. 35).

Here we further characterize the unique immunomodulatory activity of LNFPIII and determine whether LNFPIII is effective in dampening chronic inflammation and improving metabolic function in a diet-induced model of type 2 diabetes. Our results show that treatment with LNFPIII or SEA reduces inflammation and increases insulin sensitivity in WAT in an Il-10–dependent manner. Further, LNFPIII directly regulates the lipogenic program in hepatocytes and prevents obesity-induced hepatic steatosis through a newly identified link to the nuclear receptor Fxr-α.

RESULTS

LNFPIII treatment improves insulin sensitivity

LNFPIII has been shown to induce M2-like macrophage activation independent of T_H2 cytokines[30]. We confirmed that LNFPIII treatment upregulated *Arg1*, *Ym1* and macrophage galactose-type C-type lectin-1 (*Mgl1*, also known as *Cd301*) expression, albeit to a lesser extent than Il-4, in macrophages (**Fig. 1a**). In contrast, LNFPIII was more effective than Il-4 in inducing *Il10* expression and release into macrophage-conditioned media (**Fig. 1a**,**b** and **Supplementary Fig. 1a**). This effect was blunted when we treated macrophages with PD98059 to block the activity of Erk (**Fig. 1b**), which has been implicated in mediating LNFPIII signal transduction[31,34,36]. We also found that LNFPIII increased Il-10 production in dendritic cells (**Supplementary Fig. 1b**). The ability of LNFPIII to upregulate *Il10* expression was independent of signal transducer and activator of transcription 6 (Stat6) and peroxisome proliferator activator receptor δ (Ppar-δ), which are known effectors of T_H2 cytokines (**Supplementary Fig. 1c**). Taken together, LNFPIII induces an anti-inflammatory state that increases Il-10 production.

To determine whether the immunomodulatory activity of LNFPIII might be beneficial for treating metabolic diseases, we injected 8-week-old male mice (C57BL/6) with vehicle or LNFPIII (25 μg, twice a week) for 4–6 weeks after the onset of high-fat diet (HFD)-induced obesity and metabolic dysfunction. Consistent with the *in vitro* study, LNFPIII-treated mice had higher circulating concentrations of Il-10 but the same concentrations of Il-4 compared to vehicle-treated mice (**Fig. 1c**). When subjected to glucose tolerance tests (GTTs), LNFPIII-treated mice showed significantly higher glucose-handling capability compared to the vehicle-treated control group (**Fig. 1d**; area under the curve (AUC), vehicle = 36,727.5 ± 1,769.13 (mean ± s.e.m.); LNFPIII = 29,244± 1,119.7, $P = 0.0159$). LNFPIII treatment also led to higher insulin sensitivity compared to vehicle treatment, as shown by reductions in fasting serum insulin concentrations (vehicle, 1.54 ± 0.07 ng ml^{-1}; LNFPIII: 1.29 ± 0.06 ng ml^{-1}, $P < 0.05$), and improvements in both the results of insulin tolerance tests (ITTs) (AUC, vehicle = 123.58 ± 4.79; LNFPIII = 98.23 ± 3.30,

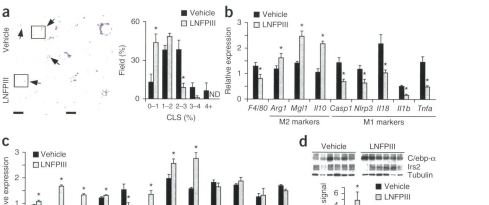

Figure 2 Reduced inflammation and enhanced insulin signaling in WAT of LNFPIII-treated mice. (**a**) WAT histology showing CLS (left). The arrows point to CLS, and the images on the right are enlargements of the boxed areas in the images on the left. Scale bar: left, 200 μm; right, 50 μm. CLS quantified in 90 fields from 30 sections (three fields per section) for each individual mouse (right). $n = 4$ mice per group. The values on the *y* axis indicate the percentage of fields that contain a certain percentage of CLS. The values on the *x* axis indicate the percentage of CLS-containing adipocytes in a given field. ND, not detected. (**b**) Real-time qPCR analyses of M1 and M2 gene expression in WAT of vehicle- and LNFPIII-treated mice ($n = 5$ mice per treatment). (**c**) Metabolic gene expression in WAT determined by real-time qPCR. FA, fatty acid. (**d**) Western blotting showing C/ebp-α and Irs2 protein abundances in WAT (top) and relative C/ebp-α and Irs2 signals normalized to tubulin (bottom). All values are expressed as means ± s.e.m. Metabolic studies were reproduced in three mouse cohorts ($n = 5$–7 mice per treatment). CLS and expression analyses were examined in one and three of the three cohorts, respectively. *$P < 0.05$ (LNFPIII compared to vehicle).

$P = 0.0357$) and the homeostasis model of assessment-insulin resistance (HOMA-IR) (**Fig. 1e**). We found enhanced insulin signaling, determined by insulin-stimulated Ser473 Akt phosphorylation, in WAT but not in liver or muscle of mice treated with LNFPIII (**Fig. 1f**,**g** and data not shown). We conducted parallel metabolic studies with SEA treatment, which led to higher circulating Il-10 and Il-4 concentrations than vehicle treatment (**Supplementary Fig. 1d**). HFD-fed mice treated with SEA also showed an improved insulin response compared to vehicle-treated mice, as determined by GTTs, ITTs, fasting insulin concentrations and HOMA-IR (**Supplementary Fig. 1e**–**g**). Treatment with LNFPIII or SEA did not affect body weight, food intake or circulating concentrations of lipids or adiponectin (**Supplementary Table 1**). These studies demonstrate the potential of using glycans derived from *S. mansoni* egg extract, including LNFPIII, to improve glucose homeostasis and insulin sensitivity.

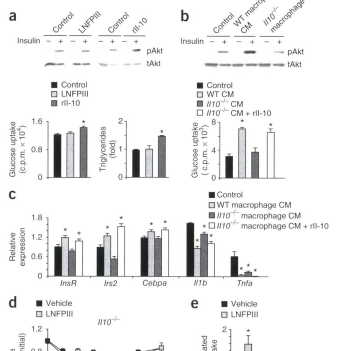

Figure 3 LNFPIII-primed macrophage conditioned medium improves insulin sensitivity in 3T3-L1 adipocytes in an Il-10–dependent manner. (**a**) Western blotting showing protein abundances of tAkt and insulin-stimulated pAkt in 3T3-L1 adipocytes treated with vehicle, LNFPIII or rII-10 (top; representative samples from three experiments are shown, each with three biological replicates). Insulin-stimulated glucose uptake determined using radioactive 2-[^{3}H]deoxy-D-glucose (bottom left) and cellular triglyceride contents measured at day 6 of 3T3-L1 adipocyte differentiation (bottom right). The vehicle controls for LNFPIII (20 μg ml^{-1}) and Il-10 (10 ng ml^{-1}) were dextran and PBS, respectively. (**b**) Western blotting showing protein abundances of tAkt and insulin-stimulated pAkt in adipocytes treated with control and conditioned medium (CM) from LNFPIII-primed WT and *Il10*$^{-/-}$ macrophages (top) and insulin-stimulated glucose uptake in adipocytes (bottom). (**c**) Gene expression in 3T3-L1 adipocytes determined by real-time qPCR. (**d**) ITT in vehicle- and LNFPIII-treated *Il10*$^{-/-}$ mice ($n = 6$ mice per treatment per genotype). AUC, area under the curve of ITT (mg dl^{-1} min). (**e**) *Ex vivo* glucose uptake assay performed in adipose tissue slices collected before and after portal vein injection of 5 U kg^{-1} insulin. All values are expressed as means ± s.e.m. For *in vitro* assays, the mean and s.e.m. were determined from 3–4 biological replicates for a representative experiment. Experiments were repeated three times. Studies in *Il10*$^{-/-}$ and control mice were conducted in one cohort ($n = 6$ mice). *$P < 0.05$ (treatment compared to control).

LNFPIII enhances WAT insulin signaling through Il-10

The interaction between resident macrophages and adipocytes has an important role in adipose tissue metabolic homeostasis[10]. WAT histological analyses demonstrated that mice given LNFPIII had lower numbers of CLSs and lower expression of *F4/80* (a macrophage marker also known as *Emr1*; **Fig. 2a**,**b**) compared to vehicle-treated mice. In addition, *Il10* and M2 genes (*Arg1* and *Mgl1*) were upregulated and *Tnfa* and genes encoding the inflammasome (*Casp1*, *Nlrp3*, *Il18*

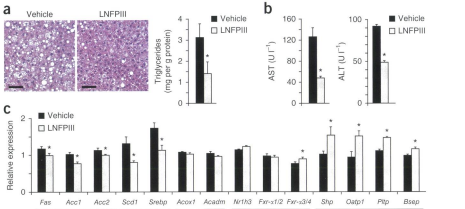

Figure 4 LNFPIII protects against hepatic steatosis induced by high-fat diet. (**a**) Liver histology and triglyceride content analyses to determine hepatic fat accumulation in vehicle- and LNFPIII-treated mice. Scale bars, 100 μm. (**b**) Circulating AST and ALT concentrations to assess liver function. (**c**) Gene expression analyses in livers from vehicle- or LNFPIII-treated mice ($n = 5$ mice per treatment) by real-time qPCR. *Fxr-α1/2*, *Fxr-α1* and *Fxr-α2*; *Fxr-α3/4*, *Fxr-α3* and *Fxr-α4*. All values are expressed as means ± s.e.m. Metabolic studies were reproduced in three mouse cohorts ($n = 5$–7 mice per treatment). Histology was examined in one of three total cohorts and lipid and expression analyses were examined in all three cohorts. $^*P < 0.05$ (LNFPIII compared to vehicle control).

and *Il1b*) were downregulated by LNFPIII treatment (**Fig. 2b**). Consistent with the higher insulin sensitivity, the expression of insulin receptor β (*InsRb*), insulin receptor substrate 2 (*Irs2*), CCAAT/enhancer binding protein α (*C/ebpa*), glucose transporter 4 (*Glut4*, also known as *Slc2a4*) and lipogenic genes was higher in WAT from LNFPIII-treated mice than from vehicle-treated control mice (**Fig. 2c**). C/ebp-α and Irs2 protein abundances were also higher in these mice than in controls (**Fig. 2d**). We obtained similar results in SEA-treated cohorts of mice (**Supplementary Fig. 2**). Of note, SEA induced *Arg1* expression in WAT to a greater extent than did LNFPIII, reflecting the fact that SEA treatment increased serum Il-4 concentrations (**Supplementary Fig. 1d**). These data support the notion that LNFPIII modulates WAT-resident macrophage inflammation and improves adipose tissue metabolic homeostasis.

Both *in vitro* and *in vivo* studies demonstrated that LNFPIII induced an anti-inflammatory phenotype characterized by elevated Il-10 concentrations, a cytokine that has been shown to improve metabolic homeostasis[20]. To address whether the insulin-sensitizing effect in WAT of LNFPIII injection is a direct action of the glycan or is mediated by Il-10, we cultured 3T3-L1 adipocytes with or without LNFPIII or recombinant Il-10 (rIl-10). We found that rIl-10, but not LNFPIII, improved insulin responsiveness, as determined by insulin-stimulated Akt phosphorylation, glucose uptake and lipogenesis (**Fig. 3a**). Conditioned medium from LNFPIII-primed wild type (WT) macrophages, which contained higher Il-10 concentrations than vehicle-primed conditioned medium (**Fig. 1b**), was able to reproduce the insulin-sensitizing activity in 3T3-L1 adipocytes, an effect that was abrogated in conditioned medium from LNFPIII-primed $Il10^{-/-}$ macrophages (**Fig. 3b**). Furthermore, conditioned medium derived from LNFPIII-primed WT, but not $Il10^{-/-}$, macrophages induced the expression of *InsR*, *Irs2* and *C/ebpa* and suppressed the expression of *Il1b* and *Tnfa* in 3T3-L1 adipocytes (**Fig. 3c**). Reconstitution of rIl-10 in conditioned medium from $Il10^{-/-}$ macrophages restored its ability to improve insulin-stimulated glucose uptake and modulate metabolic and inflammatory gene expression (**Fig. 3b**,**c**). *In vivo*, LNFPIII was unable to improve insulin tolerance (**Fig. 3d** and **Supplementary Table 1**), enhance insulin-stimulated glucose uptake (**Fig. 3e**) or inhibit WAT inflammation (**Supplementary Fig. 3a**,**b**) in $Il10^{-/-}$ mice. In addition, $Il10^{-/-}$ mice were more insulin resistant than WT control mice (**Supplementary Fig. 3c**). Reciprocally, rIl-10 injections (1 μg every other day for three total doses) improved glucose tolerance and insulin sensitivity and recapitulated the WAT phenotype in LNFPIII-treated mice (**Supplementary Fig. 3d**–**h** and **Supplementary Table 1**). Taken together, the results suggest that Il-10 is required for LNFPIII-mediated improvement in WAT insulin signaling and systemic glucose homeostasis.

LNFPIII protects against diet-induced hepatic steatosis

In addition to improving WAT function, histological and triglyceride content analyses showed a strong protective effect of treatment with LNFPIII against HFD-induced hepatic lipid accumulation compared to treatment with vehicle (**Fig. 4a**). Furthermore, overall liver function, determined by circulating concentrations of alanine aminotransferase (ALT) and aspartate aminotransferase (AST), was substantially better in LNFPIII-treated mice than in vehicle-treated control mice (**Fig. 4b**). In line with lower hepatic steatosis, the expression of lipogenic genes, including fatty acid synthase (*Fas*), acetyl-CoA carboxylases 1 and 2 (*Acc1* and *Acc2*, also known as *Acaca* and *Acacb*, respectively), stearoyl-CoA desaturase 1 (*Scd1*) and sterol regulatory element-binding protein 1c (*Srebp1c*, also known as *Srebf1*), were lower in LNFPIII-treated livers than in vehicle-treated livers (**Fig. 4c**).

Srebp-1c is a master lipogenic transcription factor whose expression and transcriptional activity are controlled by a network of nuclear receptor signaling pathways, notably, the positive regulator nuclear receptor subfamily 1, group H, member 3 (Lxr-α, also known as Nr1h3)[37] and the negative regulators Fxr-α (also known as Nr1h4) and its target nuclear receptor subfamily 0, group B, member 2 (Shp, also known as Nr0b2)[38]. The Fxr-α gene consists of two major 5′ regulatory regions, with the upstream and downstream promoters driving the expression of two isoforms of the gene, referred to here as *Fxr-α1* and *Fxr-α2*, and *Fxr-α3* and *Fxrα4*, respectively[39]. The only difference between Fxr-α1 and Fxr-α2 (or Fxr-α3 and Fxr-α4) is a four–amino-acid insertion in Fxr-α1 (or Fxr-α3). We found that expression of the *Fxr-α3/α4* isoforms, as well as several known Fxr target genes[39], including *Shp*, organic anion-transporting polypeptides (*Oatp*, also known as *Slco1a1*), phospholipid transfer protein (*Pltp*) and bile salt efflux pump (*Bsep*, also known as *Abcb11*), were upregulated in the livers of LNFPIII-treated mice compared to vehicle-treated control mice (**Fig. 4c**). The expression of the Lxr-α gene was the same in LNFPIII-treated and vehicle-treated mice. We obtained similar effects with SEA treatment, except that SEA upregulated both *Fxr-α1/α2* and *Fxr-α3/α4* (**Supplementary Fig. 4a**–**d**). Treatment with LNFPIII or SEA did not alter metabolic gene expression in muscle (**Supplementary Fig. 4e** and data not shown). These results indicate that LNFPIII prevents

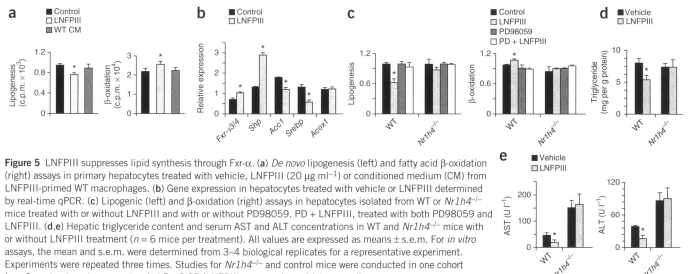

Figure 5 LNFPIII suppresses lipid synthesis through Fxr-α. (**a**) *De novo* lipogenesis (left) and fatty acid β-oxidation (right) assays in primary hepatocytes treated with vehicle, LNFPIII (20 μg ml^{-1}) or conditioned medium (CM) from LNFPIII-primed WT macrophages. (**b**) Gene expression in hepatocytes treated with vehicle or LNFPIII determined by real-time qPCR. (**c**) Lipogenic (left) and β-oxidation (right) assays in hepatocytes isolated from WT or *Nr1h4*$^{-/-}$ mice treated with or without LNFPIII and with or without PD98059. PD + LNFPIII, treated with both PD98059 and LNFPIII. (**d**,**e**) Hepatic triglyceride content and serum AST and ALT concentrations in WT and *Nr1h4*$^{-/-}$ mice with or without LNFPIII treatment ($n = 6$ mice per treatment). All values are expressed as means ± s.e.m. For *in vitro* assays, the mean and s.e.m. were determined from 3–4 biological replicates for a representative experiment. Experiments were repeated three times. Studies for *Nr1h4*$^{-/-}$ and control mice were conducted in one cohort ($n = 6$ per treatment per genotype). *$P < 0.05$ (LNFPIII compared to vehicle control).

ectopic fat accumulation in the liver and regulates the expression of transcriptional factors that are crucial for *de novo* lipogenesis.

To assess the role of LNFPIII or LNFPIII-primed macrophages in hepatic lipid homeostasis, we conducted lipogenic assays in isolated primary hepatocytes. LNFPIII, but not conditioned medium from LNFPIII-treated macrophages, suppressed lipogenesis and caused higher fatty acid β-oxidation compared to vehicle treatment (**Fig. 5a**). LNFPIII also induced expression of *Fxr-α3/α4* and *Shp* and suppressed the expression of *Srebp1c* and *Acc1* (**Fig. 5b**). As LNFPIII did not affect the expression of β-oxidation genes (**Figs. 4c** and **5b**), the increased fat burning resulting from LNFPIII treatment was probably secondary to the decreased fatty acid synthesis. These results suggest that, unlike in WAT, the effect of LNFPIII in the liver was not mediated by Il-10. Consistent with this notion, rIl-10 treatment did not affect hepatic *de novo* lipogenesis *in vitro* or *in vivo* (**Supplementary Fig. 5a–c**), and the protective effect of LNFPIII was preserved in *Il10*$^{-/-}$ liver (**Supplementary Fig. 5d,e**).

LNFPIII suppresses hepatic *de novo* lipogenesis through Fxr

The upregulation of the Fxr-α–dependent transcription program by LNFPIII suggested that LNFPIII may induce Fxr-α to inhibit fat synthesis. In fact, in hepatocytes with ablation of the Fxr-α gene

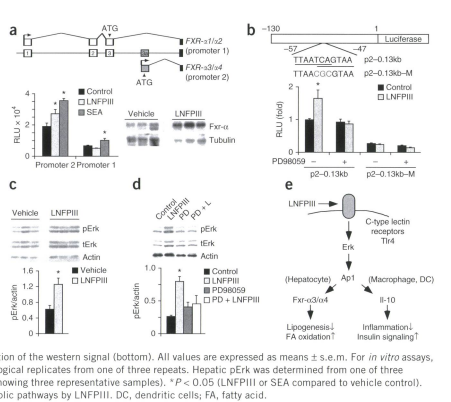

Figure 6 Induction of Fxr-α activity by LNFPIII is mediated by Erk-Ap1 signaling. (**a**) Genomic structure showing alternative promoter usage by human *FXR-α1/α2* (promoter 1) and *FXR-α3/α4* (promoter 2) (top). Relative activities (RLU) of luciferase reporters driven by human *FXR-α* promoter 1 (–2 kb) or human *FXR-α* promoter 2 (–0.13 kb) in HepG2 cells with or without LNFPIII (20 μg ml^{-1}) or SEA (2 μg ml^{-1}) treatment (bottom left) and western blotting showing Fxr-α protein abundances in livers from vehicle- or LNFPIII-treated mice (bottom right). (**b**) Diagram showing *FXR-α* promoter 2 (p2–0.13kb) or mutant (p2–0.13kb–M) reporter constructs (top). The two overlapping AP1 binding sites and the mutation are shown. Relative luciferase activities of p2–0.13kb and p2–0.13kb–M with or without LNFPIII and with or without PD98059 treatment (bottom). (**c**) Erk phosphorylation (pErk) in livers of vehicle- and LNFPIII-treated mice (top) and quantification of the western signal (bottom). (**d**) Western blot analyses showing Erk phosphorylation in hepatocytes with or without LNFPIII (L) and with or without PD98059 (PD) treatment (top; representative samples from three experiments each with three biological replicates) and quantification of the western signal (bottom). All values are expressed as means ± s.e.m. For *in vitro* assays, the mean and s.e.m. were determined from 3–4 biological replicates from one of three repeats. Hepatic pErk was determined from one of three metabolic study cohorts ($n = 5–7$ mice per cohort, showing three representative samples). *$P < 0.05$ (LNFPIII or SEA compared to vehicle control). (**e**) Model for direct and indirect regulation of metabolic pathways by LNFPIII. DC, dendritic cells; FA, fatty acid.

or inhibition of Erk by PD98059, LNFPIII was unable to inhibit *de novo* lipogenesis and increase fat oxidation (**Fig. 5c**). Furthermore, the ability of LNFPIII to reduce hepatic triglyceride accumulation, improve liver function and suppress lipogenic gene expression was lost in *Nr1h4*$^{-/-}$mice (**Fig. 5d,e** and **Supplementary Fig. 5f**), whereas the insulin-sensitizing activity of LNFPIII was unaffected (**Supplementary Fig. 5g–i** and **Supplementary Table 1**). Together, these results suggest that LNFPIII inhibits hepatic lipogenesis in a Fxr-α–dependent manner.

We next sought to determine whether Fxr-α is a molecular target of LNFPIII. As mentioned above, both the human and mouse FXR-α genes contain two major promoters (**Fig. 6a**). The 5′ proximal regulatory sequences are highly conserved between the mouse, rat and human FXR-α genes (**Supplementary Fig. 6a**). We examined the activities of reporters driven by regulatory regions of promoter 1 or promoter 2 in the FXR-α gene in HepG2 cells (human hepatoma cells). In accordance with the regulation of the Fxr-α gene in the liver or isolated hepatocytes, LNFPIII activated human promoter 2, whereas SEA induced the activity of both promoters (**Fig. 6a**). *In vivo*, Fxr-α protein abundance was higher in liver lysates from LNFPIII-treated compared to vehicle-treated mice (**Fig. 6a**). Through serial deletion of promoter 2, we defined a minimal LNFPIII-responsive region (approximately 130 bp upstream of the transcriptional start site) that contained consensus binding sites for C/EBP and AP1 (**Supplementary Fig. 6a**). Site-directed mutagenesis experiments further identified two overlapping AP1 sites (located between −57 bp and −47 bp) that were required for the induction of promoter 2 by LNFPIII (**Fig. 6b** and **Supplementary Fig. 6b**). Similarly, inhibition of Erk activation, which is upstream of AP1, by PD98059 abolished the LNFPIII-induced activity of promoter 2. In concert, LNFPIII treatment increased the amounts of phosphorylated Erk and total Erk in the liver (**Fig. 6c**) and hepatocytes (**Fig. 6d**). We obtained similar results in SEA-treated liver cells (**Supplementary Fig. 6c,d**). Collectively, these findings suggest that LNFPIII regulates hepatic lipogenesis through the Erk–Ap1–Fxr-α axis.

DISCUSSION

In this study, we demonstrate that LNPFIII (and SEA) alleviates the pathologies that are associated with HFD-induced obesity. LNFPIII treatment shifts the immune profile to an anti-inflammatory state and decreases macrophage infiltration in metabolic tissues of mice that have already become obese. This effect is, in part, driven by Il-10, which inhibits inflammation and enhances the insulin response in WAT. In the liver, LNFPIII upregulates the bile acid sensing nuclear receptor Fxr-α and its downstream transcriptional targets. Activated Fxr-α signaling suppresses lipogenesis and protects against hepatic steatosis. Taken together, our results demonstrate a therapeutic potential for LNFPIII in treating components of metabolic syndrome through its ability to directly modulate both immune and metabolic pathways.

The hygiene hypothesis attributes the increased incidence of autoimmune diseases and allergic responses in developed countries to reduced human contact with pathogens[40]. A special emphasis has been on the interaction between parasitic worms and humans[40,41]; in addition to the T_H2-biasing immune phenotype, helminth infections induce the proliferation of regulatory T cells and production of the anti-inflammatory cytokine Il-10 (ref. 42). Our data show that LNFPIII treatment is sufficient to increase Il-10 production in macrophages and dendritic cells. Regulatory T cells are probably another major source of Il-10 (ref. 42). These cells are enriched in fat tissues from lean individuals and have a role in maintaining WAT function[9]. Anti-inflammatory pathways are thought to improve metabolic homeostasis primarily through attenuating the action of proinflammatory signaling. Overexpression of Il-10 in the muscle was previously shown to improve systemic insulin resistance through suppression of inflammation[20]. We found that conditioned medium from LNFPIII-treated WT macrophages directly enhances insulin responses in adipocytes by upregulation of *InsR* and *Irs2* and increases insulin-mediated glucose uptake and lipogenesis in an Il-10–dependent manner. Acute rIl-10 injection in HFD-fed mice also improved glucose homeostasis but does not affect WAT macrophage infiltration (data not shown), suggesting that the insulin-sensitizing effect of Il-10 can be separated from its anti-inflammatory activity.

Several studies have identified *Il10* polymorphisms that are associated with insulin resistance and type 2 diabetes in humans[43,44]. Of note, a previous study has demonstrated that deficiency in hematopoietic cell–derived Il-10 in mice through transplantation of *Il10*$^{-/-}$ bone marrow does not affect HFD-induced tissue inflammation and insulin resistance[45]. However, *Il10* mRNA and protein abundances were several fold higher in WAT and liver in these mice than in mice that received WT bone marrow. It is unclear whether the compensatory increase in Il-10 production is from nonhematopoietic cells or residual WT bone marrow–derived cells. The result seems to suggest that increased Il-10 concentrations within metabolic tissues are sufficient to maintain metabolic homeostasis.

Although adipose tissue is known to produce adipokines, such as leptin, adiponectin and resistin, that modulate systemic glucose and lipid metabolism, this tissue, unlike the muscle, is not a major tissue for glucose uptake under physiological conditions. LNFPIII treatment did not affect the expression of these adipokines in WAT (**Supplementary Table 1** and data not shown). How does increased insulin sensitivity in WAT after LNFPIII treatment lead to improvement in systemic glucose homeostasis? It has been shown that GTT and ITT values in muscle-specific insulin receptor knockout (MIRKO) mice are indistinguishable from those in control mice, even though insulin-stimulated glucose uptake is substantially lower in the muscle of the knockout mice[46]. Subsequent studies attribute the normoglycemic phenotype of MIRKO mice to a threefold higher glucose deposition to the WAT compared to control mice[47], suggesting that, at least in mice, increased glucose uptake by adipocytes is able to sustain glucose homeostasis. Consistent with this notion, overexpression of the glucose transporter Glut4 in adipose tissues improves glucose tolerance[48]. Recently, increased glucose flux in adipocytes has been shown to upregulate fatty acid synthesis through a new isoform of carbohydrate-responsive element-binding protein (Chrebp-β, also known as Mlxipl)[49]. In addition, the expression of adipose *MLXIPL* and lipogenic genes positively correlates with insulin sensitivity in humans[49]. Our data demonstrate that LNFPIII treatment increases WAT glucose uptake and lipogenic gene expression, and *Mlxipl* was also induced (data not shown).

Although the mechanism through which fat synthesis in adipose tissues contributes to whole-body homeostasis is not completely understood, a lipogenic product of adipocytes has been linked to improved systemic metabolism[50]. The beneficial effect of LNFPIII could also be mediated by central regulation, in which reduced inflammation may lead to the improved central insulin sensitivity that is known to regulate hepatic glucose production[51]. However, LNFPIII does not seem to affect gluconeogenesis, as determined by pyruvate tolerance tests and the expression of gluconeogenic genes in the liver (data not shown).

After entering the body, *S. mansoni* settles in the hepatic portal system, where male and female worms mate and produce eggs[22].

Egg deposition in the liver is crucial for the induction of a systemic T_H2 response[22]. It is therefore not surprising that the liver is also a target of LNFPIII. At first glance, it seems unexpected that LNFPIII directly controls Fxr-α signaling to regulate hepatic lipid metabolism. Fxr-α senses endogenous bile acids and controls bile acid homeostasis by inhibiting production while increasing the recycling of bile acids in the enterohepatic system[52]. Fxr-α activation also suppresses lipogenesis through Shp-mediated inhibition of Srebp-1c in the liver[38]. Interestingly, *S. mansoni* is incapable of *de novo* synthesis of fatty acids and sterols but is able to synthesize complex lipids from precursors acquired from the host[53]. In addition, it has been shown that bile acids increase the number of deposited parasite eggs[54]. Therefore, the induction of Fxr-α by LNFPIII could be the host's response to limit the fatty and bile acids available to the worm. In contrast, bile acids facilitate lipid absorption in the intestine. Increased bile flow by Fxr-α may help schistosomes extract lipids from the digestive system of the host. Additionally, the induction of Fxr-α could serve as an anti-inflammatory mechanism in the liver, as Fxr-α is known to *trans* repress Nf-κb activity[55].

The signal transduction pathway of LNFPIII has not been fully characterized. In dendritic cells, LNFPIII is recognized by multiple C-type lectin receptors, including DC-SIGN (also known as Cd209), Mgl1 and mannose receptor. In addition, Erk is proposed to be a downstream effector of LNFPIII[31,56]. Erk-Ap1 has been shown to regulate *Il10* expression[36]. Indeed, the ability of LNFPIII to induce Il-10 production in the macrophage was blocked by Erk inhibition. We find that primary hepatocytes also express C-type lectin receptors, including DC-SIGN (data not shown), and LNFPIII is able to activate Erk in the liver, which mediates transcriptional regulation of the Fxr-α gene and the subsequent suppression of lipogenesis. The gene products of the two promoters (Fxr-α1 and Fxr-α2 compared to Fxr-α3 and Fxr-α4) differ by several amino acids located at the N terminus. Functional differences between the isoforms have not been reported[39]. Our data suggests that the induction of Fxr-α3 and Fxr-α4 by LNFPIII is sufficient to suppress lipogenesis. Whereas LNFPIII only activates the downstream promoter, SEA induces the activities of both promoters. This is not unexpected, as SEA is known to contain multiple bioactive glycans that could signal through different pathways[56]. Together, our data show that helminths may utilize the Erk-Ap1 signaling pathway to modulate host metabolism and immune responses (**Fig. 6e**). Our study suggests that the M2-like, anti-inflammatory activity of LNFPIII, which is probably a product of the survival strategy of helminths, may be used to treat metabolic disorders such as insulin resistance and nonalcoholic fatty liver diseases.

METHODS

Methods and any associated references are available in the online version of the paper.

Note: Supplementary information is available in the online version of the paper.

ACKNOWLEDGMENTS

We thank E. Hu and S.M. Reilly for technical support and T. Horng (Harvard School of Public Health) for providing reagents. P. Bhargava and K. Stanya were supported by a US National Institutes of Health training grant (T32ES016645). This work was supported by the American Diabetes Association, the American Heart Association and a US National Institutes of Health grant (R01AI056484, D.A.H. and R01DK075046, C.-H.L.).

AUTHOR CONTRIBUTIONS

P.B. was involved in experimental design and execution, data analyses and manuscript preparation. K.J.S., M.R.G. and C.L. conducted GTTs and ITTs with P.B. D.J. and L.D. provided technical assistance. S.L. assisted in hepatocyte isolations. C.L. provided LNFPIII and SEA preparations. D.A.H. helped with experimental design, data interpretation and manuscript writing. C.-H.L. directed the project, participated in data analyses and interpretation and wrote the manuscript.

COMPETING FINANCIAL INTERESTS

The authors declare no competing financial interests.

Published online at http://www.nature.com/doifinder/10.1038/nm.2962.
Reprints and permissions information is available online at http://www.nature.com/reprints/index.html.

1. Gregor, M.F. & Hotamisligil, G.S. Inflammatory mechanisms in obesity. *Annu. Rev. Immunol.* **29**, 415–445 (2011).
2. Arkan, M.C. *et al.* IKK-β links inflammation to obesity-induced insulin resistance. *Nat. Med.* **11**, 191–198 (2005).
3. Cai, D. *et al.* Local and systemic insulin resistance resulting from hepatic activation of IKK-β and NF-κB. *Nat. Med.* **11**, 183–190 (2005).
4. Chiang, S.H. *et al.* The protein kinase IKKε regulates energy balance in obese mice. *Cell* **138**, 961–975 (2009).
5. Nakamura, T. *et al.* Double-stranded RNA-dependent protein kinase links pathogen sensing with stress and metabolic homeostasis. *Cell* **140**, 338–348 (2010).
6. Shi, H. *et al.* TLR4 links innate immunity and fatty acid–induced insulin resistance. *J. Clin. Invest.* **116**, 3015–3025 (2006).
7. Vandanmagsar, B. *et al.* The NLRP3 inflammasome instigates obesity-induced inflammation and insulin resistance. *Nat. Med.* **17**, 179–188 (2011).
8. Wen, H. *et al.* Fatty acid–induced NLRP3-ASC inflammasome activation interferes with insulin signaling. *Nat. Immunol.* **12**, 408–415 (2011).
9. Feuerer, M. *et al.* Lean, but not obese, fat is enriched for a unique population of regulatory T cells that affect metabolic parameters. *Nat. Med.* **15**, 930–939 (2009).
10. Kang, K. *et al.* Adipocyte-derived Th2 cytokines and myeloid PPARδ regulate macrophage polarization and insulin sensitivity. *Cell Metab.* **7**, 485–495 (2008).
11. Nishimura, S. *et al.* CD8+ effector T cells contribute to macrophage recruitment and adipose tissue inflammation in obesity. *Nat. Med.* **15**, 914–920 (2009).
12. Odegaard, J.I. *et al.* Alternative M2 activation of Kupffer cells by PPARδ ameliorates obesity-induced insulin resistance. *Cell Metab.* **7**, 496–507 (2008).
13. Winer, S. *et al.* Normalization of obesity-associated insulin resistance through immunotherapy. *Nat. Med.* **15**, 921–929 (2009).
14. Weisberg, S.P. *et al.* Obesity is associated with macrophage accumulation in adipose tissue. *J. Clin. Invest.* **112**, 1796–1808 (2003).
15. Xu, H. *et al.* Chronic inflammation in fat plays a crucial role in the development of obesity-related insulin resistance. *J. Clin. Invest.* **112**, 1821–1830 (2003).
16. Lumeng, C.N., Bodzin, J.L. & Saltiel, A.R. Obesity induces a phenotypic switch in adipose tissue macrophage polarization. *J. Clin. Invest.* **117**, 175–184 (2007).
17. Gordon, S. Alternative activation of macrophages. *Nat. Rev. Immunol.* **3**, 23–35 (2003).
18. Wu, D. *et al.* Eosinophils sustain adipose alternatively activated macrophages associated with glucose homeostasis. *Science* **332**, 243–247 (2011).
19. Odegaard, J.I. *et al.* Macrophage-specific PPARγ controls alternative activation and improves insulin resistance. *Nature* **447**, 1116–1120 (2007).
20. Hong, E.G. *et al.* Interleukin-10 prevents diet-induced insulin resistance by attenuating macrophage and cytokine response in skeletal muscle. *Diabetes* **58**, 2525–2535 (2009).
21. Herbert, D.R. *et al.* Alternative macrophage activation is essential for survival during schistosomosiasis and downmodulates T helper 1 responses and immunopathology. *Immunity* **20**, 623–635 (2004).
22. Grzych, J.M. *et al.* Egg deposition is the major stimulus for the production of Th2 cytokines in murine schistosomiasis mansoni. *J. Immunol.* **146**, 1322–1327 (1991).
23. Okano, M., Satoskar, A.R., Nishizaki, K., Abe, M. & Harn, D.A. Jr. Induction of Th2 responses and IgE is largely due to carbohydrates functioning as adjuvants on *Schistosoma mansoni* egg antigens. *J. Immunol.* **163**, 6712–6717 (1999).
24. Atochina, O., Daly-Engel, T., Piskorska, D., McGuire, E. & Harn, D.A. A schistosome-expressed immunomodulatory glycoconjugate expands peritoneal Gr1+ macrophages that suppress naive CD4+ T cell proliferation via an IFN-γ and nitric oxide–dependent mechanism. *J. Immunol.* **167**, 4293–4302 (2001).
25. Everts, B. *et al.* Omega-1, a glycoprotein secreted by *Schistosoma mansoni* eggs, drives Th2 responses. *J. Exp. Med.* **206**, 1673–1680 (2009).
26. Steinfelder, S. *et al.* The major component in schistosome eggs responsible for conditioning dendritic cells for Th2 polarization is a T2 ribonuclease (omega-1). *J. Exp. Med.* **206**, 1681–1690 (2009).
27. Van der Kleij, D. *et al.* Triggering of innate immune responses by schistosome egg glycolipids and their carbohydrate epitope GalNAcβ1–4(Fucα1–2Fucα1–3)GlcNAc. *J. Infect. Dis.* **185**, 531–539 (2002).
28. Ko, A.I., Drager, U.C. & Harn, D.A. A *Schistosoma mansoni* epitope recognized by a protective monoclonal antibody is identical to the stage-specific embryonic antigen 1. *Proc. Natl. Acad. Sci. USA* **87**, 4159–4163 (1990).
29. Stahl, B. *et al.* Oligosaccharides from human milk as revealed by matrix-assisted laser desorption/ionization mass spectrometry. *Anal. Biochem.* **223**, 218–226 (1994).

30. Atochina, O., Da'dara, A.A., Walker, M. & Harn, D.A. The immunomodulatory glycan LNFPIII initiates alternative activation of murine macrophages *in vivo*. *Immunology* **125**, 111–121 (2008).
31. Harn, D.A., McDonald, J., Atochina, O. & Da'dara, A.A. Modulation of host immune responses by helminth glycans. *Immunol. Rev.* **230**, 247–257 (2009).
32. Dutta, P. *et al.* Lacto-*N*-fucopentaose III, a pentasaccharide, prolongs heart transplant survival. *Transplantation* **90**, 1071–1078 (2010).
33. van Liempt, E. *et al. Schistosoma mansoni* soluble egg antigens are internalized by human dendritic cells through multiple C-type lectins and suppress TLR-induced dendritic cell activation. *Mol. Immunol.* **44**, 2605–2615 (2007).
34. Thomas, P.G. *et al.* Maturation of dendritic cell 2 phenotype by a helminth glycan uses a Toll-like receptor 4–dependent mechanism. *J. Immunol.* **171**, 5837–5841 (2003).
35. Schnoeller, C. *et al.* A helminth immunomodulator reduces allergic and inflammatory responses by induction of IL-10–producing macrophages. *J. Immunol.* **180**, 4265–4272 (2008).
36. Dillon, S. *et al.* A Toll-like receptor 2 ligand stimulates Th2 responses *in vivo*, via induction of extracellular signal-regulated kinase mitogen-activated protein kinase and c-Fos in dendritic cells. *J. Immunol.* **172**, 4733–4743 (2004).
37. Repa, J.J. *et al.* Regulation of mouse sterol regulatory element-binding protein-1c gene (SREBP-1c) by oxysterol receptors, LXRα and LXRβ. *Genes Dev.* **14**, 2819–2830 (2000).
38. Watanabe, M. *et al.* Bile acids lower triglyceride levels via a pathway involving FXR, SHP, and SREBP-1c. *J. Clin. Invest.* **113**, 1408–1418 (2004).
39. Zhang, Y., Kast-Woelbern, H.R. & Edwards, P.A. Natural structural variants of the nuclear receptor farnesoid X receptor affect transcriptional activation. *J. Biol. Chem.* **278**, 104–110 (2003).
40. Zaccone, P., Fehervari, Z., Phillips, J.M., Dunne, D.W. & Cooke, A. Parasitic worms and inflammatory diseases. *Parasite Immunol.* **28**, 515–523 (2006).
41. Dunne, D.W. & Cooke, A. A worm's eye view of the immune system: consequences for evolution of human autoimmune disease. *Nat. Rev. Immunol.* **5**, 420–426 (2005).
42. Hesse, M. *et al.* The pathogenesis of schistosomiasis is controlled by cooperating IL-10–producing innate effector and regulatory T cells. *J. Immunol.* **172**, 3157–3166 (2004).
43. Bassols, J. *et al.* Environmental and genetic factors influence the relationship between circulating IL-10 and obesity phenotypes. *Obesity (Silver Spring)* **18**, 611–618 (2010).
44. Chang, Y.H., Huang, C.N., Wu, C.Y. & Shiau, M.Y. Association of interleukin-10 A-592C and T-819C polymorphisms with type 2 diabetes mellitus. *Hum. Immunol.* **66**, 1258–1263 (2005).
45. Kowalski, G.M. *et al.* Deficiency of haematopoietic-cell-derived IL-10 does not exacerbate high-fat-diet-induced inflammation or insulin resistance in mice. *Diabetologia* **54**, 888–899 (2011).
46. Brüning, J.C. *et al.* A muscle-specific insulin receptor knockout exhibits features of the metabolic syndrome of NIDDM without altering glucose tolerance. *Mol. Cell* **2**, 559–569 (1998).
47. Kim, J.K. *et al.* Redistribution of substrates to adipose tissue promotes obesity in mice with selective insulin resistance in muscle. *J. Clin. Invest.* **105**, 1791–1797 (2000).
48. Shepherd, P.R. *et al.* Adipose cell hyperplasia and enhanced glucose disposal in transgenic mice overexpressing GLUT4 selectively in adipose tissue. *J. Biol. Chem.* **268**, 22243–22246 (1993).
49. Herman, M.A. *et al.* A novel ChREBP isoform in adipose tissue regulates systemic glucose metabolism. *Nature* **484**, 333–338 (2012).
50. Cao, H. *et al.* Identification of a lipokine, a lipid hormone linking adipose tissue to systemic metabolism. *Cell* **134**, 933–944 (2008).
51. Porte, D. Jr., Baskin, D.G. & Schwartz, M.W. Insulin signaling in the central nervous system: a critical role in metabolic homeostasis and disease from *C. elegans* to humans. *Diabetes* **54**, 1264–1276 (2005).
52. Lefebvre, P., Cariou, B., Lien, F., Kuipers, F. & Staels, B. Role of bile acids and bile acid receptors in metabolic regulation. *Physiol. Rev.* **89**, 147–191 (2009).
53. Berriman, M. *et al.* The genome of the blood fluke *Schistosoma mansoni*. *Nature* **460**, 352–358 (2009).
54. Badr, S.G., Pica-Mattoccia, L., Moroni, R., Angelico, M. & Cioli, D. Effect of bile salts on oviposition *in vitro* by *Schistosoma mansoni*. *Parasitol. Res.* **85**, 421–423 (1999).
55. Wang, Y.D. *et al.* Farnesoid X receptor antagonizes nuclear factor κB in hepatic inflammatory response. *Hepatology* **48**, 1632–1643 (2008).
56. Harnett, W. & Harnett, M.M. Helminth-derived immunomodulators: can understanding the worm produce the pill? *Nat. Rev. Immunol.* **10**, 278–284 (2010).

nature medicine

Lymph node T cell responses predict the efficacy of live attenuated SIV vaccines

Yoshinori Fukazawa[1,2,8], Haesun Park[1,2,8], Mark J Cameron[3], Francois Lefebvre[3], Richard Lum[1,2], Noel Coombes[1,2], Eisa Mahyari[1,2], Shoko I Hagen[1,2], Jin Young Bae[1,2], Marcelo Delos Reyes III[1,2], Tonya Swanson[1,2], Alfred W Legasse[1,2], Andrew Sylwester[1,2], Scott G Hansen[1,2], Andrew T Smith[3], Petra Stafova[3], Rebecca Shoemaker[4], Yuan Li[4], Kelli Oswald[4], Michael K Axthelm[1,2], Adrian McDermott[5], Guido Ferrari[6], David C Montefiori[6], Paul T Edlefsen[7], Michael Piatak Jr[4], Jeffrey D Lifson[4], Rafick P Sékaly[3] & Louis J Picker[1,2]

Live attenuated simian immunodeficiency virus (SIV) vaccines (LAVs) remain the most efficacious of all vaccines in nonhuman primate models of HIV and AIDS, yet the basis of their robust protection remains poorly understood. Here we show that the degree of LAV-mediated protection against intravenous wild-type SIVmac239 challenge strongly correlates with the magnitude and function of SIV-specific, effector-differentiated T cells in the lymph node but not with the responses of such T cells in the blood or with other cellular, humoral and innate immune parameters. We found that maintenance of protective T cell responses is associated with persistent LAV replication in the lymph node, which occurs almost exclusively in follicular helper T cells. Thus, effective LAVs maintain lymphoid tissue-based, effector-differentiated, SIV-specific T cells that intercept and suppress early wild-type SIV amplification and, if present in sufficient frequencies, can completely control and perhaps clear infection, an observation that provides a rationale for the development of safe, persistent vectors that can elicit and maintain such responses.

It has been two decades since the first report that LAV administration can completely protect rhesus macaques from subsequent challenge with highly pathogenic, wild-type SIV[1], a degree of efficacy that is in sharp contrast to that achieved with a wide variety of alternative HIV and SIV vaccine strategies[2–6]. However, LAV-mediated protection is inversely proportional to the degree of attenuation, such that the most effective designs retain considerable pathogenic potential, precluding their development as vaccines in humans[2,7]. Although it has long been appreciated that delineation of a common immunologic mechanism for LAV efficacy would be a major advance in the field of HIV and AIDS vaccines—providing an immune response target for the development of safe and effective vaccine designs[3]—the basis of LAV efficacy, particularly the durable, complete, apparently sterilizing control characteristic of the best LAVs, remains controversial. Research using various types of LAVs and nonhuman primate (NHP) species, as well as different pathogenic challenge viruses and varying timing and routes of challenge, has variously implicated, or argued against, T cell immunity, humoral immunity, innate immunity and viral interference in LAV-mediated protection without the emergence of a unifying, consensus protective mechanism or a clear-cut definition of multiple different mechanisms acting in combination to achieve protection[2,5,6,8–16].

In this study, we sought to clarify the immunologic (or other) basis of LAV-mediated protection against highly pathogenic SIV by statistical correlation of fundamental measures of LAV-elicited immunity with efficacy after challenge in a large cohort of LAV-vaccinated rhesus macaques. Our approach was to vaccinate groups of macaques with different LAVs that varied in their level of attenuation, their degree of amino acid sequence homology with the wild-type SIVmac239 challenge virus or both with the intent of producing sufficient heterogeneity in both immune responses and protective efficacy at the level of the overall cohort to create a statistically powerful immune parameter versus efficacy matrix. We used the most stringent route of SIV challenge—high-dose intravenous administration—because LAVs are unique among SIV vaccines in their ability to completely control such a systemic SIV challenge[1–3] and hematogenous dissemination is a common step in all primary HIV and SIV infections, including those arising from mucosal surfaces[17]. In this regard, a vaccine that intercepts and completely controls hematogenous HIV spread would be applicable to both mucosal and intravenous routes of HIV entry, the latter of which is a clinically relevant way of acquiring infection that is not addressed by vaccines that are designed to elicit mucosal immunity. Notably, this experimental approach strongly and specifically identified characteristics of the SIV-specific T cell response in the lymph node (including its magnitude, effector differentiation, functional properties and kinetics of activation after challenge) as cross-platform predictors

[1]Vaccine and Gene Therapy Institute, Oregon Health and Science University, Beaverton, Oregon, USA. [2]Oregon National Primate Research Center, Oregon Health and Science University, Beaverton, Oregon, USA. [3]Vaccine and Gene Therapy Institute-Florida, Port St. Lucie, Florida, USA. [4]AIDS and Cancer Virus Program, SAIC Frederick, Inc., Frederick National Laboratory for Cancer Research, Frederick, Maryland, USA. [5]Vaccine Research Institute, US National Institute of Allergy and Infectious Diseases, Bethesda, Maryland, USA. [6]Duke University Medical Center, Durham, North Carolina, USA. [7]Statistical Center for HIV/AIDS Research and Prevention, Vaccine and Infectious Disease Division, Fred Hutchinson Cancer Research Center, Seattle, Washington, USA. [8]These authors contributed equally to this work. Correspondence should be addressed to L.J.P. (pickerl@ohsu.edu).

Received 4 June; accepted 13 August; published online 9 September 2012; doi:10.1038/nm.2934

of LAV-mediated protection against high-dose intravenous SIV challenge. We further linked the maintenance of these protective lymph-node–based T cells to the ability of replication-competent LAV to persist in follicular helper $CD4^+$ T cells in secondary lymphoid tissues. Together, these findings provide further support for the concept that early SIV infection, even the systemically distributed infection that follows high-dose intravenous challenge, is vulnerable to the high-frequency, effector-differentiated memory T cell responses that are uniquely elicited and maintained long term by persistent vectors.

RESULTS

Heterogeneous protection with different LAV types

To achieve the heterogeneity in both immune responses and protective efficacy that is necessary for robust statistical delineation of immune correlates, we selected LAV designs for study that vary in their level of attenuation and degree of amino acid sequence homology with the wild-type SIVmac239 challenge virus. These LAVs were expected to differ in the amount and persistence of SIV antigens that they provide to the immune system for elicitation of SIV-specific T cell and antibody responses (leading to differences in the magnitude, differentiation and durability of the responses resulting from each vaccine), as well as in the ability of the resulting vaccine-elicited adaptive immunity to cross-react with the challenge virus. The prototype LAV, SIVmac239(Δnef), is only moderately attenuated and is sequence matched to the challenge virus. SIVmac239(Δ3) and single-cycle SIVmac239 are also sequence matched to the challenge virus but are progressively more attenuated than SIVmac239(Δnef)[18,19]. SHIV89.6 is also only moderately attenuated, but it differs from the SIVmac239(Δnef) prototype by virtue of highly heterologous, HIV-derived *env, tat, vpu* and *rev* sequences and its ability to use chemokine (C-X-C motif) receptor 4 (CXCR4) as a co-receptor[5]. SIVsmE543(Δnef) is variably attenuated (because of its sensitivity to restrictive tripartite motif containing protein 5 (TRIM5) alleles) and is heterologous in its amino acid sequence to SIVmac239 (~15% overall divergence)[13,20]. We administered each LAV to six to eight macaques to create an overall study group of 32 vaccinated animals (**Fig. 1a**). We excluded macaques with class I major histocompatibility complex (MHC I) alleles that are associated with enhanced $CD8^+$ T cell–mediated SIV control (*Mamu-A*01*, *Mamu-B*08* and *Mamu-B*17*)[13] to focus the analysis on new correlates of protection.

Consistent with the expected characteristics of the selected LAVs, the SHIV89.6-vaccinated macaques in our study group had the highest peak LAV viremia, highest peak number of LAV RNA copies within peripheral blood mononuclear cells (PBMC) and most acute-phase effector-site $CD4^+$ T cell depletion, followed by the macaques vaccinated with SIVmac239(Δnef), SIVmac239(Δ3), SIVsmE543(Δnef) and single-cycle SIVmac239 (**Fig. 1b,c** and **Supplementary Fig. 1**). Differences in these parameters were less apparent in chronic-phase, as the replication of even the least attenuated LAVs was brought under stringent control by week 10 after vaccination, and the modest acute-phase effector-site $CD4^+$ T cell depletion was transient. Notably, however, the peak numbers of PBMC-associated LAV DNA copies established during acute-phase viremia decayed very slowly over time, providing a persistent measure of the amount of peak LAV replication (**Fig. 1c**).

After a 50-week vaccination period to allow full maturation and stabilization of immunity to SIV[2], we intravenously challenged the 32 LAV-inoculated and 6 unvaccinated control macaques with 10^3 infectious units of wild-type SIVmac239 (**Fig. 1a**). The LAV-vaccinated macaques manifested three distinct outcomes after this challenge: (i) complete protection ($n = 19$), characterized by no discernable net increase in overall plasma viral load (pvl) and either no wild-type SIVmac239, as detected by discriminatory quantitative RT-PCR ($n = 16$), or transient, low amounts of wild-type virus ($<10^3$ copies ml^{-1}; $n = 3$); (ii) partial protection ($n = 7$), defined as a clear establishment of wild-type SIV infection ($>10^4$ copies ml^{-1} of wild-type SIVmac239 RNA by discriminatory quantitative RT-PCR and persistently elevated overall pvl) but with an overall pvl that was reduced by a factor of at least 2log in the first 70 days after challenge compared to unvaccinated controls; or (iii) no protection ($n = 6$), in which the viral dynamics after challenge were indistinguishable from those of the unvaccinated controls (**Fig. 1d**). We confirmed the biologic validity of these different outcome groups by showing that completely protected macaques lacked both an anamnestic T cell response to wild-type SIV challenge (a sensitive measure of increased SIV replication) and any evidence of SIV pathogenesis (for example, loss of mucosal $CD4^+$ memory T cells), whereas partially protected and nonprotected macaques manifested both unequivocal anamnestic responses and mucosal $CD4^+$ memory T cell depletion that was commensurate with their respective pvl (**Fig. 1e,f**). Protection was highest in macaques vaccinated with LAVs that were the least attenuated and the most homologous to the challenge virus (**Fig. 1d**). The peak plasma LAV load (initial 4 weeks after vaccination) and the chronic-phase plasma LAV load immediately before challenge, as well as the number of LAV DNA copies in PBMC immediately before challenge (which, as indicated above, closely correlates with peak LAV load in plasma)—all reflections of LAV attenuation—statistically delineated macaques at each end of the protection spectrum (in particular, completely protected compared to nonprotected macaques; **Fig. 1g,h**). Notably, however, the amount of PBMC-associated LAV RNA at the time of challenge did not significantly correlate with outcome (**Fig. 1h**).

Lymph node SIV-specific T cell responses predict outcome

Before challenge, we quantified 11 primary parameters of SIV-specific immunity for assessment as potential correlates of protection, including three humoral immune parameters—SIVmac239 neutralization titers, native SIV env binding titers (neutralization of tissue-culture–adapted SIVmac251) and SIV env-directed antibody-dependent cell-mediated cytotoxicity (all in plasma samples)—and eight T cell response parameters—the magnitude of SIV proteome-specific $CD4^+$ and $CD8^+$ T cells in PBMC, bronchoalveolar lavage (BAL) fluid and lymph node tissue, as well as the breadth of these responses in PBMC. LAV-vaccinated macaques manifested a spectrum of values for each of these parameters, with the exception of SIVmac239 neutralizing antibody titers, which were detectable at low amounts in only a very small proportion of LAV-vaccinated macaques (**Supplementary Fig. 2**). It is also noteworthy that SHIV89.6-vaccinated macaques lacked antibody responses to the heterologous SIV env.

We next assessed each of these parameters for correlation with the outcome groups described above using the nonparametric Kruskal-Wallis test and adjusting for multiple comparisons using the Bonferroni method. Notably, only two parameters—the magnitude of SIV proteome-specific $CD4^+$ and $CD8^+$ responses in the lymph node—statistically delineated the outcome groups using this method (**Table 1** and **Fig. 2a**). Moreover, the SIV proteome-specific $CD4^+$ and $CD8^+$ T cell responses in the lymph node were the only parameters to statistically delineate each of the three outcome groups from each other using the Wilcoxon rank-sum test (**Fig. 2a** and **Supplementary Fig. 3**). In partially protected and nonprotected

macaques, the magnitude of the SIV-specific T cell response ($CD4^+$ and $CD8^+$) in the lymph node, but not in the blood, inversely correlated with peak viremia after challenge as determined by Spearman analysis (**Fig. 2b**), indicating that lymph-node–based T cell responses before challenge also predict the degree of SIVmac239 control once persistent infection with the wild-type virus is established. The majority of SIV-specific $CD8^+$ T cells in the lymph nodes before challenge of subsequently completely protected macaques

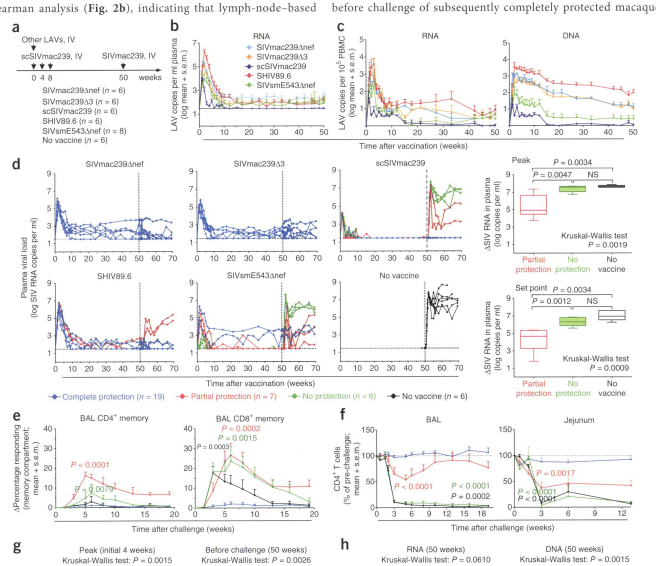

Figure 1 LAV virology and differential efficacy. (**a**) Schematic illustrating the vaccination and challenge protocol and rhesus macaque groups. IV, intravenous. (**b**,**c**) Comparison of the amount of plasma LAV RNA (**b**) and PBMC-associated LAV RNA and DNA (**c**) in the blood of the different LAV-vaccinated macaque groups during the vaccine phase. (**d**) Effect of wild-type SIVmac239 challenge on the overall amount of plasma SIV RNA in LAV-vaccinated and unvaccinated control macaques (the shaded area corresponds to results after challenge). The two whisker plots (right) compare the change from baseline (Δ) of the peak (during the initial 4 weeks after challenge) and the set point (13–19 weeks after challenge) pvl values in the partially protected, nonprotected and unvaccinated groups (completely protected macaques had no net change in pvl after challenge). The significance of the overall differences in these values was determined by Kruskal-Wallis test, and pairwise differences were determined by Wilcoxon rank-sum test when the Kruskal-Wallis *P* value was <0.05. (**e**) Analysis of the change in the frequency of total SIV-specific $CD4^+$ and $CD8^+$ T cells in BAL fluid of the designated protection groups after challenge. Significant differences in the maximal change in response frequencies after challenge were calculated by Wilcoxon rank-sum test for each protection group compared to the completely protected group. (**f**) Analysis of the depletion of $CD4^+$ memory T cells after challenge in the designated protection groups in the BAL fluid and jejunal mucosa (baseline before challenge was normalized to 100%; statistical analysis as in **e**). (**g**) Comparison of the peak plasma LAV loads and plasma LAV loads before challenge in the three protection groups (statistical analysis as described in **d**). (**h**) Comparison of PBMC-associated LAV RNA and DNA loads before challenge in the three protection groups (statistical analysis as described in **d**). NS, not significant.

Table 1 Kruskal-Wallis analysis of the 11 primary immune response predictors compared to the protection categories

Immune predictors	Unadjusted *P*	Bonferroni-corrected *P*
PBMC CD4$^+$ T cell response magnitude	0.0672	0.7392
PBMC CD8$^+$ T cell response magnitude	0.0195	0.2148
PBMC CD4$^+$ T cell response breadth	0.0301	0.3313
PBMC CD8$^+$ T cell response breadth	0.1593	1.0000
Lymph node CD4$^+$ T cell response magnitude	**0.0003**	**0.0036**
Lymph node CD8$^+$ T cell response magnitude	**0.0006**	**0.0070**
BAL fluid CD4$^+$ T cell response magnitude	0.0450	0.4950
BAL fluid CD8$^+$ T cell response magnitude	0.0221	0.2426
SIVmac239 neutralizing antibodies	0.1458	1.0000
SIV env-specific antibodies; TCLA SIVmac251 neutralization	0.0079	0.0872
SIV env-specific antibodies; ADCC	0.0073	0.0808

Values in bold are those that reached statistical significance after Bonferroni correction. TCLA, T cell line-adapted; ADCC, antibody-dependent cell-mediated cytotoxicity.

manifested phenotypic evidence of both recent activation (human leukocyte antigen DR (HLA-DR) and programmed cell death protein 1 (PD-1) expression) and effector differentiation (chemokine (C-C) motif receptor 5 (CCR5) expression) (**Fig. 2c**), suggesting an ability to manifest an immediate antiviral effector response. To ascertain whether these SIV-specific T cells could directly mediate anti-SIV effector activity, we assessed the ability of sorted populations of memory T cells from PBMC and lymph node tissue to suppress SIVmac239 replication *in vitro*. Indeed, CD8$^+$ (but not CD4$^+$) memory T cells from the lymph nodes (but not from the blood) of completely protected macaques manifested potent SIV suppression, and across the overall cohort, the extent of this suppression strongly predicted each of the three outcome groups and inversely correlated with peak pvl after challenge in the macaques that established wild-type SIVmac239 infection (**Fig. 2d**).

Persistent LAV maintains T cell responses in lymph nodes

The ability of efficacious LAVs to maintain protective T cell responses in lymph nodes seemed to depend on the preferential persistence of LAV replication in this tissue (**Fig. 3a**), as we found a highly significant correlation between the magnitude of both the SIV-specific CD4$^+$ and CD8$^+$ T cell responses in lymph nodes and the amount of lymph node cell-associated LAV RNA (a measure of ongoing LAV replication; **Fig. 3b**). Because, as noted above (**Fig. 2a–d**), the lymph-node–based SIV-specific T cell responses strongly correlate with protective efficacy, it is not surprising that the amount of LAV RNA in lymph node cells before challenge also correlated with outcome after challenge (**Fig. 3c**). The preferential persistence of LAV in the lymph node can be explained by the highly selective replication of LAV in the CD4$^+$PD-1^{hi}, inducible T cell co-stimulator (ICOS)^{hi}CD200^{hi}CCR7^{low} follicular helper T (T_{FH}) cell subset (**Fig. 3d** and **Supplementary Fig. 4**), which is localized specifically in B cell follicles and is, therefore, found almost exclusively in lymph nodes and other secondary lymphoid tissues[21–23].

An analysis of diverse tissues obtained at necropsy from ten completely protected LAV-vaccinated macaques confirmed that B cell follicle–rich secondary lymphoid tissues, including lymph nodes, spleen and colonic mucosa, contained significantly higher copy numbers of cell-associated LAV RNA and DNA per 10^5 cells than primary lymphoid tissues (bone marrow) and extra-lymphoid tissues (jejunal mucosa, liver and BAL fluid) that typically lack such B cell follicles (**Fig. 3e**). Notably, the mean frequencies of SIV-specific CD8$^+$ T cells in each tissue closely correlated with the log mean of the amount of cell-associated SIV RNA in that tissue (**Fig. 3f**), an observation that provides further evidence that the amount of ongoing LAV replication determines the frequency at which SIV-specific CD8$^+$ T cells are maintained in any given tissue. Thus, CD4$^+$ T_{FH} cells serve as a sanctuary site for LAV persistence[23,24] and concentrate LAV replication (and antigen production) in secondary lymphoid tissues, providing an immune stimulus for production and maintenance of SIV-specific T cells that is proportional to the extent of T_{FH} cell infection.

Linkage of protection to early lymph node T cell activation

Collectively, these data suggest that after intravenous challenge, the lymph node and other secondary lymphoid tissues are major sites at which LAV-generated, SIV-specific T cells intercept the nascent wild-type SIV infection, and if these T cells are present in sufficient numbers, the wild-type SIV infection can be completely controlled and possibly cleared. To probe the dynamics and characteristics of the immune response at this putative intercept, we used a microarray analysis to compare the transcriptional profiles of unfractionated lymph node cells obtained from completely protected, nonprotected and unvaccinated control macaques 7 days before and 4 and 14 days after wild-type SIVmac239 challenge. Before challenge, the gene expression profiles of unfractionated lymph node cells from completely protected and nonprotected macaques were indistinguishable from each other but were different than those from the unvaccinated control macaques (**Fig. 4a**,**b**). Gene pathways that were significant in distinguishing vaccinated from unvaccinated macaques included metabolic pathways that are associated with stress responses and survival (eukaryotic initiation factor 2 (EIF2), mammalian target of rapamycin (mTOR), oxidative phosphorylation and protein ubiquitination), as well as pathways involved in T cell activation (nuclear factor of activated T cells (NFAT), phospholipase Cγ (PLC-γ), protein kinase A (PKA) and CD28) and are therefore consistent with a low-level immune response to the LAV (**Fig. 4c** and **Supplementary Table 1**). Notably, at post-challenge day (PCD) 4 (a time point when cell-associated SIV RNA and DNA were not yet detectable in the lymph nodes of the unvaccinated control macaques), the gene expression profiles of the lymph node cells from completely protected and nonprotected (but not control) macaques, although indistinguishable from each other, differed markedly from the profiles of these cells before challenge, involving multiple pathways related to immune activation (**Fig. 4d**–**f** and **Supplementary Table 2**). A gene-level comparison of lymph node cells at PCD 4 and before challenge from completely protected, nonprotected and control macaques using an immune response gene filter revealed upregulation of T cell, inflammasome and antigen-presenting–cell genes, as well as of genes regulating the interface of innate and adaptive immunity in the vaccinated macaques compared to controls (**Fig. 4g** and **Supplementary Discussion**). Because the representation of the major cell subsets in the lymph nodes of completely protected and nonprotected macaques at PCD 4 was unchanged from that at baseline (**Supplementary Fig. 5**), these differences in gene expression profiles between baseline and PCD 4 probably reflect an *in situ* immune response. Moreover, given that the lymph node transcriptional profiles changed in vaccinated but not unvaccinated control macaques, they were likely initiated by an adaptive (LAV-elicited) memory response to challenge. From PCD 4

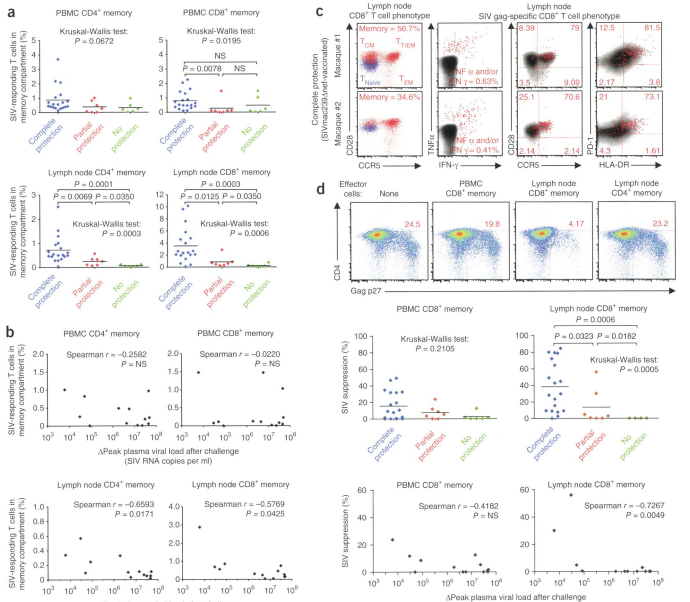

Figure 2 Immunological correlates of LAV-mediated protection. (**a**) Comparison of the magnitude of the total SIV-specific CD4+ and CD8+ T cell responses before challenge in the PBMC or lymph node memory compartments of the designated protection groups. The significance of the overall differences in these values was determined by Kruskal-Wallis test, and pairwise differences were determined by Wilcoxon rank-sum test when the Kruskal-Wallis *P* value was < 0.05. The horizontal bars show the mean values. (**b**) Spearman analysis of the correlation between the magnitude of the total SIV-specific CD4+ and CD8+ T cell responses before challenge in the PBMC or lymph node memory compartments and the peak change in pvl after challenge among the partially protected and nonprotected macaques ($n = 13$ total). (**c**) Flow cytometric analysis of the phenotype of overall (left) and SIV gag-specific (right) CD8+ T cell populations from the lymph nodes of two representative LAV-vaccinated, completely protected macaques before challenge. The profiles shown were gated on CD3+CD8+ small lymphocytes. In the plots on the left, cell clusters corresponding to the naive (blue) and total memory (red) T cell populations and the major differentiation-defined memory T cell subsets (T_{CM}, central memory; T_{TrEM}, transitional effector memory; T_{EM}, effector memory) are shown[38,39]. In the images on the right, gag-responsive cells (expressing tumor necrosis factor α (TNF-α) and/or IFN-γ) were colored red and then characterized for their memory differentiation (CD28 and CCR5 expression; left) and activation (PD-1 and HLA-DR expression) status, with the percentage of events in each quadrant shown (quadrant markers based on negative control staining). (**d**) Analysis of the ability of isolated memory T cells from LAV-vaccinated macaques to suppress SIVmac239 replication in autologous CD4+ T cells. On the top are results from a representative completely protected macaque (the percentage of gag p27+ cells is shown for each profile). In the middle is a comparison of the degree of viral suppression by sorted CD8+ memory T cells from PBMC and lymph node tissue before challenge for the designated protection groups, with the significance of differences between groups analyzed as described in **a**. On the bottom is a Spearman analysis of the correlation between the degree of viral suppression by sorted CD8+ memory T cells from PBMC or the lymph node tissue and the change in peak pvl after challenge among partially protected and nonprotected macaques ($n = 13$ total). NS, not significant.

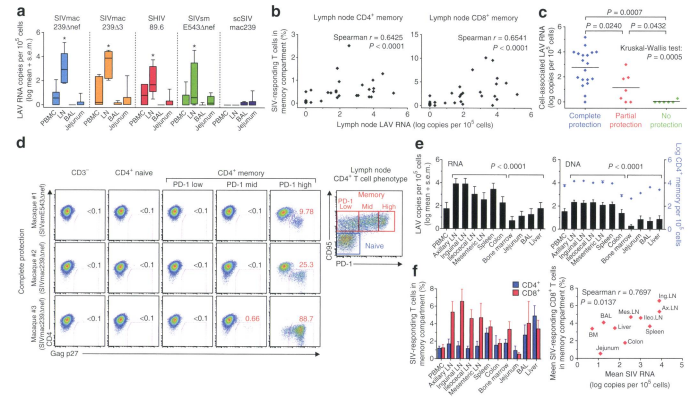

Figure 3 Association of tissue LAV replication and SIV-specific T cell responses. (**a**) Whisker plot comparing the amount of cell-associated LAV RNA before challenge in mononuclear cells from the blood, lymph node (LN), BAL fluid and jejunal mucosa in macaques vaccinated with the designated LAV. $^*P \leq 0.05$, indicating significantly higher amounts of LAV RNA in the lymph node compared to the other three tissues by Wilcoxon signed-rank test. (**b**) Spearman analysis of the correlation between the amount of cell-associated LAV RNA before challenge in unfractionated lymph node cells and the magnitude of the total SIV-specific T cell responses before challenge in the $CD4^+$ and $CD8^+$ lymph node memory T cell compartments. (**c**) Comparison of the amount of cell-associated LAV RNA before challenge in lymph node cells in the designated protection groups, with the statistical analysis performed as described in **Figure 2a** (horizontal bars show the mean values). (**d**) Isolation of replication-competent LAV from the designated sorted lymph node cell populations before challenge (inset at right) from three representative completely protected macaques using CEMx174 coculture (22 days; 10^4 sorted lymph node cells and 10^5 CEMx174 target cells per culture) with detection of infection by flow cytometric analysis of intracellular SIV gag p27 (ref. 40) (the percentage of gag $p27^+$ cells is shown for each profile). (**e**) Analysis of cell-associated SIV RNA and DNA in mononuclear cells obtained from the designated tissues of ten completely protected macaques at necropsy (all macaques were negative for wild-type SIV RNA and DNA by discriminatory RT-PCR or PCR in lymph node cells). Blue diamonds (right) indicate the number of $CD4^+$ memory T cells (potential SIV target cells) per 10^5 mononuclear cells in each tissue (right y axis). The levels of cell-associated SIV RNA or DNA in secondary lymphoid tissues (B cell–follicle rich; including all lymph nodes, spleen and colonic mucosa) compared to those in nonsecondary lymphoid tissues (B cell–follicle poor; including the bone marrow, BAL fluid, liver and jejunal mucosa) of the completely protected macaques. The P values shown were calculated by Wilcoxon rank-sum test. (**f**) The mean frequency (+ s.e.m.) of total SIV-specific T cell responses within the $CD4^+$ and $CD8^+$ memory T cell populations of the designated tissues obtained from necropsy of the same ten completely protected macaques (left). Spearman analysis showing the correlation between the mean frequencies of SIV-specific $CD8^+$ T cells in each tissue with the log mean copy number of cell-associated SIV RNA per 10^5 cells in the corresponding tissue (right). BM, bone marrow; Mes, mesenteric; Ileo, ileocecal; Ing, inguinal; Ax, axillary.

to PCD 14, the relationship between the transcriptional profiles of lymph nodes from completely protected, nonprotected and control macaques changed (**Fig. 4g** and **Supplementary Fig. 6**). Consistent with the onset of progression of wild-type SIVmac239 infection in nonprotected and control but not completely protected macaques, lymph node cells from the nonprotected and control macaques showed similar patterns of gene expression that were associated with enhanced innate interferon (IFN) and effector T and natural killer cell responses, whereas the expression of immune-related genes in lymph node cells from completely protected macaques was largely unaltered over this period (**Supplementary Discussion**).

To specifically compare the activity of memory T cells in the lymph nodes of completely protected and nonprotected macaques after wild-type SIVmac239 challenge, we examined the transcriptional profiles of sorted $CD8^+$ and $CD4^+$ memory T cells from lymph nodes obtained at PCD 4 and PCD 14. This analysis revealed that $CD8^+$ memory T cells from PCD 4 lymph nodes of completely protected macaques manifested a relative upregulation of T cell receptor signaling genes and granzymes and a downregulation of the interleukin-7 receptor (IL-7R) gene compared to nonprotected macaques (**Fig. 5**), reflecting higher T cell activation and earlier establishment of $CD8^+$ T cell effector responses in the lymph nodes of these completely protected animals[25–27] (**Supplementary Discussion**). Although fewer gene expression changes distinguished $CD4^+$ memory T cells from the lymph nodes of completely protected compared to nonprotected macaques at PCD 4, there was still significantly higher expression (fold change > 1.3, $P < 0.01$) of genes associated with antigen-specific activation of $CD4^+$ memory T cells in completely protected macaques, including CD40 ligand (CD40LG), lymphocyte-activation gene 3 (LAG3), cytotoxic T lymphocyte–associated protein 4 (CTLA4),

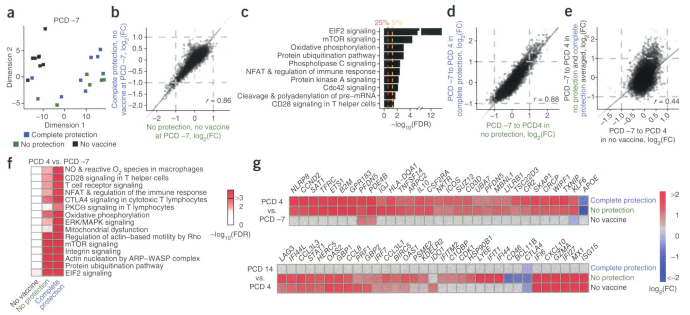

Figure 4 Transcriptional profiling of unfractionated lymph node cells before and after wild-type SIV challenge. (**a**) Comparison of the overall gene expression profiles of unfractionated lymph node cells before challenge (PCD −7) from control (unvaccinated) macaques and LAV-vaccinated macaques that were either completely protected or nonprotected after wild-type SIV challenge. Genes differentially expressed between these three groups were selected by *F* test with a 5% false discovery rate (FDR), and then multidimensional scaling was used to visualize relatedness of the data sets (control versus nonprotected versus completely protected macaques). (**b**) Scatterplot comparing gene expressions between completely protected (*y* axis) and nonprotected (*x* axis) macaques by fold change (FC) relative to unvaccinated controls. Dashed lines indicate absolute 2-fold change. (**c**) Top canonical pathways differentially expressed between vaccinated macaques (completely protected and nonprotected groups averaged) and unvaccinated controls. Yellow and red dashed lines indicate the thresholds for the pathway overrepresentation test 5% and 25% FDR estimates, respectively. (**d**) Scatterplot comparing the fold change in gene expression from PCD −7 to PCD 4 in unfractionated lymph node cells between completely protected (*y* axis) and nonprotected (*x* axis) macaques. (**e**) Scatterplot comparing the fold change in gene expression from PCD −7 to PCD 4 in unfractionated lymph node cells of unvaccinated controls (*x* axis) to the average fold change in the completely protected and nonprotected macaques (*y* axis). (**f**) Heatmap of the top 15 differentially expressed canonical pathways by $-\log_{10}$(FDR) between PCD −7 and PCD 4 for control, nonprotected and completely protected macaques (unvaccinated controls contributed no significant pathway at >5% FDR). (**g**) Heatmap of the average fold change in gene expression from PCD −7 to PCD 4 (top) and from PCD 4 to PCD 14 (bottom) in unfractionated lymph node cells for control, nonprotected and completely protected macaques. The genes shown in the heatmap were selected by having absolute fold change >2 at a 5% FDR in at least one protection outcome group and were immune filtered (Online Methods).

B and T lymphocyte attenuator (BTLA) and regulators of T cell survival (the NF-κB transcriptional pathway)[28,29] (**Supplementary Fig. 7** and **Supplementary Discussion**). By PCD 14, CD8$^+$ memory T cells from nonprotected macaques manifested transcriptional evidence of effector function[27], for example, upregulation of genes encoding granzymes, as well as transcriptional activation of innate immunity downstream of type 1 IFN signaling, protein ubiquitination and cellular proliferation pathways[30] (**Fig. 5** and **Supplementary Tables 3** and **4**), which is consistent with the late development of both adaptive and innate immune responses in these macaques. CD4$^+$ memory T cells from the lymph nodes of nonprotected macaques showed similarly increased expression of type I IFN response genes at PCD 14 (**Supplementary Fig. 7**). In contrast, CD8$^+$ and CD4$^+$ memory T cells from the lymph nodes of completely protected macaques at PCD 14 manifested relative upregulation of genes associated with long-term memory and cellular quiescence and survival[30,31] (**Fig. 5**, **Supplementary Fig. 7**, **Supplementary Table 3** and **Supplementary Discussion**). Thus, our transcriptional analysis of lymph node memory T cells provides evidence of a larger and/or earlier CD8$^+$ and CD4$^+$ T cell response to challenge in completely protected compared to nonprotected macaques (in keeping with the higher-magnitude, SIV-specific T cell responses in the lymph nodes of completely protected macaques). This early response is associated with control of infection and prevention of the marked innate and adaptive immune activation that characterizes progressive wild-type SIV infection.

DISCUSSION

Correlation analysis does not delineate cause and effect and, therefore, cannot unequivocally establish whether persistent LAV replication, the associated SIV-specific immune response or an uncharacterized covariate are mechanistically related to the observed protection. However, these data, taken together, lead most logically to a model in which persistent LAV replication elicits and maintains differentiated and activated, antiviral effector memory T cells in tissues, and if these T cells are present at a sufficient frequency before challenge, they can completely control (and perhaps clear) wild-type SIV infection in the first days after challenge. Secondary lymphoid tissues seem to be the crucial site of viral intercept after intravenous challenge, and CD8$^+$ memory T cells from lymph nodes of optimally LAV-vaccinated macaques can strongly suppress wild-type SIV replication in autologous CD4$^+$ T cells. Although CD4$^+$ memory T cells from the lymph nodes of the same macaques lacked this capability, the very strong correlation between the frequency of SIV-specific CD4$^+$ T cells in lymph node tissue and outcome suggests their crucial involvement in protection, perhaps through direct effector activity against SIV-infected macrophages, help of SIV-specific, CD8$^+$ T cell functionality

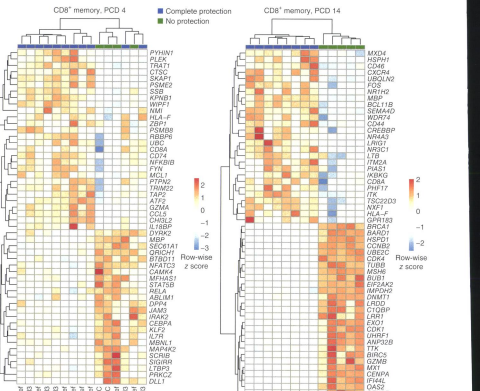

Figure 5 Transcriptional profiling of sorted lymph node CD8$^+$ T cells at days 4 and 14 after wild-type SIV challenge (PCD 4 and PCD 14). Shown are heatmap profiles of genes differentially expressed in the lymph node CD8$^+$ memory T cells of completely protected compared to nonprotected macaques at PCD 4 (left) and 14 (right). Immune-filtered gene expression is shown as a genewise standardized expression (z score), with absolute fold change >1.3, $P < 0.01$ and FDR < 25% chosen as the significance level.

or both[32,33]. Notably, lymph-node–based, SIV-specific T cell responses also delineated partial controllers from noncontrollers, suggesting that when the LAV-elicited SIV-specific T cell responses are below the threshold for complete control, an anamnestic expansion of the LAV-elicited, SIV-specific memory T cells can ensue, with the outcome being determined, as with conventional prime-boost vaccines, by a competition between the kinetics and antiviral activity of the anamnestic response and viral escape[4].

Viral interference probably does not substantially contribute to the observed protection given that LAV replication is restricted largely to CD4$^+$ T_{FH} cells, a minor subset of the total potential population of CD4$^+$ target cells. Innate immunity elicited by persistent LAV replication is another candidate mechanism for mediating protection. Although our sampling schedule may have missed a transient innate immune response, our detailed transcriptional analysis revealed no evidence of differential innate immune activation in the lymph nodes of protected compared to unprotected macaques before challenge or at 4 days after challenge and thereby argues against this possibility. In addition, the number and activation status of natural killer cells in the lymph node before and after challenge did not correlate with protection, arguing against involvement of these innate immune effectors (**Supplementary Fig. 8**). Perhaps the most compelling evidence in support of the T cell protection model of LAV efficacy is the analogous immediate and complete MHC I allele–independent control of SIV infection that is associated with the high-frequency, tissue-based, SIV-specific T cell responses elicited and maintained by SIV-protein–expressing cytomegalovirus vectors[34]. These persistent β-herpesvirus vectors have a completely different biology than LAV (target-cell tropism, innate immune interaction, immune evasion and persistence strategies) and do not elicit antibody responses to SIV inserts, factors strongly implicating tissue-based, effector-differentiated memory T cells as the common mediator of protection with these vectors.

In summary, these data identify the magnitude of SIV-specific CD4$^+$ and CD8$^+$ T cell responses in secondary lymphoid tissues (but, notably, not blood), as well as the SIV suppression capacity of CD8$^+$ memory T cells in these tissues, as strong (cross-platform) correlates of LAV-mediated protection. These results do not preclude other innate or adaptive immune mechanisms (including antibodies) as potential contributors to LAV efficacy, especially at mucosal surfaces[16], or the protection from mucosal challenge afforded by other vaccine modalities, as has been suggested recently in both clinical[35] and NHP studies[36]. However, taken together, these observations provide further support for the conclusion that effector-differentiated, SIV-specific memory T cells, when maintained at a high frequency in tissues important for SIV infection, can intercept and completely control a nascent, highly pathogenic SIV infection without anamnestic expansion[15,34]. This intercept and control may occur at mucosal sites of entry, lymphoid tissues that are involved in early spread (the latter even when mucosal infection is bypassed by intravenous inoculation) or both, but they always occur before the establishment of a 'critical mass' of replicating virus that is capable of dynamic evolution and immune escape[4]. To date, this pattern of protection has been consistently observed only with LAVs or SIV vaccines that are based on persistent cytomegalovirus vectors. These findings therefore support the exploitation of tissue-based, effector-differentiated memory T cell responses and their associated immediate and complete protection by the development of HIV and AIDS vaccines that are based on persistent, nonpathogenic vectors or on other strategies that are capable of eliciting and maintaining such effector memory T cell responses[37].

METHODS

Methods and any associated references are available in the online version of the paper.

Note: Supplementary information is available in the online version of the paper.

ACKNOWLEDGMENTS

This work was supported by the Bill and Melinda Gates Foundation (grant #41185), the International AIDS Vaccine Initiative (IAVI), the National Institute of Allergy and Infectious Diseases (including the US National Institutes of Health (NIH)

grant R37 AI054292 (L.J.P.), contract HHSN272200900037C and the Center for HIV-AIDS Vaccine Immunology (CHAVI) program), the NIH Office of Research Infrastructure Programs (P51 OD 011092) and the National Cancer Institute (contract HHSN261200800001E). The authors acknowledge R. Desrosiers (Harvard University) for providing SIVmac239Δnef and SIVmac239Δ3; P. Johnson and T. Lui (University of Pennsylvania) for SIVsmE543Δnef; C. Miller (University of California, Davis) for SHIV89.6 and wild-type SIVmac239; D. Evans (Harvard University) for a single-cycle SIVmac239; N. Letvin for TRIM5 allele typing; and R. Wiseman and D. Watkins for MHC typing. We thank N. Winstone, A. Leon, J. Clock, A. Nogueron, L. Pan, M. Cartwright, A. Filali and P. Wilkinson for technical assistance and J. McElrath, S. Self, W. Koff, A. Okoye, J. Schmitz and J. Ahler for helpful discussion and advice.

AUTHOR CONTRIBUTIONS

Y.F., R.L., N.C., E.M., S.I.H. and S.G.H. performed experiments and analyzed data, assisted by M.D.R. and J.Y.B. H.P. managed the project and analyzed data, assisted by A.S. T.S., A.W.L. and M.K.A. managed the animal protocols. M.P. and J.D.L. provided SIV and LAV quantifications, assisted by R.S., Y.L. and K.O. D.C.M. and G.F. provided neutralizing antibodies and cytotoxic antibody quantification, respectively. M.J.C., F.L., A.T.S., P.S. and R.P.S. carried out the microarray analysis and interpreted the results. P.T.E. performed the statistical analysis. L.J.P. conceived of the study, supervised experiments, analyzed data and wrote the paper, assisted by Y.F., H.P., P.T.E., A.M., R.P.S. and J.D.L.

COMPETING FINANCIAL INTERESTS

The authors declare no competing financial interests.

Published online at http://www.nature.com/doifinder/10.1038/nm.2934.
Reprints and permissions information is available online at http://www.nature.com/reprints/index.html.

1. Daniel, M.D., Kirchhoff, F., Czajak, S.C., Sehgal, P.K. & Desrosiers, R.C. Protective effects of a live attenuated SIV vaccine with a deletion in the nef gene. *Science* **258**, 1938–1941 (1992).
2. Johnson, R.P. & Desrosiers, R.C. Protective immunity induced by live attenuated simian immunodeficiency virus. *Curr. Opin. Immunol.* **10**, 436–443 (1998).
3. Koff, W.C. *et al.* HIV vaccine design: insights from live attenuated SIV vaccines. *Nat. Immunol.* **7**, 19–23 (2006).
4. Picker, L.J., Hansen, S.G. & Lifson, J.D. New paradigms for HIV/AIDS vaccine development. *Annu. Rev. Med.* **63**, 95–111 (2012).
5. Abel, K. *et al.* Simian-human immunodeficiency virus SHIV89.6-induced protection against intravaginal challenge with pathogenic SIVmac239 is independent of the route of immunization and is associated with a combination of cytotoxic T-lymphocyte and α interferon responses. *J. Virol.* **77**, 3099–3118 (2003).
6. Sugimoto, C. *et al.* Protection of macaques with diverse MHC genotypes against a heterologous SIV by vaccination with a deglycosylated live-attenuated SIV. *PLoS ONE* **5**, e11678 (2010).
7. Whitney, J.B. & Ruprecht, R.M. Live attenuated HIV vaccines: pitfalls and prospects. *Curr. Opin. Infect. Dis.* **17**, 17–26 (2004).
8. Matzner, K.J. *et al.* Effects of *in vivo* CD8$^+$ T cell depletion on virus replication in rhesus macaques immunized with a live, attenuated simian immunodeficiency virus vaccine. *J. Exp. Med.* **191**, 1921–1931 (2000).
9. Stebbings, R. *et al.* Vaccination with live attenuated simian immunodeficiency virus for 21 days protects against superinfection. *Virology* **330**, 249–260 (2004).
10. Stebbings, R. *et al.* CD8$^+$ lymphocytes do not mediate protection against acute superinfection 20 days after vaccination with a live attenuated simian immunodeficiency virus. *J. Virol.* **79**, 12264–12272 (2005).
11. Nethe, M., Berkhout, B. & van der Kuyl, A.C. Retroviral superinfection resistance. *Retrovirology* **2**, 52 (2005).
12. Schmitz, J.E. *et al.* Effect of CD8$^+$ lymphocyte depletion on virus containment after simian immunodeficiency virus SIVmac251 challenge of live attenuated SIVmac239Δ3-vaccinated rhesus macaques. *J. Virol.* **79**, 8131–8141 (2005).
13. Reynolds, M.R. *et al.* Macaques vaccinated with live-attenuated SIV control replication of heterologous virus. *J. Exp. Med.* **205**, 2537–2550 (2008).
14. Mansfield, K. *et al.* Vaccine protection by live, attenuated simian immunodeficiency virus in the absence of high-titer antibody responses and high-frequency cellular immune responses measurable in the periphery. *J. Virol.* **82**, 4135–4148 (2008).
15. Genesca, M. *et al.* With minimal systemic T-cell expansion, CD8$^+$ T cells mediate protection of rhesus macaques immunized with attenuated simian-human immunodeficiency virus SHIV89.6 from vaginal challenge with simian immunodeficiency virus. *J. Virol.* **82**, 11181–11196 (2008).
16. Reynolds, M.R. *et al.* Macaques vaccinated with simian immunodeficiency virus SIVmac239Δ nef delay acquisition and control replication after repeated low-dose heterologous SIV challenge. *J. Virol.* **84**, 9190–9199 (2010).
17. Haase, A.T. Early events in sexual transmission of HIV and SIV and opportunities for interventions. *Annu. Rev. Med.* **62**, 127–139 (2011).
18. Johnson, R.P. *et al.* Highly attenuated vaccine strains of simian immunodeficiency virus protect against vaginal challenge: inverse relationship of degree of protection with level of attenuation. *J. Virol.* **73**, 4952–4961 (1999).
19. Jia, B. *et al.* Immunization with single-cycle SIV significantly reduces viral loads after an intravenous challenge with SIV(mac)239. *PLoS Pathog.* **5**, e1000272 (2009).
20. Kirmaier, A. *et al.* TRIM5 suppresses cross-species transmission of a primate immunodeficiency virus and selects for emergence of resistant variants in the new species. *PLoS Biol.* **8**, e1000462 (2010).
21. Crotty, S. Follicular helper CD4 T cells (TFH). *Annu. Rev. Immunol.* **29**, 621–663 (2011).
22. Ma, C.S. *et al.* Early commitment of naive human CD4$^+$ T cells to the T follicular helper (T_{FH}) cell lineage is induced by IL-12. *Immunol. Cell Biol.* **87**, 590–600 (2009).
23. Hong, J.J., Amancha, P.K., Rogers, K., Ansari, A.A. & Villinger, F. Spatial alterations between CD4$^+$ T follicular helper, B, and CD8$^+$ T cells during simian immunodeficiency virus infection: T/B cell homeostasis, activation, and potential mechanism for viral escape. *J. Immunol.* **188**, 3247–3256 (2012).
24. Sugimoto, C. *et al.* nef gene is required for robust productive infection by simian immunodeficiency virus of T-cell-rich paracortex in lymph nodes. *J. Virol.* **77**, 4169–4180 (2003).
25. West, E.E. *et al.* Tight regulation of memory CD8$^+$ T cells limits their effectiveness during sustained high viral load. *Immunity* **35**, 285–298 (2011).
26. Kallies, A. Distinct regulation of effector and memory T-cell differentiation. *Immunol. Cell Biol.* **86**, 325–332 (2008).
27. Intlekofer, A.M. *et al.* Effector and memory CD8$^+$ T cell fate coupled by T-bet and eomesodermin. *Nat. Immunol.* **6**, 1236–1244 (2005).
28. Taylor, J.J. & Jenkins, M.K. CD4$^+$ memory T cell survival. *Curr. Opin. Immunol.* **23**, 319–323 (2011).
29. Kersse, K., Lamkanfi, M., Bertrand, M.J., Vanden Berghe, T. & Vandenabeele, P. Interaction patches of procaspase-1 caspase recruitment domains (CARDs) are differently involved in procaspase-1 activation and receptor-interacting protein 2 (RIP2)-dependent nuclear factor κB signaling. *J. Biol. Chem.* **286**, 35874–35882 (2011).
30. Verdeil, G., Puthier, D., Nguyen, C., Schmitt-Verhulst, A.-M. & Auphan-Anezin, N. STAT5-mediated signals sustain a TCR-initiated gene expression program toward differentiation of CD8 T cell effectors. *J. Immunol.* **176**, 4834–4842 (2006).
31. Coller, H.A., Sang, L. & Roberts, J.M. A new description of cellular quiescence. *PLoS Biol.* **4**, e83 (2006).
32. Sarkis, J.B. *et al.* Gag- and Nef-specific CD4$^+$ T cells recognize and inhibit SIV replication in infected macrophages early after infection. *Proc. Natl. Acad. Sci. USA* **106**, 9791–9796 (2009).
33. Sant, A.J. & McMichael, A. Revealing the role of CD4$^+$ T cells in viral immunity. *J. Exp. Med.* **209**, 1391–1395 (2012).
34. Hansen, S.G. *et al.* Profound early control of highly pathogenic SIV by an effector memory T-cell vaccine. *Nature* **473**, 523–527 (2011).
35. Haynes, B.F. *et al.* Immune-correlates analysis of an HIV-1 vaccine efficacy trial. *N. Engl. J. Med.* **366**, 1275–1286 (2012).
36. Barouch, D.H. *et al.* Vaccine protection against acquisition of neutralization-resistant SIV challenges in rhesus monkeys. *Nature* **482**, 89–93 (2012).
37. Vezys, V. *et al.* Memory CD8 T-cell compartment grows in size with immunological experience. *Nature* **457**, 196–199 (2009).
38. Pitcher, C.J. *et al.* Development and homeostasis of T cell memory in rhesus macaque. *J. Immunol.* **168**, 29–43 (2002).
39. Grossman, Z. & Picker, L.J. Pathogenic mechanisms in simian immunodeficiency virus infection. *Curr. Opin. HIV AIDS* **3**, 380–386 (2008).
40. Shen, A. *et al.* Novel pathway for induction of latent virus from resting CD4$^+$ T cells in the simian immunodeficiency virus/macaque model of human immunodeficiency virus type 1 latency. *J. Virol.* **81**, 1660–1670 (2007).

LETTERS

nature medicine

SAMHD1 restricts HIV-1 infection in resting CD4$^+$ T cells

Hanna-Mari Baldauf[1,2,14], Xiaoyu Pan[1,14], Elina Erikson[1,2], Sarah Schmidt[1], Waaqo Daddacha[3], Manja Burggraf[4], Kristina Schenkova[1], Ina Ambiel[1,2], Guido Wabnitz[5], Thomas Gramberg[6], Sylvia Panitz[7], Egbert Flory[7], Nathaniel R Landau[8], Serkan Sertel[9], Frank Rutsch[10], Felix Lasitschka[11], Baek Kim[3,12], Renate König[4,13], Oliver T Fackler[1] & Oliver T Keppler[1,2]

Unlike activated CD4$^+$ T cells, resting CD4$^+$ T cells are highly resistant to productive HIV-1 infection[1–8]. Early after HIV-1 entry, a major block limits reverse transcription of incoming viral genomes. Here we show that the deoxynucleoside triphosphate triphosphohydrolase SAMHD1 prevents reverse transcription of HIV-1 RNA in resting CD4$^+$ T cells. SAMHD1 is abundantly expressed in resting CD4$^+$ T cells circulating in peripheral blood and residing in lymphoid organs. The early restriction to infection in unstimulated CD4$^+$ T cells is overcome by HIV-1 or HIV-2 virions into which viral Vpx is artificially or naturally packaged, respectively, or by addition of exogenous deoxynucleosides. Vpx-mediated proteasomal degradation of SAMHD1 and elevation of intracellular deoxynucleotide pools precede successful infection by Vpx-carrying HIV. Resting CD4$^+$ T cells from healthy donors following *SAMHD1* silencing or from a patient with Aicardi-Goutières syndrome homozygous for a nonsense mutation in *SAMHD1* were permissive for HIV-1 infection. Thus, SAMHD1 imposes an effective restriction to HIV-1 infection in the large pool of noncycling CD4$^+$ T cells *in vivo*. Bypassing SAMHD1 was insufficient for the release of viral progeny, implicating other barriers at later stages of HIV replication. Together, these findings may unveil new ways to interfere with the immune evasion and T cell immunopathology of pandemic HIV-1.

Human CD4$^+$ T lymphocytes are the major target cells of HIV-1. Activated CD4$^+$ T cells are highly permissive to infection, but resting CD4$^+$ T cells circulating in peripheral blood and residing in lymphoid organs resist infection. Blocks to infection in these cells occur at different post-entry steps of the viral life cycle[1–10].

The accessory lentiviral gene product protein X (Vpx) is encoded by HIV-2 and its related simian immunodeficiency virus (SIV) strains, but not by HIV-1. It is incorporated into virions via an interaction motif in the p6 domain of the structural polyprotein Gag. Notably, delivery of Vpx by virus-like particles or by virion-packaging allows HIV-1 to overcome the early post-entry restriction at the level of reverse transcription in dendritic cells, monocytes and macrophages[11–17]. Here we asked whether Vpx would allow HIV-1 to infect resting human CD4$^+$ T cells. To efficiently incorporate Vpx into HIV-1 virions, we added a Vpx-interaction motif into the Gag p6 of the CXCR4-tropic HIV-1 strain NL4-3 to generate a replication-competent HIV-1 GFP reporter virus (HIV-1* GFP). Resting CD4$^+$ T cells generally support efficient entry of CXCR4-tropic HIV.

CD4$^+$ T cells purified from peripheral blood of healthy donors were challenged with the engineered HIV-1* GFP virions with or without packaged Vpx. Most CD4$^+$ T cells had a resting phenotype[18] with little or no expression of the activation markers CD25 and CD69, and no indicators of cell proliferation (**Supplementary Fig. 1**) or cell cycle progression (**Supplementary Fig. 2**). As expected[2–6], resting CD4$^+$ T cells were virtually refractory to infection with HIV-1* GFP (**Fig. 1a**; 0.12% GFP$^+$ cells). In contrast, infection with HIV-1* GFP virions containing Vpx from SIV_{mac239} (HIV-1* GFP plus Vpx) yielded >10% of CD25$^-$ CD69$^-$CD4$^+$ T cells that were GFP$^+$ 3 d after challenge (**Fig. 1a**) with GFP expression reflecting early viral gene expression from reverse-transcribed, integrated HIV-1 genomes. Vpx enhanced HIV-1 infection of resting CD4$^+$ T cells in a donor-dependent manner by more than 30-fold (mean: 31.3 ± 8.4; range: 2.2–199.4-fold) (**Fig. 1b**). Vpx also increased levels of late reverse transcription products (RU5/*gag*) (near full-length HIV-1 cDNA) and 2-LTR circles (HIV-1 cDNA byproduct as a marker of successful nuclear entry) (**Fig. 1c** and **Supplementary Fig. 3**), which is consistent with an effect of the accessory lentiviral protein on HIV-1 reverse transcription. Furthermore, the infection rate and accumulation of 2-LTR circles in resting CD4$^+$ T cells challenged with HIV-1* GFP virions that had incorporated Vpx proteins of SIV_{PBJ} or $HIV\text{-}2_{GH\text{-}1}$ were similar to those observed with HIV-1* GFP virions containing Vpx from SIV_{mac239} (**Fig. 1d–f**), indicating that this is a conserved function of lentiviral Vpx proteins.

[1]Department of Infectious Diseases, Virology, University of Heidelberg, Heidelberg, Germany. [2]Institute of Medical Virology, University of Frankfurt, Frankfurt, Germany. [3]Department of Microbiology and Immunology, University of Rochester Medical Center, Rochester, New York, USA. [4]Research Group "Host-Pathogen Interactions" Paul-Ehrlich-Institute, Langen, Germany. [5]Institute of Immunology, University of Heidelberg, Heidelberg, Germany. [6]Virologisches Institut, Klinische und Molekulare Virologie, Universität Erlangen-Nürnberg, Erlangen, Germany. [7]Division of Medical Biotechnology, Paul-Ehrlich-Institute, Langen, Germany. [8]Department of Microbiology, New York University School of Medicine, New York, New York, USA. [9]Department of Otolaryngology, Head and Neck Surgery, University of Heidelberg, Heidelberg, Germany. [10]Department of General Pediatrics, Münster University Children's Hospital, Münster, Germany. [11]Institute of Pathology, University of Heidelberg, Heidelberg, Germany. [12]Department of Pharmacy, College of Pharmacy, Kyung-Hee University, Seoul, South Korea. [13]Infectious & Inflammatory Disease Center, Sanford-Burnham Medical Research Institute, La Jolla, California, USA. [14]These authors contributed equally to this work. Correspondence should be addressed to O.T.F. (oliver.fackler@med.uni-heidelberg.de) or O.T.K. (oliver.keppler@kgu.de)

Received 12 April; accepted 4 September; published online 12 September 2012; doi:10.1038/nm.2964

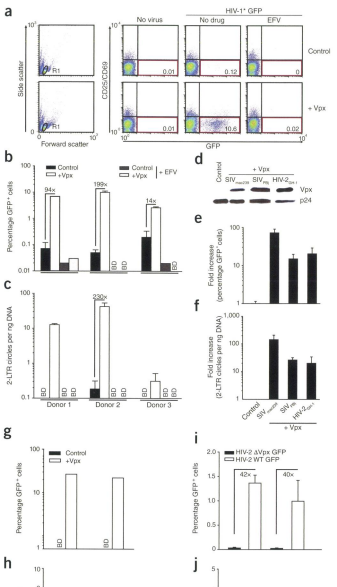

Figure 1 Vpx overcomes a restriction to HIV-1 and HIV-2 infection in resting human CD4+ T cells. (**a**–**c**) Resting CD4+ T cells were challenged with equivalent infectious units of HIV-1* GFP virions with (+Vpx) or without (Control) incorporated Vpx from SIV_{mac239} and analyzed on day 3 after infection. The reverse transcriptase inhibitor efavirenz (EFV) served as specificity control. (**a**) Dot plots of flow cytometric analysis for 1 out of 23 donors. The percentages of viable (gate R1, left graphs) resting ($CD25^-$ $CD69^-$) and infected (GFP^+) CD4+ T cells are shown in the bottom right quadrants. (**b**,**c**) Percentage of GFP^+ cells (**b**) and relative copy numbers of HIV-1 2-LTR circles (**c**). Bars represent means of triplicates + s.d., with the factors of increase by Vpx indicated. (**d**) Immunoblotting of HIV-1 virions for incorporated epitope-tagged Vpx proteins from SIV_{mac239}, SIV_{PBJ} or HIV-2_{GH-1}. HIV-1 p24 served as a loading control. (**e**,**f**) Percentage of GFP^+ cells (**e**) and relative 2-LTR circle copy numbers (**f**) of resting CD4+ T cells challenged with the Vpx-carrying viruses relative to the Vpx-negative control virus. Bars represent means + s.e.m. of the factors of increase ($n = 4$). Percentages of GFP^+ cells ranged from 0.5% to 3.1% for Vpx of SIV_{mac239}, from 0.2% to 0.7% for Vpx of SIV_{PBJ} and from 0.1% to 0.9% for Vpx of HIV-2_{GH-1}. (**g**–**j**) Resting CD4+ T cells from the same donors were challenged with equivalent infectious units of HIV-1* GFP virions with (+Vpx) or without (Control) incorporated Vpx (**g**,**h**) or HIV-2_{RDD9} GFP or HIV-2_{RDD9} ΔVpx GFP (**i**,**j**) and analyzed for the percentage of GFP^+ cells (**g**,**i**) and the amount of HIV-1 p24 or HIV-2 p27, respectively, released into the cell culture supernatant on day 3 after infection (**h**,**j**). Bars in **i**,**j** represent means of triplicates + s.d. The dotted line in **j** indicates the cut-off of the p27 ELISA. BD, below detection.

Although Vpx enabled early steps of the HIV-1 life cycle, viral progeny were not released from resting CD4+ T cells (**Fig. 1g**,**h**). Virions of the replication-competent HIV-2 strain ROD9 GFP, which naturally encodes Vpx, consistently overcame the early restriction in resting CD4+ T cells in a Vpx-dependent manner, but, similarly to Vpx-carrying HIV-1, they did not lead to the production of new virions (**Fig. 1i**,**j**). The susceptibility of resting CD4+ T cells to the Vpx-carrying HIV-1* GFP reached only ~25% of that of activated CD4+ T cells from the same donors challenged with HIV-1* GFP lacking Vpx, and virion-incorporated Vpx did not significantly enhance the HIV-1 susceptibility of activated cells ($P = 0.33$; **Supplementary Fig. 4**). Thus, Vpx overcomes a block to the early steps of HIV-1 and HIV-2 replication in resting CD4+ T cells, but additional, Vpx-insensitive blocks probably exist at later stages of the viral life cycle.

SAMHD1 is expressed in dendritic cells, monocytes and macrophages, but not in T cell lines, and it has been reported to act as a lineage-specific infection barrier for HIV-1 (refs. 19,20). Notably, SAMHD1 is targeted by Vpx for $CRL4^{DCAF1}$ ubiquitin ligase–dependent proteasomal degradation[17,19,20]. In spite of this proposed lineage specificity, we detected high levels of endogenous SAMHD1 mRNA and protein in resting CD4+ T cells that were comparable to those in the monocytic THP-1 cell line (**Fig. 2a**,**b**). Cell activation with phytohemagglutinin (PHA) and interleukin-2 (IL-2) did not affect overall SAMHD1 levels (**Fig. 2a**,**b**). SAMHD1 was also abundantly expressed in explants of human tonsil, a lymphoid tissue targeted by HIV-1 *in vivo*, where the majority of SAMHD1-expressing cells localized to the perifollicular region and were Ki67 negative, that is, nonproliferating (**Fig. 2c**). Co-staining with cell type–specific markers demonstrated SAMHD1 expression predominantly in $CD68^+$ macrophages, $DC\text{-}SIGN^+$ dendritic cells and CD4+ lymphocytes (data not shown). Nuclear-cytoplasmic fractionation and three-dimensional reconstructions of deconvolution confocal images revealed substantial amounts of SAMHD1 in the nucleus and cytoplasm of resting CD4+ T cells (**Fig. 2d**,**e** and **Supplementary Video 1**), activated CD4+ T cells and macrophages (**Supplementary Fig. 5**). Thus, SAMHD1 might directly deplete levels of dNTPs in the cytoplasm of resting CD4+ T cells where HIV-1 reverse transcription occurs.

To assess the ability of Vpx to degrade endogenous SAMHD1 in resting CD4+ T cells from healthy donors, we co-expressed Myc-tagged SIV_{mac239} Vpx and a cell surface–exposed GFP variant (Display-GFP; see Online Methods) to facilitate isolation of a homogenous population of viable, nucleofected cells. SAMHD1 pools in both the cytoplasm and the nucleus were depleted after expression of wild-type (WT) Vpx, but not after expression of the $CRL4^{DCAF1}$ interaction–deficient mutant Q76A[16,19] (**Fig. 2f** and **Supplementary Fig. 6**), irrespective of the cells' activation status (**Supplementary Fig. 6**). We also detected a potent and Q76-dependent reduction of SAMHD1 levels upon Vpx co-expression by intracellular flow cytometry (**Fig. 2g** and **Supplementary Fig. 7**). Low levels of co-expressed GFP and WT Vpx were sufficient to maximally degrade SAMHD1 and diminished intracellular SAMHD1 levels by more than 90% (**Fig. 2g**, left lower panel).

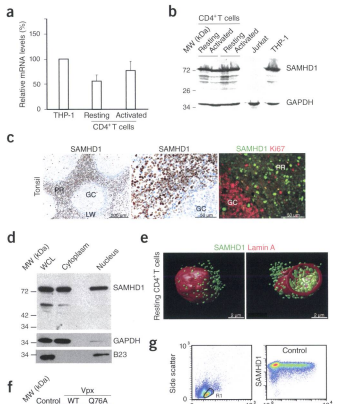

Figure 2 SAMHD1 is expressed in resting CD4⁺ T cells and depleted by Vpx. (**a**) RT-PCR–based quantification of SAMHD1 mRNA levels in CD4⁺ T cells. RNaseP-normalized mRNA levels in resting and PHA- and IL-2-activated CD4⁺ T cells are presented relative to those from THP-1 cells that were arbitrarily set to 100%. Means + s.e.m. of four donors. (**b**) Immunoblotting for endogenous expression of SAMHD1 in CD4⁺ T cells (two donors). GAPDH: loading control. (**c**) *In situ* expression of SAMHD1 in explants of human tonsil. Left and center, immunohistochemical detection of SAMHD1. Nuclei were counterstained with hematoxylin. GC, germinal center; LW, lymphocyte wall; PR, perifollicular region. Right, immunofluorescence analysis of SAMHD1 expression (green) relative to the proliferation marker Ki67 (red). (**d**) SAMHD1 immunoblot analysis of a nuclear-cytoplasmic fractionation of resting CD4⁺ T cells. WCL, whole cell lysate. GAPDH and B23 served as cytoplasmic and nuclear markers, respectively. (**e**) Three-dimensional reconstructions of deconvolution confocal microscopy images of a resting CD4⁺ T cell co-stained for SAMHD1 (green) and the nuclear envelope protein lamin A (red). At right is an optical section across the cell to show nuclear and cytoplasmic SAMHD1. (**f**) Immunoblots of endogenous SAMHD1 in nucleofected resting CD4⁺ T cells expressing WT Vpx, Vpx Q76A or an empty vector control. Co-expression of surface-exposed Display-GFP was used to purify a homogenous population of nucleofected cells. Similar results were obtained for two other donors. (**g**) Quantification of intracellular SAMHD1 amounts in nucleofected resting CD4⁺ T cells. Cells were nucleofected to co-express GFP together with WT Vpx, Vpx Q76A or an empty control and 16 h later assessed for SAMHD1 expression in relation to GFP by flow cytometry.

To explore the relationship between Vpx-mediated degradation of SAMHD1 and permissivity to HIV-1 in resting CD4⁺ T cells, we followed both parameters over time at a single-cell level. Whereas infection with HIV-1* GFP had no effect, SAMHD1 was massively depleted in 20–80% of cells 1 d after challenge with HIV-1* GFP plus SIV$_{mac239}$ Vpx (**Fig. 3a**,**b** and **Supplementary Fig. 8b**). This degree of depletion was constant until day 3 after infection, when GFP reporter expression indicated proviral integration and early viral gene expression (4.3% of cells in **Fig. 3a**). Of note, GFP* cells were detected exclusively within the population of cells containing low amounts of SAMHD1, whereas the residual cell population expressing high amounts of SAMHD1 remained refractory to HIV-1 infection. Virion-incorporated Vpx seemed insufficient to render all resting CD4⁺ T cells permissive for HIV-1 infection, suggesting either additional Vpx-insensitive limitations for HIV-1 in the post-entry phase[2,5,9] or SAMHD1 depletion by Vpx-carrying, but otherwise defective, virions.

SAMHD1 degradation in resting CD4⁺ T cells was specific to HIV-1* GFP virions containing Vpx; it was observed as early as 6 h after virion challenge and correlated in magnitude with the percentage of GFP⁺ cells (**Fig. 3a**,**b**). The peptidic virion fusion inhibitor T20 or the CXCR4 antagonist AMD3100 inhibited Vpx-dependent depletion of SAMHD1 (**Fig. 3c**), demonstrating that this process strictly depends on virus entry and subsequent release of Vpx from disassembled viral capsids. Furthermore, the depletion of SAMHD1 and the enhancement of resting T cell infection by virion-packaged Vpx was abrogated by treatment of cells with the proteasome inhibitors MG132 (**Fig. 3c**) or ALLN (data not shown). In line with the targeting of SAMHD1 for proteasomal degradation by Vpx having a central role in HIV-1* GFP infection, incorporation of the Vpx Q76A mutant, which does not deplete cellular pools of SAMHD1, failed to promote infection of resting CD4⁺ T cells (**Supplementary Fig. 8a**–**c**). Similarly, successful HIV-2 GFP infection correlated with Vpx-dependent degradation of SAMHD1 (**Fig. 1i** and **Supplementary Fig. 8d**) .

In myeloid cells, SAMHD1 hydrolyzes dNTPs, which most likely lowers their concentrations below a threshold required for synthesis of HIV-1 cDNA by reverse transcriptase[21–23]. To explore this as a mode of restriction for HIV-1 in resting CD4⁺ T cells, we added pyrimidine and purine deoxynucleosides (dNs) as dNTP precursors to the culture medium. In the absence of Vpx, dNs enhanced the permissivity of resting CD4⁺ T cells for HIV-1 GFP ninefold ($n = 8$) over solvent-treated control cells (**Fig. 3d**) while not affecting the cell cycle or activation status of the cells (**Supplementary Fig. 2a** and **Supplementary Fig. 9**). We conducted a side-by-side analysis of the efficacy of virion-packaged Vpx proteins and dN treatment in resting CD4⁺ T cells from eight donors. The strongly positive correlation of both approaches to augment infection supports a common cellular mechanism that overcomes the HIV-1 restriction ($R^2 = 0.72$; $P = 0.008$; **Fig. 3e**). Next, we directly determined the effect of T cell activation or of treatment with either dNs or virion-delivered Vpx on intracellular concentrations of dNTPs in resting CD4⁺ T cells by the single-nucleotide incorporation assay. PHA- and IL-2-mediated activation of CD4⁺ T cells increased dATP and dTTP concentrations by 2.9- to 7.8-fold (**Fig. 3f**,**g** and **Supplementary Fig. 10**), as previously reported[22,24]. Exogenous dN treatment of resting cells resulted, on average, in 4.4-fold higher cellular dNTP levels. Notably, infection of resting CD4⁺ T cells with HIV-1* GFP also moderately elevated cellular nucleotide concentrations in a Vpx-dependent manner (1.7- to 2.8-fold, $P = 0.05$–0.005; **Fig. 3f**,**g** and **Supplementary Fig. 10**). This increase was observed despite the relatively low percentage of SAMHD1-depleted cells in this experiment (17% (donor 12) and 31% (donor 13)). Collectively, these results are consistent with the concepts that pools of intracellular dNTPs in resting CD4⁺ T cells are rate limiting for HIV reverse transcription[8] and that SAMHD1 may be a key regulator of this cellular antiviral state.

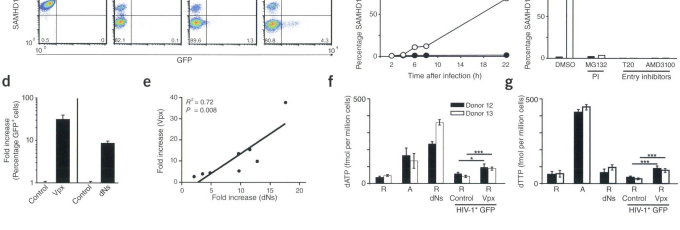

Figure 3 Susceptibility of resting CD4⁺ T cells to Vpx-carrying HIV-1 is paralleled by proteasomal degradation of SAMHD1 and increased dNTP levels. (**a**) Time course of SAMHD1 and GFP expression in resting CD4⁺ T cells after challenge with HIV-1* GFP + Vpx (SIV_{mac239}). The percentages of cells in the respective quadrants are shown. (**b**) Quantification of SAMHD1 expression in resting CD4⁺ T cells within the first 22 h after exposure to HIV-1* GFP with (+ Vpx) or without (Control) incorporated Vpx. Data points mark the percentages for cells with low SAMHD1 levels (corresponding to the bottom left quadrants in FACS panels shown in **a**). (**c**) Effect of proteasome or HIV-1 entry inhibitors on SAMHD1 levels in resting CD4⁺ T cells after exposure to HIV-1* GFP ± Vpx. Resting CD4⁺ T cells were pretreated for 1 h with either the proteasome inhibitor (PI) MG132 (10 μM), the fusion inhibitor T20 (50 μM) or the CXCR4 antagonist AMD3100 (5 μM) before infection with HIV-1* GFP with or without virion-packaged Vpx. Drugs were removed 20 h later. Shown are the percentages of resting CD4⁺ T cells with low levels of SAMHD1 24 h after infection for one of three donors. (**d**) Relative factor of increase of infection of resting CD4⁺ T cells with HIV-1* GFP by virion-packaged Vpx ($n = 15$) or by incubation with deoxynucleosides (dNs) ($n = 8$). Means + s.e.m. (**e**) Correlation between the enhancement of infection of resting CD4⁺ T cells with HIV-1* GFP either by virion-packaged Vpx or by dN treatment. Depicted is the relative factor of increase in infection for both parameters obtained in parallel experiments for cells from eight different donors. (**f**,**g**) Quantification of dATP (**f**) and dTTP (**g**) levels in primary CD4⁺ T cells under different experimental conditions determined by single-nucleotide incorporation assay. R, resting CD4⁺ T cells; A, activated CD4⁺ T cells. dNs, cultivation in the presence of dNs (2 mM) for 3 h. Challenge with HIV-1* GFP + Vpx had resulted in depletion of SAMHD1 in 17% (donor 12) or 31% (donor 13) of resting CD4⁺ T cells 24 h after challenge, respectively, at which time cells were harvested for subsequent dNTP analyses. See also **Supplementary Figure 10** for primary data of the single-nucleotide incorporation assay. $^*P < 0.05$; $^{***}P < 0.005$.

To directly probe the ability of SAMHD1 to restrict HIV-1 infection in resting CD4⁺ T lymphocytes from healthy donors, we used two RNAi strategies to silence its expression[25,26]. We activated primary CD4⁺ T cells to allow effective siRNA delivery by nucleofection or transduction with lentiviral vectors carrying shRNAs. We gradually reduced IL-2 concentrations and analyzed the cells for HIV-1 permissivity once they returned to a quiescent and HIV-1–restrictive state, typically by day 14 after activation (see also **Supplementary Figs. 11a** and **12a**). We classified post-activation CD4⁺ T cells as resting on the basis of three criteria: (i) their lack of CD25 and CD69 expression, (ii) their lack of proliferation markers and (iii) their resistance to HIV-1 infection after treatment with control siRNA (Con) (**Fig. 4a**–**g** and **Supplementary Fig. 11b**–**d**). Silencing of *SAMHD1* with three independent siRNAs markedly reduced cellular SAMHD1 levels (**Fig. 4d**–**g** and **Supplementary Fig. 11e**) and rendered post-activation resting CD4⁺ T cells from multiple donors ($n = 6$) permissive to HIV-1 infection (**Fig. 4b**–**g** and **Supplementary Fig. 11b**–**d**). The enhancement of HIV-1 infection ranged from 5.1- to 18.6-fold, depending on the donor and knockdown efficiency, corresponding to 3.6–15.3% infected GFP⁺ cells (**Fig. 4d**–**g** and **Supplementary Fig. 11d**). We observed a similar but slightly less potent increase in HIV-1 infection in post-activation resting CD4⁺ T cells when *SAMHD1* was silenced by shRNA transduction (**Supplementary Fig. 12b**–**d**) of two targeting sequences that are distinct from those of the siRNAs used. Thus, depletion of cellular SAMHD1 by RNAi is sufficient to enhance the permissiveness of resting CD4⁺ T cells for HIV-1 infection. Finally, we wanted to determine whether resting CD4⁺ T cells with a nonsense mutation in *SAMHD1* obtained from a patient with Aicardi-Goutières syndrome (AGS)[17,27] were susceptible to HIV-1 infection. By flow cytometric analysis of peripheral blood mononuclear cells (PBMCs), SAMHD1 protein was not detected in $CD25^-CD69^-CD3^+CD4^+$ T cells from this patient. Unlike cells from healthy donors, resting CD4⁺ T cells from this patient with AGS were intrinsically permissive for HIV-1 GFP infection (**Fig. 4h**–**j**).

Our results suggest that HIV-1 reverse transcription is actively suppressed in resting human CD4⁺ T cells, and we identify SAMHD1 as a long-sought cellular factor that is responsible for this restriction. SAMHD1 thus emerges as a ubiquitous and potent barrier to productive HIV-1 infection in dendritic and myeloid cells[17,19,20,22] and also in the large pool of noncycling CD4⁺ T cells *in vivo*. Although not excluding additional SAMHD1-dependent mechanisms, the available data are consistent with a scenario in which this restriction is a direct consequence of SAMHD1's enzymatic activity, which limits the availability of dNTPs required for HIV-1 reverse transcription[21–23]. Regulation of deoxynucleotide levels in resting cells by SAMHD1 may have evolved to protect T helper cells from retroviral insult without the risk of disrupting the homeostasis of these noncycling cells. Therapeutic manipulation of intracellular dNTP pools thus emerges as a potential antiretroviral strategy. Given the overall potency of virus-encoded SAMHD1 antagonists, such as Vpx, to expand the target cell population of HIV-1 to noncycling cells, it seems surprising that they were lost in lentiviral evolution[28,29]. This indicates that overcoming SAMHD1 restriction in these types of cells may in fact carry significant adverse consequences for pandemic HIV-1 and that the abortive SAMHD1-restricted

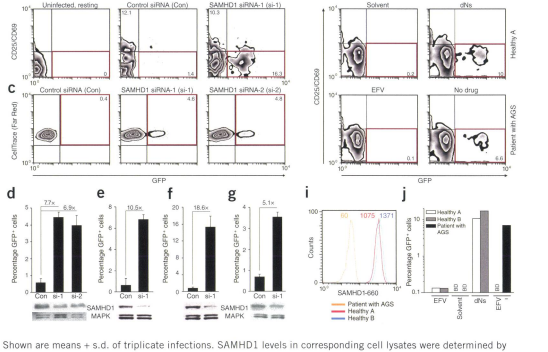

Figure 4 Silencing of *SAMHD1* by RNA interference or a homozygous nonsense mutation renders resting CD4$^+$ T cells permissive for HIV-1 infection. (**a**–**c**) Flow cytometric analysis of freshly isolated, uninfected resting CD4$^+$ T cells (staining reference) (**a**) or of post-activated resting CD4$^+$ T cells infected with HIV-1 GFP after treatment with the indicated siRNAs (**b**,**c**). Red boxes indicate populations of infected cells with relative percentages indicated. Cells' activation state was assessed by surface expression of CD25 and CD69 (**a**,**b**) or CellTrace (Far Red) dilution (**c**). (**d**–**g**) Quantification of the percentage of GFP$^+$ cells and the relative increase of HIV-1 GFP infection in resting CD4$^+$ T cells from four donors (each corresponding to a panel) following silencing with *SAMHD1*-specific siRNAs (si-1 or si-2) relative to a nontargeting control siRNA (Con). Shown are means + s.d. of triplicate infections. SAMHD1 levels in corresponding cell lysates were determined by immunoblotting. MAPK, loading control. See also **Supplementary Figure 11b**–**e** for results with cells from two additional donors, including the use of *SAMHD1* si-3. (**h**) Flow cytometric analyses of PBMCs from healthy donor A (solvent- or dN-treated, top graphs) or PBMCs from a patient with AGS with a homozygous nonsense mutation in the *SAMHD1* gene (EFV-treated or untreated, bottom graphs) 3 d after challenge with HIV-1 GFP (multiplicity of infection = 1). The percentages of resting (CD25$^-$CD69$^-$), infected (GFP$^+$) CD3$^+$CD4$^+$ PBMCs are shown in the bottom right quadrants boxed in red, with the percentage of infected cells indicated. (**i**) Intracellular SAMHD1 expression in resting CD4$^+$ T cells of PBMCs from the patient with AGS and from healthy donors A and B, as determined by flow cytometry. The mean fluorescence intensity of SAMHD1 levels is indicated. (**j**) Quantification of the percentage of infected (GFP$^+$) resting CD4$^+$ T cells from the patient with AGS and from healthy donors (see panel **h** for primary data). Shown are arithmetic means of duplicates. BD, below detection.

infection by HIV-1 contributes to innate sensing-mediated T cell immunopathology[1] and immune evasion[17,30,31], and thus to AIDS pathogenesis. Further insight into the regulation and consequences of the SAMHD1-imposed restriction in CD4$^+$ T cells will help identify new pathways for interfering with immunodeficiency in HIV-1-infected individuals.

METHODS

Methods and any associated references are available in the online version of the paper.

Note: Supplementary information is available in the online version of the paper.

ACKNOWLEDGMENTS

We thank M. Emerman (Fred Hutchinson Cancer Research Center, Seattle, USA; for pRO109, pRODP-ΔEnv-GFP, pRODP-ΔEnv-delVpx-GFP), M. Fujita (Research Institute for Drug Discovery, Kumamoto University, Japan; for pEF-FVpxHIV-$2_{(H1)}$), H.-G. Kräusslich (Department of Infectious Diseases, Virology, University of Heidelberg, Germany; for AMD3100), B. Müller (Department of Infectious Diseases, Virology, University of Heidelberg, Germany; for pDisplay GFP and sheep anti–HIV-1 p24 antibody) and J. Münch (Institute of Molecular Virology, University Hospital Ulm, Germany; for HIV-1 GFP) for reagents. We thank T. Adam, A. Imle, P. Klein, S. Kutscheid, A. Ruggieri and the Nikon Imaging Center at University of Heidelberg for technical assistance, and G. Howard for editorial assistance. This work was in part funded by the Deutsche Forschungsgemeinschaft (O.T.K., grant KE742/4-1), SFB 938/Z2 (F.L.) and the US National Institutes of Health (GM1041981 and AI049781 to B.K.; and F31 GM095190 to W.D.). O.T.F. and O.T.K. are members of the CellNetworks Cluster of Excellence EXC81 and the German Centre for Infection Research, University of Heidelberg. H.-M.B. is recipient of a fellowship of the Medical Faculty of the University of Heidelberg.

AUTHOR CONTRIBUTIONS

O.T.K. and O.T.F. conceived of the study, designed experiments and wrote the manuscript. H-M.B., X.P., E.E., S. Schmidt, W.D., M.B., K.S., B.K., S.P. and R.K. designed and conducted experiments and discussed and interpreted the data with O.T.F. and O.T.K. I.A., E.F., G.W., T.G. and N.B.L. provided reagents and expertise. S. Sertel, F.R. and F.L. provided tissue samples and expertise and interpreted data.

COMPETING FINANCIAL INTERESTS

The authors declare no competing financial interests.

Published online at http://www.nature.com/doifinder/10.1038/nm.2964.
Reprints and permissions information is available online at http://www.nature.com/reprints/index.html.

1. Doitsh, G. *et al.* Abortive HIV infection mediates CD4 T cell depletion and inflammation in human lymphoid tissue. *Cell* **143**, 789–801 (2010).
2. Ganesh, L. *et al.* The gene product Murr1 restricts HIV-1 replication in resting CD4$^+$ lymphocytes. *Nature* **426**, 853–857 (2003).
3. Korin, Y.D. & Zack, J.A. Progression to the G1b phase of the cell cycle is required for completion of human immunodeficiency virus type 1 reverse transcription in T cells. *J. Virol.* **72**, 3161–3168 (1998).
4. Pierson, T.C. *et al.* Molecular characterization of preintegration latency in human immunodeficiency virus type 1 infection. *J. Virol.* **76**, 8518–8531 (2002).
5. Stevenson, M., Stanwick, T.L., Dempsey, M.P. & Lamonica, C.A. HIV-1 replication is controlled at the level of T cell activation and proviral integration. *EMBO J.* **9**, 1551–1560 (1990).
6. Zack, J.A. *et al.* HIV-1 entry into quiescent primary lymphocytes: molecular analysis reveals a labile, latent viral structure. *Cell* **61**, 213–222 (1990).
7. Dai, J. *et al.* Human immunodeficiency virus integrates directly into naive resting CD4$^+$ T cells but enters naive cells less efficiently than memory cells. *J. Virol.* **83**, 4528–4537 (2009).
8. Plesa, G. *et al.* Addition of deoxynucleosides enhances human immunodeficiency virus type 1 integration and 2LTR formation in resting CD4$^+$ T cells. *J. Virol.* **81**, 13938–13942 (2007).
9. Yoder, A. *et al.* HIV envelope-CXCR4 signaling activates cofilin to overcome cortical

actin restriction in resting CD4 T cells. *Cell* **134**, 782–792 (2008).
10. Swingler, S. *et al.* HIV-1 Nef intersects the macrophage CD40L signalling pathway to promote resting-cell infection. *Nature* **424**, 213–219 (2003).
11. Bergamaschi, A. *et al.* The human immunodeficiency virus type 2 Vpx protein usurps the CUL4A-DDB1 DCAF1 ubiquitin ligase to overcome a postentry block in macrophage infection. *J. Virol.* **83**, 4854–4860 (2009).
12. Berger, G., Goujon, C., Darlix, J.L. & Cimarelli, A. SIVMAC Vpx improves the transduction of dendritic cells with nonintegrative HIV-1–derived vectors. *Gene Ther.* **16**, 159–163 (2009).
13. Goujon, C. *et al.* Characterization of simian immunodeficiency virus SIVSM/human immunodeficiency virus type 2 Vpx function in human myeloid cells. *J. Virol.* **82**, 12335–12345 (2008).
14. Pertel, T., Reinhard, C. & Luban, J. Vpx rescues HIV-1 transduction of dendritic cells from the antiviral state established by type 1 interferon. *Retrovirology* **8**, 49 (2011).
15. Sharova, N. *et al.* Primate lentiviral Vpx commandeers DDB1 to counteract a macrophage restriction. *PLoS Pathog.* **4**, e1000057 (2008).
16. Srivastava, S. *et al.* Lentiviral Vpx accessory factor targets VprBP/DCAF1 substrate adaptor for cullin 4 E3 ubiquitin ligase to enable macrophage infection. *PLoS Pathog.* **4**, e1000059 (2008).
17. Berger, A. *et al.* SAMHD1-deficient CD14$^+$ cells from individuals with Aicardi-Goutieres syndrome are highly susceptible to HIV-1 infection. *PLoS Pathog.* **7**, e1002425 (2011).
18. Eckstein, D.A. *et al.* HIV-1 actively replicates in naive CD4$^+$ T cells residing within human lymphoid tissues. *Immunity* **15**, 671–682 (2001).
19. Hrecka, K. *et al.* Vpx relieves inhibition of HIV-1 infection of macrophages mediated by the SAMHD1 protein. *Nature* **474**, 658–661 (2011).
20. Laguette, N. *et al.* SAMHD1 is the dendritic- and myeloid-cell–specific HIV-1 restriction factor counteracted by Vpx. *Nature* **474**, 654–657 (2011).
21. Goldstone, D.C. *et al.* HIV-1 restriction factor SAMHD1 is a deoxynucleoside triphosphate triphosphohydrolase. *Nature* **480**, 379–382 (2011).
22. Lahouassa, H. *et al.* SAMHD1 restricts the replication of human immunodeficiency virus type 1 by depleting the intracellular pool of deoxynucleoside triphosphates. *Nat. Immunol.* **13**, 223–228 (2012).
23. Powell, R.D., Holland, P.J., Hollis, T. & Perrino, F.W. Aicardi-Goutieres syndrome gene and HIV-1 restriction factor SAMHD1 is a dGTP-regulated deoxynucleotide triphosphohydrolase. *J. Biol. Chem.* **286**, 43596–43600 (2011).
24. Diamond, T.L. *et al.* Macrophage tropism of HIV-1 depends on efficient cellular dNTP utilization by reverse transcriptase. *J. Biol. Chem.* **279**, 51545–51553 (2004).
25. Wabnitz, G.H. *et al.* Sustained LFA-1 cluster formation in the immune synapse requires the combined activities of L-plastin and calmodulin. *Eur. J. Immunol.* **40**, 2437–2449 (2010).
26. Santoni de Sio, F.R. & Trono, D. APOBEC3G-depleted resting CD4$^+$ T cells remain refractory to HIV1 infection. *PLoS ONE* **4**, e6571 (2009).
27. Thiele, H. *et al.* Cerebral arterial stenoses and stroke: novel features of Aicardi-Goutieres syndrome caused by the Arg164X mutation in SAMHD1 are associated with altered cytokine expression. *Hum. Mutat.* **31**, E1836–E1850 (2010).
28. Lim, E.S. *et al.* The ability of primate lentiviruses to degrade the monocyte restriction factor SAMHD1 preceded the birth of the viral accessory protein Vpx. *Cell Host Microbe* **11**, 194–204 (2012).
29. Laguette, N. *et al.* Evolutionary and functional analyses of the interaction between the myeloid restriction factor SAMHD1 and the lentiviral Vpx protein. *Cell Host Microbe* **11**, 205–217 (2012).
30. Manel, N. *et al.* A cryptic sensor for HIV-1 activates antiviral innate immunity in dendritic cells. *Nature* **467**, 214–217 (2010).
31. Manel, N. & Littman, D.R. Hiding in plain sight: how HIV evades innate immune responses. *Cell* **147**, 271–274 (2011).

nature medicine

Evolution of an HIV glycan–dependent broadly neutralizing antibody epitope through immune escape

Penny L Moore[1,2], Elin S Gray[1], C Kurt Wibmer[1,2], Jinal N Bhiman[1,2], Molati Nonyane[1], Daniel J Sheward[3], Tandile Hermanus[1], Shringkhala Bajimaya[4], Nancy L Tumba[1], Melissa-Rose Abrahams[3], Bronwen E Lambson[1], Nthabeleng Ranchobe[1], Lihua Ping[5], Nobubelo Ngandu[3], Quarraisha Abdool Karim[6], Salim S Abdool Karim[6], Ronald I Swanstrom[5], Michael S Seaman[4], Carolyn Williamson[3] & Lynn Morris[1,2]

Neutralizing antibodies are likely to play a crucial part in a preventative HIV-1 vaccine. Although efforts to elicit broadly cross-neutralizing (BCN) antibodies by vaccination have been unsuccessful[1–3], a minority of individuals naturally develop these antibodies after many years of infection[4–7]. How such antibodies arise, and the role of viral evolution in shaping these responses, is unknown. Here we show, in two HIV-1–infected individuals who developed BCN antibodies targeting the glycan at Asn332 on the gp120 envelope, that this glycan was absent on the initial infecting virus. However, this BCN epitope evolved within 6 months, through immune escape from earlier strain-specific antibodies that resulted in a shift of a glycan to position 332. Both viruses that lacked the glycan at amino acid 332 were resistant to the Asn332-dependent BCN monoclonal antibody PGT128 (ref. 8), whereas escaped variants that acquired this glycan were sensitive. Analysis of large sequence and neutralization data sets showed the 332 glycan to be significantly under-represented in transmitted subtype C viruses compared to chronic viruses, with the absence of this glycan corresponding with resistance to PGT128. These findings highlight the dynamic interplay between early antibodies and viral escape in driving the evolution of conserved BCN antibody epitopes.

Although the role of glycans in shielding neutralizing epitopes has long been known[9–11], it has only recently become clear that many BCN responses directly target glycans, including the one at position 332 in the C3 region of the gp120 subunit of the HIV-1 envelope protein[8,12–18]. The recent isolation of monoclonal antibodies (mAbs) that target this glycan, which are the most potent yet described, has focused attention on this epitope[8]. These mAbs (PGT121–PGT123, PGT125–PGT128, PGT130, PGT131 and PGT135–PGT137) neutralize effectively across all HIV-1 subtypes, with the broadest, PGT128, neutralizing >70% of viruses tested[8]. Crystal structures of PGT127 and PGT128 have shown that these mAbs penetrate the glycan shield, recognizing high-mannose glycans at amino acids 301 and 332, in addition to a short β-strand in the C terminus of the V3 loop[19]. The conserved nature of these amino acids and the high potency of this class of mAbs suggest that this region may be an important vaccine target. Furthermore, this epitope is immunogenic, as Asn332-dependent BCN antibodies are often found in infected subjects who develop neutralization breadth[8,14–17]. However, as with other BCN antibodies, the factors that favor the emergence of Asn332-dependent BCN antibodies remain unclear. Here we hypothesize that the evolution of viral populations, which are under considerable immune and fitness selection pressures, creates BCN antibody epitopes essential for the development of neutralization breadth.

From a cohort of 79 HIV-1 subtype C–infected women studied starting at the point of acute infection, we focused on two participants who developed Asn332-dependent BCN antibodies. Subject CAP177 produced antibodies by 3 years after infection that were capable of neutralizing 88% of a large multisubtype panel of 225 heterologous viruses (M. Lacerda, P.L.M., N.N., M.S.S., E.S.G. *et al.*, unpublished data). The second individual, CAP314, neutralized 46% of 41 heterologous viruses after only 2 years of infection (**Supplementary Fig. 1**). Plasmas from CAP177 and CAP314 were unable to neutralize heterologous viruses that lacked the glycan at position 332 from the time when BCN responses were first detected and thereafter (**Fig. 1a**), confirming that their BCN activity depended on the 332 glycan, similar to the PGT128 mAb.

Single-genome amplification and gp160 sequencing from plasma viral RNA (Online Methods) was used to determine the amino acid sequence of the envelopes of circulating viral populations at multiple time points. This included the earliest available plasma samples, which were taken 2 weeks after infection for CAP177 (enabling inference of the transmitted/founder virus[20]) and 3 months after infection for CAP314. In both cases, these acute viruses lacked the predicted N-linked glycan at amino acid 332, although almost all sequences contained an intact glycosylation site at position 334 (**Fig. 1b,c**).

[1]Centre for HIV and STI, National Institute for Communicable Diseases of the National Health Laboratory Service, Johannesburg, South Africa. [2]University of the Witwatersrand, Johannesburg, South Africa. [3]Institute of Infectious Diseases and Molecular Medicine, University of Cape Town, Cape Town, South Africa. [4]Division of Viral Pathogenesis, Department of Medicine, Harvard Medical School, Beth Israel Deaconess Medical Center, Boston, Massachusetts, USA. [5]University of North Carolina at Chapel Hill, Chapel Hill, North Carolina, USA. [6]Centre for the AIDS Programme of Research in South Africa (CAPRISA), University of KwaZulu Natal, Durban, South Africa. Correspondence should be addressed to L.M. (lynnm@nicd.ac.za).

Received 30 April; accepted 27 September; published online 21 October 2012; doi:10.1038/nm.2985

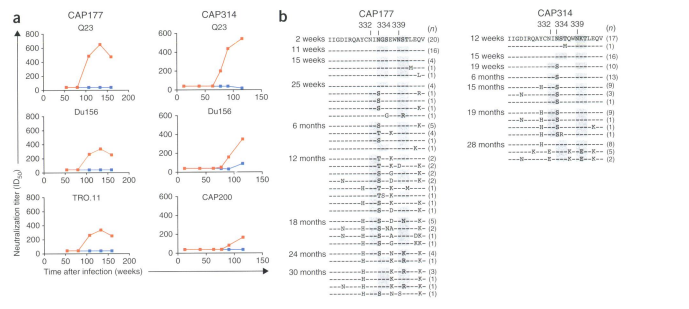

Figure 1 Characterizing the antibody specificities and viral populations in CAP177 and CAP314. (**a**) Serial plasma neutralization of three heterologous viruses (Q23, Du156 and TRO.11 for CAP177 and Q23, Du156 and CAP200 for CAP314) compared to mutant viruses where the 332 glycan was deleted by mutagenesis. Wild-type viruses are shown in orange and mutants in blue. (**b**) Sequence alignment showing part of the C3 region from 2 weeks (CAP177) or 3 months (CAP314) up to 28–30 months after infection. The number of sequences at each time point is indicated. Gray shading indicates the presence of a predicted N-linked glycan, and dashes indicate sequence identity compared to the acute sequence. HXB2 numbering is used throughout. (**c**) The frequency of the 332 glycan is shown over time (as pie charts) relative to neutralization of the acute autologous virus (corresponding to the 2-week and 3-month sequences shown above, gray line) and sensitive heterologous viruses (of subtype C in orange, subtype B in blue and subtype A in green). Plasma samples were available only up to 2 years after infection for CAP314, who received antiretroviral therapy shortly thereafter.

By 5–6 months of infection, a glycan at position 332 evolved in both CAP177 and CAP314 through an N334T or N334S substitution, which also resulted in the destruction of the neighboring glycan at position 334. By 12–15 months, when BCN antibodies became detectable, the 332 glycan was present in all sequences; however, at around 2 years the glycan reverted to position 334, most likely as a consequence of viral escape from the Asn332-dependent BCN response (**Fig. 1b**,**c**). Therefore, for both CAP177 and CAP314, the glycan that formed the basis of the BCN epitope was not present on the infecting virus but evolved shortly thereafter, coincident with the appearance of strain-specific antibodies (**Fig. 1c**).

The 332 glycan lies within the C3 region, which is highly immunogenic in HIV-1 subtype C and is often targeted by early strain-specific antibodies[21]. Indeed, we have previously shown that in CAP177 early neutralizing antibodies targeted the C3 region[22]. As viral escape often involves glycan rearrangements[10], we postulated that the shift of a glycan from position 334 to 332 in CAP177 and CAP314 may have been the result of neutralization escape from early strain-specific antibodies. To test this, we cloned the acute virus and a representative 6-month virus from CAP177 and CAP314 and inserted the 332 glycan into the acute clones by mutating the asparagine at position 334 to a serine (which also deleted the glycan at 334). We tested all three viruses from both individuals for sensitivity to autologous plasma from 6 months after infection. We detected autologous neutralizing responses against the acute viruses, whereas the 6-month clones were resistant to contemporaneous plasma, as expected (**Fig. 2a**,**b**). Introduction of the glycan at position 332 resulted in almost complete resistance to neutralization by plasma from CAP177 and reduced neutralization sensitivity to plasma from CAP314, suggesting that the 332 glycan evolved to afford escape from early strain-specific antibodies.

The absence of the glycan at position 332 on the acute viruses from CAP177 and CAP314 suggested that they might be resistant to BCN mAbs that depend on this glycan, such as PGT128. Neutralization experiments showed that CAP177 and CAP314 acute clones were resistant to PGT128, whereas the 6-month clones that contained the 332 glycan were highly sensitive, with a half-maximum inhibitory concentration

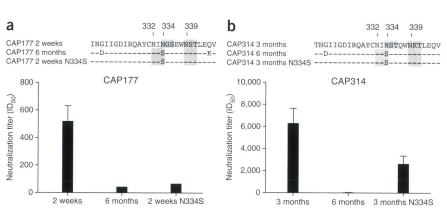

Figure 2 The glycan at position 332 mediates neutralization escape in CAP177 and CAP314. (**a**) Partial sequence alignment showing the CAP177 acute virus (CAP177 2 weeks), a representative 6-month clone (CAP177 6 months) and the acute virus mutated to contain a glycan at position 332, which deletes the glycan at position 334 (CAP177 2 weeks N334S). All three clones were tested for neutralization sensitivity to autologous serum from 6 months after infection. (**b**) Partial sequence alignment showing the CAP314 acute virus (CAP314 3 months), a representative 6-month clone (CAP314 6 months) and the mutated virus (CAP314 3 months N334S) and their sensitivity to autologous serum from 6 months after infection. Residual neutralization of the CAP314 3 months N334S mutant reflects the presence of neutralizing antibody specificities targeting other epitopes, as described previously[22]. Experiments were performed three times, and error bars represent the s.e.m.

(IC_{50}) <0.06 μg ml^{-1} (**Table 1**). We obtained similar data with a related mAb, PGT121, although the CAP177 acute clone showed moderate sensitivity (0.21 μg ml^{-1}) but was nevertheless 20-fold more resistant compared to the 6-month clone. Both N334S mutants (acute clones with a glycan introduced at position 332) were sensitive to PGT121 and PGT128, confirming the role of the 332 glycan in conferring sensitivity to these mAbs. None of the CAP177 or CAP314 clones was sensitive to the mAbs PGT135 or 2G12 (**Table 1**), which depend on additional glycans at other amino acids, that are uncommon among subtype C viruses[23–27]. Thus, whereas shifting a glycan from position 334 to 332 allowed the virus to escape autologous neutralizing antibodies, this created a new neutralizing antibody epitope that provided the antigenic stimulus to elicit BCN antibodies targeting the 332 glycan.

We assessed whether this pattern of selection of the 332 glycan was evident at a population level using more than 7,300 single-genome amplification—derived gp160 envelope sequences from acute and chronic HIV-1 infections (Online Methods)[20,28]. Sequences with evidence of dual infection were excluded. For each subject, the consensus sequence was generated and the frequency of the 332 glycan was determined. We assessed significance with Fisher's exact test. In subtype C, the 332 glycan was significantly less common among transmitted/founder viruses (45/68, 66%) compared to unmatched chronic viruses (52/62, 84%, $P = 0.0166$, **Fig. 3a**). To ensure that this was not due to adaption of HIV to neutralizing antibodies over the course of the epidemic[29], we performed the same analysis using a smaller data set of 502 matched sequences from 20 individuals, with similar results ($P = 0.0457$, **Fig. 3a**). Although we observed the same trend in subtype B sequences, it was not statistically significant (**Fig. 3a**). Taken together, these results suggest that the pattern of evolution we describe for CAP177 and CAP314 may be relatively common and that the absence of the 332 glycan on subtype C viruses may provide an advantage during transmission or early viral outgrowth.

We analyzed the phenotypes of 101 transmitted/founder subtype C viruses using envelope clones generated as part of the Vaccine Immune Monitoring Core Standard Virus Panel Consortium. For this, transmitted/founder envelope sequences were inferred from single-genome amplified and sequenced envelope amplicons derived from plasma from acutely HIV-infected subjects[30] and cloned into a mammalian expression vector. Envelope clones were transfected into 293T cells with the HIV backbone construct pSG3ΔEnv to produce envelope-pseudotyped particles, and neutralization assays were performed in TZM-bl cells as described in the Online Methods. Phenotypic analysis supported the genotypic analysis, with a high proportion (46%) of viruses resistant to PGT128 neutralization at the highest concentration tested (10 μg ml^{-1}) (**Fig. 3b** and **Supplementary Fig. 2**). Resistance strongly correlated with the absence of the 332 glycan ($P < 0.0001$) (**Fig. 3c**), although some viruses that contained the glycan were also resistant, consistent with the fact that additional residues are needed to form this epitope[8]. Of 31 viruses in which the glycan at position 332 was absent, only three showed neutralization sensitivity. Of these, two contained the glycan at position 295, which is very rare in subtype C viruses[26] but structurally proximal to the 332 glycan and shown by mutagenesis to affect the PGT128 epitope[19]. Although this virus panel was tested only against PGT128, resistance to this mAb generally extends to other Asn332-dependent PGT mAbs[8]. These data suggest that Asn332-dependent antibodies present either through passive immunotherapy or vaccination might be only partially effective in preventing subtype C infections and that combinations of antibodies targeting different epitopes may need to be tailored to match circulating viral variants[24,26,31].

In addition to the Asn332-dependent epitope, a second BCN antibody epitope that includes the glycans at amino acid positions 156 and 160 in the V2 region has been defined by the mAbs PG9, PG16 (ref. 18) and PGT145 (ref. 8). To assess whether epitope evolution was also associated with the appearance of Asn160-dependent BCN antibodies, we studied two individuals, CAP8 and CAP256, who developed this specificity[15] (**Supplementary Fig. 3a**). In both cases,

Table 1 Neutralization of CAP177 and CAP314 pseudoviruses by BCN monoclonal antibodies

mAb (IC_{50} titers)	PNG 332	PGT121	PGT128	PGT135	2G12
CAP177 2 weeks	–	0.21	>10	>10	>10
CAP177 6 months	+	0.01	0.06	>10	>10
CAP177 2 weeks N334S	+	0.04	0.71	>10	>10
CAP314 3 months	–	>10	>10	>10	>10
CAP314 6 months	+	0.03	0.03	>10	>10
CAP314 3 months N334S	+	0.03	0.07	>10	>10
TRO.11 (control)	+	0.03	0.06	0.16	0.49
Donor subtype		A	CRF02_AG	C	B
Breadth[a]		70%[8]	72%[8]	33%[8]	41%[24]

[a]Percentage of viruses neutralized with IC_{50} <50 μg ml^{-1}. Sensitivity of CAP177 and CAP314 clones to neutralization by Asn332-dependent BCN monoclonal antibodies. The acute, 6-month and N334S mutant viruses from both CAP177 and CAP314 were tested against mAbs PGT121, PGT128, PGT135 and 2G12 in a TZM-bl neutralization assay. Colors reflect neutralization IC_{50} titers >10 μg ml^{-1} (blue), 0.1–10 μg ml^{-1} (orange) and <0.1 μg ml^{-1} (red). TRO.11, a subtype B virus containing the glycan at residue 332, was included as a positive control. For the mAbs, the subtype of the donor from which they were isolated together with published data on their neutralization breadth is also included.

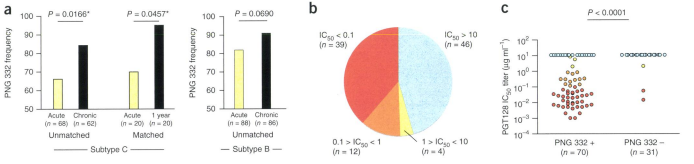

Figure 3 The glycan at residue 332 is underrepresented in subtype C transmitted/founder viruses, which are also frequently resistant to the PGT128 mAb. (**a**) Comparison of the frequency of the 332 glycan among 1,371 envelope sequences from 68 subjects with HIV-1 subtype C acute or early infection[20] and 1,111 sequences from 62 subjects with chronic HIV-1 subtype C infections (L.P., S. Joseph, J. Anderson, M.-R.A., J. Salazar-Gonzalez *et al.*, unpublished data). We also analyzed a smaller data set of matched sequences (502 sequences from 20 subjects from the CAPRISA cohort), and compared acute sequences to those from the same individual at 1 year after infection. For subtype B, a published data set of 2,715 acute sequences from 88 subjects and 2,122 sequences from 86 chronic infections was used[28]. (**b**) Neutralization sensitivity of 101 transmitted/founder viruses to neutralization by the PGT128 mAb. (**c**) Neutralization sensitivity of subtype C transmitted/founder viruses correlated strongly with the presence or absence of the 332 glycan. Colors reflect neutralization IC_{50} titers >10 μg ml^{-1} (blue), 1–10 μg ml^{-1} (yellow), 0.1–1 μg ml^{-1} (orange) and <0.1 μg ml^{-1} (red).

the glycan at amino acid 160 was absent from envelope sequences at transmission but appeared at 6 and 3 months in CAP8 and CAP256, respectively, suggesting a pattern of evolution similar to that observed with 332 glycan (**Supplementary Fig. 3b**). Furthermore, we found acute viruses to be resistant to BCN mAbs PG9, PG16 and PGT145, whereas later clones that contained the 160 glycan became sensitive to PG9 and PGT145, although not to PG16 (**Supplementary Fig. 4**). However, although insertion of the 160 glycan by site-directed mutagenesis into the resistant acute clones rendered them sensitive to PG9 and PGT145, unlike the case with the CAP177 and CAP314 mutants containing the 332 glycan, this single change did not mediate neutralization escape. It was also not possible to show selection of the 160 glycan using large sequence data sets, as it is highly conserved in both acute and chronic sequences (**Supplementary Fig. 5**).

Despite the fact that BCN epitopes are highly conserved, they only occasionally elicit BCN responses in humans. Those targeting epitopes centered around the 332 or 160 glycans develop more frequently in infected people compared to BCN antibodies directed at the CD4 binding site or membrane-proximal region[12–14]. The data presented here raise the hypothesis that, at least in the case of Asn332-directed antibodies, viral evolution may facilitate their elicitation. However, the absence of these glycans on the acute virus is not a prerequisite for the development of breadth, nor does the evolution of a BCN epitope guarantee that these antibodies will arise. Indeed, within this cohort, examples of both scenarios exist (**Supplementary Fig. 6a,b**). Furthermore, in a study of a SHIV-infected macaque[32] where the 332 glycan was present at transmission, potent and broad Asn332-dependent BCN antibodies developed within 9 months. In HIV-1 subtype C viruses, where the absence of the 332 glycan is favored at transmission, subsequent immune pressure exerted by strain-specific neutralizing antibodies results in the evolution of the 332 glycan. This process provides a mechanism for the evolution of BCN epitopes, with neutralization escape driving viral convergence toward glycan motifs that are highly conserved and serve as targets for BCN antibodies.

METHODS

Methods and any associated references are available in the online version of the paper.

Note: Supplementary information is available in the online version of the paper.

ACKNOWLEDGMENTS

We thank the participants in the CAPRISA 002 and 004 cohorts and the clinical and laboratory staff at CAPRISA for managing the cohort and providing specimens. 293T cells were obtained from G. Shaw (University of Alabama, Birmingham). We are grateful to D. Burton and W. Koff of the International AIDS Vaccine Initiative for providing the PGT monoclonal antibodies and to S. Gnanakaran (Los Alamos National Laboratories, Los Alamos, New Mexico) for providing transmitted/founder and chronic subtype B sequences. We thank Z. Valley-Omar and N. Ndabambi for generating some envelope sequences. We are grateful to B. Hahn and J. Kim, who contributed transmitted/founder subtype C clones to the Vaccine Immune Monitoring Core Standard Virus Panel Consortium. This work was funded by CAPRISA, the Centre for HIV/AIDS Vaccine Immunology, the South African HIV/AIDS Research and Innovation Platform of the South African Department of Science and Technology and by a US National Institutes of Health grant (number AI088610). CAPRISA was initially supported by the US National Institute of Allergy and Infectious Diseases, US National Institutes of Health, US Department of Health and Human Services grant U19 AI51794. M.S.S. is funded by the Bill & Melinda Gates Foundation, Vaccine Immune Monitoring Consortium of the Collaboration for AIDS Vaccine Discovery (grant 1032144). P.L.M. and E.S.G. were supported by the Columbia University-Southern African Fogarty AIDS International Training and Research Program through the Fogarty International Center, National Institutes of Health (grant 5 D43 TW000231). P.L.M. is a Wellcome Trust Intermediate Fellow in Public Health and Tropical Medicine (grant 089933/Z/09/Z).

AUTHOR CONTRIBUTIONS

P.L.M. and E.S.G. designed the study, performed experiments, analyzed data and wrote the manuscript; E.S.G., C.K.W., J.N.B., T.H. and N.L.T. performed neutralization experiments and analyzed data; E.S.G., C.K.W., D.J.S., M.N., B.E.L. and N.R. generated single-genome sequences; D.J.S. and N.N. performed part of the sequence analyses; M.-R.A., L.P., R.I.S. and C.W. contributed the subtype C acute and chronic sequences; S.B. and M.S.S. designed and performed the neutralization experiments using the panel of transmitted/founder viruses; S.S.A.K., Q.A.K. and C.W. established the CAPRISA cohorts and contributed samples and data for these subjects; and L.M. designed the study and wrote the manuscript.

COMPETING FINANCIAL INTERESTS

The authors declare no competing financial interests.

Published online at http://www.nature.com/doifinder/10.1038/nm.2985.
Reprints and permissions information is available online at http://www.nature.com/reprints/index.html.

1. Haynes, B.F. & Montefiori, D.C. Aiming to induce broadly reactive neutralizing antibody responses with HIV-1 vaccine candidates. *Expert Rev. Vaccines* **5**, 347–363 (2006).
2. Hu, S.L. & Stamatatos, L. Prospects of HIV Env modification as an approach to HIV vaccine design. *Curr. HIV Res.* **5**, 507–513 (2007).

3. Phogat, S. & Wyatt, R. Rational modifications of HIV-1 envelope glycoproteins for immunogen design. *Curr. Pharm. Des.* **13**, 213–227 (2007).
4. Li, Y. *et al.* Analysis of neutralization specificities in polyclonal sera derived from human immunodeficiency virus type 1–infected individuals. *J. Virol.* **83**, 1045–1059 (2009).
5. Sather, D.N. *et al.* Factors associated with the development of cross-reactive neutralizing antibodies during human immunodeficiency virus type 1 infection. *J. Virol.* **83**, 757–769 (2009).
6. Simek, M.D. *et al.* Human immunodeficiency virus type 1 elite neutralizers: individuals with broad and potent neutralizing activity identified by using a high-throughput neutralization assay together with an analytical selection algorithm. *J. Virol.* **83**, 7337–7348 (2009).
7. Stamatatos, L., Morris, L., Burton, D.R. & Mascola, J.R. Neutralizing antibodies generated during natural HIV-1 infection: good news for an HIV-1 vaccine? *Nat. Med.* **15**, 866–870 (2009).
8. Walker, L.M. *et al.* Broad neutralization coverage of HIV by multiple highly potent antibodies. *Nature* **477**, 466–470 (2011).
9. Richman, D.D., Wrin, T., Little, S.J. & Petropoulos, C.J. Rapid evolution of the neutralizing antibody response to HIV type 1 infection. *Proc. Natl. Acad. Sci. USA* **100**, 4144–4149 (2003).
10. Wei, X. *et al.* Antibody neutralization and escape by HIV-1. *Nature* **422**, 307–312 (2003).
11. Frost, S.D. *et al.* Neutralizing antibody responses drive the evolution of human immunodeficiency virus type 1 envelope during recent HIV infection. *Proc. Natl. Acad. Sci. USA* **102**, 18514–18519 (2005).
12. Gray, E.S. *et al.* Antibody specificities associated with neutralization breadth in plasma from HIV-1 subtype C infected blood donors. *J. Virol.* **83**, 8925–8937 (2009).
13. Tomaras, G.D. *et al.* Polyclonal B cell responses to conserved neutralization epitopes in a subset of HIV-1–infected individuals. *J. Virol.* **85**, 11502–11519 (2011).
14. Walker, L.M. *et al.* A limited number of antibody specificities mediate broad and potent serum neutralization in selected HIV-1 infected individuals. *PLoS Pathog.* **6**, e1001028 (2010).
15. Gray, E.S. *et al.* HIV-1 neutralization breadth develops incrementally over 4 years and is associated with CD4$^+$ T cell decline and high viral load during acute infection. *J. Virol.* **85**, 4828–4840 (2011).
16. Nandi, A. *et al.* Epitopes for broad and potent neutralizing antibody responses during chronic infection with human immunodeficiency virus type 1. *Virology* **396**, 339–348 (2010).
17. Tang, H. *et al.* epitopes immediately below the base of the V3 loop of gp120 as targets for the initial autologous neutralizing antibody response in two HIV-1 subtype B–infected individuals. *J. Virol.* **85**, 9286–9299 (2011).
18. Walker, L.M. *et al.* Broad and potent neutralizing antibodies from an African donor reveal a new HIV-1 vaccine target. *Science* **326**, 285–289 (2009).
19. Pejchal, R. *et al.* A potent and broad neutralizing antibody recognizes and penetrates the HIV glycan shield. *Science* **334**, 1097–1103 (2011).
20. Abrahams, M.R. *et al.* Quantitating the multiplicity of infection with HIV-1 subtype C reveals a non-Poisson distribution of transmitted variants. *J. Virol.* **83**, 3556–3567 (2009).
21. Moore, P.L. *et al.* The C3–V4 region is a major target of autologous neutralizing antibodies in human immunodeficiency virus type 1 subtype C infection. *J. Virol.* **82**, 1860–1869 (2008).
22. Moore, P.L. *et al.* Limited neutralizing antibody specificities drive neutralization escape in early HIV-1 subtype C infection. *PLoS Pathog.* **5**, e1000598 (2009).
23. Gray, E.S., Moore, P.L., Pantophlet, R.A. & Morris, L. N-linked glycan modifications in gp120 of human immunodeficiency virus type 1 subtype C render partial sensitivity to 2G12 antibody neutralization. *J. Virol.* **81**, 10769–10776 (2007).
24. Binley, J.M. *et al.* Comprehensive cross-clade neutralization analysis of a panel of anti-human immunodeficiency virus type 1 monoclonal antibodies. *J. Virol.* **78**, 13232–13252 (2004).
25. Bures, R. *et al.* Regional clustering of shared neutralization determinants on primary isolates of clade C human immunodeficiency virus type 1 from South Africa. *J. Virol.* **76**, 2233–2244 (2002).
26. Gray, E.S., Meyers, T., Gray, G., Montefiori, D.C. & Morris, L. Insensitivity of paediatric HIV-1 subtype C viruses to broadly neutralising monoclonal antibodies raised against subtype B. *PLoS Med.* **3**, e255 (2006).
27. Zhang, M. *et al.* Tracking global patterns of N-linked glycosylation site variation in highly variable viral glycoproteins: HIV, SIV, and HCV envelopes and influenza hemagglutinin. *Glycobiology* **14**, 1229–1246 (2004).
28. Gnanakaran, S. *et al.* Recurrent signature patterns in HIV-1 B clade envelope glycoproteins associated with either early or chronic infections. *PLoS Pathog.* **7**, e1002209 (2011).
29. Bunnik, E.M. *et al.* Adaptation of HIV-1 envelope gp120 to humoral immunity at a population level. *Nat. Med.* **16**, 995–997 (2010).
30. Salazar-Gonzalez, J.F. *et al.* Deciphering human immunodeficiency virus type 1 transmission and early envelope diversification by single-genome amplification and sequencing. *J. Virol.* **82**, 3952–3970 (2008).
31. Gorny, M.K. & Zolla-Pazner, S. Immunoprophylaxis against mother-to-child transmission of HIV-1. *PLoS Med.* **3**, e259 (2006).
32. Walker, L.M. *et al.* Rapid development of glycan-specific, broad, and potent anti-HIV-1 gp120 neutralizing antibodies in an R5 SIV/HIV chimeric virus infected macaque. *Proc. Natl. Acad. Sci. USA* **108**, 20125–20129 (2011).

nature medicine

NOTCH1 promotes T cell leukemia-initiating activity by RUNX-mediated regulation of PKC-θ and reactive oxygen species

Vincenzo Giambra[1], Christopher R Jenkins[1], Hongfang Wang[2], Sonya H Lam[1], Olena O Shevchuk[1], Oksana Nemirovsky[1], Carol Wai[1], Sam Gusscott[1], Mark Y Chiang[3], Jon C Aster[2], R Keith Humphries[1], Connie Eaves[1] & Andrew P Weng[1]

Reactive oxygen species (ROS), a byproduct of cellular metabolism, damage intracellular macromolecules and, when present in excess, can promote normal hematopoietic stem cell differentiation and exhaustion[1–3]. However, mechanisms that regulate the amount of ROS in leukemia-initiating cells (LICs) and the biological role of ROS in these cells are largely unknown. We show here that the ROS^{low} subset of CD44$^+$ cells in T cell acute lymphoblastic leukemia (T-ALL), a malignancy of immature T cell progenitors, is highly enriched in the most aggressive LICs and that ROS accumulation is restrained by downregulation of protein kinase C θ (PKC-θ). Notably, primary mouse T-ALLs lacking PKC-θ show improved LIC activity, whereas enforced PKC-θ expression in both mouse and human primary T-ALLs compromised LIC activity. We also show that PKC-θ is regulated by a new pathway in which NOTCH1 induces runt-related transcription factor 3 (RUNX3), RUNX3 represses RUNX1 and RUNX1 induces PKC-θ. NOTCH1, which is frequently activated by mutation in T-ALL[4–6] and required for LIC activity in both mouse and human models[7,8], thus acts to repress PKC-θ. These results reveal key functional roles for PKC-θ and ROS in T-ALL and suggest that aggressive biological behavior *in vivo* could be limited by therapeutic strategies that promote PKC-θ expression or activity, or the accumulation of ROS.

Current therapies for T-ALL are curative in 80% of pediatric cases, but only 40% of adults with T-ALL survive beyond 5 years[9]. The ineffectiveness of chemotherapeutic regimens in both age groups may be attributed to an inability to target LICs[10–12], which have increased quiescence, resistance to apoptosis and expression of DNA repair enzymes and drug efflux pumps and are localized within protective or inaccessible niches[13]. More efficient targeting of LICs could thus lead to marked improvements in patient outcomes.

Much recent interest has focused on the role of ROS in normal and malignant stem cell biology[14]. ROS are chemically reactive molecules that participate in self-propagating reactions and, if allowed to accumulate, can cause oxidative damage to intracellular macromolecules, including DNA, proteins and lipids[15,16]. Normal hematopoietic stem cells are uniquely sensitive to ROS[1–3], and some cancer stem cells that have low amounts of ROS lose stem activity or become nonviable when the amounts of ROS are increased[17,18].

To address the role of ROS in T-ALL, we focused first on LICs in a well-defined mouse model in which mice are reconstituted with syngeneic bone marrow cells that have been transduced with retrovirus encoding ΔE, a constitutively activated form of NOTCH1 lacking the extracellular ligand-binding domain. This approach produces aggressive, serially transplantable T cell leukemias within 8–12 weeks that are highly similar to human T-ALL[19–21]. Transplantation of primary NOTCH1-ΔE leukemia cells at a limiting dilution into secondary recipients revealed the LIC frequency to be 1 in ~6,100 total cells (95% CI 1 in 2,800–13,200 cells) (**Fig. 1a** and Online Methods). Using the cell-permeable indicator dye dichlorodihydrofluorescein diacetate (DCFDA) to assess the amount of intracellular ROS[22] in combination with various surface markers, we noted that the CD44$^+$ fraction contained a subset of cells with low amounts of ROS (**Fig. 1b**). To determine whether LIC activity was asymmetrically distributed within this subpopulation, we prospectively isolated CD44$^+$ROS^{low}, CD44$^+$ROS^{high} and CD44$^-$ cell subsets by fluorescence-activated cell sorting (FACS) and injected them into immunocompetent syngeneic (C57BL/6) and immunocompromised nonobese diabetic severe combined immunodeficiency (NOD/SCID) *Il2rg*$^{-/-}$ (NSG) recipient mice. Notably, the CD44$^+$ROS^{low} fraction showed substantially enriched LIC activity as compared to the complementary CD44$^+$ROS^{high} and CD44$^-$ fractions and recapitulated the original tumor heterogeneity (**Fig. 1c** and **Supplementary Fig. 1**). Cells sorted only for CD44 expression also showed enriched LIC activity, albeit less so than CD44$^+$ROS^{low} cells (**Supplementary Fig. 2**). We obtained similar findings in a second T-ALL model initiated by the G12D mutation of Kras[19] (**Fig. 1d**), indicating that enriched LIC activity within the CD44$^+$ROS^{low} fraction is not confined to the NOTCH1 model.

[1]Terry Fox Laboratory, British Columbia Cancer Agency, Vancouver, British Columbia, Canada. [2]Department of Pathology, Brigham and Women's Hospital/Harvard Medical School, Boston, Massachusetts, USA. [3]Division of Hematology/Oncology, University of Michigan Comprehensive Cancer Center, Ann Arbor, Michigan, USA. Correspondence should be addressed to A.P.W. (aweng@bccrc.ca).

Received 10 September 2010; accepted 29 August 2012; published online 21 October 2012; doi:10.1038/nm.2960

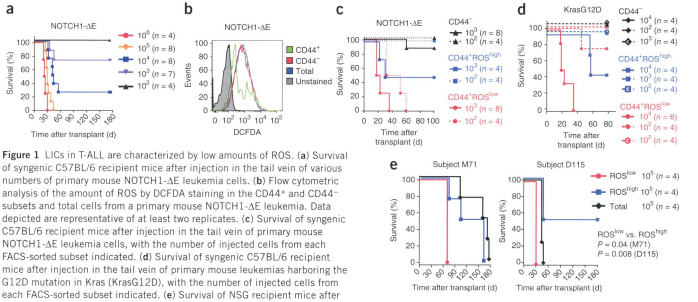

Figure 1 LICs in T-ALL are characterized by low amounts of ROS. (**a**) Survival of syngenic C57BL/6 recipient mice after injection in the tail vein of various numbers of primary mouse NOTCH1-ΔE leukemia cells. (**b**) Flow cytometric analysis of the amount of ROS by DCFDA staining in the CD44+ and CD44− subsets and total cells from a primary mouse NOTCH1-ΔE leukemia. Data depicted are representative of at least two replicates. (**c**) Survival of syngenic C57BL/6 recipient mice after injection in the tail vein of primary mouse NOTCH1-ΔE leukemia cells, with the number of injected cells from each FACS-sorted subset indicated. (**d**) Survival of syngenic C57BL/6 recipient mice after injection in the tail vein of primary mouse leukemias harboring the G12D mutation in Kras (KrasG12D), with the number of injected cells from each FACS-sorted subset indicated. (**e**) Survival of NSG recipient mice after injection in the tail vein of xenograft-expanded primary human T lymphoblasts from subject M71 or D115, with the number of injected cells from each FACS-sorted subset indicated. Statistical significance in **e** was calculated by log-rank test. Raw survival data for all transplant experiments are summarized in **Supplementary Table 1**. Throughout the figure, *n* indicates the number of mice in each group.

To assess the relevance of these findings to human disease, we transplanted FACS-sorted ROS^{high} or ROS^{low} subsets of human T-ALL samples into NSG recipients. These samples had previously been expanded in NSG mice[20] to obtain sufficient material for replicate studies. We did not include CD44 in the LIC sorting strategy because most of the xenograft-expanded human samples in our collection already contained high percentages of CD44+ cells (data not shown). Consistent with our observations in mouse models, LIC activity was enriched in the ROS^{low} fraction in the human leukemias (**Fig. 1e**). Taken together, these results show that LICs in both mouse and human T-ALL are characterized by low amounts of ROS.

PKC-θ is a crucial signaling intermediate downstream of the T cell receptor (TCR) and preTCR[23,24] and is activated in T-ALLs arising in Notch3 intracellular domain (Notch3-IC) transgenic mice[23]. PKC-θ has also been implicated in ROS production in normal T cells[25]. To explore whether PKC-θ might be involved in regulating the amount of ROS in T-ALL cells, we first surveyed PKC-θ expression in the NOTCH1-ΔE mouse model. We noted that the amount of PKC-θ protein varied among the primary leukemias (**Fig. 2a**) and that the amounts of PKC-θ and ROS were correlated (**Fig. 2b**). Moreover, T-ALLs generated from PKC-θ^{null} bone marrow[24] had very low amounts of ROS, and restoration of PKC-θ expression by retroviral transduction markedly increased the amount of ROS (**Fig. 2c**). Of note, mature T cells from the spleens of normal PKC-θ^{null} and wild-type mice had similar amounts of ROS (**Supplementary Fig. 3**), suggesting that the effects of PKC-θ are context dependent. A survey of human T-ALL cell lines and xenograft-expanded human T-ALL samples also revealed varying amounts of PKC-θ protein (**Fig. 2d**). Of note, retroviral PKC-θ expression in HPB-ALL cells (which have low amounts of endogenous PKC-θ) increased the amount of ROS, whereas shRNA-mediated knockdown of PKC-θ in RPMI 8402 cells (which have high amounts of endogenous PKC-θ) decreased the amount of ROS in these cells (**Fig. 2e**,**f** and **Supplementary Figs. 4** and 5). Taken together, these data support a dominant role for PKC-θ in regulating the amount of ROS in both mouse and human T-ALL.

We next asked whether the low amount of ROS that characterizes the LIC-enriched fractions might be caused by reduced PKC-θ expression. Indeed, LIC-enriched CD44+ and CD44+ROS^{low} fractions from mouse leukemias had significantly less PKC-θ mRNA and protein than corresponding LIC-depleted CD44− and CD44+ROS^{high} fractions, respectively (**Fig. 2g**,**h** and **Supplementary Fig. 6a**,**b**). Similarly, LIC-enriched ROS^{low} fractions of human leukemias had significantly less PKC-θ mRNA and protein than corresponding LIC-depleted ROS^{high} fractions (**Fig. 2i**,**j** and **Supplementary Fig. 6c**). These data suggest that varied expression of PKC-θ contributes to heterogeneous ROS amounts and LIC activities in subpopulations of T-ALL cells.

To address directly the role of PKC-θ in regulating LIC activity, we performed competitive transplants between PKC-θ^{null} and wild-type leukemias, the latter of which had either high or low expression of endogenous PKC-θ. In each case, recipient mice developed leukemias within 3–4 weeks that were composed predominantly of PKC-θ^{null} cells (**Supplementary Fig. 7a**). Of note, we detected a minor population of PKC-θ^{low} cells in some recipients of PKC-θ^{null} plus PKC-θ^{low} cells, as might be expected if increasing PKC-θ 'dose' progressively compromised LIC activity. We also performed competitive transplants between isogenic PKC-θ^{RV} (PKC-θ^{null} cells transduced with retroviral PKC-θ) and parental PKC-θ^{null} cells. The recipient mice all developed leukemias within 3 weeks that were composed almost entirely of PKC-θ^{null} cells (**Fig. 3a**,**b**), which is consistent with an antagonistic effect of enforced PKC-θ expression on LIC activity. Notably, PKC-θ^{RV} cells produced leukemia under noncompetitive transplant conditions (**Fig. 3a**,**b**), which excludes a nonspecific toxic effect of enforced PKC-θ expression. In addition, lentiviral expression of a constitutively activated form of PKC-θ^{26} in xenograft-expanded human T-ALL cells abrogated LIC activity (**Fig. 3c** and **Supplementary Fig. 7b**), again supporting the idea that increasing the PKC-θ dose has increasingly substantial negative effects on LIC activity.

The frequencies of LICs in PKC-θ^{null} and wild-type leukemias were very similar (**Supplementary Fig. 8a**,**b**), indicating that reduced PKC-θ expression is permissive to, but not sufficient for, LIC activity. Of note, PKC-θ^{null} and wild-type leukemias showed similar latencies

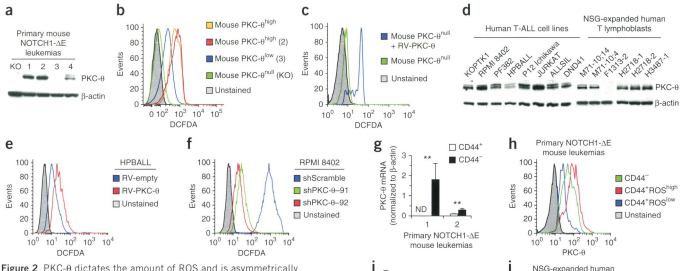

Figure 2 PKC-θ dictates the amount of ROS and is asymmetrically distributed to LIC-depleted cell fractions. (**a**) Western blot analysis of PKC-θ protein expression in primary mouse NOTCH1-ΔE leukemias from wild-type (samples 1–4) and PKC-θ^{null} (KO) backgrounds. (**b**,**c**) Flow cytometric analysis of the amounts of intracellular ROS by DCFDA staining in mouse NOTCH1-ΔE leukemias with naturally varying (PKC-θ^{high} and PKC-θ^{low}) and engineered amounts of PKC-θ expression. RV-PKC-θ, PKC-θ retrovirus. (**d**) Western blot analysis of PKC-θ protein expression in human T-ALL cell lines and primary human T lymphoblasts after expansion as xenografts in NSG mice. The two samples for each 'M71' and 'H2718' label represent different mice engrafted with the same human sample. (**e**,**f**) Flow cytometric analysis of the amounts of intracellular ROS by DCFDA staining in human T-ALL cell lines with engineered amounts of PKC-θ expression. RV-empty, empty retrovirus control; shPKC-θ–91 and shPKC-θ–92, two different lentiviral shRNAs targeting PKC-θ; shScramble, scrambled shRNA negative control. (**g**–**j**) Analysis of PKC-θ expression in FACS-sorted LIC-enriched (CD44$^+$ and/or ROS^{low}) compared to LIC-depleted (CD44$^-$ or ROS^{high}) subsets from freshly explanted mouse NOTCH1-ΔE leukemias (**g**,**h**) and xenograft-expanded primary human T-ALLs (**i**,**j**). (**g**,**i**) Quantitative RT-PCR analysis of PKC-θ mRNA levels. Error bars indicate s.d. (**h**,**j**) Flow cytometric analysis of PKC-θ protein expression. All data depicted in this figure are representative of at least two replicates. *$P < 0.05$, **$P < 0.01$ by Student's t test. ND, not detected.

in both primary and secondary transplant assays (**Supplementary Fig. 8a**–**c**), and PKC-θ overexpression or knockdown did not affect cell proliferation (**Supplementary Fig. 8d**,**e**), arguing against the possibility that leukemias with lower expression of PKC-θ prevail *in vivo* simply as a result of differential rates of proliferation. Rather, these data support the idea that PKC-θ has a dominant role in determining the ability of T-ALL cells to reconstitute or 'initiate' disease *in vivo*. Of note, T-ALL cells with reduced PKC-θ expression or activity showed

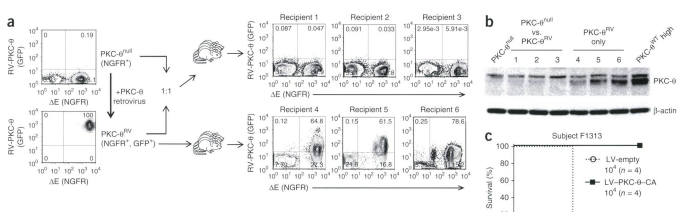

Figure 3 Increased PKC-θ expression compromises disease reconstitution *in vivo*. (**a**) Flow cytometric analysis of C57BL/6 recipient mice co-injected with 1×10^4 PKC-θ^{null} (nerve growth factor receptor (NGFR)$^+$GFP$^-$) plus 1×10^4 PKC-θ^{RV} (NGFR$^+$GFP$^+$) NOTCH1-ΔE leukemia cells (competitive transplant, upper arm; $n = 4$, recipients 1–3 depicted) or 1×10^4 PKC-θ^{RV} cells only (noncompetitive transplant, lower arm; $n = 4$, recipients 4–6 depicted). Data depicted are representative of two replicate experiments. Numbers in the corners of the plots indicate the percentage of total events in each quadrant. (**b**) Western blot analysis for PKC-θ protein expression in leukemias arising from competitive (recipients 1–3) and noncompetitive (recipients 4–6) transplant assays, as depicted in **a**. (**c**) Survival of NSG recipient mice injected with human T-ALL cells (T lymphoblasts from a xenograft-expanded human sample with very low or nondetectable amounts of endogenous PKC-θ expression (F1313-2 in **Fig. 2d**)) that had been transduced with lentivirus (LV) encoding a constitutively activated form of PKC-θ (A148E; PKC-θ-CA) or empty vector control (empty) and FACS sorted for the viral GFP marker. The significance P value was calculated by log-rank test. Throughout the figure, n indicates the number of mice in each group.

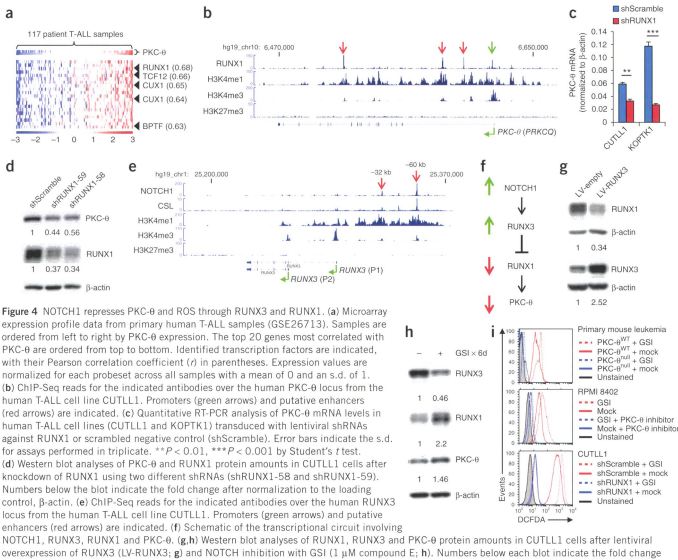

Figure 4 NOTCH1 represses PKC-θ and ROS through RUNX3 and RUNX1. (**a**) Microarray expression profile data from primary human T-ALL samples (GSE26713). Samples are ordered from left to right by PKC-θ expression. The top 20 genes most correlated with PKC-θ are ordered from top to bottom. Identified transcription factors are indicated, with their Pearson correlation coefficient (*r*) in parentheses. Expression values are normalized for each probeset across all samples with a mean of 0 and an s.d. of 1. (**b**) ChIP-Seq reads for the indicated antibodies over the human PKC-θ locus from the human T-ALL cell line CUTLL1. Promoters (green arrows) and putative enhancers (red arrows) are indicated. (**c**) Quantitative RT-PCR analysis of PKC-θ mRNA levels in human T-ALL cell lines (CUTLL1 and KOPTK1) transduced with lentiviral shRNAs against RUNX1 or scrambled negative control (shScramble). Error bars indicate the s.d. for assays performed in triplicate. $^{**}P < 0.01$, $^{***}P < 0.001$ by Student's *t* test. (**d**) Western blot analyses of PKC-θ and RUNX1 protein amounts in CUTLL1 cells after knockdown of RUNX1 using two different shRNAs (shRUNX1-5B and shRUNX1-59). Numbers below the blot indicate the fold change after normalization to the loading control, β-actin. (**e**) ChIP-Seq reads for the indicated antibodies over the human RUNX3 locus from the human T-ALL cell line CUTLL1. Promoters (green arrows) and putative enhancers (red arrows) are indicated. (**f**) Schematic of the transcriptional circuit involving NOTCH1, RUNX3, RUNX1 and PKC-θ. (**g**,**h**) Western blot analyses of RUNX1, RUNX3 and PKC-θ protein amounts in CUTLL1 cells after lentiviral overexpression of RUNX3 (LV-RUNX3; **g**) and NOTCH inhibition with GSI (1 μM compound E; **h**). Numbers below each blot indicate the fold change after normalization to the loading control, β-actin. (**i**) Flow cytometric analysis of the amounts of intracellular ROS by DCFDA staining in T-ALL cells treated with GSI (3 d), myristoylated PKC-θ pseudosubstrate inhibitor (added 24 h before assay) and/or transduced with RUNX1 shRNAs. Gated live events are shown. Data depicted are representative of at least two replicates.

resistance to chemotherapy and radiation *in vitro* (**Supplementary Fig. 9**), suggesting that low PKC-θ expression or activity might contribute to poor outcome in patients undergoing standard therapy.

To explore how PKC-θ expression is regulated in T-ALL, we examined available microarray data and discovered that the transcription factor RUNX1, which was recently described as a tumor suppressor in T-ALL[27–29], was highly correlated with PKC-θ expression in four separate patient cohorts totaling 264 primary samples[30–33] (**Fig. 4a** and **Supplementary Fig. 10**). Chromatin immunoprecipitation sequencing (ChIP-Seq) for RUNX1 in the NOTCH1-mutated human T-ALL cell line CUTLL1 revealed four high-confidence RUNX1 binding sites within the PKC-θ locus, one of which was located at the proximal promoter (associated with histone H3 trimethyl Lys4 (H3K4me3) chromatin marks) and three of which were within putative intronic enhancers (associated with H3K4me1 chromatin marks)[34] (**Fig. 4b**), suggesting that RUNX1 might regulate PKC-θ expression. Consistent with this idea, shRNA-mediated knockdown of RUNX1 resulted in decreased amounts of PKC-θ mRNA and protein (**Fig. 4c**,**d**). Given that RUNX3 has been reported to repress RUNX1 in some contexts[35], we found it notable that ChIP-Seq in CUTLL1 cells[36] revealed two high-confidence NOTCH1 and CBF1/RBPJ-suppressor of hairless-Lag1 (CSL) binding sites located 30–60 kb upstream of the RUNX3 P1 promoter with associated H3K4me1 chromatin marks (**Fig. 4e**). This suggested that NOTCH1 might regulate RUNX3 expression, and thus we hypothesized that a transcriptional circuit might be active in T-ALL cells in which NOTCH1 activates RUNX3, RUNX3 represses RUNX1 and RUNX1 activates PKC-θ (**Fig. 4f**). In fact, RUNX3 overexpression or knockdown resulted in reciprocal changes in RUNX1 expression, whereas blocking NOTCH by treating cells with γ-secretase inhibitor (GSI) decreased the expression of RUNX3 and increased the expression of RUNX1 and PKC-θ (**Fig. 4g**,**h** and **Supplementary Fig. 11a**–**d**). Dominant-negative mastermind-like 1 (DN-MAML)[37] recapitulated the effects of GSI on RUNX3, confirming that these effects are specific to NOTCH signaling (**Supplementary Fig. 11e**,**f**). Furthermore, GSI treatment caused the amounts of ROS to increase, a response that did not occur in PKC-θ^{null} mouse leukemias and was

abrogated by PKC-θ inhibition or RUNX1 knockdown in human T-ALL cells (**Fig. 4i** and **Supplementary Fig. 12**). Despite these effects, PKC-θ^{null} leukemia cells remained sensitive to GSI-induced growth arrest *in vitro*[6,20,37] (**Supplementary Fig. 13**). These results reveal a previously unknown mechanism connecting NOTCH1 to LIC activity though negative regulation of PKC-θ expression, thus resulting in reduced amounts of intracellular ROS, and are consistent with prior studies showing that NOTCH1 promotes LIC activity[7,8]. Of note, we also observed NOTCH1 to contribute to regulation of CD44 expression (**Supplementary Fig. 14**), further supporting its role in defining LICs. Variation among individual cell lines suggests that other factors probably impinge on components of the NOTCH1–RUNX3–RUNX1–PKC-θ transcriptional circuit; however, the overall consistent effects support the relevance of these results. Prior studies have identified mouse T-ALL LICs to be enriched in either the c-Kit^{mid}CD3^{+} fraction (VEC-Cre/PTEN^{null} model)[38] or the CD4^{-}CD8^{-} (double negative or DN) fraction (SIL-SCL/Lck-LMO1 model)[39]. In the NOTCH1-ΔE model used here, we found LICs to be enriched in the CD44^{+}ROS^{low} fraction but to show variable expression of CD4 and CD8 (**Supplementary Fig. 15**). Further studies will be needed to determine to what extent these LIC-containing populations overlap and how different oncogenes affect LIC identity.

Our findings suggest that PKC-θ may have a broad role in regulating LIC activity in T-ALL. Although the identified pathway linking NOTCH1 and PKC-θ is probably most relevant in tumors with activating NOTCH1 (ref. 6) or inactivating F-box and WD-40 domain protein 7 (FBW7)[4,5] mutations, PKC-θ expression may be similarly reduced in tumors with loss-of-function RUNX1 mutations (recently reported to occur in 4–18% of T-ALLs[27–29]) or elevated expression of RUNX3 or by mechanisms that are independent of NOTCH1 and RUNX. Alternatively, cell signaling events that modulate PKC-θ activity rather than expression *per se*[40] may also have important effects on LIC activity. Further studies will be required to explore the intriguing possibility that therapies that promote PKC-θ expression, activity or both may antagonize LICs and thereby improve clinical outcomes in patients with T-ALL.

METHODS

Methods and any associated references are available in the online version of the paper.

Note: Supplementary information is available in the online version of the paper.

ACKNOWLEDGMENTS

We would like to thank Z. Sun (City of Hope, Duarte, California) for providing PKC-θ knockout mice, J. Fletcher and W. Ou (Brigham and Women's Hospital, Boston, Massachusetts) for PKC-θ shRNA lentivectors, E. Kieff (Brigham and Women's Hospital, Boston, Massachusetts) for CSL antibody, I. Bernstein (Fred Hutchinson Cancer Research Center, Seattle, Washington) for Ig-DL1 ligand, F. Pflumio (Commissariat à l'Énergie Atomique Fontenay-aux-Roses, France) for the MS5-DL1 cell line and E. Martignani for help with immunofluorescence. We would also like to thank P. Ballerini (Hôpital Armand Trousseau, Paris, France), T. Leblanc (Hôpital Saint-Louis, Paris, France), L. Matherly (Karmanos Cancer Institute, Detroit, Michigan) and M.J. You (MD Anderson Cancer Center, Houston, Texas) for providing patient T-ALL samples. This work was supported by grants from the Canadian Institutes of Health Research/Terry Fox Foundation, the Leukemia and Lymphoma Society of Canada, the Cancer Research Society, the Lymphoma Foundation Canada (to A.P.W.) and the US National Cancer Institute (P01CA119070 to J.C.A.). M.Y.C. was supported by a career development award from the US National Cancer Institute (K08CA120544). A.P.W. was a Michael Smith Foundation for Health Research Scholar.

AUTHOR CONTRIBUTIONS

V.G. and A.P.W. designed the experiments. V.G., C.R.J., S.H.L., O.O.S., O.N., C.W. and S.G. generated the data. V.G. and A.P.W. interpreted the results. M.Y.C. provided reagents and advice. H.W. and J.C.A. generated and analyzed ChIP-Seq data. R.K.H. and C.E. provided advice and discussion. V.G. and A.P.W. wrote the paper.

COMPETING FINANCIAL INTERESTS

The authors declare no competing financial interests.

Published online at http://www.nature.com/doifinder/10.1038/nm.2960.
Reprints and permissions information is available online at http://www.nature.com/reprints/index.html.

1. Ito, K. *et al.* Reactive oxygen species act through p38 MAPK to limit the lifespan of hematopoietic stem cells. *Nat. Med.* **12**, 446–451 (2006).
2. Owusu-Ansah, E. & Banerjee, U. Reactive oxygen species prime *Drosophila* haematopoietic progenitors for differentiation. *Nature* **461**, 537–541 (2009).
3. Tothova, Z. *et al.* FoxOs are critical mediators of hematopoietic stem cell resistance to physiologic oxidative stress. *Cell* **128**, 325–339 (2007).
4. O'Neil, J. *et al.* FBW7 mutations in leukemic cells mediate NOTCH pathway activation and resistance to γ-secretase inhibitors. *J. Exp. Med.* **204**, 1813–1824 (2007).
5. Thompson, B.J. *et al.* The SCFFBW7 ubiquitin ligase complex as a tumor suppressor in T cell leukemia. *J. Exp. Med.* **204**, 1825–1835 (2007).
6. Weng, A.P. *et al.* Activating mutations of NOTCH1 in human T cell acute lymphoblastic leukemia. *Science* **306**, 269–271 (2004).
7. Armstrong, F. *et al.* NOTCH is a key regulator of human T-cell acute leukemia initiating cell activity. *Blood* **113**, 1730–1740 (2009).
8. Tatarek, J., *et al.* Notch1 inhibition targets the leukemia-initiating cells in a Tal1/Lmo2 mouse model of T-ALL. *Blood* **118**, 1579–1590 (2011).
9. Pui, C.H. & Evans, W.E. Treatment of acute lymphoblastic leukemia. *N. Engl. J. Med.* **354**, 166–178 (2006).
10. Cox, C.V. *et al.* Characterization of a progenitor cell population in childhood T-cell acute lymphoblastic leukemia. *Blood* **109**, 674–682 (2007).
11. Gerby, B. *et al.* Expression of CD34 and CD7 on human T-cell acute lymphoblastic leukemia discriminates functionally heterogeneous cell populations. *Leukemia* **25**, 1249–1258 (2011).
12. Chiu, P.P., Jiang, H. & Dick, J.E. Leukemia-initiating cells in human T-lymphoblastic leukemia exhibit glucocorticoid resistance. *Blood* **116**, 5268–5279 (2010).
13. Reya, T., Morrison, S.J., Clarke, M.F. & Weissman, I.L. Stem cells, cancer, and cancer stem cells. *Nature* **414**, 105–111 (2001).
14. Kobayashi, C.I. & Suda, T. Regulation of reactive oxygen species in stem cells and cancer stem cells. *J. Cell. Physiol.* **227**, 421–430 (2012).
15. Valko, M. *et al.* Free radicals and antioxidants in normal physiological functions and human disease. *Int. J. Biochem. Cell Biol.* **39**, 44–84 (2007).
16. Ady, A.A.M. Oxidative stress and disease: an updated review. *Res. J. Immunol.* **3**, 129–145 (2010).
17. Guzman, M.L. *et al.* The sesquiterpene lactone parthenolide induces apoptosis of human acute myelogenous leukemia stem and progenitor cells. *Blood* **105**, 4163–4169 (2005).
18. Diehn, M. *et al.* Association of reactive oxygen species levels and radioresistance in cancer stem cells. *Nature* **458**, 780–783 (2009).
19. Chiang, M.Y. *et al.* Leukemia-associated NOTCH1 alleles are weak tumor initiators but accelerate K-ras–initiated leukemia. *J. Clin. Invest.* **118**, 3181–3194 (2008).
20. Medyouf, H. *et al.* Acute T-cell leukemias remain dependent on Notch signaling despite PTEN and INK4A/ARF loss. *Blood* **115**, 1175–1184 (2010).
21. Pear, W.S. *et al.* Exclusive development of T cell neoplasms in mice transplanted with bone marrow expressing activated Notch alleles. *J. Exp. Med.* **183**, 2283–2291 (1996).
22. Eruslanov, E. & Kusmartsev, S. Identification of ROS using oxidized DCFDA and flow-cytometry. *Methods Mol. Biol.* **594**, 57–72 (2010).
23. Felli, M.P. *et al.* PKCθ mediates pre-TCR signaling and contributes to Notch3-induced T-cell leukemia. *Oncogene* **24**, 992–1000 (2005).
24. Sun, Z. *et al.* PKC-θ is required for TCR-induced NF-κB activation in mature but not immature T lymphocytes. *Nature* **404**, 402–407 (2000).
25. Kaminski, M., Kiessling, M., Suss, D., Krammer, P.H. & Gulow, K. Novel role for mitochondria: protein kinase Cθ-dependent oxidative signaling organelles in activation-induced T-cell death. *Mol. Cell. Biol.* **27**, 3625–3639 (2007).
26. Baier-Bitterlich, G. *et al.* Protein kinase C-θ isoenzyme selective stimulation of the transcription factor complex AP-1 in T lymphocytes. *Mol. Cell. Biol.* **16**, 1842–1850 (1996).
27. Della Gatta, G. *et al.* Reverse engineering of TLX oncogenic transcriptional networks identifies RUNX1 as tumor suppressor in T-ALL. *Nat. Med.* **18**, 436–440 (2012).
28. Grossmann, V. *et al.* Prognostic relevance of RUNX1 mutations in T-cell acute lymphoblastic leukemia. *Haematologica* **96**, 1874–1877 (2011).
29. Zhang, J. *et al.* The genetic basis of early T-cell precursor acute lymphoblastic leukaemia. *Nature* **481**, 157–163 (2012).
30. Coustan-Smith, E. *et al.* Early T-cell precursor leukaemia: a subtype of very high-risk acute lymphoblastic leukaemia. *Lancet Oncol.* **10**, 147–156 (2009).
31. Gutierrez, A. *et al.* The BCL11B tumor suppressor is mutated across the major molecular subtypes of T-cell acute lymphoblastic leukemia. *Blood* **118**, 4169–4173 (2011).

32. Homminga, I. *et al.* Integrated transcript and genome analyses reveal *NKX2-1* and *MEF2C* as potential oncogenes in T cell acute lymphoblastic leukemia. *Cancer Cell* **19**, 484–497 (2011).
33. Winter, S.S. *et al.* Identification of genomic classifiers that distinguish induction failure in T-lineage acute lymphoblastic leukemia: a report from the Children's Oncology Group. *Blood* **110**, 1429–1438 (2007).
34. Heintzman, N.D. *et al.* Distinct and predictive chromatin signatures of transcriptional promoters and enhancers in the human genome. *Nat. Genet.* **39**, 311–318 (2007).
35. Spender, L.C., Whiteman, H.J., Karstegl, C.E. & Farrell, P.J. Transcriptional cross-regulation of RUNX1 by RUNX3 in human B cells. *Oncogene* **24**, 1873–1881 (2005).
36. Wang, H. *et al.* Genome-wide analysis reveals conserved and divergent features of Notch1/RBPJ binding in human and murine T-lymphoblastic leukemia cells. *PNAS* **108**, 14908–14913 (2011).
37. Weng, A.P. *et al.* Growth suppression of pre-T acute lymphoblastic leukemia cells by inhibition of notch signaling. *Mol. Cell. Biol.* **23**, 655–664 (2003).
38. Guo, W. *et al.* Multi-genetic events collaboratively contribute to Pten-null leukaemia stem-cell formation. *Nature* **453**, 529–533 (2008).
39. Tremblay, M. *et al.* Modeling T-cell acute lymphoblastic leukemia induced by the SCL and LMO1 oncogenes. *Genes Dev* **24**, 1093–1105 (2010).
40. Isakov, N. & Altman, A. Protein kinase Cθ in T cell activation. *Annu. Rev. Immunol.* **20**, 761–794 (2002).

nature medicine

PDGFR blockade is a rational and effective therapy for NPM-ALK–driven lymphomas

Daniela Laimer[1,25], Helmut Dolznig[2,25], Karoline Kollmann[3,25], Paul W Vesely[4,24,25], Michaela Schlederer[5], Olaf Merkel[6,24], Ana-Iris Schiefer[1], Melanie R Hassler[1,7], Susi Heider[1], Lena Amenitsch[1], Christiane Thallinger[7], Philipp B Staber[8,9], Ingrid Simonitsch-Klupp[1], Matthias Artaker[10], Sabine Lagger[10,24], Suzanne D Turner[11], Stefano Pileri[12], Pier Paolo Piccaluga[12], Peter Valent[13,14], Katia Messana[15], Indira Landra[15], Thomas Weichhart[2], Sylvia Knapp[16,17], Medhat Shehata[13], Maria Todaro[15], Veronika Sexl[3], Gerald Höfler[4], Roberto Piva[15,18], Enzo Medico[19,20], Bruce A Ruggeri[21], Mangeng Cheng[21], Robert Eferl[22], Gerda Egger[1], Josef M Penninger[23], Ulrich Jaeger[13], Richard Moriggl[5], Giorgio Inghirami[15,19] & Lukas Kenner[1,5]

Anaplastic large cell lymphoma (ALCL) is an aggressive non-Hodgkin's lymphoma found in children and young adults. ALCLs frequently carry a chromosomal translocation that results in expression of the oncoprotein nucleophosmin–anaplastic lymphoma kinase (NPM-ALK). The key molecular downstream events required for NPM-ALK–triggered lymphoma growth have been only partly unveiled. Here we show that the activator protein 1 family members JUN and JUNB promote lymphoma development and tumor dissemination through transcriptional regulation of platelet-derived growth factor receptor-β (PDGFRB) in a mouse model of NPM-ALK–triggered lymphomagenesis. Therapeutic inhibition of PDGFRB markedly prolonged survival of NPM-ALK transgenic mice and increased the efficacy of an ALK-specific inhibitor in transplanted NPM-ALK tumors. Notably, inhibition of PDGFRA and PDGFRB in a patient with refractory late-stage NPM-ALK$^+$ ALCL resulted in rapid, complete and sustained remission. Together, our data identify PDGFRB as a previously unknown JUN and JUNB target that could be a highly effective therapy for ALCL.

ALCLs are T cell lymphomas[1,2] comprising 10–20% of all non-Hodgkin's lymphoma cases in children and 3% in adults[3]. About half of ALCL cases are positive for the NPM-ALK fusion chimera caused by the t(2;5)(p23;q35) translocation[4]. ALK translocations or point mutations have also been described in diffuse large B cell lymphomas and in several nonlymphoid neoplasms[5–8]. Inhibition of ALK fusion proteins by specific compounds such as crizotinib showed promising clinical responses in ALCL and non–small cell lung cancer[9,10]. However, ALK mutations conferring resistance to crizotinib have also been reported[11].

Recent studies have linked NPM-ALK expression to induction of the activator protein 1 (AP-1) transcription factors JUNB and JUN[12,13]. To investigate their role in NPM-ALK–driven T cell lymphomas, we conditionally deleted JUN and/or JUNB in T cells of transgenic mice carrying the human NPM-ALK fusion protein under the control of the mouse CD4 promoter[14] (*CD4*-NPM-ALK) (**Fig. 1a**). We confirmed gene deletion by DNA genotyping (data not shown), real-time PCR, western blotting and immunohistochemistry (**Supplementary Fig. 1a–c**). JUN deletion did not affect expression of oncogenic NPM-ALK in T cells (**Supplementary Fig. 1a–c**), and all genetic cohorts showed normal T cell development before onset of lymphoma (**Supplementary Fig. 1d,e** and data not shown). *CD4*-NPM-ALK mice developed T cell lymphomas around 8 weeks after birth. The overall survival was not affected by deletion of JUN or JUNB alone (**Fig. 1b**), but survival was substantially prolonged in mice in which both JUN

[1]Clinical Institute of Pathology, Medical University of Vienna, Vienna, Austria. [2]Institute of Medical Genetics, Medical University of Vienna, Vienna, Austria. [3]Institute of Pharmacology and Toxicology, Veterinary University Vienna, Vienna, Austria. [4]Institute of Pathology, Medical University of Graz, Graz, Austria. [5]Ludwig Boltzmann Institute for Cancer Research, Vienna, Austria. [6]Laboratory for Immunological and Molecular Cancer Research, 3rd Medical Department of the Paracelsus Medical University, Salzburg, Austria. [7]Department of Internal Medicine I, Division of Oncology, Medical University of Vienna, Vienna, Austria. [8]Division of Hematology, Medical University of Graz, Graz, Austria. [9]Harvard Stem Cell Institute, Harvard Medical School, Boston, Massachusetts, USA. [10]Department of Medical Biochemistry, Max F. Perutz Laboratories, Medical University of Vienna, Vienna Biocenter, Vienna, Austria. [11]Division of Molecular Histopathology, Department of Pathology, University of Cambridge, Addenbrooke's Hospital, Cambridge, UK. [12]Pathology and Hematopathology Unit, Department of Hematology and Oncology 'L. and A. Seràgnoli,' S. Orsola-Malpighi Hospital, University of Bologna, Bologna, Italy. [13]Department of Internal Medicine I, Division of Hematology and Hemostaseology, Comprehensive Cancer Center Drug & Target Screening Unit, Medical University of Vienna, Vienna, Austria. [14]Ludwig Boltzmann Cluster Oncology, Vienna, Austria. [15]Department of Molecular Biotechnology and Health Science, Center for Experimental Research and Medical Studies, University of Turin, Turin, Italy. [16]Center for Molecular Medicine of the Austrian Academy of Sciences, Vienna, Austria. [17]Department of Medicine I, Division of Infectious Diseases and Tropical Medicine, Medical University of Vienna, Vienna, Austria. [18]Department of Pathology and NYU Cancer Center, New York University School of Medicine, New York, New York, USA. [19]Department of Oncological Sciences, University of Turin, Turin, Italy. [20]Laboratory of Oncogenomics, Institute for Cancer Research and Treatment, Candiolo, Italy. [21]Worldwide Discovery Research, Cephalon, Inc., West Chester, Pennsylvania, USA. [22]Department of Internal Medicine I, Institute for Cancer Research, Comprehensive Cancer Center, Medical University of Vienna, Vienna, Austria. [23]Institute of Molecular Biotechnology of the Austrian Academy of Science, Vienna, Austria. [24]Present addresses: The Scripps Research Institute, La Jolla, California (P.W.V.), National Center for Tumor Diseases, Heidelberg, Germany (O.M.) and Wellcome Trust Centre for Cell Biology, University of Edinburgh, Edinburgh, UK (S.L.). [25]These authors contributed equally to this work. Correspondence should be addressed to L.K. (lukas.kenner@meduniwien.ac.at).

Received 23 July; accepted 10 September; published online 14 October 2012; doi:10.1038/nm.2966

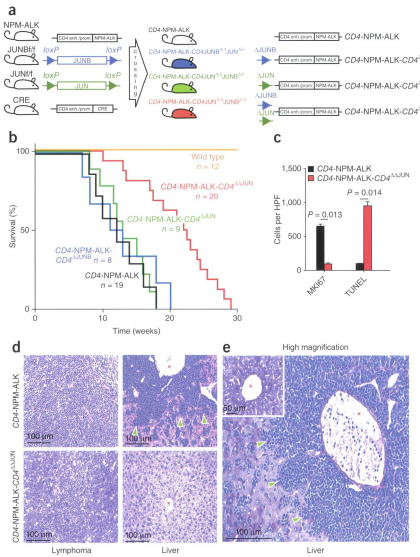

Figure 1 Effects of JUN and JUNB deletion on NPM-ALK lymphomas in mice. (**a**) Generation of mouse strains with T cell–specific *CD4*-NPM-ALK expression and T cell–specific deletion of JUNB (*CD4*-NPM-ALK-*CD4*$^{\Delta JUNB}$), JUN (*CD4*-NPM-ALK-*CD4*$^{\Delta JUN}$) or both (*CD4*-NPM-ALK-*CD4*$^{\Delta JUNB;\Delta JUN}$). CD4 enh./prom., CD4 enhancer and promoter. (**b**) Kaplan-Meier curves depicting overall survival of *CD4*-NPM-ALK-*CD4*$^{\Delta JUNB}$, *CD4*-NPM-ALK-*CD4*$^{\Delta JUN}$ and *CD4*-NPM-ALK-*CD4*$^{\Delta JUNB;\Delta JUN}$ mice. Isogenic wild-type mice are shown as controls. (**c**) Assessment of apoptosis (TUNEL staining) and proliferation (Ki-67 staining, MKI67) in sections of *CD4*-NPM-ALK and *CD4*-NPM-ALK-*CD4*$^{\Delta JUN}$ lymphomas. The mean numbers of TUNEL- and MKI67-positive cells per high-power field (HPF) among 2,000 cells per tumor sample were determined using TissueQuest software. Data are mean values ± s.d. for five mice. (**d**) H&E staining of lymphoma and liver tissues of *CD4*-NPM-ALK and *CD4*-NPM-ALK-*CD4*$^{\Delta JUN}$ mice. Disseminating tumor cells in CD4-NPM-ALK mice (green arrowheads) have largely destroyed the liver architecture around the blood vessels (asterisks). (**e**) Periodic acid Schiff staining in liver from *CD4*-NPM-ALK and *CD4*-NPM-ALK-*CD4*$^{\Delta JUN}$ (small inset) mice. Tumor cells (green arrowheads) are clearly visible in the liver parenchyma of *CD4*-NPM-ALK mice; red asterisks denote blood vessels.

and JUNB were deleted (*CD4*-NPM-ALK-*CD4*$^{\Delta JUN}$) (**Fig. 1b**). Lymphomas from *CD4*-NPM-ALK-*CD4*$^{\Delta JUN}$ mice showed markedly reduced proliferation and significantly ($P = 0.014$) increased apoptosis compared to lymphomas from *CD4*-NPM-ALK mice (**Fig. 1c** and **Supplementary Fig. 2a**,**b**). Consistently, *CD4*-NPM-ALK-*CD4*$^{\Delta JUN}$ but not *CD4*-NPM-ALK lymphoma cells failed to grow *in vitro* (data not shown), and Cre-mediated deletion of *loxP*-flanked *Jun* and *Junb* in established *CD4*-NPM-ALK cell lines (*CD4*-NPM-ALK-JUN$^{flox/flox}$;JUNB$^{flox/flox}$) induced cell death (**Supplementary Fig. 2c**). Freshly isolated *CD4*-NPM-ALK-*CD4*$^{\Delta JUN}$ lymphoma cells formed palpable tumors when engrafted into severe combined immunodeficient (SCID) mice, albeit after a long latency (**Supplementary Fig. 2d**). These results show that JUN and JUNB are important regulators of NPM-ALK–driven T cell lymphoma development.

T cell lymphomas spread to many organs in *CD4*-NPM-ALK transgenic mice[14]. Although *CD4*-NPM-ALK-*CD4*$^{\Delta JUN}$ mice eventually developed lymphomas, we did not detect dissemination of tumor cells (**Fig. 1d**,**e** and **Supplementary Fig. 2e**). Notably, blood vessel numbers were significantly decreased in primary lymphomas of *CD4*-NPM-ALK-*CD4*$^{\Delta JUN}$ mice compared to *CD4*-NPM-ALK controls (**Fig. 2a**). Expression and activation of the pericyte marker PDGFRB was readily detectable in lymphoma cells of *CD4*-NPM-ALK mice but essentially absent in T cell lymphomas of *CD4*-NPM-ALK-*CD4*$^{\Delta JUN}$ mice (**Fig. 2b**,**c**). Tumor cells from single mice lacking only JUNB or JUN (designated *CD4*-NPM-ALK-*CD4*$^{\Delta JUNB}$ and *CD4*-NPM-ALK-*CD4*$^{\Delta JUN}$, respectively) showed intermediate PDGFRB protein expression (**Supplementary Fig. 3a**). PDGFRB mRNA expression was also decreased in lymphomas of *CD4*-NPM-ALK-*CD4*$^{\Delta JUN}$ mice when compared to *CD4*-NPM-ALK lymphomas (**Fig. 2d**), suggesting transcriptional regulation of PDGFRB by JUN proteins. Consistently, AP-1 consensus sequences were identified within the mouse PDGFRB promoter and the first intron and were conserved among other species[15,16] (**Supplementary Fig. 3b**,**c**). Analysis of ENCODE transcription factor binding tracks revealed binding of JUN and JUNB to the PDGFRB intronic AP-1 site in the human K562 leukemia cell line[15,17] (**Supplementary Fig. 3d**). Electrophoretic mobility shift assay analysis of nuclear extracts from NPM-ALK lymphomas demonstrated AP-1 DNA binding to the consensus sequence, which was reduced after antibody-mediated JUN and JUNB depletion (**Fig. 2e**). Moreover, binding of JUN and JUNB to the PDGFRB promoter was confirmed by chromatin immunoprecipitation assays of human dermal fibroblasts (**Fig. 2f**), mouse NPM-ALK cell lines and tumor tissues (**Supplementary Fig. 3e**,**f**) and luciferase reporter assays in Jurkat cells (**Fig. 2g**) and HeLa cells using PDGFRB promoter constructs with and without an AP-1 site (**Supplementary Fig. 3g**). These data demonstrate transcriptional regulation of PDGFRB by JUN and JUNB. PDGFRs have not been implicated in ALCL but are known physiologic regulators of tumor growth[18–20]. We therefore investigated the effects of the PDGFR kinase inhibitor imatinib on established mouse A333, MEL406 and CD4-417 lymphoma cell lines. Imatinib also blocks activity of the BCR-ABL kinase, the

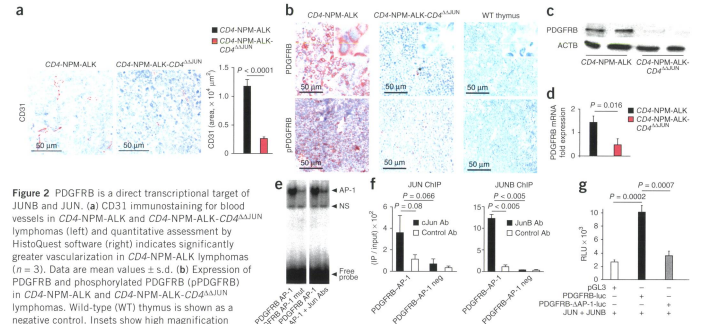

Figure 2 PDGFRB is a direct transcriptional target of JUNB and JUN. (**a**) CD31 immunostaining for blood vessels in *CD4*-NPM-ALK and *CD4*-NPM-ALK-*CD4*$^{\Delta AJUN}$ lymphomas (left) and quantitative assessment by HistoQuest software (right) indicates significantly greater vascularization in *CD4*-NPM-ALK lymphomas ($n = 3$). Data are mean values ± s.d. (**b**) Expression of PDGFRB and phosphorylated PDGFRB (pPDGFRB) in *CD4*-NPM-ALK and *CD4*-NPM-ALK-*CD4*$^{\Delta AJUN}$ lymphomas. Wild-type (WT) thymus is shown as a negative control. Insets show high magnification (×600). The asterisk (top middle) indicates PDGFRB expression in stromal pericytes. (**c**) Western blot analysis of PDGFRB expression in *CD4*-NPM-ALK and *CD4*-NPM-ALK-*CD4*$^{\Delta AJUN}$ lymphomas. Expression of β-actin (ACTB) is shown as a control. (**d**) Quantitative PCR analysis of PDGFRB mRNA expression in *CD4*-NPM-ALK-*CD4*$^{\Delta AJUN}$ and *CD4*-NPM-ALK tumors ($n = 3$) normalized to GAPDH mRNA. Mean values ± s.d. are shown. (**e**) Electrophoretic mobility shift assay analysis using a conserved PDGFRB AP-1 site (PDGFRBAP-1) and a mutated version (PDGFRBAP-1 mut). JUNB and JUN depletion using a mixture of monoclonal antibodies (Jun Abs) resulted in strong reduction of DNA binding. NS, nonspecific binding. (**f**) Chromatin immunoprecipitation (ChIP) using antibodies (Ab) to JUN (cJun), JUNB and immunoglobulin-γ (control) in the human fibroblast cell line BJ-1 confirmed binding of JUNB and JUN to the AP-1 consensus sequence in the PDGFRB locus (PDGFRB-AP-1). Reduced binding was detected when a negative 3′ control region (PDGFRB-AP-1neg) ($n = 3$) was used. Mean values ± s.e.m. are shown. (**g**) Luciferase reporter assay to determine functionality of the AP-1 site for PDGFRB promoter regulation. pGL3, promoterless luciferase vector (control); pPDGFRB-luc, luciferase vector with PDGFRB promoter; pPDGFRB-ΔAP-1-luc, luciferase vector with PDGFRB promoter lacking AP-1 site; pJUN + pJUNB, JUN and JUNB expression vectors. Cells were co-transfected with 0.05 μg of a β-galactosidase expression vector and subjected to a BetaGlo assay for normalization. Mean values for relative luminescence units (RLU) ± s.d. are shown ($n = 3$).

receptor tyrosine kinase KIT and PDGFRA with high affinity[21], but it has no effect on ALK[22,23]. The NPM-ALK lymphoma cell lines did not express BCR-ABL (data not shown) or PDGFRA, but they expressed KIT at variable levels (**Fig. 3a** and **Supplementary Fig. 4a**,**b**). PDGFRB expression ranged from high to non-detectable (**Fig. 3a** and **Supplementary Fig. 4a**). We then used tumor cell transplantation experiments to evaluate the effects of imatinib on tumor growth. Notably, imatinib treatment of tumor-bearing mice resulted in markedly reduced tumor growth (**Fig. 3b** and **Supplementary Fig. 4c**). The response rate of individual transplanted cell lines correlated with the level of PDGFRB expression, as A333-derived lymphomas (lacking PDGFRB but expressing high levels of KIT) were not affected by imatinib treatment (**Fig. 3b**). We obtained similar results using nilotinib (**Supplementary Fig. 4d**), another PDGFRB kinase inhibitor[24,25]. Imatinib treatment did not affect expression of ALCL-associated cytokines and their receptors (such as IL-9 and IL-22 (refs. 26,27; **Supplementary Fig. 4e**), peripheral and splenic T cell populations (**Supplementary Fig. 5a**–**c**) or tumor-infiltrating T cell subsets (**Supplementary Fig. 5d**,**e**). These results indicate that inhibition of PDGFRB markedly impairs growth of transplanted ALCL tumor cells.

We next explored the effects of imatinib on primary lymphomas in *CD4*-NPM-ALK mice. Imatinib treatment substantially increased overall survival (**Fig. 3c**), reduced *in vivo* tumor cell proliferation and enhanced apoptosis (**Fig. 3d**). Imatinib also blocked proliferation and enhanced cell death of mouse PDGFRB$^+$ lymphoma cell lines *in vitro* (**Supplementary Fig. 6a**,**b**). As expected, imatinib reduced PDGFRB phosphorylation in *CD4*-NPM-ALK cell lines (**Supplementary Fig. 6c**) and in tumor tissues from *CD4*-NPM-ALK mice (**Fig. 3e**), resulting in reduced phosphorylation of protein kinase B (PKB, also known as AKT) and signal transducer and activator of transcription 3 (STAT3) but not of extracellular signal–regulated kinase (ERK) (**Supplementary Fig. 6d**,**e**). Furthermore, PDGFRB phosphorylation in PDGF-β (PDGFB)-stimulated lymphoma cells was impaired by imatinib in a dose-dependent manner (**Supplementary Fig. 6f**,**g**), resulting in reduced proliferation (**Supplementary Fig. 6h**). Imatinib also reduced PDGFRB mRNA levels (**Supplementary Fig. 6i**) in *CD4*-NPM-ALK lymphomas, indicating an autoregulatory PDGF secretion loop. Notably, in imatinib-treated *CD4*-NPM-ALK-*CD4*$^{\Delta AJUN}$ mice, no tumors developed during the 30-week observation period (**Fig. 3c**), and tumor cell dissemination to distant organs was completely blocked (**Supplementary Fig. 7a**). This is probably owing to an additional effect of imatinib on the tumor stroma, which has been reported for other cancers[28,29] (**Supplementary Fig. 7b**–**f**).

We next tested imatinib treatment in combination with the ALK inhibitor crizotinib[9]. Imatinib and crizotinib synergistically reduced tumor growth of grafted mouse NPM-ALK$^+$ lymphoma cells (**Fig. 3f**). Similar results were obtained with the ALK inhibitor CEP28122 (ref. 30). Imatinib reduced lymphoma growth and the percentage

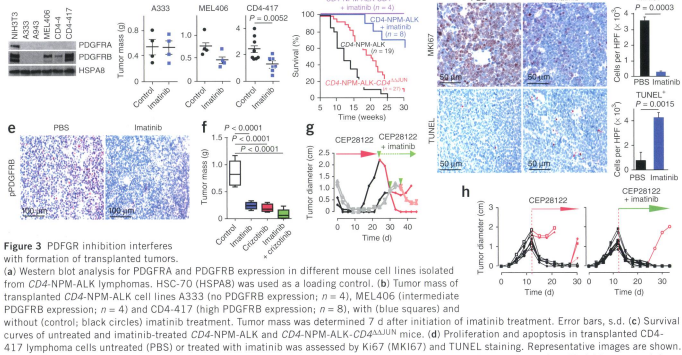

Figure 3 PDFGR inhibition interferes with formation of transplanted tumors. (**a**) Western blot analysis for PDGFRA and PDGFRB expression in different mouse cell lines isolated from *CD4*-NPM-ALK lymphomas. HSC-70 (HSPA8) was used as a loading control. (**b**) Tumor mass of transplanted *CD4*-NPM-ALK cell lines A333 (no PDGFRB expression; $n = 4$), MEL406 (intermediate PDGFRB expression; $n = 4$) and CD4-417 (high PDGFRB expression; $n = 8$), with (blue squares) and without (control; black circles) imatinib treatment. Tumor mass was determined 7 d after initiation of imatinib treatment. Error bars, s.d. (**c**) Survival curves of untreated and imatinib-treated *CD4*-NPM-ALK and *CD4*-NPM-ALK-*CD4*$^{\Delta JUN}$ mice. (**d**) Proliferation and apoptosis in transplanted CD4-417 lymphoma cells untreated (PBS) or treated with imatinib was assessed by Ki67 (MKI67) and TUNEL staining. Representative images are shown. Graphs indicate the mean positive cell number per high-power field (HPF) ± s.d. as determined by HistoQuest software ($n = 5$). (**e**) Immunostaining for phosphorylated PDGFRB (pPDGFRB) expression in untreated (PBS) and imatinib-treated *CD4*-NPM-ALK mice. (**f**) Reduction of tumor size in MEL406 transplant recipient mice, untreated (control) or treated with imatinib, crizotinib or both. Mean tumor mass ± s.d. is shown. $n = 10$ mice per group. (**g**) Tumor diameter after implantation of ALCL cells from ALK$^+$ BALB/c mice into syngeneic BALB/c mice ($n = 4$) and treatment with CEP28122. Mice were treated until relapse occurred and tumors began to regrow (20–30 d). Thereafter, mice were treated with CEP28122 and imatinib (beginning of combination treatment for each mouse is indicated by green arrowheads). (**h**) Tumor diameter in BALB/c mice injected with syngeneic ALK$^+$ ALCL cells. After 12 d of tumor growth, mice were treated with CEP28122 alone or CEP28122 combined with imatinib. Data from individual mice are shown.

of lymphomas that relapsed after CEP28122 treatment (**Fig. 3g,h**). These results show that therapeutic blockade of PDGFRs can markedly alleviate relapse of ALCLs after ALK inhibition.

The vast majority of human NPM-ALK$^+$ and NPM-ALK$^-$ ALCLs showed high expression of JUNB, JUN, PDGFRA and PDGFRB mRNA[31–34] (**Fig. 4a**) and protein (**Fig. 4b** and **Supplementary Fig. 8a,b**). In contrast to peripheral T-cell lymphoma not otherwise specified (PTCL-NOS) and angioimmunoblastic T cell lymphoma (AITL), most ALCL samples showed high expression of both PDGFRA and PDGFRB. Consistently, two highly conserved AP-1 binding sites were identified in the human PDGFRA promoter (**Supplementary Fig. 8c**). We did not detect wild-type or mutated forms of KIT or BCR-ABL in ALK$^+$ lymphomas (**Supplementary Fig. 8d** and data not shown). Established human ALK$^+$ ALCL cell lines were negative for PDGFRA and PDGFRB (**Supplementary Fig. 8e**), but ALK expression was required to maintain JUNB mRNA expression (**Supplementary Fig. 8f**). These results demonstrate that primary human ALK$^+$ ALCLs express high levels of PDGFRA, PDGFRB and JUNB.

On the basis of our results, we tried imatinib treatment in a patient with an ALCL of poor prognosis. This NPM-ALK$^+$, JUNB$^+$, JUN$^+$, PDGFRA$^+$, PDGFRB$^+$, KIT$^-$ ALCL (**Fig. 4c**) was refractory to conventional chemotherapy and relapsed after autologous stem cell transplantation. The patient entered complete clinical remission with reduced tumor markers and diminished PDGFB levels after 10 d of imatinib therapy (**Fig. 4d–g**). The patient is now free of ALCL 22 months after initiation of imatinib therapy (**Supplementary Case Report**). We also observed high PDGFB levels in the serum of four additional patients with ALCL (**Supplementary Fig. 8g**).

JUNB and JUN are thus crucial for the growth and metastasis of NPM-ALK$^+$ ALCL, exerting this effect through the direct regulation of PDGFR expression. ALK induces the expression of JUNB and JUN[12,13], which subsequently bind to and activate the PDGFRB promoter. We show that PDGFR expression and activation is a key driver of ALCL proliferation, lymphoma cell survival and tumor cell dissemination. PDGFRs might promote ALCL formation through a combined effect on lymphoma cells and tumor stroma. The mechanism by which PDGFRs promote ALCL formation in the tumor stroma and the qualitative contribution of stromal effects to drug responses in the mouse models are unclear at present, and further experiments will be required to address these issues. Although the precise mechanism is not fully understood, inhibition of PDGFRB by imatinib resulted in an excellent therapeutic response in the *CD4*-NPM-ALK ALCL mouse model and in a terminally sick patient with NPM-ALK$^+$ ALCL.

Our patient data show that PDGFRs are present in NPM-ALK$^+$ T cell lymphomas but also in highly malignant NPM-ALK$^-$ ALCL. This would imply that, in the absence of ALK, other kinases drive the expression of PDGFRs, through AP-1 or other transcription factors. It should be noted that we have not proven that PDGFRs functions within the context of the signaling networks in ALK$^-$ tumor cells. Future experiments will be required to investigate whether PDGFR expression is a crucial common driver for lymphomagenesis.

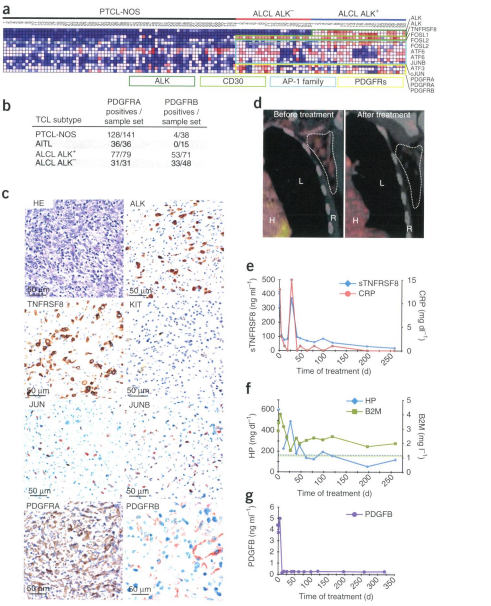

Figure 4 Complete remission of ALCL in a patient after imatinib treatment. (**a**) Gene expression profiles obtained from three publicly available data sets (GSE6338, GSE14879 and GSE19069) and proprietary and unpublished data sets including PTCL-NOS and ALK− and ALK+ ALCL. Genes encoding JUNB; JUN; AP-1 members FOSL1, FOSL2; ATF3 and ATF6; and PDGFRs are highly expressed, as well as CD30 (TNFRSF8). (**b**) Quantification of immunohistochemistry for PDGFRA and PDGFRB on >280 tumor samples from patients with PTCL-NOS, AITL, ALK+ ALCL and ALK− ALCL. The differences in sample set numbers are due to tissue microarray (TMA) consumption or lack of representativeness of some cores. (**c**) H&E staining and immunohistochemistry for the indicated markers on tumor sections from a 27-y-old patient with grade 3 ALK+ ALCL that was refractory to standard treatment. (**d**) Positron emission tomography–computed tomography (PET-CT) scans before and 10 d after initiation of imatinib treatment (400 mg per day). Axillary lymph nodes (delineated by white dotted line) were PET-CT negative after treatment. L, lung; H, heart; R, rib cage. (**e**,**f**) Serum concentrations of tumor markers β2 microglobulin (B2M) and soluble CD30 (sTNFRSF8) and acute phase parameters haptoglobin (HP) and C-reactive protein (CRP) returned to normal levels after imatinib treatment. The transient increase of CRP around day 27 (**e**) was due to an infection. Shading in **f** indicates normal ranges for B2M (light green) and HP (light blue) serum concentrations. (**g**) PDGFB concentration was elevated in platelet-low plasma before treatment in the patient and reverted to normal (shaded area) within 10 d of beginning imatinib therapy.

The major clinical challenge in treating NPM-ALK+ ALCL is its high rate of relapse. Notably, we have shown here that the dual inhibition of ALK and PDGFR reduces lymphoma growth and alleviates relapse rates. Our findings suggest that imatinib is a potential therapeutic option for patients with crizotinib-resistant lymphomas[11].

In summary, we provide evidence that PDGFR inhibition is a highly effective treatment for NPM-ALK+ ALCL, and these findings might also be relevant for ALK− lymphomas. We are now designing a clinical trial on the basis of PDGFR expression in tumors, for which we will enroll patients with second-stage ALCL.

METHODS

Methods and any associated references are available in the online version of the paper.

Note: Supplementary information is available in the online version of the paper.

ACKNOWLEDGMENTS

We thank E.F. Wagner for providing the $JUN^{flox/flox}$ and $JUN^{flox/flox}$ mice, A. Ostman for helpful discussions and technical help with PDGFRB analysis, and S. Reichmann for technical help with soluble-CD30 and PDGFB assays. L.K. is supported by the Fonds zur Förderung der wissenschaftlichen Forschung (FWF, P-18478-B12) and the Genome Research in Austria InflammoBiota project. R.M., V.S. and R.E. are supported by the FWF (SFB-F28) and V.S. is supported by FWF project 19723. G.E. is supported by an Elise Richter Fellowship (FWF V102-B12) and an FP7 Marie Curie International Reintegration Grant (IRG 230984). H.D. is supported by the Herzfelder Family Foundation and the Niederösterreichische Forschungs- und Bildungsges.m.b.H. P.W.V. and P.B.S. were supported by Jubiläumsfonds of the Österreichische Nationalbank (P-12147), and P.W.V. was awarded an E. Schroedinger Grant (J 2922). T.W. is supported by the Else-Kröner Fresenius Stiftung. S.P. and G.I. are supported by Italian Association for Cancer Research (AIRC) Special Program in Clinical Molecular Oncology, Milan (5x1000 No. 10007). G.I. is supported by Regione Piemonte (ONCOPROT, CIPE 25/2005); ImmOnc ('Innovative approaches to bust the immune responses', Programma Operativo Regionale, Piattaforme Innovative BIO F.E.S.R. 2007/13, Asse 1 'Ricerca e innovazione' della LR 34/2004) and the Oncology Program of Compagnia di San Paolo, Torino. R.P. is supported by AIRC grant IG-8675. R.E. is supported by the FWF Doktoratskolleg-plus Inflammation and Immunity grant, the Comprehensive Cancer Center Vienna Research Grant and the Austrian Federal Ministry of Science and Research GENAU Austromouse grant. J.M.P. is supported by the Austrian Academy of Sciences and an Advanced Grant from the European Research Council. This study was performed on behalf of the European Research Initiative on ALCL (ERIA).

AUTHOR CONTRIBUTIONS

H.D., P.W.V., K.K., O.M., P.V., T.W., M. Shehata, V.S., G.H., G.E., J.M.P., U.J., R.M., G.I., R.E. and L.K. designed experiments. D.L., H.D., K.K., P.W.V., M. Schlederer, O.M.,

A.-I.S., M.R.H., S.H., L.A., C.T., P.B.S., I.S.-K., M.A., S.P., P.P.P., K.M., I.L., S.K., M. Shehata, M.T., S.I., S.D.T., R.P., E.M., G.E., R.M., M.C. and B.A.R. performed experiments and collected and analyzed data. H.D., V.S., R.M., J.M.P., G.I., R.E. and L.K. wrote the manuscript. All authors discussed the results and edited the manuscript.

COMPETING FINANCIAL INTERESTS

The authors declare no competing financial interests.

Published online at http://www.nature.com/doifinder/10.1038/nm.2966.
Reprints and permissions information is available online at http://www.nature.com/reprints/index.html.

1. Kadin, M.E. Ki-1/CD30^{+} (anaplastic) large-cell lymphoma: maturation of a clinicopathologic entity with prospects of effective therapy. *J. Clin. Oncol.* **12**, 884–887 (1994).
2. Kadin, M.E. Primary Ki-1-positive anaplastic large-cell lymphoma: a distinct clinicopathologic entity. *Ann. Oncol.* **5** (suppl. 1), 25–30 (1994).
3. Stein, H. *et al.* CD30+ anaplastic large cell lymphoma: a review of its histopathologic, genetic, and clinical features. *Blood* **96**, 3681–3695 (2000).
4. Morris, S.W. *et al.* Fusion of a kinase gene, *ALK*, to a nucleolar protein gene, *NPM*, in non-Hodgkin's lymphoma. *Science* **263**, 1281–1284 (1994).
5. Chen, Y. *et al.* Oncogenic mutations of ALK kinase in neuroblastoma. *Nature* **455**, 971–974 (2008).
6. George, R.E. *et al.* Activating mutations in ALK provide a therapeutic target in neuroblastoma. *Nature* **455**, 975–978 (2008).
7. Janoueix-Lerosey, I. *et al.* Somatic and germline activating mutations of the ALK kinase receptor in neuroblastoma. *Nature* **455**, 967–970 (2008).
8. Soda, M. *et al.* Identification of the transforming *EML4-ALK* fusion gene in non-small cell lung cancer. *Nature* **448**, 561–566 (2007).
9. Gambacorti-Passerini, C., Messa, C. & Pogliani, E.M. Crizotinib in anaplastic large-cell lymphoma. *N. Engl. J. Med.* **364**, 775–776 (2011).
10. Kwak, E.L. *et al.* Anaplastic lymphoma kinase inhibition in non–small cell lung cancer. *N. Engl. J. Med.* **363**, 1693–1703 (2010).
11. Choi, Y.L. *et al. EML4-ALK* mutations in lung cancer that confer resistance to ALK inhibitors. *N. Engl. J. Med.* **363**, 1734–1739 (2010).
12. Mathas, S. *et al.* Aberrantly expressed c-JUN and JunB are a hallmark of Hodgkin lymphoma cells, stimulate proliferation and synergize with NF-κB. *EMBO J.* **21**, 4104–4113 (2002).
13. Staber, P.B. *et al.* The oncoprotein NPM-ALK of anaplastic large-cell lymphoma induces *JUNB* transcription via ERK1/2 and JunB translation via mTOR signaling. *Blood* **110**, 3374–3383 (2007).
14. Chiarle, R. *et al.* NPM-ALK transgenic mice spontaneously develop T cell lymphomas and plasma cell tumors. *Blood* **101**, 1919–1927 (2003).
15. Kent, W.J. *et al.* The human genome browser at UCSC. *Genome Res.* **12**, 996–1006 (2002).
16. Cartharius, K. *et al.* MatInspector and beyond: promoter analysis based on transcription factor binding sites. *Bioinformatics* **21**, 2933–2942 (2005).
17. The ENCODE Project Consortium. A user's guide to the encyclopedia of DNA elements (ENCODE). *PLoS Biol.* **9**, e1001046 (2011).
18. Andrae, J., Gallini, R. & Betsholtz, C. Role of platelet-derived growth factors in physiology and medicine. *Genes Dev.* **22**, 1276–1312 (2008).
19. Claesson-Welsh, L. Signal transduction by the PDGF receptors. *Prog. Growth Factor Res.* **5**, 37–54 (1994).
20. Nissen, L.J. *et al.* Angiogenic factors FGF2 and PDGF-BB synergistically promote murine tumor neovascularization and metastasis. *J. Clin. Invest.* **117**, 2766–2777 (2007).
21. Pardanani, A. & Tefferi, A. Imatinib targets other than *bcr/abl* and their clinical relevance in myeloid disorders. *Blood* **104**, 1931–1939 (2004).
22. Ergin, M. *et al.* Inhibition of tyrosine kinase activity induces caspase-dependent apoptosis in anaplastic large cell lymphoma with NPM-ALK (p80) fusion protein. *Exp. Hematol.* **29**, 1082–1090 (2001).
23. Gunby, R.H. *et al.* Structural insights into the ATP binding pocket of the anaplastic lymphoma kinase by site-directed mutagenesis, inhibitor binding analysis, and homology modeling. *J. Med. Chem.* **49**, 5759–5768 (2006).
24. Hantschel, O., Rix, U. & Superti-Furga, G. Target spectrum of the BCR-ABL inhibitors imatinib, nilotinib and dasatinib. *Leuk. Lymphoma* **49**, 615–619 (2008).
25. Stover, E.H. *et al.* The small molecule tyrosine kinase inhibitor AMN107 inhibits TEL–PDGFRB and FIP1L1–PDGFR-α *in vitro* and *in vivo*. *Blood* **106**, 3206–3213 (2005).
26. Qiu, L. *et al.* Autocrine release of interleukin-9 promotes Jak3-dependent survival of ALK^{+} anaplastic large-cell lymphoma cells. *Blood* **108**, 2407–2415 (2006).
27. Savan, R. *et al.* A novel role for IL-22R1 as a driver of inflammation. *Blood* **117**, 575–584 (2011).
28. Pietras, K. *et al.* Inhibition of PDGF receptor signaling in tumor stroma enhances antitumor effect of chemotherapy. *Cancer Res.* **62**, 5476–5484 (2002).
29. Sumida, T. *et al.* Anti-stromal therapy with imatinib inhibits growth and metastasis of gastric carcinoma in an orthotopic nude mouse model. *Int. J. Cancer* **128**, 2050–2062 (2011).
30. Cheng, M. *et al.* CEP-28122, a highly potent and selective orally active inhibitor of anaplastic lymphoma kinase with antitumor activity in experimental models of human cancers. *Mol. Cancer Ther.* **11**, 670–679 (2012).
31. Iqbal, J. *et al.* Molecular signatures to improve diagnosis in peripheral T cell lymphoma and prognostication in angioimmunoblastic T cell lymphoma. *Blood* **115**, 1026–1036 (2010).
32. Piccaluga, P.P. *et al.* Gene expression analysis of peripheral T cell lymphoma, unspecified, reveals distinct profiles and new potential therapeutic targets. *J. Clin. Invest.* **117**, 823–834 (2007).
33. Eckerle, S. *et al.* Gene expression profiling of isolated tumour cells from anaplastic large cell lymphomas: insights into its cellular origin, pathogenesis and relation to Hodgkin lymphoma. *Leukemia* **23**, 2129–2138 (2009).
34. Piva, R. *et al.* Gene expression profiling uncovers molecular classifiers for the recognition of anaplastic large-cell lymphoma within peripheral T cell neoplasms. *J. Clin. Oncol.* **28**, 1583–1590 (2010).

nature medicine

The Toll-like receptor 5 ligand flagellin promotes asthma by priming allergic responses to indoor allergens

Rhonda H Wilson[1,4], Shuichiro Maruoka[1,2,4], Gregory S Whitehead[1], Julie F Foley[1], Gordon P Flake[1], Michelle L Sever[1], Darryl C Zeldin[1], Monica Kraft[3], Stavros Garantziotis[1], Hideki Nakano[1] & Donald N Cook[1]

Allergic asthma is a complex disease characterized by eosinophilic pulmonary inflammation, mucus production and reversible airway obstruction[1]. Exposure to indoor allergens is a risk factor for asthma, but this disease is also associated with high household levels of total and particularly Gram-negative bacteria[2]. The ability of bacterial products to act as adjuvants[3] suggests they might promote asthma by priming allergic sensitization to inhaled allergens. In support of this idea, house dust extracts (HDEs) can activate antigen-presenting dendritic cells (DCs) *in vitro* and promote allergic sensitization to inhaled innocuous proteins *in vivo*[4]. It is unknown which microbial products provide most of the adjuvant activity in HDEs. A screen for adjuvant activity of microbial products revealed that the bacterial protein flagellin (FLA) stimulated strong allergic airway responses to an innocuous inhaled protein, ovalbumin (OVA). Moreover, Toll-like receptor 5 (TLR5), the mammalian receptor for FLA[5,6], was required for priming strong allergic responses to natural indoor allergens present in HDEs. In addition, individuals with asthma have higher serum levels of FLA-specific antibodies as compared to nonasthmatic individuals. Together, these findings suggest that household FLA promotes the development of allergic asthma by TLR5-dependent priming of allergic responses to indoor allergens.

To investigate the ability of microbial products to promote asthma-like responses in mice, we separately instilled individual products into the airway together with the innocuous protein, chicken ovalbumin (OVA). Control mice receiving either OVA alone or microbial products alone did not become sensitized and failed to develop airway inflammation after subsequent challenge with OVA (**Fig. 1a–c** and **Supplementary Fig. 1a**). However, instillation of some microbial products together with OVA caused the mice to become sensitized to this protein because after a subsequent OVA challenge, inflammatory leukocytes accumulated in the airway (**Fig. 1c**). Some mice displayed an allergic form of inflammation, as evidenced by large numbers of eosinophils in the airway (**Fig. 1c**). We observed strong allergic responses in mice receiving OVA together with standard FLA (sFLA) from *Salmonella typhimurium*, a partially purified product that contains lipopolysaccharide (LPS), or a highly purified recombinant FLA (rFLA) produced in insect cells and lacking detectable LPS (see Online Methods for details). Ultrapure LPS, which signals through TLR4, was similar to rFLA in its ability to promote allergic responses (**Supplementary Fig. 1b**), suggesting that impurities in crude preparations of LPS can reduce its potency as an adjuvant.

The clinical features of asthma stem largely from the actions of $CD4^+$ T helper type 2 (T_H2) cells that produce the cytokines interleukin-4 (IL-4), IL-5 and IL-13 and promote IgE synthesis, eosinophilic inflammation and mucus and airway hyperresponsiveness (AHR), respectively. IL-17 production by T_H17 cells also contributes to asthma severity by promoting neutrophil accumulation and AHR[7–9]. We found that pulmonary IL-4, IL-5, IL-13 and IL-17 (**Fig. 1d**) and serum IgE (**Fig. 1e**) were all elevated in OVA-challenged mice previously sensitized with sFLA plus OVA or rFLA plus OVA. Mucus was present in the lungs of most mice that showed eosinophilic responses, but it was generally restricted to the large airways. However, mice sensitized with sFLA plus OVA also had mucus in preterminal and terminal bronchioles (**Fig. 2a**,**b**). Invasive measurements of airway resistance revealed that mice sensitized with either sFLA plus OVA (**Fig. 2c**) or rFLA plus OVA (**Fig. 2d**) developed strong AHR after a single OVA challenge, whereas mice sensitized to LPS plus OVA developed only modest AHR (**Fig. 2c**). Mice sensitized with OVA together with either sFLA or rFLA also displayed inflammation and AHR after OVA challenge on seven consecutive days (**Supplementary Fig. 2a**,**b**). T cells from lung-draining lymph nodes of these mice produced the Th2 cytokines IL-4, IL-5 and IL-13, as well as the Th17 cytokine IL-17, after restimulation with OVA *ex vivo* (**Fig. 2e**). Also, intracellular staining of $CD4^+$ T cells from the lung revealed that they contain IL-13 and IL-17 (**Fig. 2f** and **Supplementary Fig. 2c**), confirming that inhaled FLA promotes T_H2 and T_H17 cell differentiation in adult mice.

Unlike highly purified rFLA, sFLA contains only 10% FLA and is contaminated with LPS (see Online Methods for details). However, *Tlr4*$^{-/-}$ mice were readily sensitized to OVA when sFLA was used as an adjuvant, as evidenced by airway eosinophil accumulation in the airway following subsequent challenge with OVA (**Fig. 3a**). By contrast, *Tlr5*$^{-/-}$ mice, which cannot respond to extracellular FLA[6], had significantly lower levels of airway eosinophils and IL-5 than wild-type (WT) mice and showed a trend toward lower airway

[1]Laboratory of Respiratory Biology, National Institute of Environmental Health Sciences (NIEHS), National Institutes of Health, Research Triangle Park, North Carolina, USA. [2]Division of Respiratory Medicine, Nihon University School of Medicine, Tokyo, Japan. [3]Duke Asthma, Allergy and Airway Center, Duke University Medical Center, Durham, North Carolina, USA. [4]These authors contributed equally to this work. Correspondence should be addressed to D.N.C. (cookd@niehs.nih.gov).

Received 17 November 2011; accepted 8 August 2012; published online 14 October 2012; doi:10.1038/nm.2920

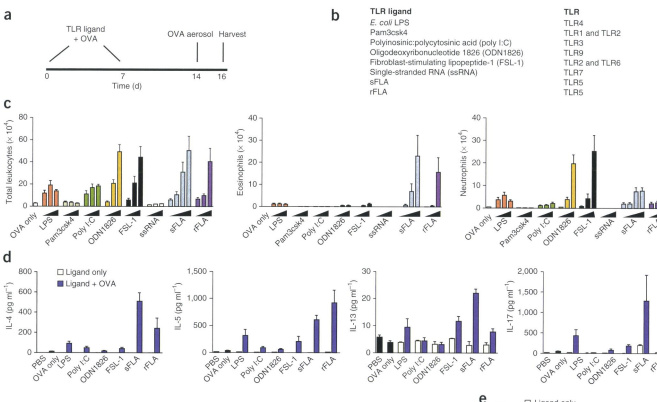

Figure 1 Adjuvant activity of microbial products in the airways of C57BL/6 mice. (**a**) Timeline for sensitizations and challenges. (**b**) Microbial products used and the TLRs that mediate signaling responses to each product. (**c**) Airway inflammation in sensitized and challenged mice: total leukocytes (left), eosinophils (middle) and neutrophils (right) in the presence of increasing amounts (25 ng, 125 ng and 625 ng) of microbial products used during sensitizations; sFLA also includes 1,250 ng. $n = 5$–8 mice per group. Numbers reflect cell number ± s.e.m. in bronchoalveolar lavage fluid (BALF). (**d**) Pulmonary cytokine concentrations (mean values ± s.e.m.) in BALF for IL-4, IL-5 and IL-17, or in supernatants from OVA-stimulated, cultured whole lungs for IL-13. (**e**) Total serum IgE concentration ± s.e.m. Data are from one of three similar experiments. $n = 5$–8 mice per group.

IL-17 and serum IgE (**Fig. 3a**,**b**) By contrast, numbers of airway neutrophils were lower in *Tlr4*$^{-/-}$ mice than in WT mice, suggesting that LPS contributed to the T_H17 response. The reduced allergic response of *Tlr5*$^{-/-}$ mice sensitized with OVA plus sFLA was not due to a general immune deficit in these animals because, unlike *Tlr4*$^{-/-}$ mice, the *Tlr5*$^{-/-}$ mice were readily sensitized to OVA when we used LPS as an adjuvant (**Supplementary Fig. 3**). The inflammasome-associated molecule NLR family CARD domain-containing protein 4 (Nlrc4) responds to intracellular FLA[10,11], but we found that *Nlrc4*$^{-/-}$ mice were efficiently sensitized by OVA-FLA and developed strong allergic responses to subsequent OVA challenge (**Supplementary Fig. 4**). By contrast, similarly treated mice lacking myeloid differentiation factor 88 (*Myd88*), an adapter protein used by all TLRs except TLR3, had virtually no eosinophils, neutrophils or inflammatory cytokines in the lung after sensitization with OVA plus rFLA and challenge with OVA (**Fig. 3a**,**b**). Together, these data suggest that although multiple microbial products contribute to the adjuvant activity of sFLA, the primary adjuvant component in this preparation is FLA. This is consistent with our finding that rFLA, which lacks detectable LPS, can prime allergic responses. In addition to monomeric FLA, airway instillations of heat-killed *Pseudomonas aeruginosa* (PA01), a ubiquitous flagellated strain of bacteria, also primed allergic responses to OVA, whereas a similar strain lacking FLA (PA01ΔfliC) was significantly less effective at stimulating airway eosinophilia and IgE (**Fig. 3c**). Thus, multiple forms of FLA can prime allergic responses to inhaled OVA.

The two major DC populations in the lung ($CD103^+$ and $CD11b^{hi}$)[12] expressed low but detectable levels of *Tlr5* RNA (**Supplementary Fig. 5a**). Alveolar macrophages expressed intermediate levels, and airway epithelial cells expressed the highest levels of *Tlr5* mRNA. To investigate the requirement of different FLA-responsive cell compartments during allergic sensitization, we used WT and *Tlr5*$^{-/-}$ mice to generate reciprocal bone marrow–chimeric mice (**Supplementary Fig. 5b**). WT mice receiving WT marrow showed the strongest eosinophilic responses to rFLA-OVA sensitization and OVA challenge. Compared to these animals, WT mice receiving *Tlr5*$^{-/-}$ marrow, as well as *Tlr5*$^{-/-}$ mice receiving WT marrow, had lower numbers of eosinophils, although this difference did not reach statistical significance (**Fig. 3d**). *Tlr5*$^{-/-}$ mice receiving marrow from *Tlr5*$^{-/-}$ mice had almost no eosinophilic inflammation (**Fig. 3d**). This suggests that *Tlr5* expression in radiosensitive hematopoietic cells and radio-resistant structural cells contributes to FLA-mediated allergic sensitization, in agreement with a previous report[13]. Mice in which *Myd88* expression is restricted to *Cd11c*-expressing cells[14] did not become sensitized to OVA when we used rFLA as an adjuvant (**Fig. 3e**), although $CD11c^+$ cells prepared from lungs of these mice were able to respond to FLA, as evidenced by production of tumor

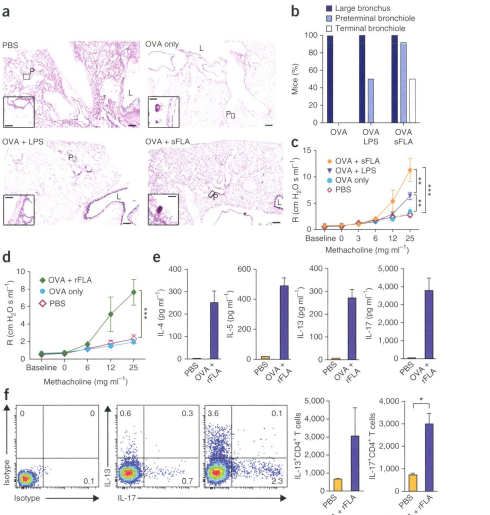

Figure 2 FLA promotes asthma-like responses to OVA. (**a**) Periodic acid-Schiff and Alcian blue staining of mucus-producing cells in the airway. Representative low-magnification images are shown (scale bars, 50 μm). Insets show expanded images of the indicated regions (scale bars, 10 μm). L, large airway; P, preterminal bronchioles. (**b**) Percentage of mice with mucus staining in the indicated regions of the lung. $n = 8$–10 mice per group. (**c**,**d**) Mean values ± s.e.m. of airway resistance (R) for intubated mice inhaling air (baseline) or aerosols of PBS containing the indicated concentrations of methacholine. $n \geq 8$ mice per group. (**e**) Cytokine concentrations (mean values ± s.e.m.) in cultures of total cell suspensions from lymph nodes excised from mice sensitized with PBS ($n = 1$) or OVA + rFLA ($n = 5$). Cells were stimulated *ex vivo* with OVA. (**f**) Intracellular staining for cytokines in pulmonary T cells. Shown are representative flow plots with percentages of positive cells indicated in each quadrant and bar histograms of mean ± s.e.m. numbers of $CD4^+$ cells staining for IL-13 (left) and IL-17 (right). $n = 2$ for PBS group; $n = 3$ for OVA + rFLA–treated group. Data are from one of three similar experiments.*$P < 0.05$; **$P < 0.01$; ***$P < 0.001$.

necrosis factor-α (**Supplementary Fig. 5c**). Thus, FLA responsiveness in DCs and alveolar macrophages is not sufficient for FLA-mediated allergic sensitization through the airway. Previous reports have indicated that the airway epithelium contributes to innate immune responses to FLA[15,16] and to LPS-mediated T_H2 responses by rapidly releasing proinflammatory cytokines[17]. We found that the amounts of IL-25 and IL-33 in the airway were strongly increased within 2 h of rFLA instillation, whereas amounts of thymic stromal lymphopoietin (TSLP) increased within 4 h of treatment compared to those in PBS-treated animals (**Fig. 3f**). We also observed increased amounts of TSLP in supernatants of rFLA-treated primary airway epithelial cells from WT mice, but not in their *Tlr5*$^{-/-}$ counterparts (**Fig. 3g**). No increases were seen for IL-25 or IL-33 in these primary cell cultures (data not shown). Together, these results suggest that FLA might promote allergic sensitization to inhaled allergens by inducing secretion of proinflammatory cytokines by epithelial cells.

Having found that multiple forms of FLA can function as strong adjuvants in the airway, we next tested whether FLA is a naturally occurring, environmental adjuvant. Common house dust represents a readily available source of airborne material that is inhaled daily. Several different HDEs promoted allergic responses to inhaled OVA, although they differed in potency (**Fig. 4a**). Western blot analysis (**Fig. 4b** and **Supplementary Fig. 6a**) revealed immunoreactive proteins within the expected molecular weight range of FLA, from 30 kDa to 65 kDa[18]. The two major bands observed might represent FLA from different species of bacteria or different forms of FLA from a single species. To determine the individual contributions of LPS and FLA to the adjuvant activity of HDEs, we examined HDE-mediated allergic responses to OVA in *Tlr4*$^{-/-}$ and *Tlr5*$^{-/-}$ mice. After sensitization with HDE plus OVA, followed by OVA challenge, *Tlr4*$^{-/-}$ mice had fewer airway neutrophils and showed a trend toward lower concentrations of IL-17 in bronchoalveolar lavage fluid (BALF) compared with WT mice (**Fig. 4c** and **Supplementary Fig. 6b**). However, numbers of airway eosinophils and the concentration of IL-5 in BALF were not lower in *Tlr4*$^{-/-}$ mice compared with WT mice (**Fig. 4c** and **Supplementary Fig. 6b**), indicating that, for this extract, LPS is dispensable for HDE-mediated eosinophilic airway inflammation but is required for neutrophilic airway inflammation and might contribute to AHR. By contrast, *Tlr5*$^{-/-}$ mice had fewer airway eosinophils (**Fig. 4c**) and had lower concentrations of IL-5 than did WT or *Tlr4*$^{-/-}$ mice (**Supplementary Fig. 6b**). WT and *Tlr4*$^{-/-}$ mice sensitized with HDE plus OVA developed AHR after OVA challenge, whereas this response was markedly reduced in *Tlr5*$^{-/-}$ mice (**Fig. 4d**). These findings suggest that FLA is a major component of HDE for priming asthma-like responses to inhaled antigens.

OVA is widely used in animal models of allergic pulmonary inflammation, but it is not a clinically relevant allergen for asthma. Household dust typically contains many allergens, including those derived from dust mites, cockroaches and animal dander. Multiple instillations of HDE alone (without OVA) is sufficient to trigger allergic responses in mice[19]. Each of the seven HDEs we tested contained several allergens, as well as various levels of LPS (**Supplementary Table 1**). To determine if LPS and FLA promote sensitization to these natural indoor allergens, we tested responses in *Tlr4*$^{-/-}$ and *Tlr5*$^{-/-}$ mice to

an HDE (#7) that contained multiple indoor allergens. In WT mice, sensitization and challenge with HDE alone elicited eosinophilic and neutrophilic airway inflammation (**Fig. 4e**). However, some of this neutrophilic inflammation was due to innate immune responses to LPS, because WT mice, but not *Tlr4*$^{-/-}$ mice, displayed airway neutrophil infiltration after only a single HDE instillation (**Fig. 4e**, middle). By contrast, eosinophil accumulation in the airways of WT mice was dependent on adaptive immune responses because these cells were present only in HDE-challenged mice that had been previously sensitized with HDE (**Fig. 4e**, right). Like WT mice, *Tlr4*$^{-/-}$ mice had large numbers of eosinophils in the airway after HDE challenge, suggesting that LPS in this extract was dispensable for eosinophilic responses. However, *Tlr5*$^{-/-}$ mice had significantly fewer eosinophils in the airway than did WT mice (**Fig. 4e**, right). These data suggest that interactions between FLA and TLR5 promote the eosinophilic component of allergic responses to indoor allergens.

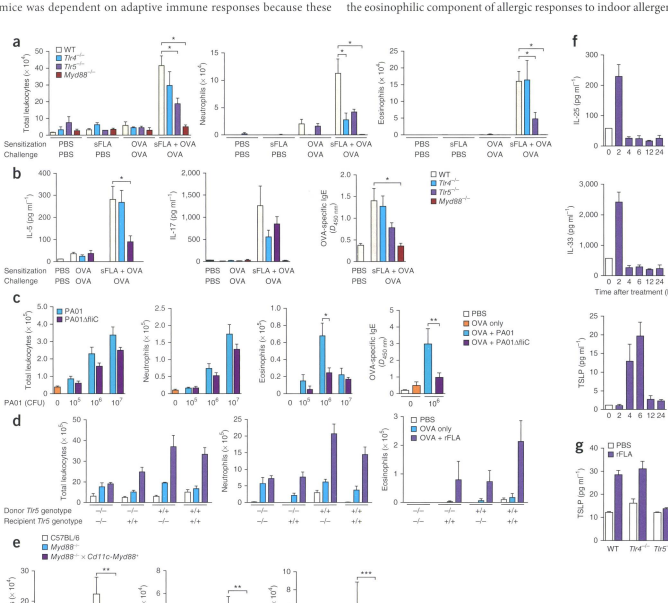

Figure 3 FLA possesses potent, TLR5-dependent adjuvant activity in the airway. (**a**) Mean numbers ± s.e.m. of total leukocytes (left), neutrophils (middle) and eosinophils (right) in mice sensitized and challenged as indicated. $n = 6$ mice per group. (**b**) Concentrations of IL-5 (left) and IL-17 (middle) in BALF and relative amounts of serum OVA-specific IgE (right) in mice of the indicated genotypes. (**c**) Left to right: total leukocytes, neutrophils, eosinophils and OVA-specific IgE in mice sensitized to OVA using either WT (PA01) or FLA-deficient (PA01ΔfliC) heat-killed *P. aeruginosa* as an adjuvant. (**d**) Total leukocytes (left), neutrophils (middle) and eosinophils (right) in bone marrow–chimeric mice generated with WT and *Tlr5*$^{-/-}$ mice, sensitized as indicated. (**e**) Total leukocytes, neutrophils and eosinophils in mice expressing a *Myd88* transgene in CD11c^{+} cells only. Experiments were done at least twice with similar results. $n \geq 6$ mice per group. $^{*}P < 0.05$. Values ± s.e.m. of cytokines in the BALF at the indicated time points after rFLA instillation. (**g**) TSLP concentration in supernatants of FLA-treated primary airway epithelial cells from the indicated mice.

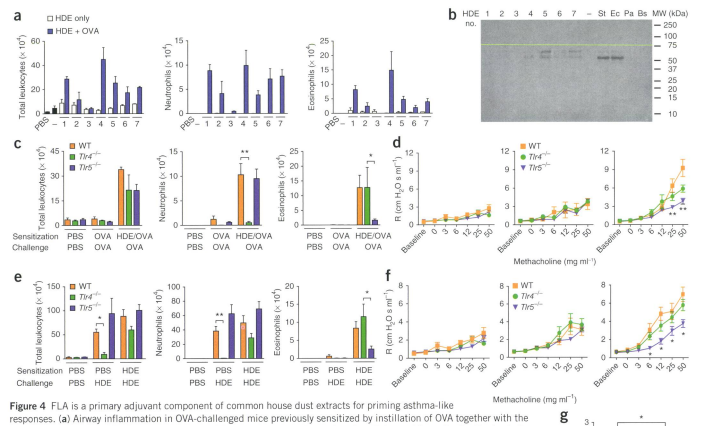

Figure 4 FLA is a primary adjuvant component of common house dust extracts for priming asthma-like responses. (**a**) Airway inflammation in OVA-challenged mice previously sensitized by instillation of OVA together with the indicated sample of HDE. (**b**) Western blot of HDEs probed with an *S. typhimurium* FLA–specific antibody. Also loaded were FLA from *S. typhimurium* (St) (100 ng), *E. coli* (Ec) (400 ng), *P. aeruginosa* (Pa) (400 ng) and *Bacillus subtilis* (Bs) (400 ng). MW, molecular weight. (**c**,**d**) Airway inflammation (**c**) and AHR (**d**) in the indicated strains of mice treated with PBS (left) or OVA-challenged mice previously sensitized with OVA only (middle) or OVA plus HDE#7 (right). (**e**,**f**) Airway inflammation (**e**) and AHR (**f**) in mice given PBS (left), a single instillation of HDE#7 (middle) or two instillations of HDE#7 (right). $n = 8$ mice per group. Experiments shown are pooled data from two experiments yielding similar results. $^{*}P < 0.05$ and $^{**}P < 0.01$ versus values for WT mice. (**g**) Relative titers ± s.e.m. of IgG antibodies to *S. typhimurium* FLA in individuals with or without asthma. $n = 17$ each group. *P* value by *t* test.

When sensitized and challenged with HDE, WT mice developed strong AHR (**Fig. 4f**), whereas mice exposed to HDE on a single occasion did not develop AHR (**Fig. 4f**). These results indicate that adaptive immune responses to HDE are required for AHR. *Tlr4*$^{-/-}$ mice also developed AHR after repeated instillation of HDE, although their responses were slightly decreased compared with WT mice. Therefore, LPS in this HDE probably contributes to, but is not essential for, HDE-induced AHR. By contrast, AHR was markedly lower in *Tlr5*$^{-/-}$ mice compared to WT mice, again indicating that FLA present in this HDE promotes asthma-like responses to natural indoor allergens. We confirmed these findings using two additional extracts (**Supplementary Fig. 6c**). Although the absolute levels of inflammation and AHR varied according the individual HDE used, *Tlr5*$^{-/-}$ mice had less AHR or eosinophilia than WT mice for each of the three extracts tested. *Tlr5*$^{-/-}$ mice also showed less airway inflammation than WT mice following sensitization and challenge with a preparation of cockroach antigens (**Supplementary Fig. 6d**).

We reasoned that if FLA-TLR5 interactions contribute to human asthma, individuals exposed to high amounts of FLA might be at increased risk for developing this disease. We therefore assessed titers of antibodies specific to FLA in sera from humans with mild to moderate asthma as an indirect measure of their exposure to FLA. Compared with age- and gender-matched subjects with healthy airways, subjects with asthma had significantly higher titers of antibodies to FLA (**Fig. 4g** and **Supplementary Fig. 7a**), suggesting that exposure to FLA might be a risk factor for asthma. An alternative explanation is that antibodies to FLA reflect exposure to bacterial products in general. Individuals with asthma also had slightly higher levels of antibodies to LPS than did control subjects, but this difference did not reach statistical significance (**Supplementary Fig. 7b**). When taken together with the reduced eosinophilic and AHR responses of *Tlr5*$^{-/-}$ mice to HDE-mediated allergic sensitization, our data suggest that environmental FLA participates directly in priming allergic responses to indoor allergens.

The relationship between allergic asthma and TLR signaling is complex. Whereas some studies have found that exposure to LPS protects against the development of asthma[20–22], others have found that LPS levels positively correlate with asthma[23,24]. These contradictory conclusions might be due to differences in timing or amounts of LPS, which can affect the nature of immune responses[25]. Recent evidence suggests that gene-environment interactions can also have an impact on the effect of TLR ligand exposure on allergic asthma[26–28]. Although several polymorphisms have been identified in the human *TLR5* gene[29], it remains to be determined whether gene-gene or gene-environment interactions also affect the relationship between FLA exposure and allergic asthma.

Previous reports have shown that, depending on the experimental setting, FLA can prime T_H1 responses[30,31], T_H2 responses[32], or both T_H1 and T_H17 responses[33]. Direct comparison of these

studies is confounded by differences in FLA preparation and routes of administration. In addition, the context of FLA presentation is probably important. Thus, soluble monomeric FLA can prime T_H2 responses, whereas FLA associated with *S. typhimurium* is reported to prime T_H1 responses[34]. Similarly, a fusion protein of rFLA and OVA suppressed T_H2 responses in a mouse model of intestinal allergy, whereas concurrent administration of OVA and rFLA as separate molecules can enhance responses[35]. Although the evolutionary benefit of FLA-mediated eosinophilic responses in the airway is unclear, eosinophils are reported to promote clearance of some bacteria[36].

There is no known single structural feature that is common to all allergens. Some possess protease activity, whereas others possess carbohydrate moieties, bind lipids or interact with a TLR signaling complex[37,38]. It is currently unknown whether FLA can promote sensitization to all allergens residing in house dust or only to a subset of them. Future studies that address the relationships between FLA, allergens and other TLR ligands should improve understanding of how various environmental exposures impact affect initiation of allergic responses that ultimately lead to allergic asthma.

METHODS

Methods and any associated references are available in the online version of the paper.

Note: Supplementary information is available in the online version of the paper.

ACKNOWLEDGMENTS

This work was supported by the Intramural Research Program of the US National Institutes of Health NIEHS. We thank the human subjects for their blood donations and B. Yingling, J. Marshburn and A. Rice of the NIEHS Clinical Research Unit and D. Beaver of Duke University for assistance with patient recruitment and serum isolation. J. Hollingsworth (Duke University) with permission from R. Medzhitov (Yale University) provided CD11c-*Myd88* transgenic mice on a *Myd88*$^{-/-}$ background. S. Akira (Osaka University) provided *Tlr2*$^{-/-}$, *Tlr4*$^{-/-}$ and *Myd88*$^{-/-}$ mice and J. Ting (University of North Carolina) provided *Nlrc4*$^{-/-}$ mice. D. Wozniak (Ohio State University) provided both strains of *P. aeruginosa*, F-S. Shu (Wayne State University) provided purified FLA from *P. aeruginosa* and A. Gewirtz (Emory University) provided FLA from *Escherichia coli*. We also thank NIEHS members K. Nakano for genotyping, L. Perrow for mouse colony management, N. Flagler for histology, J. Aloor for measuring endotoxin levels in HDEs, M. Sifre and C. Bortner for help with FACS-based cell sorting, J. Ciemcewicki for advice on airway epithelial cell culture and M. Fessler and S. London for suggestions on the manuscript.

AUTHOR CONTRIBUTIONS

R.H.W. and S.M. conducted the majority of the experiments, designed experiments and helped prepare the manuscript. G.S.W. performed some assays and mouse experiments, including most airway physiology experiments. D.C.Z. and M.L.S. provided dust samples from US households, and M.L.S. performed the Multiplex Array for Indoor Allergens. J.F.F. and G.P.F. analyzed and graded lung sections for mucus production and took photographs. H.N. helped with flow cytometry and experimental design. M.K. and S.G. provided sera from patients with asthma and control subjects. D.N.C. conceived of the project and helped with experimental design and writing of the manuscript. All authors discussed the results and commented on the manuscript.

COMPETING FINANCIAL INTERESTS

The authors declare no competing financial interests.

Published online at http://www.nature.com/doifinder/10.1038/nm.2920.
Reprints and permissions information is available online at http://www.nature.com/reprints/index.html.

1. Busse, W.W. & Lemanske, R.F. Jr. Asthma. *N. Engl. J. Med.* **344**, 350–362 (2001).
2. Ross, M.A. *et al.* Association of asthma symptoms and severity with indoor bioaerosols. *Allergy* **55**, 705–711 (2000).
3. Iwasaki, A. & Medzhitov, R. Regulation of adaptive immunity by the innate immune system. *Science* **327**, 291–295 (2010).
4. Ng, N., Lam, D., Paulus, P., Batzer, G. & Horner, A.A. House dust extracts have both TH2 adjuvant and tolerogenic activities. *J. Allergy Clin. Immunol.* **117**, 1074–1081 (2006).
5. Gewirtz, A.T., Navas, T.A., Lyons, S., Godowski, P.J. & Madara, J.L. Cutting edge: bacterial flagellin activates basolaterally expressed TLR5 to induce epithelial proinflammatory gene expression. *J. Immunol.* **167**, 1882–1885 (2001).
6. Hayashi, F. *et al.* The innate immune response to bacterial flagellin is mediated by Toll-like receptor 5. *Nature* **410**, 1099–1103 (2001).
7. Barczyk, A., Pierzchala, W. & Sozanska, E. Interleukin-17 in sputum correlates with airway hyperresponsiveness to methacholine. *Respir. Med.* **97**, 726–733 (2003).
8. McKinley, L. *et al.* T_H17 cells mediate steroid-resistant airway inflammation and airway hyperresponsiveness in mice. *J. Immunol.* **181**, 4089–4097 (2008).
9. Wilson, R.H. *et al.* Allergic sensitization through the airway primes T_H17-dependent neutrophilia and airway hyperresponsiveness. *Am. J. Respir. Crit. Care Med.* **180**, 720–730 (2009).
10. Franchi, L. *et al.* Cytosolic flagellin requires Ipaf for activation of caspase-1 and interleukin 1β in *Salmonella*-infected macrophages. *Nat. Immunol.* **7**, 576–582 (2006).
11. Miao, E.A. *et al.* Cytoplasmic flagellin activates caspase-1 and secretion of interleukin 1β via Ipaf. *Nat. Immunol.* **7**, 569–575 (2006).
12. Sung, S.S. *et al.* A major lung CD103 (α_E-β_7 integrin–positive epithelial dendritic cell population expressing Langerin and tight junction proteins. *J. Immunol.* **176**, 2161–2172 (2006).
13. Sanders, C.J., Moore, D.A. III, Williams, I.R. & Gewirtz, A.T. Both radioresistant and hemopoietic cells promote innate and adaptive immune responses to flagellin. *J. Immunol.* **180**, 7184–7192 (2008).
14. Pasare, C. & Medzhitov, R. Control of B-cell responses by Toll-like receptors. *Nature* **438**, 364–368 (2005).
15. Janot, L. *et al.* Radioresistant cells expressing TLR5 control the respiratory epithelium's innate immune responses to flagellin. *Eur. J. Immunol.* **39**, 1587–1596 (2009).
16. Mijares, L.A. *et al.* Airway epithelial MyD88 restores control of *Pseudomonas aeruginosa* murine infection via an IL-1–dependent pathway. *J. Immunol.* **186**, 7080–7088 (2011).
17. Hammad, H. *et al.* House dust mite allergen induces asthma via Toll-like receptor 4 triggering of airway structural cells. *Nat. Med.* **15**, 410–416 (2009).
18. McDonough, M.W. & Smith, S.E. Molecular weight variation among bacterial flagellins. *Microbios* **16**, 49–53 (1976).
19. McKinley, L., Kim, J., Bolgos, G.L., Siddiqui, J. & Remick, D.G. Reproducibility of a novel model of murine asthma-like pulmonary inflammation. *Clin. Exp. Immunol.* **136**, 224–231 (2004).
20. Braun-Fahrländer, C. *et al.* Environmental exposure to endotoxin and its relation to asthma in school-age children. *N. Engl. J. Med.* **347**, 869–877 (2002).
21. El-Sharif, N., Douwes, J., Hoet, P. & Nemery, B. Childhood asthma and indoor aeroallergens and endotoxin in Palestine: a case-control study. *J. Asthma* **43**, 241–247 (2006).
22. Gehring, U. *et al.* Exposure to house dust endotoxin and allergic sensitization in adults. *Allergy* **59**, 946–952 (2004).
23. Bolte, G. *et al.* Early endotoxin exposure and atopy development in infants: results of a birth cohort study. *Clin. Exp. Allergy* **33**, 770–776 (2003).
24. Thorne, P.S. *et al.* Endotoxin exposure is a risk factor for asthma: the national survey of endotoxin in United States housing. *Am. J. Respir. Crit. Care Med.* **172**, 1371–1377 (2005).
25. Eisenbarth, S.C. *et al.* Lipopolysaccharide-enhanced, toll-like receptor 4–dependent T helper cell type 2 responses to inhaled antigen. *J. Exp. Med.* **196**, 1645–1651 (2002).
26. Custovic, A. *et al.* Effect of day care attendance on sensitization and atopic wheezing differs by Toll-like receptor 2 genotype in 2 population-based birth cohort studies. *J. Allergy Clin. Immunol.* **127**, 390–397 (2011).
27. Eder, W. *et al.* Opposite effects of CD14/-260 on serum IgE levels in children raised in different environments. *J. Allergy Clin. Immunol.* **116**, 601–607 (2005).
28. Simpson, A. *et al.* Endotoxin exposure, CD14, and allergic disease: an interaction between genes and the environment. *Am. J. Respir. Crit. Care Med.* **174**, 386–392 (2006).
29. Merx, S., Zimmer, W., Neumaier, M. & Ahmad-Nejad, P. Characterization and functional investigation of single nucleotide polymorphisms (SNPs) in the human *TLR5* gene. *Hum. Mutat.* **27**, 293 (2006).
30. Strindelius, L., Filler, M. & Sjoholm, I. Mucosal immunization with purified flagellin from Salmonella induces systemic and mucosal immune responses in C3H/HeJ mice. *Vaccine* **22**, 3797–3808 (2004).
31. Wang, B.Z. *et al.* Incorporation of membrane-anchored flagellin into influenza virus-like particles enhances the breadth of immune responses. *J. Virol.* **82**, 11813–11823 (2008).
32. Didierlaurent, A. *et al.* Flagellin promotes myeloid differentiation factor 88–dependent development of T_H2-type response. *J. Immunol.* **172**, 6922–6930 (2004).
33. Uematsu, S. *et al.* Regulation of humoral and cellular gut immunity by lamina propria dendritic cells expressing Toll-like receptor 5. *Nat. Immunol.* **9**, 769–776 (2008).
34. Cunningham, A.F. *et al.* Responses to the soluble flagellar protein FliC are T_H2, while those to FliC on *Salmonella* are T_H1. *Eur. J. Immunol.* **34**, 2986–2995 (2004).
35. Schulke, S. *et al.* A fusion protein of flagellin and ovalbumin suppresses the T_H2 response and prevents murine intestinal allergy. *J. Allergy Clin. Immunol.* **128**, 1340–1348 (2011).
36. Yousefi, S. *et al.* Catapult-like release of mitochondrial DNA by eosinophils contributes to antibacterial defense. *Nat. Med.* **14**, 949–953 (2008).
37. Karp, C.L. Guilt by intimate association: what makes an allergen an allergen? *J. Allergy Clin. Immunol.* **125**, 955–960 (2010).
38. Trompette, A. *et al.* Allergenicity resulting from functional mimicry of a Toll-like receptor complex protein. *Nature* **457**, 585–588 (2009).

nature medicine

TECHNICAL REPORTS

Computed tomography–based biomarker provides unique signature for diagnosis of COPD phenotypes and disease progression

Craig J Galbán[1,2], Meilan K Han[3], Jennifer L Boes[1,2], Komal A Chughtai[1,2], Charles R Meyer[1,2], Timothy D Johnson[4], Stefanie Galbán[2,5], Alnawaz Rehemtulla[2,5], Ella A Kazerooni[1], Fernando J Martinez[3] & Brian D Ross[1,2]

Chronic obstructive pulmonary disease (COPD) is increasingly being recognized as a highly heterogeneous disorder, composed of varying pathobiology. Accurate detection of COPD subtypes by image biomarkers is urgently needed to enable individualized treatment, thus improving patient outcome. We adapted the parametric response map (PRM), a voxel-wise image analysis technique, for assessing COPD phenotype. We analyzed whole-lung computed tomography (CT) scans acquired at inspiration and expiration of 194 individuals with COPD from the COPDGene study. PRM identified the extent of functional small airways disease (fSAD) and emphysema as well as provided CT-based evidence that supports the concept that fSAD precedes emphysema with increasing COPD severity. PRM is a versatile imaging biomarker capable of diagnosing disease extent and phenotype while providing detailed spatial information of disease distribution and location. PRM's ability to differentiate between specific COPD phenotypes will allow for more accurate diagnosis of individual patients, complementing standard clinical techniques.

COPD is an increasingly prevalent disorder characterized by incompletely reversible airflow limitation[1,2]. Presently, it is the fourth leading cause of death in the United States, with over 11 million people suffering from the disease. The immense scope of this disease has led to major US National Institutes of Health–funded initiatives such as COPDGene[3]. COPD is a heterogeneous disorder that arises from pathological processes including emphysematous lung tissue destruction, gross airway disease and functional small-airways disease (fSAD) in varying combinations and severity within an individual. It is widely accepted that fSAD and emphysema are two main components of COPD and that a spectrum of COPD phenotypes with varying contributions of these components exists in individual patients; thus, the ability to diagnose the underlying phenotypes could improve prognostication and treatment of individuals afflicted by this disease[2,4].

CT is a minimally invasive imaging technique capable of providing both high-contrast and high-resolution detail of the lungs and airways. CT has proven instrumental in identifying structural abnormalities associated with COPD. Although most of the clinically useful information today from lung CT comes from qualitative visual inspection, extensive research has been devoted to the application of quantitative techniques to high-resolution CT data sets using a wide variety of quantitative CT-based metrics to define COPD structural abnormality and disease severity. The percentage of emphysema, well accepted for identifying and quantifying the emphysema component of COPD, is determined using an attenuation-based method in which the sum of all image voxels, the smallest measureable unit of volume in an image data set, less than −950 Hounsfield units (HU) is normalized by the total lung volume on the inspiratory CT scan[5,6]. This metric is easily calculated from data acquired using standard imaging protocols. However, this metric only identifies one component of the heterogeneous COPD process. The second component, fSAD, remains a quantitative CT challenge, owing to the complexity of the histopathological features of COPD-affected lung tissue. Other attenuation-based techniques, such as the sum of all image voxels less than −856 HU normalized by the total lung volume on the expiratory CT scan, have been proposed as a measure of gas trapping but are unable to distinguish the contributions of small airways disease and emphysema from the gas-trapping measurement[3]. This challenge has prompted research that strives toward a more accurate and complete quantitative tool for the evaluation of COPD[7–15].

The motivation for the present study was to develop a robust CT-based imaging biomarker that would allow for visualization and quantification of COPD phenotypes. Previously, we developed the PRM as a voxel-based method for improving the sensitivity of diffusion-magnetic resonance imaging (MRI) data for identifying early therapeutic response in patients with glioma[16]. This technique has since been validated as an early surrogate imaging biomarker of survival for gliomas, head and neck cancer, breast cancer and metastatic prostate cancer to the bone[17–20]. In 2009, we also demonstrated

[1]Department of Radiology, University of Michigan, Ann Arbor, Michigan, USA. [2]Center for Molecular Imaging, University of Michigan, Ann Arbor, Michigan, USA. [3]Department of Internal Medicine, University of Michigan, Ann Arbor, Michigan, USA. [4]Department of Biostatistics, University of Michigan, Ann Arbor, Michigan, USA. [5]Department of Radiation Oncology, University of Michigan, Ann Arbor, Michigan, USA. Correspondence should be addressed to B.D.R. (bdross@umich.edu).

Received 23 February; accepted 30 May; published online 7 October 2012; doi:10.1038/nm.2971

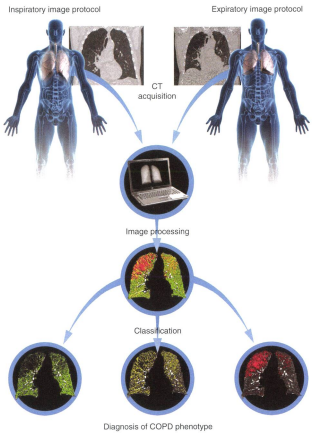

Figure 1 Schematic diagram of the PRM method. PRM is a fundamentally distinct approach from conventional CT-based quantitative measures. This methodology classifies lung attenuation maps on a voxel-by-voxel basis through image co-registration of inspiratory and expiratory images to provide a global measure as well as the local distribution and extent of COPD phenotypes. The PRM method consists of three key steps: image acquisition, image processing and classification. Acquisition of CT scans was performed using imaging protocols that emphasize high resolution with sufficient signal-to-noise ratio on both serial CT scans as defined by the COPDGene study. Image processing consists primarily of lung segmentation followed by deformable volumetric registration. Deformable registration spatially aligns the expiration scan to the inspiration scan such that both share the same spatial geometry. Segmentation of the lung bronchus from the parenchyma is required for further analysis. Classification of voxels from attenuation maps into discrete zones allows for quantification of global measures of normal parenchyma (PRM^{Normal}, green), fSAD (PRM^{fSAD}, yellow) and emphysema (PRM^{Emph}, red) that reveals the extent of COPD while retaining spatial information for visualization of the location of disease phenotypes within the lung. The PRM method is a sensitive prognostic imaging biomarker capable of elucidating the complexity and severity of COPD.

using temporal perfusion-MRI that PRM is a generalized method, not restricted to diffusion, for assessing early clinical outcome in cancer patients[21]. Here we have considerably modified the PRM analytical approach to leverage the power of its pairwise analysis on inspiratory and expiratory CT lung scans to allow for quantification of fSAD separately from emphysema, which is not possible when the scans are analyzed independently. Our proposed PRM method is therefore a unique quantitative biomarker approach for assessment of COPD severity, phenotype and spatial heterogeneity using CT images. There are three fundamental steps in applying PRM to CT data before clinical diagnosis (**Fig. 1**). These steps involve image acquisition, image processing (that is, segmentation and co-registration) and classification of voxels with HU values characteristic of lung parenchyma representing normal (green), fSAD (yellow) or emphysema (red). The PRM method proposed in this study is a fundamentally new and distinct application from prior work using this technique and a distinctly different approach from other CT-based quantitative measures (see **Supplementary Note**). Commonly used CT metrics for diagnosis of lung disease use tissue volumetric summary statistics of lung fields such as the percentage of emphysema and mean lung density from inspiratory and expiratory phases. PRM, however, classifies local variations in lung function on the basis of a voxel-by-voxel comparison of lung attenuation changes from digitally co-registered inspiratory and expiratory CT scans to provide both global and local evaluation of COPD severity and phenotype. Using a well-defined COPD cohort, we show that this methodology allows for detection and quantification of not only emphysema but also tissue that comprises fSAD that can be monitored longitudinally in a single unified approach. PRM, being able to distinguish the relative contributions of fSAD and emphysema in COPD phenotypes, may serve as a complementary readout to current pulmonary function tests (PFTs) and CT-based metrics that will allow for more accurate diagnosis and improve the treatment management of individual patients.

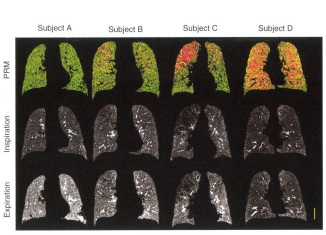

Figure 2 COPD phenotypes identified by PRM. The strength of PRM to identify fSAD (PRM^{fSAD}) from emphysema (PRM^{Emph}) is demonstrated in representative coronal PRM images with corresponding inspiratory and expiratory CT scans from four individuals with varying GOLD status. From the three classifications, normal lung tissue is denoted green, fSAD is denoted yellow and emphysema is denoted red. Yellow scale bar indicates 5 cm. A modified figure has also been provided for easier visualization for those with some forms of color blindness (**Supplementary Fig. 4**).

RESULTS

Inspiratory and expiratory CT scans were acquired from 10,000 subjects as part of the COPDGene study. Of these, we used 194 with varying GOLD status, a classification of severity of airflow limitation in COPD based on post-bronchodilator PFTs (**Supplementary Table 1**) to demonstrate the PRM method for quantifying fSAD and emphysema. The ability of PRM to identify individuals with varying phenotypes of COPD is shown in representative coronal PRM images with corresponding inspiratory and expiratory CT scans from four subjects with varying GOLD status (**Fig. 2** and **Table 1**). Details on the classification scheme are provided in the **Supplementary Methods** and **Supplementary Figure 1**. In the extreme cases, forced expiratory volume in 1 s (FEV_1) and percentage of emphysema, defined as

Table 1 Subject measures

Subject	A	B	C	D
GOLD	NA	2	2	4
FEV_1	99	55	59	18
Percentage emphysema	4	5	19	23
PRM^{Normal}	85	66	54	21
PRM^{Emph}	1	4	16	28
PRM^{fSAD}	6	26	22	45

NA, not applicable. Percentage emphysema is the relative volume of lung with attenuation < −950 HU on the inspiratory scan.

percentage of lung < −950 HU (percentage emphysema in **Table 1**), accurately assess the severity of COPD, with subjects A and D having low and high levels, respectively, of emphysema (**Fig. 2**). Where PRM is most useful is in the identification of the underlying COPD phenotypes and the location of the specific disease classifications. Subjects B and C had near-identical FEV_1 measurements, yet the percentage of emphysema was elevated in subject C compared to subject B. Current techniques for assessing COPD severity were unable to accurately diagnose subject B, leaving the subject's clinician to presume on the basis of FEV_1 and percentage of emphysema that the COPD in this individual is due primarily to airway obstruction. Our PRM measurements revealed that 26% of the lung tissue in subject B was fSAD (PRM^{fSAD}) tissue localized primarily in the upper lobes of both lungs, with minimal signs of emphysema (PRM^{Emph}). In subject C, we found that emphysema had progressed throughout the upper left lung, identified by the low attenuation on the inspiratory CT scan as a hallmark of emphysema. PRM easily identified, quantified and spatially displayed fSAD expanding in the right upper lobe, which would have been missed by current clinical diagnostic methods such as percentage of emphysema.

The ability of PRM to identify and track individual voxels from inspiratory and expiratory scans allows for the individual components of COPD to be quantified and monitored (**Supplementary Fig. 2**). In addition, PRM provided unique information on the contribution of fSAD and emphysema in a variety of clinical tests that have been identified as being prognostic of COPD (**Supplementary Table 2**). We also found our PRM metrics highly sensitive when modeling airway obstruction while controlling for other CT-based airway measurements (**Supplementary Table 3**).

We observed a trend that involved the spatial distribution and association of fSAD tissue with emphysema (**Fig. 3**). We further analyzed PRM signatures for each individual to identify a pattern of disease progression in our cohort of 194 subjects. As part of the PRM approach, each voxel is classified on the basis of its location within a coordinate system. **Figure 3a** (see **Supplementary Results** for details) depicts the distribution of voxels with varying values at inspiration and expiration for a subject with normal status as determined by spirometry (FEV_1/forced vital capacity (FVC) = 83%, FEV_1 = 81%). Most of the voxels reside within the normal lung classification of PRM (green field), with voxels generally having more attenuation at expiration than inspiration as indicated by the hyperintensity of the expiration CT scan (**Fig. 3a**). In contrast, an individual with GOLD 4 status (FEV_1/FVC = 25%, FEV_1 = 18%) had a PRM signature distinct from the normal status. For this individual, voxels reside primarily within the fSAD (yellow field) and emphysema (red field) classifications. We observed similar attenuation on CT scans at inspiration and expiration and extensive emphysema (33% based on COPDGene percentage of emphysema metric) (**Fig. 3b**), which is characteristic of an individual with dyspnea (Modified Medical Research Council Dyspnea Scale = 3). As observed for these two subjects, voxels tended to concentrate on the Cartesian plot (that is, the PRM signature), with red and blue regions denoting high and low voxel density, respectively, such that an elliptical pattern is generated that has a location, distribution and orientation that is unique for each individual. On the basis of the distribution of voxels (**Fig. 3a**,**b**), we calculated for each subject the center of distribution that is the median values of all voxel data for both axes (position of the arrows) and the direction of largest covariance component (that is, the principal eigenvector that designates the longest axes of the ellipse) of each subject's scatter plot (arrows; direction of arrowheads are arbitrarily chosen) and plotted data from all individuals on the inspiration-expiration diagram (that is, the Cartesian plot), which consists of the three PRM color codes defined in **Figure 1**. We observed a pattern suggestive of COPD progression that, to our knowledge, has never been demonstrated previously by CT-based measures. In fact, the data from the 194 subjects studied suggests that fSAD precedes emphysema in the progression of COPD. We also identified a unique relationship between fSAD and emphysema when plotting PRM^{fSAD} against PRM^{Emph} for all 194 subjects (**Supplementary Fig. 3**). We found that many of the

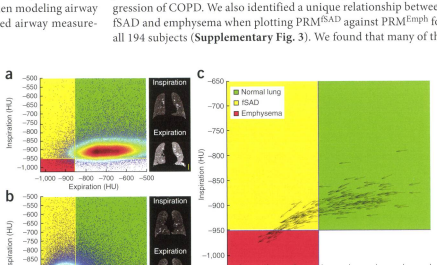

Figure 3 COPD progression as determined by PRM. (**a**,**b**) The distribution of voxels with varying values at inspiration and expiration for an individual with normal status as determined by spirometry (FEV_1/FVC = 83%, FEV_1 = 99%) (**a**) and an individual with GOLD 4 status (FEV_1/FVC = 25, FEV_1 = 18) (**b**). Representative coronal slices of CT images at inspiration (top) and expiration (bottom) are provided for each subject. The distribution of voxels generates an elongated elliptical pattern with voxels highly concentrated in the center (red) and decreasing on the periphery (blue). (**c**) As observed for the two cases (**a** and **b**), a unique attribute of PRM is the distinct signature, distribution and location of the voxels in the inspiration-expiration plots. Calculation of the center of distribution that is the median value for both axes (position of the arrows) and principal eigenvector of the data determined by the principal component analysis (arrows) provide information on location and direction of the principal distribution, respectively. A plot of these two metrics for each subject with the three PRM color-codes for COPD is shown. Yellow scale bars indicate 5 cm.

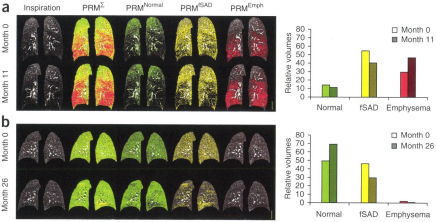

Figure 4 PRM as an imaging biomarker of COPD progression. Inspiratory CT scans, PRM and spirometry data are presented from two subjects not part of the COPDGene study. (**a**) PRM analysis of serial CT data acquired 11 months apart from an individual identified as GOLD 4. Conventional FEV_1 measurements were 18% and 17% 11 months later. (**b**) The PRM analysis of serial CT data acquired 26 months apart from an individual identified as GOLD 2. FEV_1 percentage were 66% to 75% at follow-up. PRM superscripts indicate the tissue classification (that is, normal, fSAD and emphysema), with Σ denoting all three classifications presented in the map. Yellow scale bars indicate 5 cm.

subjects have less than 10% emphysema, yet some can have fSAD that makes up 10–30% of their lung parenchyma (**Supplementary Fig. 3**). Notably, there appears to be a plateau in the amount of fSAD that can be present in the lung. More severe lung obstruction, as determined by FEV_1 (GOLD 3 and 4), seems to be attributable to contributions of both fSAD and emphysema, with PRM^{fSAD} plateauing around 40–50% and PRM^{Emph} increasing to >20% of the lung volume (**Supplementary Fig. 3**). These results suggest that fSAD precedes the onset of emphysema (**Fig. 3** and **Supplementary Fig. 3**). Our findings agree with a recent study that demonstrated by pathology the narrowing and disappearance of small airways before the onset of emphysema in subjects with COPD[22]. Notably, our data (**Fig. 3c** and **Supplementary Fig. 3**) are not longitudinal but rather snap shots of a cohort of individual subjects at various stages of the disease. This finding, obtained from a heterogeneous population, shows a specific trend in the CT data analyzed by our PRM methodology that suggests that airway obstruction associated with fSAD seems to be a precursor to the development of emphysema.

To provide some insight into the feasibility of PRM as an imaging biomarker to monitor individuals longitudinally over time, we obtained additional retrospective imaging data outside of the COPDGene study from subjects who had previously visited the University of Michigan pulmonary clinic and underwent an inspiratory/expiratory CT scanning protocol over a period of time. We present here examples from two different subjects along with the time intervals between CT exams, the PRM metrics provided as relative volumes and the FEV_1 acquired as a standard PFT (**Fig. 4**). The subject who had considerable emphysema and fSAD at the baseline scan (month 0), had at 11 months later progressive emphysema greater than the loss of fSAD, as there was an additional loss of normal functional lung, as well (**Fig. 4a**). FEV_1 was unchanged from 18% to 17% over this time interval. These two pathologies, fSAD and emphysema, seemed to coexist in high percentages throughout the disease duration of this subject. In contrast, another subject with COPD had a largely asthmatic component with no emphysema (**Fig. 4b**). Over a 26-month period, the amount of normal lung increased, corresponding with a decrease in fSAD and an increase in FEV_1 from 66% to 75%. These human examples reveal the potential of using PRM to monitor COPD over time to provide a phenotype classification basis for patient response or progression.

DISCUSSION

In this study we demonstrate the ability of PRM, as a new application of an existing voxel-based image post-processing technique, to serve as a quantitative imaging biomarker to assess phenotypic contributions of fSAD and emphysema in COPD when applied to inspiratory and expiratory CT images[21]. This is a new application of PRM in that cyclic physiological respiratory states, not changes in biological tissue as a response to disease or treatment, are being captured through imaging and compared on a voxel-by-voxel basis by image co-registration. In this analysis, the registered CT images share the same geometric space, that is, lung tissue at expiration is spatially aligned with the same lung tissue at inspiration. We developed a unique classification scheme based on specific thresholds that allows for spatial information about the disease to be retained. This is accomplished by classifying voxels into discrete zones that can be analyzed as a global metric (that is, relative volumes) but also supports the ability to identify local phenomena of the individual PRM metrics. PRM can be used not only as a versatile imaging biomarker to diagnose disease extent and phenotype but also to provide detailed spatial information related to disease distribution and precise location. Moreover, PRM can potentially be used to reveal the nature of COPD progression as it pertains to small airways disease and emphysema.

The natural history of COPD within an individual has been primarily based on pulmonary function tests[23]. Although the breadth of this knowledge has provided detailed information used to improve patient clinical care, it does not address the progression of the underlying phenotypes of COPD[24]. Such understanding would allow clinicians to tailor therapeutic intervention to a particular COPD phenotype, as most cases have varying degrees of fSAD and emphysema. A key feature of PRM not easily attained by other methodologies is its potential to localize the disease states and possibly detect and identify the COPD progression pathway. This is made possible through the unique PRM signature for each individual and the sufficiently large population available for such an analysis. When plotting the metrics center of distribution and principle eigenvector for each of the 194 subjects, we observed not a random distribution of values within our inspiration-expiration plot (the Cartesian plot) but a continuous ribbon originating from healthy lung, through fSAD and ending at emphysema (**Fig. 3**). As each arrow is only a snapshot of disease state, we acquired additional longitudinal data from individuals not accrued as part of the COPDGene study to demonstrate the utility of PRM as an imaging biomarker for monitoring changes in COPD phenotype (**Fig. 4**). Although we consider these data promising, further validation of the use of PRM to follow COPD progression in subjects will need to be performed in a larger cohort of imaging data collected from a longitudinal study. Nevertheless, our results suggest that PRM provides a tool for improving understanding of the relationship between fSAD and emphysema in COPD progression.

Another potential use of this technique is as a secondary biomarker of therapeutic response in pharmacological trials. Few pharmaceutical advances in COPD have been made over the past few decades, primarily due to the lack of accurate biomarkers of the disease[25,26]. In an effort to rigorously test potential therapies for COPD, the US Food and Drug Administration has set guidelines for potential biomarkers in specific contexts, which include stratification of patient populations, dose-ranging and use as a disease outcome. Currently, no well-validated biomarker of COPD has been identified other than FEV_1, which is limited to whole-lung airway obstruction. Inclusion of the PRM approach proposed herein as a secondary endpoint may aid in pharmacological trials by stratifying patients as having fSAD- or emphysema-dominant COPD. For example, the relative volume of fSAD lung tissue (yellow voxels) could be used as a surrogate of treatment efficacy in routine patient care and in drug trials. A change of yellow voxels into green voxels should indicate lung tissue that has been rescued by therapeutic intervention.

The PRM approach differs from previous approaches because the classification process imposed on individual voxels allows the capture of the unique signature specific to the disease state of an individual patient. To date, groups who evaluate the prognostic value of registered data sets typically use statistically based metrics, such as the mean of the Jacobian, differences in HU or dissimilarity measures based on the histograms of the CT images where information from the measure is pooled throughout the lung into a single outcome measure, which forfeits the spatial information that is inherent in the CT images[9,10,14,27].

Given the prevalence and impact of COPD worldwide, there is a crucial need to develop quantitative imaging methodologies, which can more objectively characterize the disease and, ideally, define response to therapy. PRM provides a quantitative imaging application that has promise in classifying COPD by disease subtype and can be applied to facilitate individualized treatment strategies. PRM provides for parenchymal analysis as well as analysis of lung airway disease through a systematic algorithmic workflow for quantification of lung function in a high-volume, time-constrained clinical environment.

METHODS

Methods and any associated references are available in the online version of the paper.

Note: Supplementary information is available in the online version of the paper.

ACKNOWLEDGMENTS

We would like to acknowledge S. Sarkar, M. Bule and S.A. Blanks for their indispensable contribution in processing the CT data sets. We would also like to acknowledge D.A. Lynch and the COPDGene investigators for providing the CT scans from National Jewish Health and recruiting the subjects included in this analysis. This work was supported by the US National Institutes of Health research grant P50CA93990 and COPDGene grants U01HL089897 and U01HL089856. J.L.B. is a recipient of support from the US National Institutes of Health training grant T32EB005172.

AUTHOR CONTRIBUTIONS

C.J.G. conducted data and statistical analyses and wrote the manuscript, M.K.H. acquired images, PFT data and clinical information from COPDGene, C.R.M. and J.L.B. optimized and performed image registrations, K.A.C. aided in image registration and performed PRM on image data, T.D.J. assisted with the statistical analysis, S.G. and A.R. contributed to the design of the study and E.A.K., F.J.M. and B.D.R. supervised the project, including data analysis and manuscript preparation.

COMPETING FINANCIAL INTERESTS

The authors declare competing financial interests: details are available in the online version of the paper.

Published online at http://www.nature.com/doifinder/10.1038/nm.2971.
Reprints and permissions information is available online at http://www.nature.com/reprints/index.html.

1. Buist, A.S. *et al.* The Burden of Obstructive Lung Disease Initiative (BOLD): rationale and design. *COPD* **2**, 277–283 (2005).
2. Agusti, A. & Vestbo, J. Current controversies and future perspectives in COPD. *Am. J. Respir. Crit. Care Med.* **184**, 507–513 (2011).
3. Regan, E.A. *et al.* Genetic epidemiology of COPD (COPDGene) study design. *COPD* **7**, 32–43 (2010).
4. Han, M.K. *et al.* Chronic obstructive pulmonary disease phenotypes: the future of COPD. *Am. J. Respir. Crit. Care Med.* **182**, 598–604 (2010).
5. Gevenois, P.A., de Maertelaer, V., De Vuyst, P., Zanen, J. & Yernault, J.C. Comparison of computed density and macroscopic morphometry in pulmonary emphysema. *Am. J. Respir. Crit. Care Med.* **152**, 653–657 (1995).
6. Gevenois, P.A. *et al.* Comparison of computed density and microscopic morphometry in pulmonary emphysema. *Am. J. Respir. Crit. Care Med.* **154**, 187–192 (1996).
7. Newman, K.B., Lynch, D.A., Newman, L.S., Ellegood, D. & Newell, J.D., Jr. Quantitative computed tomography detects air trapping due to asthma. *Chest* **106**, 105–109 (1994).
8. Eda, S. *et al.* The relations between expiratory chest CT using helical CT and pulmonary function tests in emphysema. *Am. J. Respir. Crit. Care Med.* **155**, 1290–1294 (1997).
9. Gorbunova, V. *et al.* Early detection of emphysema progression. *Med. Image Comput. Comput. Assist. Interv.* **13**, 193–200 (2010).
10. Gorbunova, V. *et al.* Weight preserving image registration for monitoring disease progression in lung CT. *Med. Image Comput. Comput. Assist. Interv.* **11**, 863–870 (2008).
11. Kubo, K. *et al.* Expiratory and inspiratory chest computed tomography and pulmonary function tests in cigarette smokers. *Eur. Respir. J.* **13**, 252–256 (1999).
12. Matsuoka, S. *et al.* Quantitative assessment of air trapping in chronic obstructive pulmonary disease using inspiratory and expiratory volumetric MDCT. *AJR Am. J. Roentgenol.* **190**, 762–769 (2008).
13. Matsuoka, S., Kurihara, Y., Yagihashi, K. & Nakajima, Y. Quantitative assessment of peripheral airway obstruction on paired expiratory/inspiratory thin-section computed tomography in chronic obstructive pulmonary disease with emphysema. *J. Comput. Assist. Tomogr.* **31**, 384–389 (2007).
14. Reinhardt, J.M. *et al.* Registration-based estimates of local lung tissue expansion compared to xenon CT measures of specific ventilation. *Med. Image Anal.* **12**, 752–763 (2008).
15. Li, B., Christensen, G.E., Hoffman, E.A., McLennan, G. & Reinhardt, J.M. Pulmonary CT image registration and warping for tracking tissue deformation during the respiratory cycle through 3D consistent image registration. *Med. Phys.* **35**, 5575–5583 (2008).
16. Moffat, B.A. *et al.* Functional diffusion map: a noninvasive MRI biomarker for early stratification of clinical brain tumor response. *Proc. Natl. Acad. Sci. USA* **102**, 5524–5529 (2005).
17. Galbán, C.J. *et al.* A feasibility study of parametric response map analysis of diffusion-weighted magnetic resonance imaging scans of head and neck cancer patients for providing early detection of therapeutic efficacy. *Transl. Oncol.* **2**, 184–190 (2009).
18. Hamstra, D.A. *et al.* Functional diffusion map as an early imaging biomarker for high-grade glioma: correlation with conventional radiologic response and overall survival. *J. Clin. Oncol.* **26**, 3387–3394 (2008).
19. Ma, B. *et al.* Voxel-by-voxel functional diffusion mapping for early evaluation of breast cancer treatment. *Inf. Process. Med. Imaging* **21**, 276–287 (2009).
20. Reischauer, C. *et al.* Bone metastases from prostate cancer: assessing treatment response by using diffusion-weighted imaging and functional diffusion maps–initial observations. *Radiology* **257**, 523–531 (2010).
21. Galbán, C.J. *et al.* The parametric response map is an imaging biomarker for early cancer treatment outcome. *Nat. Med.* **15**, 572–576 (2009).
22. McDonough, J.E. *et al.* Small-airway obstruction and emphysema in chronic obstructive pulmonary disease. *N. Engl. J. Med.* **365**, 1567–1575 (2011).
23. Kohansal, R., Soriano, J.B. & Agusti, A. Investigating the natural history of lung function: facts, pitfalls, and opportunities. *Chest* **135**, 1330–1341 (2009).
24. Oga, T. *et al.* Multidimensional analyses of long-term clinical courses of asthma and chronic obstructive pulmonary disease. *Allergol. Int.* **59**, 257–265 (2010).
25. Cazzola, M. *et al.* Outcomes for COPD pharmacological trials: from lung function to biomarkers. *Eur. Respir. J.* **31**, 416–469 (2008).
26. Martinez, F.J., Donohue, J.F. & Rennard, S.I. The future of chronic obstructive pulmonary disease treatment–difficulties of and barriers to drug development. *Lancet* **378**, 1027–1037 (2011).
27. Yamamoto, T. *et al.* Investigation of four-dimensional computed tomography-based pulmonary ventilation imaging in patients with emphysematous lung regions. *Phys. Med. Biol.* **56**, 2279–2298 (2011).

nature medicine

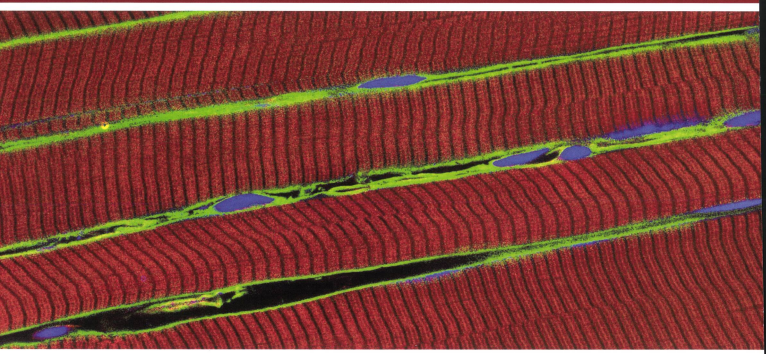

ePoster on Metabolic Syndrome

Diabetes and obesity are often referred to as the twin epidemics, owing to their high prevalence and mechanistic relatedness. A key concept that has emerged over the past few years is that different organs have different, but integrated, roles in the pathogenesis of the metabolic syndrome. This ePoster, a collection of figures prepared by leaders in the field, presents a comprehensive view of the molecular pathophysiology of the metabolic syndrome at the systems and cellular levels. Published originally in 2011, the 2012 version features a new organ -- the pancreas -- plus updates for the existing organs to reflect key advances of the past year.

Access the ePoster FREE online!
www.nature.com/nm/poster

Image credit: Tom Deerinck, UCSD

Sponsored by

Takeda

nature publishing group npg

naturejobs medicine

www.naturejobs.com

Please get in touch with your regional sales office to place your advert in this journal

Europe/ROW: +44 (0)20 78434961 - naturejobs@nature.com
USA: +1 (212) 726 9254 - naturejobs@natureny.com
Asia - Pacific: +81 (3) 3 267 8765 - y.fukiwara@natureasia.com

UCLA

Chief of the Division of Rheumatology at the David Geffen School of Medicine at UCLA

The Department of Medicine of the University of California at Los Angeles is seeking an exceptional leader with the expertise and skills needed to be the Chief of Rheumatology at UCLA. We are seeking a world class scientist that will continue the distinguished research that has been the hallmark of the Division over many decades. The Division includes 31 faculty members and an ACGME accredited fellowship training program consisting of 8 fellowship positions.

Individuals interested in this position should have a national/international reputation in the field of academic Rheumatology. The candidates must have a strong background in basic research in Rheumatology-related research themes with emphasis on novel approaches, a track record of extramural research funding, and publications consistent with this position. The selected individual will facilitate and coordinate all Rheumatology clinical and research activities of the Division. The candidate should have a willingness to foster collaborative interactions between clinical and laboratory scientists, and a strong interest in mentoring of junior faculty/fellows.

A tenured faculty appointment at a rank commensurate with experience will be considered.

This position will control substantial resources from the Department of Medicine, and commands a competitive salary enhanced by an attractive benefits package, including medical malpractice coverage and a collegial work environment.

The David Geffen School of Medicine at UCLA is an Affirmative Action/Equal Opportunity Employer. Women and Minorities are encouraged to apply.

Candidates should email their curriculum vitae, a letter with a statement of career goals, and the names of three references to the Chair of the Search Committee: Charalabos Pothoulakis, M.D. Professor of Medicine, David Geffen School of Medicine at UCLA, c/o Juan Vaquerano, Administrator e-mail: jvaquerano@mednet.ucla.edu

NM2298761

UNIVERSITY OF OTTAWA HEART INSTITUTE
INSTITUT DE CARDIOLOGIE DE L'UNIVERSITÉ D'OTTAWA

President and Chief Executive Officer

The University of Ottawa Heart Institute (UOHI) is one of Canada's foremost cardiovascular health centres dedicated to understanding, treating and preventing heart disease. The UOHI was founded in 1976 by a partnership between The Ottawa Hospital and the University of Ottawa, and is a bilingual, provincially incorporated, not-for-profit organization.

The UOHI has fundamental clinical responsibility for the delivery of specialized cardiovascular care to patients of The Ottawa Hospital within the population base of Eastern and Northern Ontario, Western Quebec, and Nunavut. The Institute is separately funded and solely responsible for its own budget since the enactment of the *University of Ottawa Act* by the Ontario legislature in 1999. The Institute works in close cooperation with The Ottawa Hospital in the delivery of the Hospital's cardiac care services and their relationship is governed by a Service Agreement and a series of sub-agreements. The Institute is also an important training site for undergraduate, residency and graduate programs of several Departments of the Faculty of Medicine of the University of Ottawa. A world leader in cardiac care, research, education and disease prevention, the UOHI is in the midst of a period of tremendous growth, with a dramatic increase in research, clinical activity, and physical infrastructure.

The University of Ottawa Heart Institute is seeking its next President and CEO – a strategic, visionary leader who will champion the opportunity to further enhance the Institute's capacity and reputation. Reporting to the UOHI Board of Directors, the CEO is responsible for the overall leadership and management of all aspects of the UOHI's activities in clinical care, research, education, fundraising, and collaborative stakeholder relations at the community, provincial and national levels. The new CEO will oversee a 50% expansion in UOHI's space dedicated to clinical care.

The CEO will occupy the Gordon Henderson Chair in Leadership at the University of Ottawa. The ideal candidate will bring an exceptional record of personal achievement in scholarship and clinical/professional leadership that inspires respect and confidence, combined with immediate recognition in the cardiovascular community.

For more information about the UOHI, please visit **www.ottawaheart.ca.**

Consideration of candidates will begin in November 2012. Written nominations, applications, or expressions of interest for the position should be submitted in confidence to the address shown below.

Janet Wright & Associates Inc.
174 Bedford Road, Toronto, Ontario M5R 2K9
uohi-president&ceo@jwasearch.com

Janet Wright & Associates Inc.
Senior-level recruitment for the public and not-for-profit sectors
www.jwasearch.com

JWA

NM2298759R

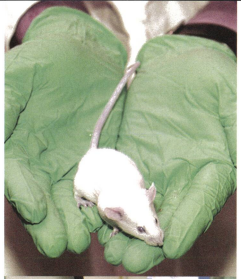

VIVARIUM
RESEARCH FACILITY

The state-of-the-art animal Research Facilities at King Abdullah International Medical Research Center are designed according to international standards to ensure the safety and humane care of research animals. Three vivariums will be inaugurated this summer in Riyadh, Dammam and Al Hassa, respectively. The animal Research Vivarium in Riyadh covers a vast 7500 square meters and offers a unique research environment that combines housing, laboratories, imaging and surgery suites located in the same area. It comprises pathogen-free housing areas equipped with the newest individualized environmental cages that can hold up to 60,000 rodents. Likewise, automated animal housing and hygienic equipments are provided for rabbits, dogs, and sheep to warrant the highest possible care. Unique to the Gulf region, the facility also accommodates aquatic animals such as Zebrafish and Xenopus. The Vivarium Research Facility provides a complete range of equipment for recombinant DNA research, and Transgenesis, together with the latest generation of Optical Imaging, Positron Emission Tomography and Magnetic Resonance Imaging. Each vivarium is staffed with highly qualified veterinarians to ensure proper handling, care and use of animals in scientific research and education in accordance with the highest scientific, humane and ethical principles. Further, each Vivarium Research Facility is open for international accreditation and regular monitoring by the Institutional Animal Care and Use Committee.

* Saudi Arabia's Population : 28.08 million

* The largest spender on healthcare in the GCC with investments totaling $24.2bn last year, according to Frost & Sullivan

* Government plans to spend $373 billion between 2010 and 2014 on social development and infrastructure projects to advance economic development

* Set to be 6th richest economy in the World in terms of GDP per capita by 2050, according to a forecast by Citibank

* The largest free economic market in the Middle East, holding 25% of the total gross national Arab income

King Abdullah International Medical Research Center

Today's Question. Tomorrow's Answer

We are an international translational health science research institution that believes in creating a knowledge-based society through our channel of extraordinary human talent.

www.kaimrc.med.sa
research1@ngha.med.sa

NM228610R

INTERNATIONAL OKAMOTO AWARD 2013

FOR A RESEARCHER WHO HAS ACHIEVED HIGHLY REMARKABLE AND INTERNATIONALLY APPRECIATED ACCOMPLISHMENT IN BASIC RESEARCH ON VASCULAR DISEASES SUCH AS HYPERTENSION, ARTERIOSCLEROSIS, DIABETES AND SO FORTH.

The Award was established in 1985, in celebration of the monumental contribution of Dr. KOZO OKAMOTO who did pioneering works on vascular diseases by the establishment of Spontaneously Hypertensive Rat (SHR). The recipients since year 2000, including one Nobel laureate, are Drs. Oliver Smithies , Kazuo Murakami , Kenji Kangawa , Marc A. Pfeffer, Antonio M. Gotto, Jr. , Kazuwa Nakao , Michael A. Gimbrone, Jr. , Toshio Ogihara, Pavel Hamet, Yo-ichi Nabeshima, Peter Libby, Theodore W. Kurtz, Shuh Narumiya and Nilesh J. Samani.

How to apply:

Only by recommendation. Please send ① letter of recommendation, ② brief curriculum vitae of the candidate, ③ summary of the candidate's research , ④ list of publications, and ⑤ reprints of some major works no more than 5 , using a set of formats fixed by the Foundation. Please ask the Secretariat to send the formats to the address of the recommender.

Deadline: January 20, 2013

The Awardee will be selected by the Award Committee of the Foundation and nominated at Board of Directors Meeting. The nomination will be announced before the end of March, 2013.

The Award:

Gold Medal and the Accessory Prize of 2 million Japanese yen.

The Award Ceremony

Is to be held in Tokyo, Japan September 6, 2013 at the 49th Annual Scientific Meeting of Society for Hypertension Related Disease Model Research. The Awardee will be invited to the ceremony by the foundation. NM228228A

JAPAN VASCULAR DISEASE RESEARCH FOUNDATION

Kokusai Kenju Bldg. 1F, 86 Jodoji Shimobanba-cho, Sakyo-ku, Kyoto 606-8413, Japan. Fax: +81-75-761-2382

NHS
National Institute for Health Research

NIHR RESEARCH PROFESSORSHIPS

Nominations are invited from Higher Education Institutions, in partnership with NHS organisations, in England for a limited number of prestigious NIHR Research Professorships. The objective of these awards is to fund leaders in the early part of their careers to lead research, to promote effective translation of research ('bench to bedside' [T_1] and 'campus to clinic' [T_2]) and to strengthen research leadership at the highest academic levels.

Up to five NIHR Research Professorships will be available in this third round. The posts aim to:

- Enable outstanding early career academics to spend a fixed 5-year period dedicated to translational (T_1 or T_2) research at Professorial level;
- Facilitate strong research leadership and develop research capacity in areas critical to accelerating the transfer of research ideas into improved health.

These awards are open to researchers who have an outstanding record of clinical and applied health research and its effective translation for improved health. Competitive candidates will demonstrate a steep career trajectory over the last 5-10 years, on course to becoming the country's most outstanding research leaders. They will currently be at consultant grade or equivalent, and be at an early career stage having spent no more than five years at their current level of seniority at the time of application (whether as Professor, Reader, Senior Lecturer/Fellow, Clinician Scientist, Group Leader or similar.) Nominees should be working in the fields of experimental medicine, public health medicine, health services research, or methodological research.

A continuing link with service delivery will be essential. NIHR Research Professors will therefore be funded to continue to spend up to 2 sessions a week delivering service directly or, if the candidate is not a health professional, an equivalent time collaborating with service. Non-NHS institutions must provide a statement from an associated NHS service provider explaining how the provider will empower the individual to promote translation at a local level directly or in collaboration.

Each award will consist of a package to support a professorship, a post-doctoral appointment, research running costs, a travel fund, access to the NIHR Leadership Programme, and the opportunity for a sabbatical, as well as the basic salary costs of the individual plus indirect costs.

Deadline for institutional nominations is **Wednesday 12th December 2012.** A maximum of two nominations will be accepted per institution. Previous applicants may reapply. Further details can be found at www.nihrtcc.nhs.uk

NM229784R

nature jobs
Attention Employers!
Stay up to date with deadlines and upcoming Naturejobs features:
Sign up for FREE employer e-alerts:
www.naturejobs.com/ealerts

United States Postal Service Statement of Ownership, Management, and Circulation (All Periodicals Publications Except Requester Publications) 1. Publication Title: Nature Medicine 2. Publication Number: 013-435 3. Filing Date: 10/1/12 4. Issue Frequency: Monthly 5. Number of Issues Published Annually: 12 6. Annual Subscription Price: $225.00 7. Complete Mailing Address of Known Office of Publication: Nature Publishing Group 75 Varick Street, 9th Floor New York, NY 10013-1917 USA Contact Person: Karen Dawson Telephone: 212-726-9369 8. Complete Mailing Address of Headquarters or General Business Office of Publisher: Nature Publishing Group 75 Varick Street, 9th Floor New York, NY 10013-1917 USA 9. Full Names and Complete Mailing Addresses of Publisher, Editor, and Managing Editor. Publisher: Melanie Brazil 75 Varick Street, 9th Floor New York, NY 10013-1917 USA Editor: Juan Carlos Lopez Nature Publishing Group 75 Varick Street, 9th Floor New York, NY 10013-1917 USA Managing Editor: Melanie Brazil 75 Varick Street, 9th Floor New York, NY 10013-1917 USA 10. Owner: Nature America, Inc. 75 Varick Street, 9th Floor New York, NY 10013-1917 USA 11. Known Bondholders, Mortgagees, and Other Security Holders Owning or Holding 1 Percent or More of Total Amount of Bonds, Mortgages or Other Securities. None. 12. Tax Status: Has Not Changed During Preceding 12 Months. 13. Publication Title: Nature Medicine14. Issue Date for Circulation Data: August 2012.15. Extent and Nature of Circulation: Average No. Copies Each Issue During Preceding 12 Months: No. Copies of Single Issue Published Nearest to Filing Date a. Total Number of Copies: 3,013; 2,875 b. Paid Circulation (1) Mailed Outside-County Paid Subscriptions Stated on PS form 3541: 926; 925 (2) Mailed In-County Paid Subscriptions Stated on PS form 3541: None; None. (3) Paid outside mail through Dealers and Carriers, Street Vendors, Counter Sales, and Other Paid Distribution Outside USPS: 1,500; 1,494 (4) Paid Distribution by other Classes Mailed Through the USPS: None; None. c. Total Paid Circulation: 2,426; 2,419 d. Free Distribution by Mail (1) Free or nominal rate Outside-County Included on PS Form 3541: 67; 68 (2) Free or Nominal Rate In-County Copies Included on PS Form 3541: None; None. (3) Free or Nominal Rate Copies Mailed at Other Classes Mailed Through the USPS: None; None. (4) Free or Nominal Rate Distribution Outside the Mail: 114; 49 e. Total Free or Nominal Rate Distribution: 182; 117 f. Total Distribution: 2,608; 2,536 g. Copies not Distributed: 405; 339 h.Total: 3,013; 2,875 i Percent Paid: 93.0%; 95.4% 16. Publication of Statement of Ownership. Publication required. Will be printed in the October 2012 issue of this publication. 17. Signature and Title of Editor, Publisher, Business Manager, or Owner: Nick Kemp, Senior Vice President of Operations Date: 10/1/12 I certify that all information furnished on this form is true and complete. I understand that anyone who furnishes false or misleading information on this form or who omits material or information requested on the form may be subject to criminal sanctions (including fines and imprisonment) and/or civil sanctions (including civil penalties). PS Form 3526, September 2007

nature OUTLOOK

Published in the 27 September issue of *Nature* and available free online for six months

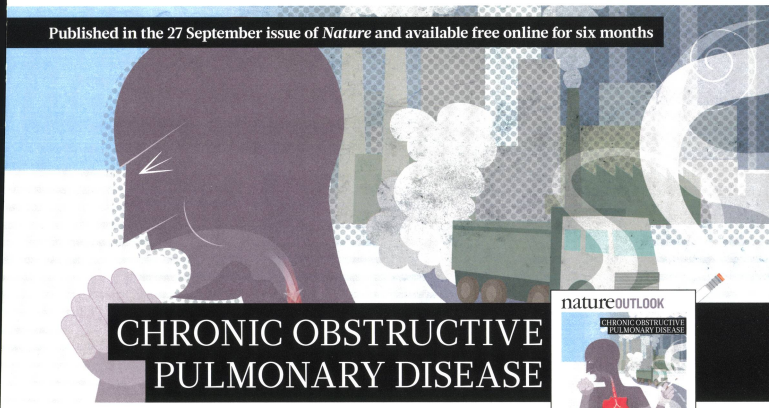

CHRONIC OBSTRUCTIVE PULMONARY DISEASE

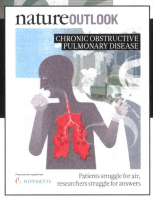

Chronic obstructive pulmonary disease (COPD) robs tens of millions of people of the ability to easily draw in the air they need to live a normal life. Although this incurable, progressive condition is difficult to diagnose, a bevy of new treatment options — including drug combinations, artificial lungs, and dietary supplements — could give COPD patients a breath of fresh air.

Access the Outlook free online for six months.
nature.com/nature/outlook/COPD

Scan this tag to access the Outlook on your smartphone

Produced with support from: NOVARTIS

If you would be interested in partnering with *Nature* on a similar project please contact: sponsorship@nature.com

It's about time

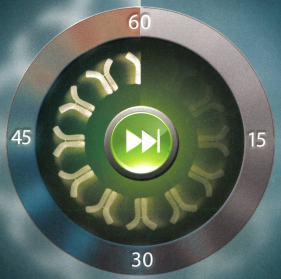

Fast forward your research with the
1-hour, 1-wash Cell Signaling Assay

eBioscience®
An Affymetrix Company

InstantOne™ Phospho ELISA

The evolution of phospho ELISAs leaps forward with the efficient sensitivity and flexibility of InstantOne ELISAs.

- **Fast:** Less than 1/3 the time of traditional ELISAs
- **Easy:** 1/4 the effort with only 1 wash step
- **Flexible:** Enables the detection of total and/or phospho protein levels of a single protein up or down a pathway on a single plate
- **Sensitive:** Meeting or exceeding industry standards with only 2-3,000 cells needed
- **Compatible:** Colorimetric detection; uses standard plate readers
- **Complete:** Over 60 kits available covering many of today's hottest targets

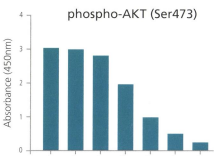

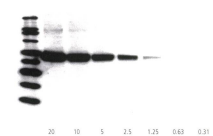

HEK cells are treated with 20% FBS for 15 min prior to lysis.

Follow us, engage with us and challenge us to support your studies.

ORDER 888.999.1371 • TECH 888.810.6168 • INQUIRIES info@eBioscience.com • WEB www.eBioscience.com
For Research Use Only. Not for use in diagnostic or therapeutic procedures.